



# CVR JOURNAL OF SCIENCE AND TECHNOLOGY

Vol.No. 18, June 2020  
P-ISSN 2277 - 3916

DOI 10.32377/CVRJST18  
E-ISSN 2581 - 7957



CVR COLLEGE OF ENGINEERING  
In Pursuit of Excellence

## ***PATRONS***

*Dr. Raghava V. Cherabuddi, President & Chairman*

*Dr. K. Rama Sastri, Director*

*Dr. K.S. Nayanathara, Principal*

***Editor*** : **Dr. K. Lal Kishore, Professor and Dean - Research, CVRCE**

***Associate Editor*** : **Dr. S. Venkateshwarlu, Professor & Head, Dept. of EEE, CVRCE**

***Technical support*** : **Mr. K. Veeranjanyulu, Asst. Prof., Dept. of CSE, CVRCE**

### ***Editorial Board :***

*Dr.M.V. Seshagiri Rao* Professor & Dean-Planning & Coordination, CVRCE

*Prof. L.C. Siva Reddy* Professor & Vice-Principal, CVRCE

*Dr. Rameshwar Rao* Professor & Dean- Projects & Consultancy, CVRCE

*Dr. N.V. Rao* Professor & Dean-Academics, CVRCE

*Dr. T. Muralidhara Rao* Professor & Head, Dept. of Civil Engg., CVRCE

*Dr. K. Venkateswara Rao* Professor & Head, Dept. of CSE, CVRCE

*Dr.K. Lalithendra* Professor & Head, Dept. of ECE, CVRCE

*Dr. S. Harivardhagini* Professor & Head, Dept. of EIE, CVRCE

*Dr. Bipin Bihari Jayasingh* Professor & Head, Dept. of IT, CVRCE

*Dr. M. Venkata Ramana* Professor & Head, Dept. of Mech. Engg., CVRCE

*Dr. H.N. Lakshmi* Professor & Head, Dept. of CSIT, CVRCE

*Dr. G. Bikshamaiah* Professor & Head, Dept. of H&S, CVRCE

### ***International Review Board:***

*Prof. Tzung-Pei Hong* Chair Professor, Dept. of CSI Engg., AI Research Center National University of Kaohsiung 811, Taiwan

*Dr. Tomonobu Senjyu* Professor, Department of Electrical Engineering, University of the Ryukyus, Nishihara-cho, Nakagami Okinawa, Japan

*Dr Masoud Mohammadian* Assoc. Professor, Faculty of Science and Technology, University of Canberra, Australia

*Dr. Rubén Ruiz García* Full Professor, Head of the Applied Optimization Systems Group, Department of Applied Statistics, Universitat Politècnica de València, Camino de Vera, Spain

*Dr. Ray-Hwa Wong* Professor, Department of Mech. Engg., Hwa-Hsia University of Technology, Taipei, Taiwan

*Dr. Stefan Talu* Faculty of Mech. Engineering, DMCDI, The Technical University of Cluj-Napoca, B-dul Muncii Street, No. 103-105, Cluj-Napoca, 400641, Romania

*Assoc. Prof. Ir. Dr. Norhaliza Abdul Wahab* Director, Control & Mechatronics Engg. Dept., Faculty of Electrical Engineering, UTM Skudai 81310 Johor

*Dr. R. Venkata Rao* Professor, Department of Mech Engg., Sardar Vallabhbhai National Institute of Technology (SVNIT), Surat, Gujarat State – 395 007, India

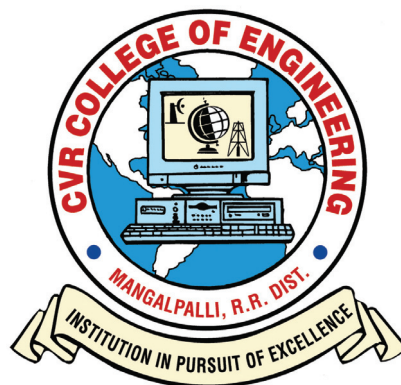
*Dr. Vijay Janyani* Professor Dept. of ECE, Malaviya National Institute of Technology (MNIT), Jaipur - 302017 (Rajasthan)

*Dr.V. Prasanna Venkatesan* Prof. & Head, Department of Banking Technology, School of Management, R.V.Nagar, Kalapet, Pondicherry University, Puducherry

# CVR JOURNAL OF SCIENCE AND TECHNOLOGY

## Indexed by

- Google Scholar
- Directory of Research Journals Indexing (DRJI)
- Scientific Indexing Services (SIS)
- International Institute of Organised Research (I2OR)
- Scholar Impact - Journal Index
- Citefactor
- Member Crossref / DOI



***NIRF Ranking of 141 in the Country***

**Accredited by NAAC with 'A' GRADE**

## **CVR COLLEGE OF ENGINEERING**

(UGC Autonomous - Affiliated to JNTU Hyderabad)

Mangalpalli (V), Ibrahimpatnam (M),

R.R. District, Telangana. – 501510

<http://cvr.ac.in>



# EDITORIAL

We are delighted to bring out Volume – 18 of the Biannual- CVR Journal of Science and Technology, due in June 2020, almost in time, without any delay, despite the difficulties created by COVID-19 Pandemic. Corona Virus has affected the whole world. Educational field is also badly affected. On-Line Teaching methods, video conferences, meetings etc. are used effectively, by many in post CIVID-19 scenario. New methods and technology usage may be seen in teaching - learning process.

This Volume has DOI number and e-ISSN number along with print ISSN number on the cover page. Every research article published is given DOI number and they can be accessed on- line. On-line portal is also created for the Journal. This Volume is also brought out in time, with the co-operation of all the authors and editorial team, despite some issues with Anti-plagiarism software. We are thankful to the Management for supporting this activity, and permitting to publish the journal in color print, using quality printing paper.

Editorial Team of CVR Journal thanks all the authors, contributors, reviewers and the management in helping us in bringing out Volume-18, almost in time in this difficult period. As all educational institutions were closed for a long time, authors and reviewers had many constraints, but Wi-Fi connectivity is very well used to overcome the difficulties and we all could connect successfully in completing the task in time.

The Volume covers research articles in the following disciplines: the breakup of papers is:

**CIVIL – 3, ECE – 7, EEE – 4, EIE – 3, CSE – 3, MECH – 4, H & S – 1**

In this issue also, total number of research articles published is increased to 25.

This issue carries an interesting article on the effect of several admixtures in the strength of light weight clay pertaining to civil engineering. In the same area, two more research articles relating to Fiber concrete and FEM Method are published. A research paper on implementation of 2x2 MIMO-OFDM system and another on gender classification from speech signal are also published in the branch of electronics and communication engineering. Rapid diagnosis of Malaria, a method using blood smear is explained in one article. Research papers published in this issue are expected to be of much interest to the readers.

I am thankful to all the members of the Editorial Board for their help in reviewing and short listing the research papers for inclusion in the current Volume of the journal. I wish to thank **Dr. S. Venkateshwarlu, HOD, EEE** for the effort made in bringing out this Volume. Thanks are due to **HOD, H & S, Dr. G. Bhikshamaiah** and the staff of English Department for reviewing the papers. I am also thankful to **Smt. A. Sreedevi, DTP Operator** in the Office of Dean Research for the preparation of research papers in Camera - Ready form.

For further clarity on waveforms, graphs, circuit diagrams and figures, readers are requested to browse the soft copy of the journal, available on the college website [www.cvr.ac.in](http://www.cvr.ac.in) wherein a link is provided. Authors can also submit their papers through our online open journal system(OJS) [www.ojs.cvr.ac.in](http://www.ojs.cvr.ac.in) or [www.cvr.ac.in/ojs](http://www.cvr.ac.in/ojs)

**Prof. K. Lal Kishore**  
**Editor**



## Patrons:

**Dr. Raghava V. Cherabuddi**  
President & Chairman  
CVR College of Engineering,  
Vastunagar, Mangalpalli (V),  
Ibrahimpatnam (M)  
Rangareddy (D),  
Telangana 501 510.  
E-mail: drcvraghava@gmail.com  
Phone: 040-42204001, 02,03

**Dr. K. Rama Sastri**  
Director  
CVR College of Engineering,  
Vastunagar, Mangalpalli (V),  
Ibrahimpatnam (M)  
Rangareddy (D), Telangana 501 510.  
E-mail: director@cvr.ac.in  
Phone: 08414-661666, 661601,661675

**Dr. K.S. Nayanathara**  
Principal  
CVR College of Engineering,  
Vastunagar, Mangalpalli (V), Ibrahimpatnam (M)  
Rangareddy (D), Telangana 501 510.  
E-mail: principal@cvr.ac.in  
Phone: 08414-6616602, 661601,661675

## Editor:

**Dr. K. Lal Kishore**  
Professor and Dean Research  
CVR College of Engineering  
Vastunagar, Mangalpalli (V),  
Ibrahimpatnam (M)  
Rangareddy (D), Telangana 501  
510.  
E-mail: lalkishorek@gmail.com  
lalkishore@cvr.ac.in  
Mobile: +91 8309105423 , +91  
9618023478  
Phone: 08414-661658,  
661601,661675

## Associate Editor:

**Dr. S. Venkateswarlu**  
Professor & Head  
Dept of Electrical and Electronics  
Engineering  
CVR College of Engineering  
Vastunagar, Mangalpalli (V),  
Ibrahimpatnam (M)  
Rangareddy (D), Telangana 501 510.  
E-mail: svip123@gmail.com  
hod.eee@cvr.ac.in  
Mobile: +91 9490749568  
Phone: 08414-661661

## Technical Support:

**Mr. K. Veeranjanyulu**  
Asst. Prof.  
Dept. of Computer Science & Engineering  
CVR College of Engineering  
Vastunagar, Mangalpalli (V), Ibrahimpatnam (M)  
Rangareddy (D),  
Telangana 501 510.  
E-mail: kveeru876@gmail.com  
Mobile: +91 9177462507

## Editorial Board:

**Dr.M.V. Seshagiri Rao**  
Professor & Dean-Planning &  
Coordination  
CVR College of Engineering  
Vastunagar, Mangalpalli (V),  
Ibrahimpatnam (M)  
Rangareddy (D),  
Telangana 501 510.  
E-mail:  
rao\_vs\_meduri@yahoo.com  
sheshagiri.rao@cvr.ac.in  
Mobile: +91 9440361817  
Phone:08414-661617

**Prof. L.C. Siva Reddy**  
Professor & Vice-Principal  
CVR College of Engineering  
Vastunagar, Mangalpalli (V),  
Ibrahimpatnam (M)  
Rangareddy (D),  
Telangana 501 510.  
E-mail: siva\_reddy@cvr.ac.in  
Mobile: +91 9885806151  
Phone:08414-661656

**Dr. Rameshwar Rao**  
Professor & Dean- Projects &  
Consultancy  
CVR College of Engineering  
Vastunagar, Mangalpalli (V),  
Ibrahimpatnam (M)  
Rangareddy (D),  
Telangana 501 510.  
E-mail:  
rameshwar\_rao@hotmail.com  
rameshwar\_rao@cvr.ac.in  
Mobile: +91 9394483591  
Phone:08414-661659

**Dr. N.V. Rao**  
Professor & Dean-Academics  
CVR College of Engineering  
Vastunagar, Mangalpalli (V),  
Ibrahimpatnam (M)  
Rangareddy (D),  
Telangana 501 510.  
E-mail:  
nvraghresh@gmail.com  
nv.rao@cvr.ac.in  
Mobile: +91 9440506701  
Phone:08414-661667

**Dr. T. Muralidhara Rao**  
Professor & Head  
Dept. of Civil Engineering  
CVR College of Engineering  
Vastunagar, Mangalpalli (V),  
Ibrahimpatnam (M)  
Rangareddy (D),  
Telangana 501 510.  
E-mail:  
tmuralidhararao@gmail.com  
tmuralidhararao@cvr.ac.in  
Mobile: +91 9989214274  
Phone:08414-661653

**Dr. K. Venkateswara Rao**  
Professor & Head  
Dept. of Computer Science &  
Engineering  
CVR College of Engineering  
Vastunagar, Mangalpalli (V),  
Ibrahimpatnam (M)  
Rangareddy (D),  
Telangana 501 510.  
E-mail:  
kvenkat.cse@gmail.com  
kv.rao@cvr.ac.in  
Mobile: +91 9493809566  
Phone:08414-661655

**Dr.K. Lalithendra**  
Professor & Head  
Dept. of Electronics and  
Communication Engineering  
CVR College of Engineering  
Vastunagar, Mangalpalli (V),  
Ibrahimpatnam (M)  
Rangareddy (D),  
Telangana 501 510.  
E-mail: lkurra@gmail.com  
lalithendra@cvr.ac.in  
Mobile: +91 9871483379  
Phone:08414-661660

**Dr. S. Harivardhagini**  
Professor & Head  
Dept of Electronics and  
Instrumentation Engineering  
CVR College of Engineering  
Vastunagar, Mangalpalli (V),  
Ibrahimpatnam (M)  
Rangareddy (D),  
Telangana 501 510.  
E-mail:  
Harivardhagini@gmail.com  
Mobile: +91 9985147962  
Phone:08414-661653

**Dr. Bipin Bihari Jayasingh**  
Professor & Head  
Dept. of Information Technology  
CVR College of Engineering  
Vastunagar, Mangalpalli (V),  
Ibrahimpatnam (M)  
Rangareddy (D),  
Telangana 501 510.  
E-mail:  
bipinbjayasingh@cvr.ac.in  
Mobile: +91 9440476544  
Phone:08414-661664

**Dr. M. Venkata Ramana**  
Professor & Head  
Dept. of Mechanical Engg  
CVR College of Engineering  
Vastunagar, Mangalpalli (V),  
Ibrahimpatnam (M)  
Rangareddy (D),  
Telangana 501 510.  
E-mail:  
vramanamaringanti@cvr.ac.in  
Mobile: +91 9948084192  
Phone:08414-661689

**Dr. H. N. Lakshmi**  
Professor & Head  
Dept. of Computer Science &  
Information Technology  
CVR College of Engineering  
Vastunagar, Mangalpalli (V),  
Ibrahimpatnam (M)  
Rangareddy (D),  
Telangana 501 510.  
E-mail: hn.lakshmi@cvr.ac.in  
Mobile: +91 9849698045

**Dr. G. Bikshamaiah**  
Professor & Head  
Dept. of Humanities and Science  
CVR College of Engineering  
Vastunagar, Mangalpalli (V),  
Ibrahimpatnam (M)  
Rangareddy (D),  
Telangana 501 510  
E-mail: gbcvr17@gmail.com  
hod.hns@cvr.ac.in  
Mobile: +91 9949565350  
Phone:08414-661631





## International Review Board

### Prof. Tzung-Pei Hong

Chair Professor  
Department of Computer  
Science and Information  
Engineering  
AI Research Center  
National University of  
Kaohsiung  
No. 700, Kaohsiung University  
Road, Nan-Tzu District  
Kaohsiung 811, Taiwan  
Tel:(07)5919191, 5919398  
Fax:(07)5919049  
Email: [tphong@nuk.edu.tw](mailto:tphong@nuk.edu.tw)  
Website: [tphong.nuk.edu.tw](http://tphong.nuk.edu.tw)

### Dr. Ray-Hwa Wong

Professor  
Department of Mechanical Eng.,  
Hwa-Hsia University of Technology, Taiwan,  
111 Gong Jhuan Rd., Chung Ho,  
Taipei, Taiwan, R.O.C.  
E-mail : [rhwong@cc.hwh.edu.tw](mailto:rhwong@cc.hwh.edu.tw)  
Phone / Mobile Number : +886-2-8941-5129  
ex 2108/+886-918-706-985

### Dr. R. Venkata Rao

Professor, Department of Mechanical  
Engineering  
Sardar Vallabhbhai National Institute of  
Technology (SVNIT), Surat  
Ichchanath, Surat, Gujarat State – 395 007,  
India,  
Contact Nos.: 02612201982(O),  
02612201661(R), 9925207027(M)  
Email ID: [ravipudirao@gmail.com](mailto:ravipudirao@gmail.com),  
[rvr@med.svnit.ac.in](mailto:rvr@med.svnit.ac.in)  
Website:  
[http://svnit.ac.in/facup/5274Rao-  
Resume.pdf](http://svnit.ac.in/facup/5274Rao-Resume.pdf)

### Dr. Tomonobu Senjyu

Professor  
Department of Electrical  
Engineering  
University of the Ryukyus,  
Nishihara-cho,  
Nakagami Okinawa, Japan  
Tel:( +81-98-895-8686)  
Email: [b985542@tec.u-  
ryukyu.ac.jp](mailto:b985542@tec.u-ryukyu.ac.jp)

### Dr. Stefan Talu

DMCDI  
The Technical University of Cluj-Napoca  
Faculty of Mechanical Engineering,  
B-dul Muncii Street, No. 103-105, Cluj-  
Napoca, 400641,  
Romania  
<http://research.utcluj.ro>.  
E-mail([uri](mailto:stefanta@mail.utcluj.ro)) [stefanta@mail.utcluj.ro](mailto:stefanta@mail.utcluj.ro),  
[stefan\\_talu@yahoo.com](mailto:stefan_talu@yahoo.com)  
Telephone(s) Fixed line phone:  
004 0264 401 200.  
Mobile phone: 004 0744263660

### Dr. Vijay Janyani

Professor  
Dept. of Electronics and Communication  
Engineering  
Malaviya National Institute of  
Technology (MNIT)  
Jaipur - 302017 (Rajasthan)  
India.  
[www.mnit.ac.in](http://www.mnit.ac.in)  
Email ID: [vijay.janyani@ieee.org](mailto:vijay.janyani@ieee.org)

### Dr. Rubén Ruiz García

Full Professor. Head of the  
Applied Optimization Systems  
Group  
Department of Applied Statistics,  
Operations Research and Quality  
Universitat Politècnica de  
València  
Camino de Vera s/n, Edificio 7A,  
46022, Valencia, Spain  
[r Ruiz@eio.upv.es](mailto:r Ruiz@eio.upv.es)  
<http://soa.iti.es/r Ruiz>

### Dr Masoud Mohammadian

Associate Professor  
Faculty of Science and  
Technology  
University of Canberra ACT  
2601  
Phone: +61 (0)2 6201 2917  
Fax: +61 (0)2 6201 5231  
Email:[masoud.mohammadian  
@canberra.edu.au](mailto:masoud.mohammadian@canberra.edu.au)  
Website:[https://research  
profiles.canberra.edu.au/en/p  
ersons/masoud-mohammadian](https://researchprofiles.canberra.edu.au/en/persons/masoud-mohammadian)

### Assoc. Prof. Ir. Dr Norhaliza Abdul Wahab

Director,  
Control & Mechatronics Engineering  
Department  
Faculty of Electrical Engineering  
UTM Skudai 81310 Johor  
Malaysia  
Phone: +607-5557023, 012-5444297 (HP)  
Email: [aliza@fke.utm.my](mailto:aliza@fke.utm.my)  
URL: <http://norhaliza.fke.utm.my/>

### Dr.V.Prasanna Venkatesan

Prof. & Head  
Department of Banking Technology,  
School of Management, R.V.Nagar,  
Kalapet, Pondicherry University,  
Puducherry – 605014,  
India.Telephone No: 0413 - 2654 652  
Mobile No: 0091-9486199939  
Email: [prasanna.btm@pondiuni.edu.in](mailto:prasanna.btm@pondiuni.edu.in),  
[prasanna\\_v@yahoo.com](mailto:prasanna_v@yahoo.com)



## CONTENTS

Page No.

1. Effect of Mineral Admixture, W/B Ratio and Elevated Temperature on Strength of Lightweight Expanded Clay Aggregate Concrete <i>V. Sravan, T. Manoj, Dr. M. V. Seshagiri Rao</i>	1
2. Influence of Temperature on the Fracture Parameters of Basalt Fiber Concrete <i>N. Shiva kumar, Dr. T. Muralidhara Rao</i>	8
3. Analysis of Beam-Column Joints using FEM <i>Ch. Harika, Dr. N. Murali Krishna</i>	14
4. Implementation of 2x2 MIMO-OFDM System using Universal Software Radio Peripherals <i>Dr. Yedukondalu Kamatham, Naveen Talati</i>	22
5. Exploring Gender Classification from Speech Signal using Java-DSP Tool <i>Dr. G. Sasi</i>	28
6. A Cluster Head Routing Protocol for Improving Network Lifetime in Wireless Sensor Networks <i>Dr. Gaurav Sharma</i>	32
7. Low Power PCI Controller using Design Compiler <i>T. Subha Sri Lakshmi</i>	38
8. Implementation of Pilot Channel Estimation Techniques for OFDM System with Low Mean Square Error <i>T Padmavathi, Dr. Kusma Kumari Cheepurupalli, Dr. R Madhu</i>	43
9. ARM Based Smart Living System using Brain Computer Interface <i>K. Arun Kumar, R. Satya Prakash, M. Vinod Kumar Reddy</i>	49
10. Flood Inundation Warning and Relief System Based on GIS and Remote Sensing <i>B. Teena, Dhruva R. Rinku</i>	55
11. Fast-Converging Speed and Zero Oscillation MPPT Method for PV system <i>Dr. G. Sree Lakshmi, Dr. S. Harivardhagini</i>	62
12. Design of Enhanced PLL for Single-Phase Grid Connected Transformerless Inverters <i>G. Janardhan, Dr. G.N.Srinivas, Dr. N.N.V. Surendrababu</i>	71
13. Optimal Supplementary Controller Design for IPFC to Damp Low-Frequency Oscillations in Power Systems <i>Dr. Shankarappa F Kodad, Dr. Dakka. Obulesu, Manjunatha S C</i>	76
14. Cascaded H-Bridge Inverter for Wind Driven Isolated Squirrel Cage Induction Generators <i>G. Manohar, K Chiranjeevi</i>	81
15. Rapid Diagnosis of Malaria using Images of Stained Blood Smear <i>Dr. Narendra B. Mustare</i>	88
16. A Smart Machine Vision based Inspection System <i>Dr. Santosh Kumar Sahoo</i>	94
17. Machine Vision based Color Recognition by Robotic Arm using LabVIEW <i>Y. Divya, C. Pramod Kumar</i>	100
18. Loan Delinquency Prediction using Machine Learning Techniques <i>B. Ashwin Kumar, Chadive Koushik Reddy, Chilukamarri Krishna Srinivas, Koya Lokesh Reddy</i>	105
19. Blockchain-based E-Voting System using Proof of Voting (PoV) Consensus Algorithm <i>S Srinivas, B. Ashwin Kumar, R. Srishylam</i>	110
20. Reducing Overfitting Problem in Machine Learning using L1/4 Activation Function <i>Sathya Prakash Racharla, Mohammad Umar, V. D. S. Krishna</i>	115
21. Yttrium Chloride as Corrosion Inhibitor for 6061Al- SiC Composites in 1:1 mixture of HNO <sub>3</sub> + HCl <i>P. Lava Kumar</i>	119
22. Hazard Rate Diagnosis of Heavy Earth Moving Machinery using 2-parameter Weibull Analysis <i>A. Suresh</i>	124
23. CFD Analysis of DI Diesel Engine using Exhaust Gas Recirculation <i>Sk. Mohammad Shareef, A. L .N. Arun Kumar, T. Venkatesh</i>	132
24. Optimization of Machining Process by Desirability Function Analysis (DFA): A Review <i>Pathalavathi Bhaskar, Sarat Kumar Sahoo</i>	138
25. Microwave Assisted One Pot Synthesis of Functionalized Pyrrole Derivatives Catalyzed by Uranyl Nitrate Hexa Hydrate <i>Dr. K. Venkatesan, Dr. Pagadala Ramakanth, Dr. Ch. Anjaneyulu</i>	144
➤ <i>Appendix: Template of CVR Journal</i>	148
● <i>Papers accepted for next issue (Vol.19, December 2020)</i>	150



# Effect of Mineral Admixture, W/B Ratio and Elevated Temperature on Strength of Lightweight Expanded Clay Aggregate Concrete

Veeramala sravan<sup>1</sup>, Tangudu Manoj<sup>2</sup> and Dr. M. V. Seshagiri Rao<sup>3</sup>

<sup>1</sup>PG Scholar, CVR College of Engineering/Civil Engg. Department, Hyderabad, India  
Email: sravanveeramalla999@gmail.com

<sup>2</sup>Asst. Professor, CVR College of Engineering/Civil Engg. Department, Hyderabad, India  
Email: manoj.tangudu03@gmail.com

<sup>3</sup>Professor, CVR College of Engineering/Civil Engg. Department, Hyderabad, India  
Email: rao\_vs\_meduri@yahoo.com

**Abstract:** The present paper focused on development of structural lightweight concrete by using light weight expanded clay aggregate (LECA) with unit weight of 1700 kg/m<sup>3</sup> to 1900 kg/m<sup>3</sup> and compressive strength of 40 MPa. In this study, investigation was done using LECA as coarse aggregate in concrete by replacing normal aggregate in three differing volume fractions i.e., 30%, 40% and 50% with different w/b ratios 0.40, 0.50 and 0.60 to produce lightweight expanded clay aggregate concrete (LECAC) with addition of chemical admixture. For that, concrete mix design was done using IS method and replacement of lightweight aggregate was calculated based on volume batching. The effect of mineral admixture (i.e., 10% microsilica) on the properties of lightweight expanded clay aggregate concrete and normal weight aggregate concrete such as workability of fresh concrete, compressive strength and flexural strength of concrete were compared. The studies also include the effect of elevated temperature on light weight expanded clay aggregate concrete and normal weight aggregate concrete.

**Index Terms:** Normal weight aggregate concrete (NWAC), Light weight expanded clay aggregate (LECA), Light weight expanded clay aggregate concrete (LECAC), Elevated temperature.

## I. INTRODUCTION

Light weight expanded clay aggregate is a special type of aggregate which is formed by heating clay with no or very little content of lime. The clay is dried, heated and burned in rotary kiln at a temperature of 1100°C - 1300°C. Since it is exposed to high temperature as a result, gas is released inside the pellets and entrapped in it during cooling whilst the organic compounds burnt off forcing the pellets to bloated producing ceramic pellets with porous and formed a honeycombed structure. Outer surface of each granule is sintered. Pore structure gives light weight and high crushing resistance, thermal as well as sound insulation to the material. It has a circular or a potato shape formed due to circular movements in the kiln.

LECA consist of rounded pellets with a vesicular texture. In generally, LECA is a dark brown or reddish or grey in colour. These differences in colours could be associated to the varieties in LECA chemical composition. LECA is available in different sizes varying 0.1 mm to 25 mm, which

is suitable for fine aggregate, coarse aggregate, and both of them. Bulk density of LECA ranges from 250 to 750 kg/m<sup>3</sup>. It is used in making lightweight concrete products and for other uses.

The aim of the present study is to determine the mechanical properties of LECAC. The LECA was used in place of normal weight coarse aggregate in three differing volume fractions i.e., LECAC30(30% LECA+70% GRAVEL), LECAC40(40% LECA +60% GRAVEL) and LECAC50 (50% LECA+ 50% GRAVEL), with different w/b ratios 0.40, 0.50 and 0.60 to produce a lightweight expanded clay aggregate concrete (LECAC). The effect of elevated temperature on the mechanical properties of the light weight expanded clay aggregate concrete is also studied.

## II. LITERATURE REVIEW

Alaa M.Rashad studied use of light weight expanded clay aggregate as a building material. An overview of LECA as a building material is given. According to the study conclusions are LECA has a positive effect on workability, decreases the specific tensile creep. It improves sound isolation.

K. Akcaozoglu, S.Akcaozoglu made experimentally studied on the effect of elevated temperature on the lightweight concrete produced by expanded clay aggregate and calcium aluminate cement. The residual strength of mixtures produced by expanded clay aggregate were higher than the concrete produced by natural aggregates.

Abhijitsinh Parmar, Urvish Patel studied the fresh concrete properties using Lightweight Expanded clay aggregate (LECA) and Expanded Polystyrene Beads (EPS) by replacing coarse aggregates. LECA can be used as a replacement for coarse aggregate compared to EPS with low workability.

Anil Kumar R, P. Prakash studied the mechanical properties of structural concrete by blending cinder and LECA. The strength properties of lightweight concrete produced by replacing coarse aggregate for M30 grade of concrete were studied. Concrete with 60% Cinder and LECA 40% had an average compressive strength of 36.52N/mm<sup>2</sup> and split tensile strength of 2.5N/mm<sup>2</sup>.

**Omar A. Abdulkareem, A.M. Mustafa al Bakri** examined that effect of elevated temperatures on the thermal behavior and mechanical performance of fly ash geopolymer paste, mortar and light weight concrete. They presented the characteristics of the FA geopolymer paste, mortar and LWAGC before and after exposed to elevated temperatures of 400°C, 600°C and 800°C.

**III. MATERIALS**

*Cement*

Ordinary Portland cement of 53 grade cement is used. The Physical properties are tested according to IS 4031-1998 and results are tabulated in Table I.

TABLE I.  
PHYSICAL PROPERTIES OF OPC 53

S. No.	Property	Test method	Test Results	IS Specification
1	Fineness	Sieve test	2.4%	10%
2	Specific Gravity	Specific gravity bottle	3.14	3.10-3.25
3	Normal Consistency	Vicat apparatus	31%	26-33%
4	Initial Setting time	Vicat apparatus	45 min	Not less than 30 min

*COARSE AGGREGATE*

*Gravel*

Aggregates passing from 12mm and retained on 20 mm aggregates are used. Properties of coarse aggregates are tabulated in Table II.

*LECA*

Light weight expanded clay aggregate of size from 8mm to 12mm is used as coarse aggregate. properties of LECA are tested and results are tabulated in Table II.

TABLE II.  
PHYSICAL PROPERTIES OF F.A, C.A(GRAVEL AND LECA)

S.No.	Property	Fine Aggregate	Coarse Aggregate	
			Gravel	LECA
1	Fineness modulus	3.08	6.41	5.84
2	Specific gravity	2.6	2.88	0.66
3	Bulk density	1440 Kg/m <sup>3</sup>	1450 kg/m <sup>3</sup>	413 kg/m <sup>3</sup>
4	Water absorption	1%	0.6%	15%

*Water*

Portable water is used in the preparation of concrete mixes.

*Super Plasticizer*

CONPLAST SP 430 is used as the chemical admixture.

*Micro Silica*

Micro silica is used as a mineral admixture in the concrete.

TABLE III.  
QUANTITIES REQUIRED FOR 1 M<sup>3</sup>

w/c ratio	Cement Kg/m <sup>3</sup>	Micro silica Kg/m <sup>3</sup>	Water Kg/m <sup>3</sup>	SP dosage %	Fine aggregate Kg/m <sup>3</sup>	Coarse aggregate Kg/m <sup>3</sup>		
						LECAC30 (30%LECA +70%Gravel) Kg/m <sup>3</sup>	LECAC40 (40%LECA +60%Gravel) Kg/m <sup>3</sup>	LECAC50 (50%LECA +50%Gravel) Kg/m <sup>3</sup>
0.4	331	0	132	1.5%	711	96.228+952.56	128.30+816.48	160.38+680.4
0.4	331	33.1	145	1.5%	702	95.04+940.8	126.72+806.04	158.4+672
0.5	331	0	165	1%	718	89.1+882	118.8+756	148.5+630
0.5	331	33.1	182	1%	704	84.38+860	108.504+740.88	135.64+575.4
0.6	331	0	199	0%	723	82.368+815.36	109.824+698.88	137.2+582.4
0.6	331	33.1	218	0%	697	80.388+795.76	107.18+682.08	133.98+568.4

*FINE AGGREGATE*

River sand is used as fine aggregate. The requirements of sand is confirming to IS: 383-1970 and the properties of fine aggregate tested are tabulated in Table II.

**IV. EXPERIMENTAL STUDY**

*Workability*

The workability is measured by conducting the Slump cone test using standard Procedure prescribed in IS: 1199 - 1959. Results are tabulated in Table IV.

TABLE IV.  
WORKABILITY AND UNIT WEIGHT

w/c ratio.	LECA vol. fraction %	SP dosage	Without Micro silica		With micro silica	
			Slump (mm)	Unit weight (kg/m <sup>3</sup> )	Slump (mm)	Unit weight (kg/m <sup>3</sup> )
0.40	0	1.5%	50	2288	47	2388
	30	1.5%	52	1829.8	50	1890.2
	40	1.5%	52	1754.2	54	1825.1
	50	1.5%	55	1731.2	58	1746.2
0.50	0	1%	52	2314	49	2341
	30	1%	56	1821.4	52	1882.3
	40	1%	60	1749.5	58	1820.4
	50	1%	67	1728.6	66	1745.5
0.60	0	0%	64	2256	62	2286
	30	0%	70	1809	66	1874.4
	40	0%	73	1747.8	68	1813.5
	50	0%	88	1722.5	75	1742.9

*Compressive strength*

Cube size of 150mm x150mm x 150mm cube specimens are caste and cured for 28 days and tested under Automatic compression testing machine of 3000KN capacity and the results are tabulated in Table V.

TABLE V.  
PERCENTAGE INCREASE IN COMPRESSIVE STRENGTH ATAGE OF 28 DAYS WITH AND WITHOUT ADDITION OF MINERAL ADMXTURE (MICROSILICA).

w/c ratio	leca vol. fraction %	compressive strength mpa		% of increase in compressive strength
		without micro silica	with micro silica	
0.4	0	55	59	7.2
	30	27.04	29.2	7.9
	40	24.93	27.04	8.5
	50	20.56	24.9	21.1
0.5	0	52	56.36	8.4
	30	24.7	27.04	9.5
	40	23.3	25.73	10.4
	50	18.8	22.66	20.53
0.6	0	46.6	50.7	9.2
	30	22.1	24.24	9.7
	40	20.66	22.88	10.7
	50	18.2	21.53	18.34

*Flexural strength*

Prisms of size 100mm x100mm x500mm were caste and cured for 28 days and tested in flexural testing machine and results are tabulated in Table VI and Table VII.

TABLE VI.  
FLEXURAL STRENGTH OF NWC MIXES WITH AND WITHOUT MICROSILICA

W/C ratio	Flexural strength (MPa)	
	Without Micro silica	With Micro silica
0.4	5.19	5.3
0.5	4.9	5.2
0.6	4.7	4.9

TABLE VII.  
FLEXURAL STRENGTH OF LECAC30 MIXES WITH AND WITHOUT MICRO SILICA

W/C ratio	Flexural strength (MPa)	
	Without Micro silica	With Micro silica
0.4	3.64	3.8
0.5	3.4	3.6
0.6	3.2	3.4

*Effect of elevated temperature*

High temperature furnace of 1000°C capacity is used to evaluate the fire resistance. The casted cubes are placed in the high temperature furnace for 02 hrs at different temperatures 200°C, 400°C, 600°C & 800°C. After two hours cubes were taken out and tested residual compressive strength, weight loss and the results are tabulated in Table VIII - Table XIII.

TABLE VIII.  
RESIDUAL COMPRESSIVE STRENGTH OF NWAC CUBES

W/C	Temperature (°C)	Compressive strength (MPa)		% of variation	
		NWAC Without micro silica	NWAC with micro silica	NWAC without micro silica	NWAC with micro silica
0.4	0	55	59	0	0
	200	50.63	52.4	7.9	11.1
	400	49.2	49.4	10.5	16.2
	600	44.9	45	18.3	23.7
	800	18	21	67.2	64.4
0.5	0	52	57	0	0
	200	44.8	47.2	13.8	17.1
	400	42.3	35.4	18.6	37.8
	600	38.4	28.3	26.1	50.3
	800	11.65	18.4	77	67.7
0.6	0	46.6	50.9	0	0
	200	36.9	38.9	20.8	23.5
	400	32.16	32.63	30.9	35.8
	600	27.14	22.6	41.7	55
	800	9.4	12.8	79.8	74.8

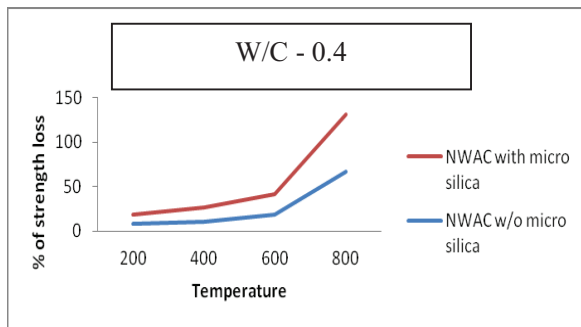


Figure 1. Loss of compressive strength at different temperatures - NWAC

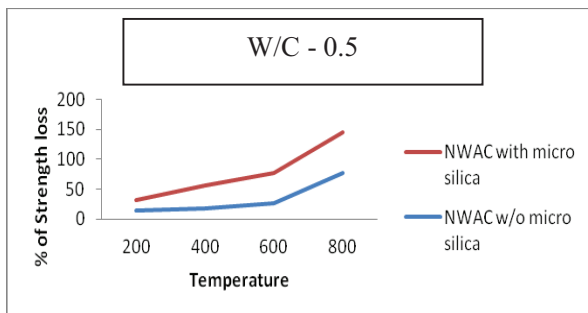


Figure 2. loss of compressive strength at different temperatures - NWAC

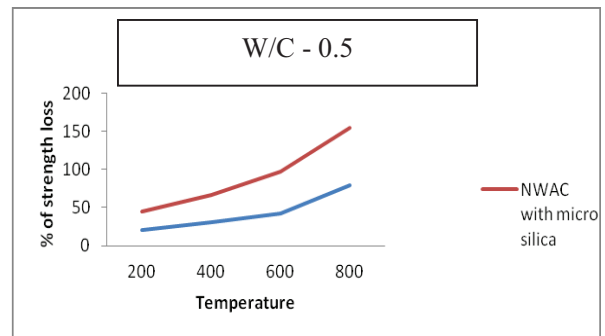


Figure 3. Loss of compressive strength at different temperatures - NWAC

TABLE IX.  
RESIDUAL COMPRESSIVE STRENGTH OF LECAC30 CUBES

W/C	Temperature (°C)	Compressive strength (MPa)		% of variation	
		LECAC 30 without micro silica	LECAC 30 with micro silica	LECAC 30 without micro silica	LECAC 30 with micro silica
0.4	0	27.04	29.20	0	0
	200	26.6	28.2	1.6	3.4
	400	24.7	27.96	8.6	4.2
	600	22.5	26.4	16.8	9.5
	800	18.53	21.3	31.4	27
0.5	0	24.7	27.2	0	0
	200	23.73	27	3.9	7.3
	400	21.76	24.56	11.9	9.7
	600	18.92	21.1	23.4	22.4
	800	10.93	15.1	55.7	44.4
0.6	0	22.1	23.9	0	0
	200	18.25	21.6	17.4	19.6
	400	17.86	21.5	19.1	10.0
	600	16.5	18.1	25.3	24.2
	800	7.54	12	66	49.7

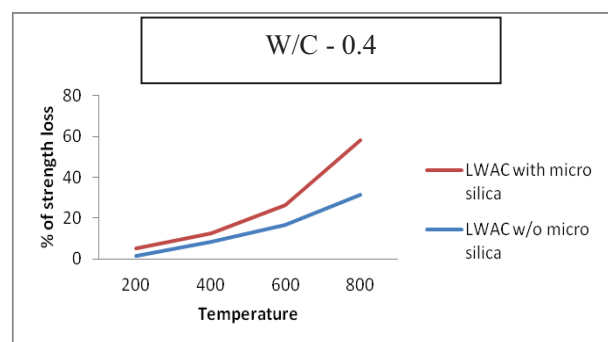


Figure 4. Loss of compressive strength at different temperatures - LECAC30



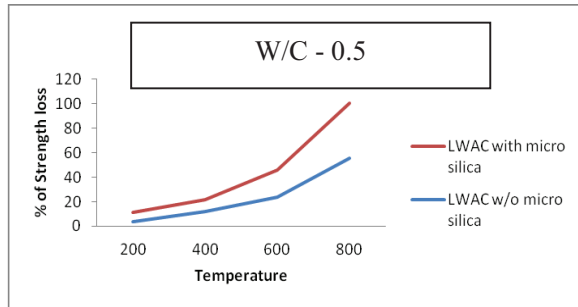


Figure 5. Loss of compressive strength at different temperatures – LECAC30

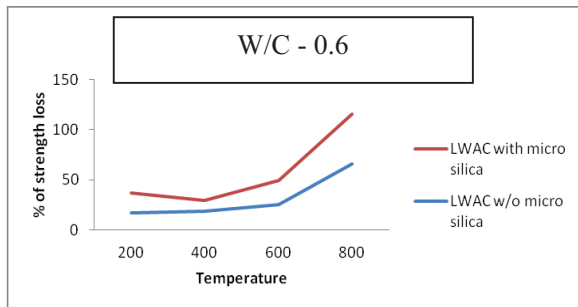


Figure 6. Loss of compressive strength at different temperatures – LECAC30

TABLE X.  
AVERAGE PERCENTAGE OF WEIGHT LOSS OF NWAC WITHOUT MICROSILICA AT DIFFERENT TEMPERATURES

W/C	Temperature (°C)	Weight before placing in furnace (kg)	Weight after placing in furnace (kg)	% of variation
0.4	200	8.57	8.52	1.0
	400	8.55	8.25	3.5
	600	8.37	8.02	4.1
	800	8.48	8.03	5.3
0.5	200	8.39	8.29	1.1
	400	8.58	8.28	3.4
	600	8.45	7.99	5.4
	800	8.43	7.92	6.0
0.6	200	8.54	8.4	1.6
	400	8.29	7.91	4.5
	600	8.36	7.88	5.7
	800	8.29	7.58	8.5

TABLE XI.  
AVERAGE PERCENTAGE OF WEIGHT LOSS OF NWAC WITH MICROSILICA AT DIFFERENT TEMPERATURES

W/C	Temperature (°C)	Weight before placing in furnace (kg)	Weight after placing in furnace (kg)	% of variation
0.4	200	8.32	8.23	1.6
	400	8.4	8.03	4.4
	600	8.29	7.66	7.5
	800	8.37	7.65	8.6
0.5	200	8.55	8.44	1.2
	400	8.04	7.66	4.7
	600	8.16	7.59	6.9
	800	8.42	7.8	7.3
0.6	200	8.25	8.12	1.6
	400	8.36	7.9	5.5
	600	8.35	7.52	9.9
	800	8.37	7.48	10.6

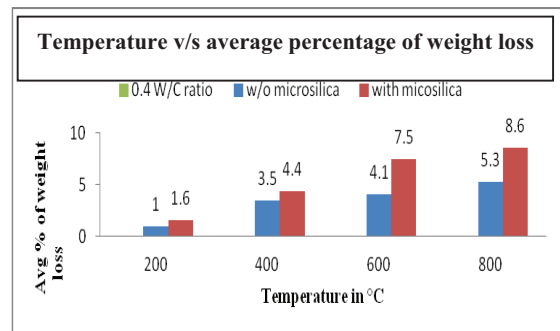


Figure 7. Average percentage loss of weight at different temperatures- NWAC

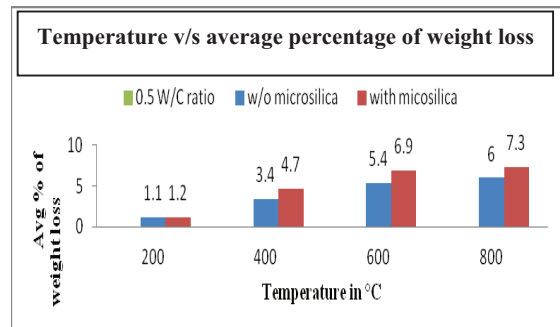


Figure 8. Average percentage loss of weight at different temperatures- NWAC

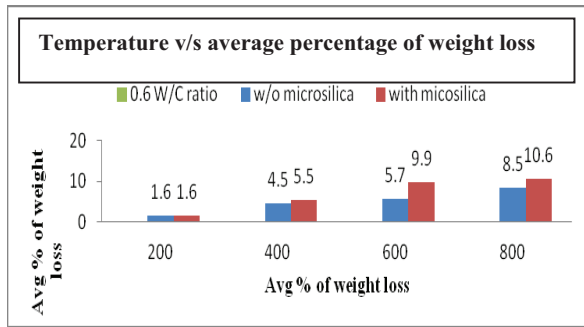


Figure 9. Average percentage loss of weight at different temperatures- NWAC

TABLE XII.  
AVERAGE PERCENTAGE OF WEIGHT LOSS OF LECAC30 WITHOUT  
MICROSILICA AT DIFFERENT TEMPERATURES

W/C	Temperature (°C)	Weight before placing in furnace (kg)	Weight after placing in furnace (kg)	% of variation
0.4	200	7.58	7.37	2.7
	400	7.48	7.09	5.2
	600	7.53	7.13	5.3
0.5	800	7.58	7.1	6.3
	200	7.26	7.16	1.3
	400	7.43	7.02	5.5
	600	7.5	7.03	6.2
0.6	800	7.5	6.88	7.2
	200	7.29	7.19	1.3
	400	7.4	7.06	4.5
	600	7.3	6.72	7.9

TABLE XIII.  
AVERAGE PERCENTAGE OF WEIGHT LOSS OF LECAC30 WITH  
MICROSILICA AT DIFFERENT TEMPERATURES

W/C	Temperature (°C)	Weight before placing in furnace (kg)	Weight after placing in furnace (kg)	% of variation
0.4	200	7.505	7.3	2.7
	400	7.57	7.22	5.6
	600	7.54	6.99	6.8
	800	7.57	6.92	8.5
0.5	200	7.58	7.45	1.7
	400	7.4	7.13	3.6
	600	7.64	7.11	6.9
	800	7.44	6.83	8.5
0.6	200	7.48	7.34	1.8
	400	7.25	6.79	6.3
	600	7.46	6.78	9.1
	800	7.42	6.71	9.5

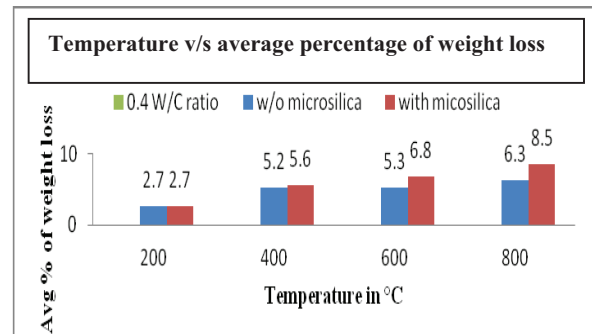


Figure 10. Average percentage loss of weight at different temperatures- LECAC30

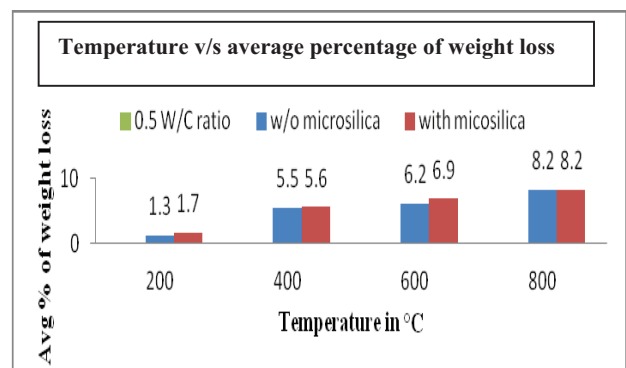


Figure 11. Average percentage loss of weight at different temperatures- LECAC30

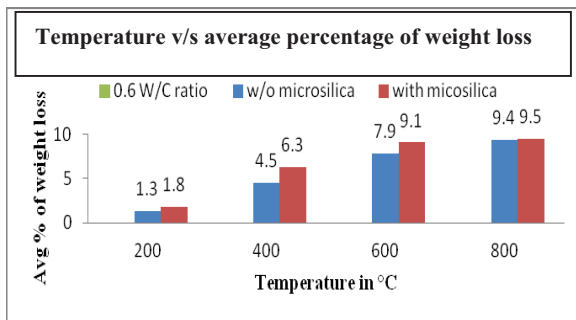


Figure 12. Average percentage loss of weight at different temperatures- LECAC30

## V. CONCLUSIONS

The unit weight of LECAC30, LECAC40 & LECAC50 mixes was found to be in the range of 1700 kg/m<sup>3</sup> to 1890 kg/m<sup>3</sup>, which is less than the unit weight of Normal Weight Aggregate concrete.

The addition of chemical admixture (Conplast SP430) improved the workability of LECAC and the optimum dosage for water- cement ratios 0.40, 0.50, and 0.60 is 1.5 %, 1 %, and 0 % were respectively to achieve medium workability.

The optimum replacement of LECA to NWA for all w/b ratios 0.40, 0.50 and 0.60 is 30% i.e. 30 % LECA & 70 % Gravel.

Compressive strength and flexural strength are observed to be maximum for LECAC30 at 0.4 w/b ratio with 10 % Micro silica. The values obtained were 29.2 MPa and 3.8 MPa respectively.

The addition of 10 % mineral admixture (Micro silica) to NWAC, LECAC30, LECAC40 and LECAC50 results an improvement in compressive strength of 8.26 %, 9.03 %, 9.86 % and 19.99 % respectively.

The addition of Micro silica improved the compressive strength more in LECAC50 when compared to NWAC, LECAC30 and LECAC40 as Micro silica reacts with the water available in the pores of the partially saturated surface dry LECA.

The compressive strength loss was minimum for LECAC30 with 0.4 w/b ratio at all temperatures 200°C, 400°C, 600°C and 800°C. And the average loss of compressive strength at 800°C temperature for NWAC and LECAC30 obtained are 74.66 % and 51 % respectively.

The weight loss is also minimum for LECAC30 with 0.4 w/b ratio at all temperatures 200°C, 400°C, 600°C and 800°C. And the average loss of weight at 800°C temperature for NWAC and LECAC30 obtained were 8.9 % and 8.4 % respectively.

LECAC30 has high resistance to the elevated temperatures with respect to compressive strength and weight loss.

## REFERENCES

[1] Alaa M. Rashad, "Light weight expanded clay aggregate as a building material – an overview", *Construction and building materials*, 170, pp. 757- 775, 2018

[2] H. Costa, R. N . F. Carmo, E.Julio, "Influence of light weight aggregates concrete on the bond strength of concrete – to – concrete interfaces". *Construction and building materials*, 180, pp. 519- 530, 2018

[3] K. Akcaozoghu, S. Akcaozoghu, "The effect of elevated temperature on the light weight concrete produced by expanded clay aggregate and calcium aluminate cement", *Bilge international journal of science and technology research*, 1(2): pp. 59 – 70, 2017.

[4] R.N.Rajprakash, A.krishnamoorthi, "Experimental study on light weight concrete using LECA", *International journal of chemistry technology research*, vol.10, No.8, pp 98- 109, 2017.

[5] N. Sellakkannu, C. Tamilarasan, "Feasibility study on light weight aggregates in concrete – A review", *International journal for specific research and development (IJSRD)* vol. 3, Issue 12, 2016.

[6] Abhijitsinh parmar, Urvish patel, "Fresh concrete properties of light weight concrete using EPS and LECA as a replacement of normal aggregates", *IJEDR*, vol. 4, Issue 1, 2016.

[7] Hanmanth Shebannavar, Maneeth P. D, Brijbhushan S, "Comparative study of LECA as a replacement of coarse aggregate by ACI method with equivalent lankness of strength of IS method", *International research journal of engineering and technology ( IRJET)*, vol. 02 Issue : 08, 2015.

[8] Anil kumar R, Dr.P. Prakash , "Mechanical properties structural light weight concrete by bleeding cinder & LECA", *International advanced research journal in science, engineering and technology*, vol . 2, Issue 10, 2015.

[9] T. Sonia, R. Subashini, "Experimental investigation on mechanical properties of light weight concrete using LECA", (2015). *International journal of science and research (IJSR)*, Index Copernicus value: 78.96, Impact factor : 6.391, 2015.

[10] Omar A. Abdulkareem, A.M. Mustafa Al Bakri, "Effects of elevated temperatures on the thermal behavior and mechanical performance of fly ash geopolymer paste, mortar and lightweight concrete", *Construction and building materials*, 50, pp. 377 – 387, 2014.

[11] J. Alexandre Bogas, J.de Brito, J.Cabaco, "Long term behaviour of concrete produced with recycled light weight expanded clay aggregate concrete", (2014). *Construction and building materials* 65, pp. 470 – 479, 2014.

[12] Cheer – germ go, Jun- ren tang, "Fire resistance property of reinforced lightweight aggregate concrete wall" *Construction and building materials* 30, pp. 725 – 733, 2012.

# Influence of Temperature on the Fracture Parameters of Basalt Fiber Concrete

N. Shiva kumar<sup>1</sup> and Dr. T. Muralidhara Rao<sup>2</sup>

<sup>1</sup>PG Scholar, CVR College of Engineering/Civil Engg. Department, Hyderabad, India  
Email: nshivakumarneela@gmail.com

<sup>2</sup>Professor, CVR College of Engineering/Civil Engg. Department, Hyderabad, India  
Email: tmuralidhararao@gmail.com

**Abstract:** In the present study, the effect of elevated temperatures on the strength parameters and fracture parameters of plain and basalt fiber high strength concrete was studied at the end of 28 days of conventional curing. The study was done for 100°C, 300°C, 500°C, 700°C and 900°C temperatures for 02 hours in a high temperature furnace of 1000°C capacity. The percentage decrease in strength parameters and fracture parameters was increased for plain and basalt fiber concrete specimens with the increase in the temperature.

**Index Terms:** Elevated temperatures, compressive strength, modulus of elasticity, fracture energy, fracture toughness, basalt fiber

## I. INTRODUCTION

Basalt is a type of igneous rock formed by the rapid cooling of lava at the surface of earth. Crushed basalt rock is the only raw material required for manufacturing the fiber. Characteristics of Basalt rock vary from the source of lava, cooling rate, and historical exposure to the elements. Though basalt rocks are available in different compositions, only certain compositions and characteristics can be used for making the continuous filaments with a diameter range of 9 to 24 microns. Basalt rocks with SiO<sub>2</sub> content about 46% (acid basalt) are suitable for fiber production. Basalt fiber is composed of minerals plagioclase, pyroxene, and olivine. Basalt fibers are available in different lengths of 3,6,9,12,18 and 24mm having diameters 13-20 microns.

## II. LITERATURE REVIEW

Aathithya Raja M, Saravanan G, Satheesh.V. S [3] used basalt chopped fibre of length 6mm and 12mm to study the compressive strength, flexural strength and split tensile strength. The addition of basalt chopped fibres to concrete improved the tensile strength and flexural strength significantly compared to plain concrete due to the ability to hold on crack surfaces of concrete.

N. Gopi, P. Baskar, B. Dharani and P. Abinaya[4] investigated the Mechanical properties of fiber reinforced concrete cubes, cylinders and prisms (M20 Grade) by varying the percentage of fibers (0.20%, 0.25%, and 0.30%). It was found that the addition of basalt fibre in concrete changes the mode of failure from brittle to ductile failure when subjected to compression, bending and impact. The

experimental results showed that the compressive strength of Basalt fibre concrete was 38.34 N/mm<sup>2</sup> which is 22% higher than control concrete of 31.34 N/mm<sup>2</sup>. The Basalt fibre concrete exhibited higher tensile strength than the normal concrete. The tensile strength of basalt fibre concrete was 7.66 N/mm<sup>2</sup> which is 45% higher than the tensile strength of normal concrete (5.26 N/mm<sup>2</sup>).

Mohammed Ishtiyaque and M.G. Ghaikh[5] studied the effect of addition of basalt fibers at 0.25%, 0.5%, 0.75%, 1% (of volume of concrete) on fracture properties of concrete was studied. The test results showed an improvement in tensile strength and fracture properties of basalt fiber reinforced concrete mixes when compared with the normal mix. Tensile strength increased by 11% with addition of 0.25% basalt fibers. Fracture toughness also increased by 402% and 269% with addition of 0.25% and 0.75% of basalt fibers. But workability and compressive strengths reduced with the increased basalt fiber percentage.

M.P.Sureshkumar, S.Ramesh, P.Easwaran, P.Pruthviraj [7] discussed about the properties, advantages and application of basalt fiber in various concrete works. Basalt fiber has high oxidation resistance, high softening and melting temperatures, higher young's modulus and tensile strength properties than that of glass fiber and it has better fire resisting property compared to the glass fiber. The basalt fiber rebar having full resistance against corrosion may be good alternative for the reinforcement of concrete structures, like RC bridge girders subjected to an environmental attack. Finally, it was concluded that the basalt fiber can be used as a good alternative strengthening material instead of glass fiber, carbon fiber, steel fiber, etc.

Suchita Hirde and Sagar Shelar[8] studied the variation of compressive strength, flexural strength and split tensile strength of M40 grade concrete with various percentages (0% to 5 % by weight of cement at interval of 1%) of basalt fiber. The length of fiber used was 18 mm length. The compressive strength increased by 7.31% for 3 % basalt fiber content. Flexural strength increased by 57.14 % for 5 % basalt fiber. Split tensile strength increased by 33.6% for 4 % basalt fiber content.

### III. EXPERIMENTAL STUDY

#### A. Cement

Ordinary Portland Cement of 53 grade conforming to IS:8112-1989 was used in the present study.

#### B. Aggregates

The physical properties of Fine aggregate and coarse aggregate used in the present study are presented in Table I.

TABLE I.  
PHYSICAL PROPERTIES OF AGGREGATES

Physical property	Fine aggregates	Coarse aggregates
Specific Gravity	2.65	2.70
Fineness Modulus	2.87	7.10
Water Absorption	1.5 %	0.8 %

Fine aggregate in the concrete mix was taken in the following proportions. 2.36 mm=10% ;1.18 mm=30% ; 600 microns=25% ; 300 microns=25%; 150 microns=10%. Coarse aggregate in the concrete mix was taken in the following proportions. 20mm passing and 10 mm retained=60%; 10mm passing and 4.75 mm retained=40%.

#### C. Water

Potable water was used in the preparation of concrete. Water used conforms to IS:456-2000.

#### D. Mineral Admixture

Ultrafine material ‘Alcofine1203’ conforming to IS:12089-1987 and IS:456-2000 (Clause No:5.2.2) was used as a supplementary cementitious material. Its particle size is much finer than the cement particle size. Ten percent of cement is replaced by alcofine1203. 10% replacement of cement is found to be the optimum percentage of replacement to produce the desired high strength concrete. The physical properties and chemical properties of Alcofine 1203 are given in Table II and Table III respectively.

TABLE II.  
PHYSICAL PROPERTIES OF ALCCOFINE 1203

Specific gravity	Bulk density (kg/m <sup>3</sup> )	Fineness (cm <sup>2</sup> /gm)	Particle size distribution (μ)		
			D10	D50	D90
2.9	680	12000	1-2	4-5	8-9

TABLE III.  
CHEMICAL PROPERTIES OF ALCCOFINE 1203

CaO	Al <sub>2</sub> O <sub>3</sub>	SiO <sub>2</sub>	Fe <sub>2</sub> O <sub>3</sub>	SO <sub>3</sub>	MgO	Glass
34%	24%	35%	1.2%	0.13%	8.2%	>90%

#### E. Chemical Admixture

Superplasticizer used in the present study was MasterEASE3709(BASF Product). It is based on the modified polycarboxylic ether used for workability of concrete at fresh state. 1.5% by weight of binder was used in the concrete mix for workability.

#### F. Basalt fiber

In the present study 18mm length basalt fibers were used. The chemical composition of basalt fiber is shown in the below Table IV.

TABLE IV.  
CHEMICAL COMPOSITION OF BASALT FIBER

S.No	Chemical Name	Percentage
1	SiO <sub>2</sub>	51.6%-59.3%
2	Al <sub>2</sub> O <sub>3</sub>	14.6%-18.3%
3	CaO	5.9%-9.44%
4	MgO	3.0%-5.33%
5	Na <sub>2</sub> O+K <sub>2</sub> O	3.6%-5.2%
6	TiO <sub>2</sub>	0.8%-2.25%
7	Fe <sub>2</sub> O <sub>3</sub> +FeO	9.0%-14%
8	Others	0.09%-0.13%

#### Physical Properties of Basalt fibers:

Sustained operating temperature	-	+680° C
Minimum operating temperature	-	(-260° C
Melting Temperature	-	1450° C
Density	-	2.6 g/cm <sup>3</sup>
Elastic Modulus	-	93 Gpa
Elongation at break	-	3.15%
Tensile Strength	-	3200- 3850Mpa
Filament Diameter	-	13- 20 microns

#### G. Mix Proportion

Mix proportion used was 1:0.556:1.629:0.25. Using Absolute Volume Method, materials required are calculated as Cement = 721.643 kg/m<sup>3</sup>; Fine Aggregate = 401.233 kg/m<sup>3</sup>; Coarse Aggregate = 1175.556 kg/m<sup>3</sup>; Water = 180.410 kg/m<sup>3</sup>.

### IV. TEST RESULTS

#### A. Compressive strength

Eighteen, 100mm plain concrete cubes and eighteen 100mm basalt fiber concrete cubes were cast and tested for studying the effect of elevated temperatures on the compressive strength. Each cube was tested for residual compressive strength under 3000kN Compression Testing Machine.

At the end of 28 days of conventional curing, cubes cast were taken out and air dried and tested for 100<sup>0</sup>C, 300<sup>0</sup>C, 500<sup>0</sup>C, 700<sup>0</sup>C and 900<sup>0</sup>C temperatures for 02 hours in a high temperature furnace of 1000<sup>0</sup>C capacity. After 02 hours, cubes were taken out of the furnace and allowed to cool.

TABLE V.  
**COMPRESSIVE STRENGTH OF PLAIN AND BASALT FIBER  
CONCRETE CUBES**

Plain concrete cubes		
Temperature (°C)	Avg residual compressive strength (Mpa)	Percentage decrease in avg. residual strength
20	79.2	--
100	75.5	4.7
300	72.5	8.5
500	71.5	9.7
700	42	46.9
900	14.5	81.7
Basalt fiber concrete cubes		
Temperature (°C)	Avg residual compressive strength (Mpa)	Percentage decrease in avg. residual strength
20	81.5	---
100	80	1.84
300	77.5	4.9
500	77	5.5
700	58	28.8
900	33	59.5

TABLE VI.  
**FLEXURAL STRENGTH OF PLAIN AND BASALT FIBER  
CONCRETE PRISMS**

Plain concrete prisms		
Temperature (°C)	Avg residual flexural strength (Mpa)	Percentage decrease in avg. residual flexure
20	18.45	--
100	16.91	8.4
300	16.38	11.2
500	13.81	25.2
700	7.5	59.35
900	5.4	70.7
Basalt fiber concrete prisms		
Temperature (°C)	Avg residual flexural strength (Mpa)	Percentage decrease in avg. residual flexure
20	22.35	--
100	21.25	4.9
300	20.5	8.27
500	19.14	14.36
700	13.98	37.5
900	12.75	42.9

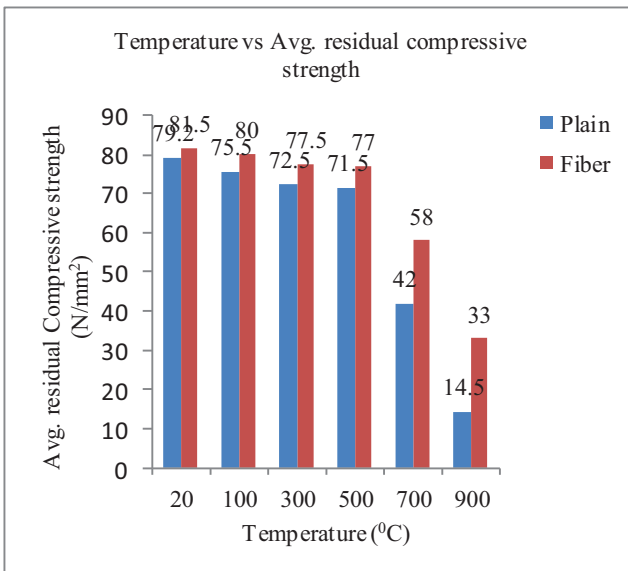


Figure 1. Average residual Compressive strength of Plain and Basalt fiber concrete cubes at different temperatures

room temperature before testing for their compressive strength.

The average residual compressive strength and percentage decrease in average residual compressive strength of 100mm plain and basalt fiber concrete cubes are presented in Table V and Fig. 1.

**B. Flexural strength**

Eighteen, 100mmX100mmX420mm plain concrete prisms and eighteen 100mmX100X420mm basalt fiber concrete prisms were cast and tested for studying the effect of elevated temperatures on the Flexural strength. Each prism

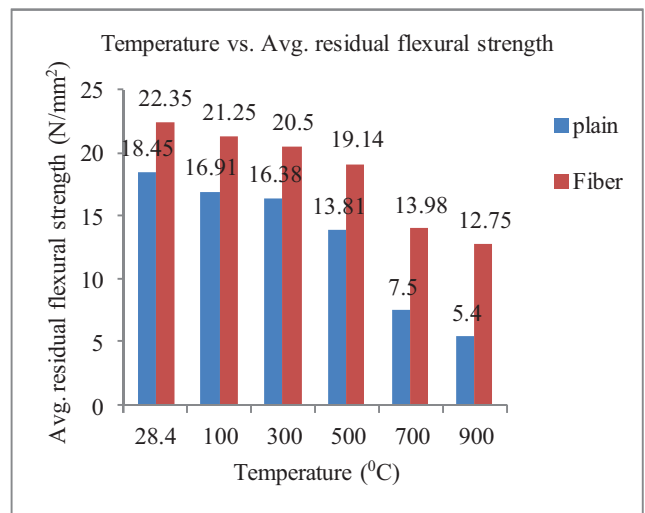


Figure 2. Residual Flexural strength of plain concrete prisms and fiber concrete prisms at different temperatures

was tested for residual flexural strength under Universal Testing Machine.

At the end of 28 days of conventional curing, prisms were taken out from water and air dried and tested for 100°C, 300°C, 500°C, 700°C and 900°C temperatures for 02 hours in a high temperature furnace of 1000°C capacity. After 02 hours, prisms were taken out of the furnace and allowed to cool at room temperature before testing for their flexural strength.

The average residual flexural strength and percentage decrease in average residual flexural strength of 100mmX100mmX420mm plain and basalt fiber concrete prisms are presented in Table VI and Fig. 2.

Between 100°C to 900°C, the percentage decrease in residual flexural strength was increased for both plain concrete prisms and basalt fiber concrete prisms.

**C. Split tensile strength**

Eighteen, 300mm length and 150mm diameter plain concrete cylinders and eighteen 300mm length and 150mm diameter basalt fiber concrete cylinders were cast and tested

for studying the effect of elevated temperatures on the split tensile strength. Each cylinder was tested for residual split tensile strength under compression Testing Machine.

At the end of 28 days of conventional curing, cylinders cast were taken out and air dried and tested for 100°C, 300°C, 500°C, 700°C and 900°C temperatures for 02 hours in a high temperature furnace of 1000°C capacity. After 02 hours, cylinders were taken out of the furnace and allowed to cool at room temperature before testing for their split tensile strength. The average residual split tensile strength and percentage decrease in average residual split strength of 300mm length and 150mm diameter plain and basalt fiber concrete cylinders are presented in Table VII and Fig. 3.

Between 100°C to 900°C, the percentage decrease in residual split tensile strength was increased for both plain concrete cylinders and basalt fiber concrete cylinders.

TABLE VII.  
**SPLIT TENSILE STRENGTH OF PLAIN AND BASALT FIBER CONCRETE CYLINDERS**

Plain concrete cylinders		
Temperature (°C)	Avg residual split tensile strength (Mpa)	Percentage decrease in avg. residual split tensile strength
20	5.16	--
100	4.95	4
300	4.13	19.9
500	3.25	37
700	2.26	56.2
900	1.82	64.7
Basalt fiber concrete cylinders		
Temperature (°C)	Avg residual split tensile strength (Mpa)	Percentage decrease in avg. residual split tensile strength
20	6.1	--
100	5.94	2.62
300	5.58	8.52
500	5.21	14.59
700	4.83	20.81
900	3.35	45.08

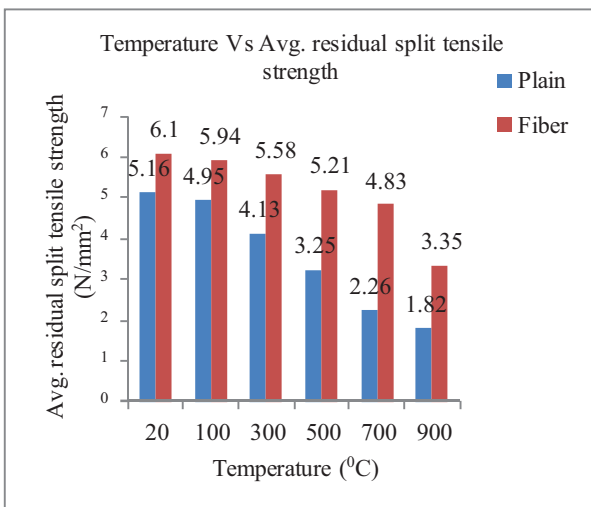


Figure 3. Average residual split tensile strengths of plain concrete cylinders and fiber concrete cylinders at different temperatures.

**D. Modulus of Elasticity**

Eighteen,300mm length and 150mm diameter plain concrete cylinders and eighteen 300mm length and 150mm diameter basalt fiber concrete cylinders were cast and tested or studying the effect of elevated temperatures on the Modulus of Elasticity. Each cylinder was tested for residual Modulus of Elasticity under compression Testing Machine.

At the end of 28 days of conventional curing, cylinders cast were taken out and air dried and tested for 100°C, 300°C, 500°C, 700°C and 900°C temperatures for 02 hours in a high temperature furnace of 1000°C capacity. After 02 hours, cylinders were taken out of the furnace and allowed to cool at room temperature before testing for their Modulus of Elasticity.

The average Modulus of Elasticity and percentage decrease in average Modulus of Elasticity of 300mm length and 150mm diameter plain and basalt fiber concrete cylinders are presented in Table VIII and Fig. 4.

TABLE VIII.  
**MODULUS OF ELASTICITY OF PLAIN AND BASALT FIBER CONCRETE CYLINDERS**

Plain concrete cylinders		
Temperature (°C)	Modulus of Elasticity (Mpa)	Percentage decrease in Modulus of Elasticity
20	41668	--
100	39130	6.1
300	35986	13.6
500	31425	24.6
700	23568	43.3
900	15580	62.61
Basalt fiber concrete cylinders		
Temperature (°C)	Modulus of Elasticity (Mpa)	Percentage decrease in Modulus of Elasticity
20	43500	--
100	41392	4.8
300	39000	10.3
500	37700	13.3
700	32040	26.3
900	25415	41.6

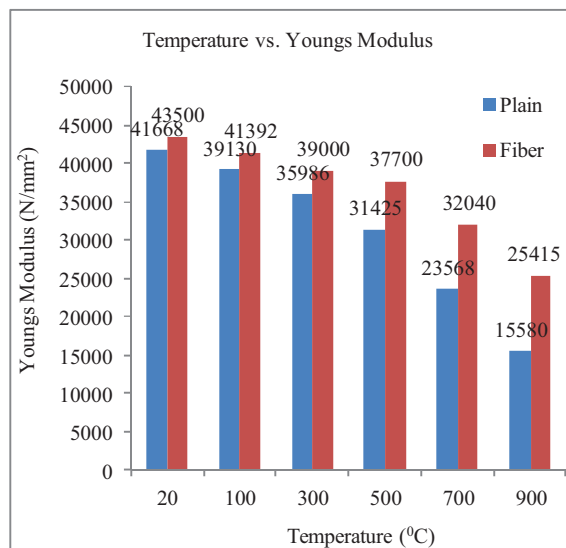


Figure 4. Average Youngs Modulus of plain concrete cylinders and fiber concrete cylinders at different temperatures.

**E. Fracture Energy and Fracture Toughness**

Eighteen, 100mmX100mmX420mm plain concrete prisms and eighteen 100mmX100X420mm basalt fiber concrete prisms were cast and tested under Universal Testing Machine for studying the effect of elevated temperatures on the Fracture energy and Fracture toughness.

At the end of 28 days of conventional curing, prisms cast were taken out and air dried and tested for 100<sup>0</sup>C, 300<sup>0</sup>C, 500<sup>0</sup>c, 700<sup>0</sup>C and 900<sup>0</sup>C temperatures for 02 hours in a high temperature furnace of 1000<sup>0</sup>C capacity. After 02 hours, prisms were taken out of the furnace and allowed to cool at room temperature before testing for their Fracture energy and Fracture toughness.

The average Fracture energy, Fracture toughness and percentage decrease in average fracture energy and Fracture toughness of 100mmX100mmX420mm plain and basalt fiber concrete prisms are presented in Table IX, Table X, Fig.5 and Fig.6. Load-Deflection of Plain concrete prisms and basalt fiber concrete prisms at different temperatures is shown in fig.7 and fig. 8 respectively.

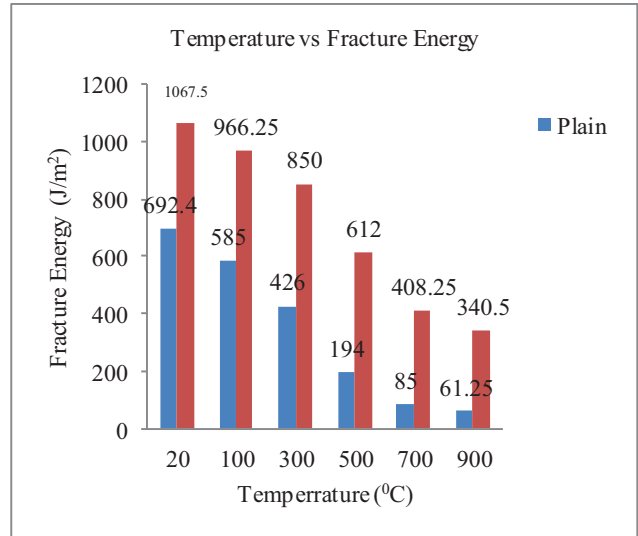


Figure 5. Fracture Energy of Plain and basalt Fiber concrete prisms at different temperatures.

TABLE IX.  
FRACTURE ENERGY OF PLAIN AND BASALT FIBER  
CONCRETE PRISMS

Plain concrete prisms		
Temperature (°C)	Avg Fracture Energy (J/m <sup>2</sup> )	Percentage decrease in Fracture Energy
20	692.5	-
100	585	15.52
300	426	38.48
500	194	71.9
700	85	87.7
900	61.25	91.1
Basalt fiber concrete prisms		
Temperature (°C)	Avg Fracture Energy (J/m <sup>2</sup> )	Percentage decrease in Fracture Energy
20	1067.5	-
100	966.25	9.48
300	850	20.37
500	612	42.66
700	408.25	61.75
900	340.5	68.10

TABLE X.  
FRACTURE TOUGHNESS OF PLAIN AND BASALT  
FIBER CONCRETE PRISMS

Plain concrete prisms		
Temperature (°C)	Fracture Toughness(K <sub>ic</sub> )	Percentage decrease in fracture toughness
20	169.86	-
100	153.98	9.34
300	131.39	22.64
500	78.08	54.03
700	44.75	73.6
900	34.97	79.4
Basalt fiber concrete concrete prisms		
Temperature (°C)	Fracture Toughness(K <sub>ic</sub> )	Percentage decrease in fracture toughness
20	215.49	-
100	199.98	7.2
300	182.07	15.5
500	151.89	29.51
700	114.36	46.93

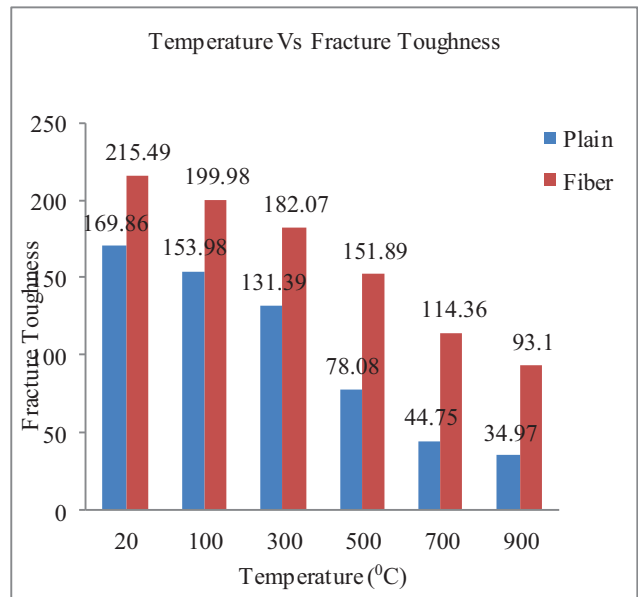


Figure 6. Fracture Toughness of Plain and basalt Fiber concrete prisms at different temperatures.



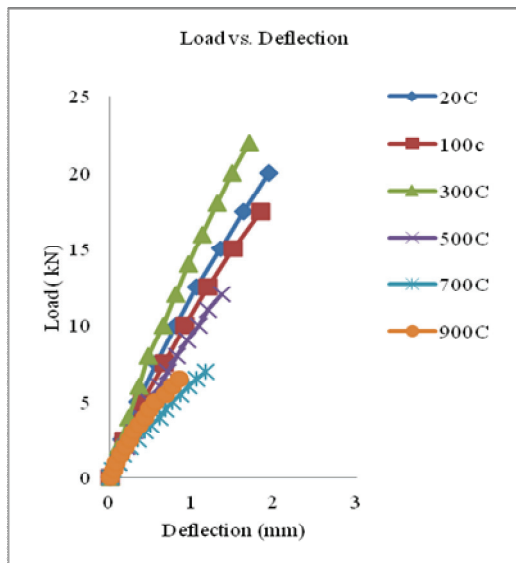


Figure 7. Load-Deflection of Plain concrete prisms at different temperatures

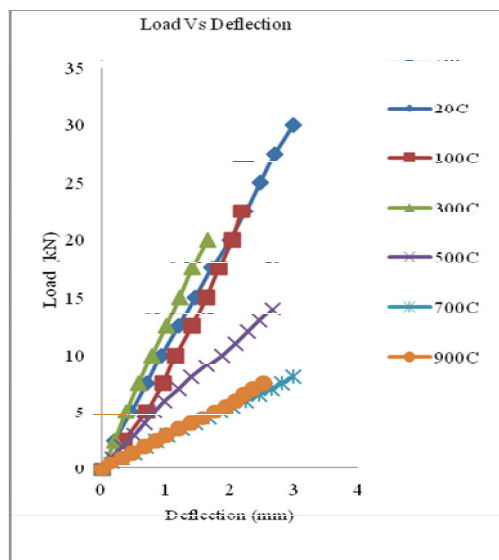


Figure 8. Load-Deflection of Fiber concrete prisms at different temperatures

## V. CONCLUSIONS

The sustaining temperature and melting temperature of Basalt fiber is  $680^{\circ}\text{C}$  and  $1450^{\circ}\text{C}$  respectively. Since the sustaining temperature of Basalt fiber is  $680^{\circ}\text{C}$ , the decrease in residual compressive strength, flexural strength, split tensile strength and modulus of elasticity is less than 15% up to  $500^{\circ}\text{C}$ . The percentage decrease in average Fracture energy (single point loading) and fracture toughness at  $500^{\circ}\text{C}$  for basalt fiber concrete prisms was 42.66% and 29.51% respectively. Even at  $900^{\circ}\text{C}$ , the average percentage decrease in fracture energy and fracture toughness was 68.1% and 56.79% respectively. Due to the strong flexural resistance of basalt fiber, there was less decrease in the strength parameters and fracture parameters. Hence, use of Basalt fiber in high strength concrete is recommended.

## REFERENCES

- [1] Duaa Fadil, Nildem Taysi, Abdullah Ahmed “The investigation of basalt and glass fibers on the Behavior of reinforced concrete beams”. International Journal of Advances in Mechanical and Civil Engineering, Volume-5, Issue-3, Jun.-2018.
- [2] T. Parthiban, G. Pavithran, C. Pradeep, BA. Praveen Kumar, Mrs. Devi S. “Durability of concrete by adding basalt fiber”. International Research Journal of Engineering and Technology (IRJET), Volume: 04 Issue: 09, September -2017.
- [3] M Aathithya Raja, G Saravanan, V.S Satheesh. “Flexural Behaviour of Basalt Chopped Strands Fibre Reinforced Concrete Beams”. International Journal of Engineering Science and Computing, Volume 7 Issue No.3, March 2017.
- [4] N. Gopi, P. Baskar, B. Dharani and P. Abinaya “Experimental investigation of concrete with basalt fibre”. International Journal of Emerging Technology in Computer Science & Electronics (IJETCSE) Volume 21 Issue 1 – April 2016.
- [5] Mohammed Ishtiyaque and M.G. Shaikh “Fracture behavior of concrete reinforced with basalt fiber” Journal for advanced research in applied sciences, volume-4, Issue 7, 2017.
- [6] Kirankumar, chetan V R “Experimental investigation on basalt fiber reinforced concrete”. International journal of scientific Development and Research. Volume 2, Issue 6, June 2017.
- [7] M.P.Suresh kumar, S. Ramesh, P.eshwaran, P.Pruthiraj “Basalt fiber application in concrete”. International Journal of advanced science and research. Volume 1, Issue 1, June 2016.
- [8] Suchita Hirde and Sagar Shelar"Effect of Basalt Fiber on Strength of Cement Concrete". International Journal of Current Engineering and Technology, 2017.
- [9] Zhenshan Wang, Kai Zhao, Zhe Li, Hui Ma “Experimental Study on Durability and Mechanical Properties of Basalt Fiber Reinforced Concrete under Sodium Sulfate Erosion”. volume 62, 2017.
- [10] C.V.Neilson, and N.Bicanic" Residual fracture energy of high performance and normal concrete subject to high temperatures”. Materials and structures volume 36, October 2006.

# Analysis of Beam-Column Joints using FEM

Ch. Harika<sup>1</sup> and Dr. N. Murali Krishna<sup>2</sup>

<sup>1</sup>Asst. Professor, CVR College of Engineering/Civil Engg. Department, Hyderabad, India  
Email: harikareddy2771995@gmail.com

<sup>2</sup>Professor, CVR College of Engineering/Civil Engg. Department, Hyderabad, India  
Email: nmuralikrishna1956@gmail.com

**Abstract:** Members of space frame structures are in general subjected to axial force, biaxial shear, biaxial moments and torque. The structural designing of frameworks are carried-out so as to meet the critical stress levels of each individual structural member. In this context even though the sectional sizes of the individual members are adequate to withstand the forces they carry, the junctions where many such members meet, may not be adequate to withstand the combined effects. This problem is common to all kinds of structural joints made up of both steel and concrete.

In the present paper the beam-column junction portion made in RCC is analyzed using the FEM package ANSYS. The loads that act at the beam-column joint are obtained from the output of structural analysis of framed structure. These loads are used on the FEM model of beam-column joint. The aim of the present study is to replace the beam-column joint in a structural frame work with the equivalent strut-beam frame work to carry out the structural analysis. By this approach it is intended to use the same software package used for the analysis of skeletal frame work to the one with the beam-column joints also.

**Index Terms:** Beam-column joint, equivalent strut, axial force, shear and torque.

## I. INTRODUCTION

Structural designing of a framed structure involves the design of slabs, beams, columns and footings. The design of slabs and footings do not interfere with the designing of beams and columns but the reverse is not always true. In the RCC limit state method of structural design, the beams are checked against their capacity to with-stand the combined effect of maximum bending moment and maximum the shear-force, that comes on to them. The structural design of column elements on the other-hand is verified against the combined effect of maximum axial force and the biaxial moments.

The present practice of structural designing is considered adequate if the structural designing concepts of individual elements are safe. Their combined action near the joint where more than one member meets is never checked. As on date, there exists no formal procedure to evaluate the magnitude of structural distress that comes due to the combined action from different elements meeting near the joint. If the joint is between beam and column elements it is called a beam-column joint. Hence, even through the individual structural elements are found safe, the joint where

they are connected may not be always safe since it is not checked. Apart from this, the structural analysis of beam-column joint is never an integral part of any current structural analysis/design software packages.

Due to the above reasons, in-depth study on the structural analysis of beam-column joint is essential. The studies using analytical and experimental approaches needs to be carried-out and the results obtained shall be validated. The analytical approaches may be either classical or computational methods like finite difference/finite element methods. The experimental studies may be carried-out on either prototype models or scale models. Currently active research on the behavior of beam-column joints is being pursued all over the world.

### A. Need of the study

As on date there exists no specific structural design methodology to check the safety of the beam-column joints. The reasons are due to the lack of information regarding composition of materials near joint, the non-availability of suitable theoretical concepts and the amount cumbersomeness involved in its implementation. However, the inability to verify the structural safety of beam/column joints can be quoted as an excuse in a comprehensive structural design. This leaves the overall stability of the structural system in doubt. This prompts the urgent need to take-up the research leading to estimate the structural distress in beam-column joints.

### B. Objective of the study

Having appreciated well, the need to study the performance of beam-column joints, it is proposed to develop a simple model representing the behaviour of beam-column joints to evaluate the safety of the beam column joint in a framed structure. The model to be proposed shall be simple, amenable and adoptable with the conventional structural analysis packages dealing with discrete structures.

## II. LITERATURE REVIEW

The studies on beam-column joints are on since early 1960's. The studies in general may broadly be categorized as analytical or experimental or both. Most of the researchers have carried-out experiments on scale models of beam-column joints and have proposed analytical expressions to arrive at their strength and stiffness contributions. Some of the research works which have been carried-out since 2004 is presented below.

The FEM analysis of hybrid structural frames with reinforced concrete columns and steel beams was carried out

by Hiroshi Noguchi and Kazuhiro Uchida. Two specimens, which had different beam-column joint detailing, were analyzed using the nonlinear three-dimensional finite element method. The failure process and shear resisting mechanisms of differently shaped beam-column joints (interior, exterior, interior top, and corner) were understood by analytical results of the stress-strain relationship among concrete elements, shear force of the beam-column joints, the contribution of shear resisting elements, and deformation components, which were not obtained in the experiment. [1]

The behavior of exterior beam column joints sub assemblages with transverse reinforcements detailed as per IS 456 and IS 13920 was compared by K.R. Bindhu, P.M. Sukumar and K.P. Jaya. A six storied RC building in Zone III was analyzed, and one of the exterior beam column joints at an intermediate storey was designed. The test specimen was reduced to 1/3<sup>rd</sup> size of prototype. [2]

Rajaram, A. Murugesan and G.S.Thirugnanam had carried-out analytical and experimental studies on interior beam column joint subjected to cyclic loading. The model was subjected to cyclic loading to find its behavior during earthquake. The same model was analyzed by FEM analysis using ANSYS. The results from experiments were compared with those obtained from FEM model analyzed using ANSYS. It was concluded that experimental and analytical behavior of the interior beam column joint was in agreement. Based on the results obtained from their experiments, they had presented about the influence of parameters such as ductility, energy absorption, stiffness degradation etc., on beam/column joint in the event of seismic disturbance. [3]

Bing Li and Sudhakar A. Kulkarni carried out an experimental and numerical investigation on RC wide beam-column joints when subjected to seismic loads. The behavior of the joints under the influence of critical influencing factors like column axial load, transverse beam, and beam bar anchorage ratio were also analyzed through the parametric studies carried out. The DIANA software was used for the FE analysis. The concrete was modeled using 20-node 3D quadratic solid elements while the reinforcing bars were modeled as truss elements. [4]

An experimental and analytical investigation on the seismic behaviour of fibre reinforced polymer (FRP) and textile reinforced mortar (TRM) upgraded RC exterior beam column joints was carried out by Mohammad S. Alhaddad, Nadeem A. Siddiqui, Aref A. Abadel, Saleh H. Alsayed and Yousef A. Al-Salloum. The results obtained from the FEM analysis were compared with the test results, and it was observed that the FEM analysis predicts the satisfactory results with control specimen, FRP, TRM strengthened exterior RC beam column joint. [5]

The analytical study of reinforced beam column joint subjected to monotonic loading was investigated by S. S. Patil, S. S. Manekari. In this study ANSYS software was

used for performing the FEM analysis of beam column joint. It was concluded that, the displacement, maximum stress and minimum stress values were observed to be less in fixed support condition of beam column joint when compared to hinge support condition. And the behaviour of corner and exterior joints are different. And as the stiffness of structure changes, the displacement, maximum stress and minimum stress changes Non-linearly. [6]

Finite element modelling of reinforced concrete beam column joint was carried out by Syed Sohailuddin S and M G Shaikh. The FEM analysis was done by ANSYS 11.0. All specimens were subjected to similar reverse cyclic loading to simulate the earthquake loading in structures. From this analysis it was found that the test specimen with diagonal confining bars of 8 mm in the beam region have shown better performance, exhibiting higher strength with minimum cracks in the joint. All the specimens failed by developing tensile cracks at interface between beam and column. [7]

The experimental findings of HSC interior beam column joints under column axial compressive loading were performed by Bing Li, M.ASCE and Chee Lai Leong. It was observed that HSC improved the bond condition of reinforcing bars of larger diameters. The various parameters influencing the strength and bond of HSC beam column joints were studied by parametric studies of FEM modelling. Based on test results and FE analysis, some relaxation of the bond requirements in beam-column joints is recommended when HSC is used because bond strength increases with the increase in concrete compressive strength. [8]

The experimental investigation of Hybrid Fibre Reinforced Concrete of Exterior Beam-Column Joint under Cyclic loading was done by C.Geethajali, P.Muthu Priya, Dr. R.Venkatasubramani. Results shown that the fibers when used in a hybrid form could result in superior composite performance compared to their individual fibre-reinforced concretes. It was observed that the ultimate load carrying capacity increases by 38% for hybrid fibre when compared to steel fibre beam column joint specimen. [9]

The details of finite element analysis of beam column joints wrapped with glass fibre reinforced polymer sheets (GFRP) carried out by Shabana T S, K.A Abubaker, Renny Varghees using the package ANSYS were presented in this paper. ETABS was used for modelling and analysis of G+4 office building. During the analysis both the ends of column were hinged. Static load was applied at the free end of the cantilever beam up to a controlled load. The percentage of increase in efficiency of wrapped over unwrapped was found to be 37% for beam column joint designed as per IS 456:2000 and 20% for designed as per IS 13920:1993. [10]

### III. METHODOLOGY

#### A. The Analysis and Design of RCC Building in ETABS

The study is carryout by having a sample of beam-column joints with full data available regarding the sizes, materials and the loads. The data is possible only if a space framed building is analysed with the available geometric and load data. For the purpose of study an existing building frame data is obtained. With the data available the 3-D building frame model is developed using ETABS package and the linear static analysis of the structural frame is carried out using ETABS-17 package.

ETABS is a sophisticated, easy to use, special purpose analysis and design program developed specifically for building systems. ETABS 2017 features an intuitive and powerful graphical interface coupled with unmatched modelling, analytical, design, and detailing procedures, all integrated using a common database. Although quick and easy for simple structures, ETABS can also handle the largest and most complex building models, including a wide range of nonlinear behaviours necessary for performance-based design, making it the tool of choice for structural engineers in the building industry.

The following is the list of steps to be followed in ETABS for the analysis and design of a reinforced concrete building.

- Step - 1: Opening Screen: Selection of base units and design codes
- Step - 2: Creation of Grid points & Generation of structure
- Step - 3: Defining of material and section properties
- Step - 4: Assigning of Property
- Step - 5: Assigning of Supports
- Step - 6: Defining of loads
- Step - 7: Assigning of Dead loads
- Step - 8: Assigning of Live loads
- Step - 9: Assigning of load combinations
- Step - 10: Analysis
- Step - 11: Design

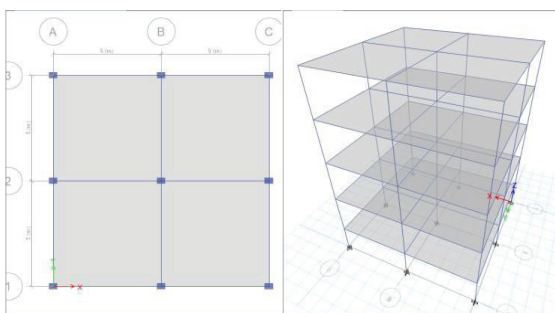


Figure 1. Plan and isometric view of RC building

#### B. The FEM analysis in ANSYS

The FEM analysis of beam-column joint is a very complicated task and hence, is undertaken as detailed below.

For the purpose of FEM analysis ANSYS software is used for the modelling of beam-column joint.

- 1. Pre-processor module
  - i) Geometric modelling of beam-column joint
  - ii) Element modelling
  - iii) Material modelling
  - iv) Meshing of the model
  - v) Loads and boundary conditions
- 2. Analysis Module
- 3. Post processor Module

The very purpose of the present research on beam-column joints is to propose a feasible method which may be simple to be adopted, yet accurate to represent the true behaviour of the beam-column joint. In this context the strain energy stored within the beam column interface comprising of the reinforced cement concrete is calculated first using the ANSYS software. The concrete mass in the beam-column joint location is replaced with the equivalent beam/strut concrete elements as described under. Along the interfaces of the beam-column joints square cross section members representing the beam elements are placed parallel to the beam and column orientations along the edges of the beam-column interfaces. Next, strut members of the same cross-sectional area are placed joining the mid points of the beam and column surfaces. The material adopted for the both beam and strut elements are the same as that of the concrete representing the column members. The strain energy carried by such equivalent beam/strut concrete elements is calculated in combination with the beam-column elements once again using the ANSYS software. Equivalence in the energies between the two different models is not possible as the later one more flexible. The sizes of the members representing the equivalent beam/strut elements are revised using a penalty factor.

The intention of the present study is to terminate all the beam/column elements in a conventional structural analysis near the beam-column interfaces and introduce the equivalent beam/strut concrete elements within the beam-column interface. The connectivity beam/column elements and the equivalent struts shall be established. There after the structural analysis may be carried out for the framed structure considering the revised beam/column elements and together with the equivalent beam/strut elements. This kind of treatment is considered more rational and hence acceptable. The complicated stress analysis to evaluate the condition of beam-column junction can be avoided.

The magnitude of the penalty factor is obtained by dividing the strain energy corresponding to the full concrete in the beam-column joint location with the strain energy due to the equivalent beam/strut model. The sizes of the members of the equivalent beam/strut elements are revised next upward based on the magnitude of the penalty factor. The magnitudes of the penalty factor differ depending on the size and grades of the concrete beam-column elements meeting at the joint. As evident due to the flexibility of the discrete beam/strut elements proposed the magnitude of the penalty factor is always larger than one.

Such studies are to be carried out on different beam-column junctions by varying the sizes of sectional dimensions and grades of concrete. It is proposed to use the output of the results from a large set of such studies to train a neural net algorithm. The trained net facilitates obtaining the sizes of the equivalent beam/strut elements for any new beam-column joint. These beam/strut elements may be modelled in place of the beam-column joints in a conventional structural frame work to be designed using the structural design packages. Though conservative, the safety of the equivalent beam/strut elements ensures the safety of the beam-column joints.

#### IV. SPECIMEN CALCULATIONS

In this present study the three types of beam-column joints are considered and the FEM analysis is carried out by ANSYS software. The ANSYS program has many finite element capabilities, ranging from a simple linear static analysis to the complex non linear transient dynamic analysis. In this chapter the three types of beam-column joints with and without the equivalent beam/strut elements varying the grade of concrete of beams/columns and varying the cross sectional dimensions of beams/columns are explained.

##### *Interior Beam-Column Joint*

The interior beam-column joint which is at fourth storey level is taken and the analysis is carried out in ETABS. The results obtained from ETABS analysis are used here to carry out the FEM analysis.

To model the interior beam-column joint the solid 185 element is taken. Solid 185 element is a 3D element with 8 nodes in it. It is used for 3D modelling of solid structures. It is defined by 8 nodes having 3 degrees of freedom at each node; translations in the nodal x, y and z directions.

For this analysis two material properties are taken. The first material property describes the properties of concrete such as young's modulus as 25e3 and poisons ratio as 0.3. And the second material property describes the thin rigid plate which is having young's modulus as 2e10 and poisons ratio as 0.15.

For the modelling of the interior beam-column joint solid modelling method is used. By this method, directly solid with volumes are created. The cross sectional dimension of the beams are taken as 300 X 500 mm and 400 X 500 mm and the cross sectional dimension of the column is taken as 300 X 400 mm. From the beam-column joint the beam extends to right, left and front, back sides by 1 metre. The thin rigid plates are attached to the faces of the beams and columns to transfer the loads uniformly.

By using mesh tool, mesh the geometry of the structure with the mapped volume mesh. The 1 metre length beams and columns are divided into ten element divisions and the dimensions of width of the column and depth of the beam are divided into eight element divisions and the depth of the column and width of the beam are divided into six element divisions. The thin rigid plate is attached to surface of beams/columns for load application are also

divided into the same number of parts so that nodal connectivity intact.

The rigid plates of 10 mm thick are placed at every face of the beams/columns to transfer the loads uniformly. From analysis of G+4 storey RCC structure in ETABS, the displacements are found out at every one metre distance from the joint. So the displacement values obtained from the ETABS are given as boundary conditions at central nodes of the rigid plates placed on every face of beams and columns.

The loads are applied at the central node of the faces of the beams and columns. A rigid plate of 10 mm thick is placed on the faces of beams and columns to transfer the loads to the structure uniformly. The interior beam column joint at the fourth storey level is taken and the axial force which is coming to the column is applied here and the shear force and bending moments are applied to the beams.

TABLE I.  
DISPLACEMENTS AND ROTATIONS OF THE INTERIOR BEAM-COLUMN JOINT

Displacements(mm) and rotations(radian)	X	Y	Z	R <sub>x</sub>	R <sub>y</sub>	R <sub>z</sub>
Top beam	0.24	- 3.445	0.073	0	0	0
Bottom beam	0.017	- 3.185	0.082	0	0	0
Right column	0.199	- 4.139	0.075	- 0.001	0	0
Left column	0.130	- 4.021	0.081	0.001	0	0
Front beam	0.126	- 4.215	0.072	0	0	- 0.001
Back beam	0.123	- 3.675	0.083	0	0	0
At junction	0.124	- 3.358	0.078	0	0	0

TABLE II.  
AXIAL FORCES TO THE COLUMN.

Location	Axial force(N)
Top column	-534147
Bottom column	1047983

TABLE III.  
SHEAR FORCE AND BENDING MOMENT TO THE BEAM.

Location	Shear force(N)	Bending moment(N.mm)
Right beam	-121540	-93880
Left beam	121540	93880
Front beam	-125290	-103430
Back beam	125290	103430

In the post-processor menu the results are obtained. In this present problem, displacements and the strain energies are to be known to study the behaviour of the exterior beam-column joint.

The FEM analysis of interior beam-column joint is completed. Now the main objective of the study is to replace the beam-column joint with the equivalent beam-strut elements. Here the replacing of beam-column junction is based on the strain energy concepts. The strain energy obtained with concrete in the beam-column junction location with proposed beam-strut elements is compared.

For the replacing of the beam-column joint with the equivalent beam/struts, keeping the junction portion empty here after, place the equivalent beam/strut elements at the junction portion. The beam elements are placed parallel to the beam and column orientation at the joint. And the strut elements are placed joining the midpoints of beam and column surfaces.

By taking the beam as element, the beams are drawn initially with 100X100 mm dimensions at the beam-column interface. To draw the beams, beam 188 element is taken. Beam 188 element is linear two noded in 3-D. It has six degrees of freedom at each node; translations in the x, y and z directions and rotations about the x, y and z directions. The struts are drawn with Link 180 element. Link 180 is a 3D spar element that is useful for variety of engineering applications. The element can be used for modelling of trusses links, springs etc. Link 180 element is a uniaxial tension compression element with three degrees of freedom at each node: translations in the nodal x, y and z directions.

The element is defined by two nodes and the cross sectional area of the link element is defined by the sectional type command. The area of link is given as 10000mm<sup>2</sup>. If the strain energy of the model with the equivalent beam/strut

elements having 10000mm<sup>2</sup> area is matching with the strain energy of the model without struts then the equivalent beam/strut area can be fixed as 10000 mm<sup>2</sup>.

To model the equivalent beam/strut elements the material properties are same as beam-column joint. Here the equivalent beam-strut element is assumed like a concrete material and the properties are given. The young's modulus of beam-strut is given as 25e3 and the poisons ratio is given as 0.3.

After modelling of the interior beam-column joint with the equivalent beam-strut elements, the boundary conditions and the loads of same as the interior beam-column joint without struts are applied. The struts are kept in three directions x, y and z directions.

The strain energy calculations with proposed equivalent beam/strut element are found to be less when the beam-column joint has full concrete mass. The ratio of strain energy with full concrete mass to the strain energy with equivalent beam/strut model is taken as the penalty factor for the particular beam column joint the dimensions of beam-strut element are revised upward by multiplying with the original beam/strut elements with the penalty factor. These results can obtain more rational beam-strut dimensions. However, the equivalent beam/strut elements cannot replace the action of full concrete mass as the discrete element frame work is flexible in comparison to the full concrete mass.

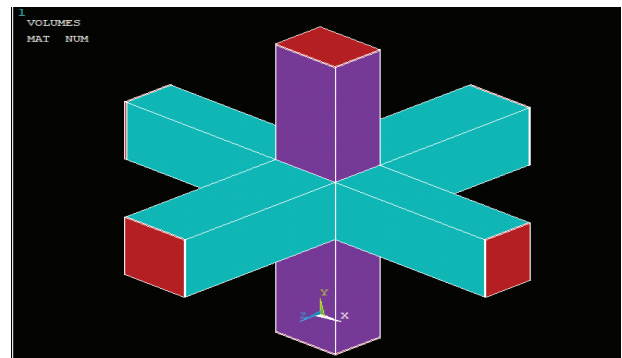


Figure 2. Interior beam-column joint without struts

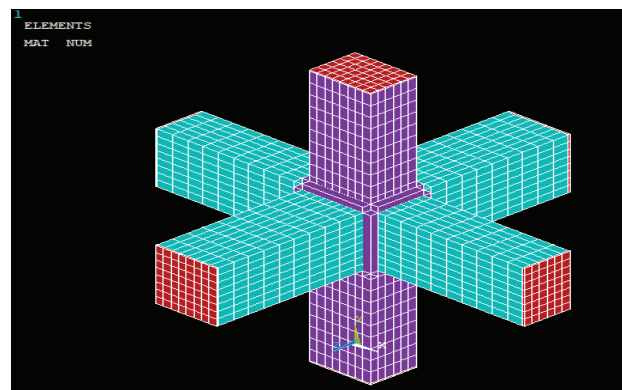


Figure 3. Interior beam-column joint with struts

The following models are developed by using the above procedure.

- 1) Exterior beam-column joint
  - 2) Corner beam-column joint
  - 3) Interior beam-column joint varying grades of concrete and dimensions of beams/columns
  - 4) Exterior beam column joint varying grades of concrete and dimensions of beams/columns
  - 5) Corner beam column joint varying grades of concrete and dimensions of beams/columns
- Total 18 models are developed and analysed.

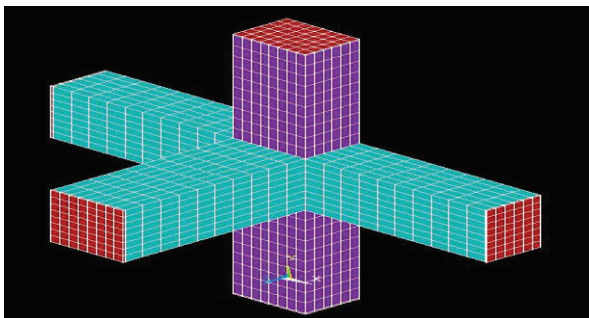


Figure 4. Exterior beam-column joint without struts

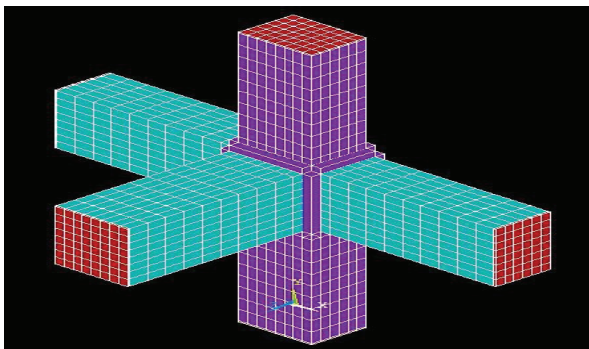


Figure 5. Exterior beam-column joint with struts

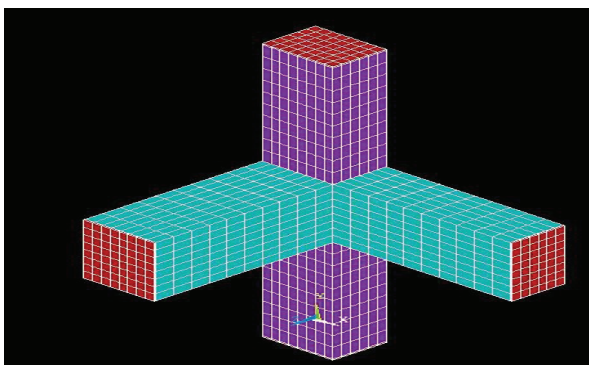


Figure 6. Corner beam-column joint without struts

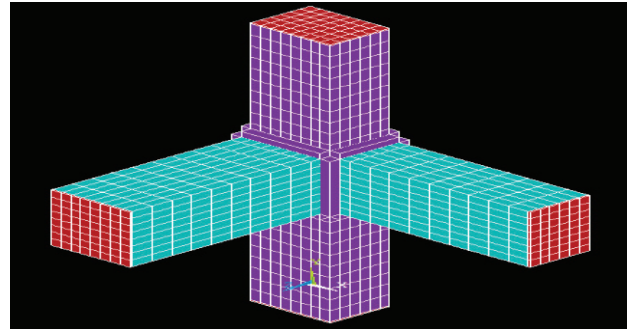


Figure 7. Corner beam-column joint with struts

## V. RESULTS AND DISCUSSIONS

### Results

After having analysed the RCC beam-column joints using FEM approach in ANSYS package, the results are obtained for maximum displacements and strain energies are tabulated below. The studies are carried out firstly with the full concrete beam-column joints and then replacing of junction portion with the equivalent beam/strut elements.

1) The analysis of beam-column joint having beam cross sectional dimensions as 300X400 mm and 400X500 mm and the column cross sectional dimensions as 300X400 mm. And the grade of concrete of beams and columns is same that is M25. Initially the dimensions of equivalent beam/strut elements are taken as 100X100 mm.

TABLE IV.  
THE RESULTS OF THE INTERIOR BEAM-COLUMN JOINT

Results	Without struts	With struts
Maximum Displacements(mm)	4.24114	4.24113
Strain energy(N.mm)	224042	180572

Penalty factor = 1.240

The revised dimensions of the equivalent beam/strut elements are 111mm X 111 mm.

TABLE V.  
THE RESULTS OF THE EXTERIOR BEAM-COLUMN JOINT

Results	Without struts	With struts
Maximum Displacements(mm)	3.5656	3.56533
Strain energy(N.mm)	141464	97599.4

Penalty factor = 1.449

The revised dimensions of the equivalent beam/strut elements are 120mm X 120 mm.

TABLE VI.  
THE RESULTS OF THE CORNER BEAM-COLUMN JOINT

Results	Without struts	With struts
Maximum Displacements(mm)	2.59199	2.62161
Strain energy(N.mm)	71401.6	32893.9

Penalty factor = 2.170

The revised dimensions of the equivalent beam/strut elements are 147 mm X 147 mm.

2) The analysis of beam-column joint having beam cross sectional dimensions as 300X400 mm and 400X500 mm and the column cross sectional dimensions as 300X400 mm. And the grade of concrete of beams as M20 and columns as M40 are taken. Initially the dimensions of equivalent beam/strut elements are taken as 100X100 mm.

TABLE VII.  
THE RESULTS OF THE INTERIOR BEAM-COLUMN JOINT

Results	Without struts	With struts
Maximum Displacements(mm)	4.64301	4.64297
Strain energy(N.mm)	112102	87215

Penalty factor = 1.285

The revised dimensions of the equivalent beam/strut elements are 113mm X 113 mm.

TABLE VIII.  
THE RESULTS OF THE EXTERIOR BEAM-COLUMN JOINT

Results	Without struts	With struts
Maximum Displacements(mm)	3.377781	3.77747
Strain energy(N.mm)	78173	50612.5

Penalty factor = 1.544

The revised dimensions of the equivalent beam/strut elements are 124 mm X 124 mm.

TABLE IX.  
THE RESULTS OF THE CORNER BEAM-COLUMN JOINT

Results	Without struts	With struts
Maximum Displacements(mm)	2.59465	2.61702
Strain energy(N.mm)	46059.4	22367.2

Penalty factor = 2.059

The revised dimensions of the equivalent beam/strut elements are 143 mm X 143 mm.

3) The analysis of beam-column joint having beams cross sectional dimension as 400X500 mm and the column cross sectional dimensions as 400X400 mm. And the grade of concrete of beams and columns is same that is M25. Initially the dimensions of equivalent beam/strut elements are taken as 100X100 mm.

TABLE X.  
THE RESULTS OF THE INTERIOR BEAM-COLUMN JOINT

Results	Without struts	With struts
Maximum Displacements(m)	3.62549	3.62547
Strain energy(N.mm)	73572	56313.4

Penalty factor = 1.306

The revised dimensions of the equivalent beam/strut elements are 114 mm X 114 mm

TABLE XI.  
THE RESULTS OF THE EXTERIOR BEAM-COLUMN JOINT

Results	Without struts	With struts
Maximum Displacements(mm)	2.93612	2.93565
Strain energy(N.mm)	51606	34636.7

Penalty factor = 1.489

The revised dimensions of the equivalent beam/strut elements are 122 mm X 122 mm

TABLE XII.  
THE RESULTS OF THE CORNER BEAM-COLUMN JOINT

Results	Without struts	With struts
Maximum Displacements(mm)	1.99536	1.98692
Strain energy(N.mm)	27800.4	12598.2

Penalty factor = 2.206

The revised dimensions of the equivalent beam/strut elements are 148 mm X 148 m.

### Discussions

The modelling of the beam-column joint with equivalent beam/strut elements is carried out as given under. The struts are placed joining the central points of the beam faces running parallel to the beams in both the directions as well as the central points of the column faces above and below, running parallel to the column axis. Due to the applied loads on the beam-column joint making use of ANSYS package the finite element analysis of the model using linear elastic analysis module of ANSYS is carried out. The strain energy stored within the beam-column joint portion of the concrete



mass is evaluated. Next, the RC mass in the beam-column joint portion is replaced with the equivalent beam-strut model and the analysis is once again carried out. Here, an arbitrary size of beam-strut element is used. The strain energy stored by the beam-strut element is worked out and is compared with that obtained due to total concrete mass. The size of the beam-strut elements are revised upward using a penalty factor, defined later in the specimen calculation chapter.

The intension of the present study is to replace the beam-column joint in a structural frame work with the equivalent strut frame work to carry out the structural analysis. By this it is intended to use the same software package used for the skeletal frame work to the one with the beam-column joints also.

From the results, the strain energy of beam-column joint is always greater compared to the strain energy of the beam-column joint with the equivalent beam/strut elements. As compared to the three beam-column joints, the interior one is much stronger than the other two.

## VI. CONCLUSIONS

Based on the limited studies carried out on beam-column joint models using finite element analysis, the following conclusions are drawn:

1. The equivalent beam/strut dimensions were found to be 16.8% larger for the interior joints as compared to the exterior joints, when the concrete mix for the beams and columns is the same.
2. When the grade of concrete used for columns is much superior to the grade used for beams, the sectional dimensions of the equivalent beam/strut elements are larger as compared to the ones with same concrete mix for both beams and columns, all other conditions remain the same.
3. When the cross sectional dimensions of the beams are increased the equivalent beam/strut dimensions were found to be larger by 14.52% between the interior joint and the exterior joint.

## REFERENCES

- [1] Hiroshi Noguchi and Kazuhiro Uchida, “The FEM analysis of hybrid structural frames with reinforced concrete columns and steel beams”, ASCE (2004).
- [2] K.R. Bindhu, P.M. Sukumar and K.P. Jaya, “Performance of exterior beam-column joints under seismic type loading”, ISET (2009).
- [3] P. Rajaram, A. Murugesan and G.S.Thirugnanam, “Experimental study of interior beam column joint subjected to cyclic loading”, ISET (2010).
- [4] Bing Li and Sudhakar A. Kulkarni, “Seismic behaviour of RC exterior wide beam-column joints”, ASCE (2010).
- [5] Mohammad S. Alhaddad, Nadeem A. Siddiqui, Aref A. Abadel, Saleh H. Alsayed and Yousef A. Al-Salloum, “Numerical Investigations on the Seismic Behaviour of FRP and TRM Upgraded RC Exterior Beam-Column Joints”, ASCE (2012).
- [6] S. S. Patil, S. S. Manekari “Analysis of reinforced beam-column joint subjected to monotonic loading”, IJEIT (2013)
- [7] Syed Sohailuddin S and M G Shaikh, “Finite element modelling of reinforced concrete beam column joint using ANSYS”, IJSCER (2013).
- [8] Bing Li, M.ASCE and Chee Lai Leong, “Experimental and Numerical Investigations of the Seismic Behaviour of High-Strength Concrete Beam-Column Joints with Column Axial Load”, ASCE (2014).
- [9] C.Geethajali, Dr.P.Muthu Priya, Dr.R.Venkatasubramani, “Behaviour of HFRC Exterior Beam-Column Joints under Cyclic loading”, IJSTER (2014).
- [10] Shabana T S, Dr. K.A Abubaker, Renny Varghees, “Finite Element Analysis of Beam Column Joint with GFRP under Dynamic Loading”, IJETT (2015).
- [11] Miss.Kane Kruthika R and Miss. Samarth Gauri V, “Study of Behaviour & Strengthening of Beam-Column Joint”, IJRITCC (2017).
- [12] Dr. S. R. Uma, Prof. A. Meher Prasad, “Seismic behaviour of beam column joints in RC moment resisting frames”.

# Implementation of 2x2 MIMO-OFDM System using Universal Software Radio Peripherals

Dr. Yedukondalu Kamatham<sup>1</sup> and Naveen Talati<sup>2</sup>

<sup>1</sup>Professor, CVR College of Engineering/ECE Department, Hyderabad, India  
Email: kyedukondalu@gamil.com

<sup>2</sup>PG Scholar, CVR College of Engineering/ECE Department, Hyderabad, India  
Email: naveenthalati741@gmail.com

**Abstract:** The 2x1 and 2x2 Multiple Input Multiple Output (MIMO) systems with Orthogonal Space-Time Block Code (OSTBC) are implemented using Universal Software Radio Peripherals (USRPs) and LabVIEW. Bit Error Rate (BER) is estimated and compared for both systems using different M-ary Quadrature Amplitude Modulation (QAM) i.e. 4 QAM, 16 QAM, 64 QAM. The BER is reduced for a 2x2 MIMO than a 2x1. To improve spectral efficiency, Orthogonal Frequency Division Multiplexing (OFDM) is combined with MIMO configuration, known as MIMO-OFDM. 2x2 MIMO-OFDM with OSTBC is implemented with M-ary QAM and N IFFT (32, 64, 128 IFFT). Among these, better BER performance is observed for 2x2 MIMO with 64-IFFT. The MIMO-OFDM is used in Worldwide Interoperability for Microwave Access (WiMAX) which is the standard of IEEE 802.16.

**Index Terms:** Multiple Input and Multiple Output (MIMO), Orthogonal Frequency Division Multiplexing (OFDM), Bit Error Rate (BER), Universal Software Radio Peripheral (USRP)

## I. INTRODUCTION

In wireless communications systems, the current technology demands reliability and high data rates with improved spectral efficiency and Quality of Service (QoS) with various users at the same time. Improved spectral efficiency can be offered by Orthogonal Frequency Division Multiplexing (OFDM) and Multiple Input Multiple Output (MIMO) offers high data rates with spatial multiplexing and reliability with spatial diversity gain [1-2]. The reduced Bit Error Rate (BER) is obtained by diversity gain which provides several copies of transmitted signals at the receiver. Spatial multiplexing is also a MIMO technology that transmits different data streams over multiple antennas simultaneously without an increase in bandwidth results in high data rates. A decade ago, extensive research on MIMO has been started. In the 1990s, the Alamouti scheme was proposed in the literature [3] with simple transmit diversity scheme for two transmit antenna systems and the spatial multiplexing scheme was first proposed in literature [4]. The principle behind the spatial multiplexing scheme is as follows: the transmission of high data rate of bit sequence is de-multiplexed into a low data rate of M subsequences, is modulated and transmitted over different transmit antennas simultaneously using the same frequency band. The interference cancellation algorithm is used to separate transmitted sequences at the receiver [5].

The combined technology of MIMO with OFDM gained more attention due to high data rates with spectral efficiency. OFDM is a popular technology used in wireless communications systems because of multi-carrier transmission in which a wide bandwidth is split into parallel 'n' sub-bands with sub-carriers i.e. each subcarrier experiences a narrow band. The advantage of OFDM is immunity to multipath fading and Inter Symbol Interference (ISI). ISI occurs when modulated symbol time is less than the delay-spread results in a non-deductible error floor which reduces the performance of the system significantly. To overcome ISI, equalization [6] is carried out on the receiver side. Various detection algorithms are available at the receiver side for the frequency flat fading that is categorized by different trade-offs between performance and complexity. To reduce the complexity, a linear receiver is a better choice.

This paper focuses to achieve better BER performance with 2x1 and 2x2 MIMO systems. In this paper, a 2x2 MIMO-OFDM system is implemented with the help of Universal Software Radio Peripherals (USRPs) and LabVIEW. BER performance is compared by increasing the FFT size of OFDM and with different M-QAM modulations. LabVIEW is a graphical programming language that provides inbuilt blocks like Fast Fourier Transform (FFT) and Inverse Fast Fourier Transform (IFFT) which are used to sample the real-time signals [7]. National Instruments (NI) USRPs are the Software Defined Radios (SDRs), which is a range of programmable Field Programmable Gate Array (FPGA) based Tx/Rx SDR made by Ettus research. With high speed and resolution ADCs and DACs, these high-quality devices take a modular approach and allow us to use a selection of a transmitter, a receiver, and transceiver. Radio Frequency (RF) daughter boards that are optimized to work at various frequencies [8].

The rest of the paper is organized as follows: Section II introduces an implementation of a simple MIMO system. The implementation of a 2x2 MIMO-OFDM system is presented in detail in section III. Section IV discusses the results and discussions. Section V deals with the conclusion of the paper.

## II. IMPLEMENTATION OF THE MIMO SYSTEM

MIMO communications system developed in the year 1990s and they became an integral part of the present wire

or wireless communications systems. Multipath propagation is the advantage in MIMO, various paths are formed due to bounces of vehicles, buildings and other obstacles and reach the receiver in different directions and at different times, this increases the receiver signal capturing power [9].

The transmitted sequence bits are modulated using M-ary Quadrature Amplitude Modulation (M-QAM), two parallel streams and in that first stream transmit through Tx1 antenna and other is through Tx2 antenna using Alamouti Space Time Block Code encoding scheme. Orthogonal Space-Time Block Code (OSTBC) is a superior kind of Space-Time Block Code (STBC) in which each column in the matrix of this code is orthogonal to individuals. Full diversity is achieved over the coherent channel at low computational cost using STBC. The STBC encoding and decoding procedure for a 2x1 MIMO is clearly shown in Fig 1, where p1, p2, p3, p4 are transmitting symbols, the same pair of symbols p1 and p2 transmitted through two different antennas twice over two symbol periods [10]. The transmitted symbols at the physical antenna have a little variation at each symbol timing. At the symbol time t1 direct symbols p1 and p2 are transmitted and at the symbol time t2 modified symbols p2\* and p1\* are transmitted as shown in Table I. Where p1\* and p2\* are conjugate of p1 and p2 respectively. h1 and h2 are channel coefficients represented with noise and fading. If there is no fading, interference, and noise present in the channel, the receiver decodes the transmitted data successfully without complicated transmission but in real-time, it is not possible. y1 and y2 are the signals at the receiver antennas 1 and 2 respectively [11]. The receiver does not process the data at each symbol. It waits till it receives two received symbols and combined them to decode and separate the symbols p1 and p2 with the help of weight vectors. The decoding procedure is as follows:

TABLE I.  
SYMBOL TRANSMISSION AT THE TRANSMITTER SIDE

Antenna's	Time slot 1	Time slot 2
1	p1	-p2*
2	p2	p1*

The received signal is represented as  $\vec{y} = H\vec{p} + \vec{n}$  (1)

Where Y is the signal received at the receiver, H is the channel matrix, p is the symbols transmitted at the transmitter and n is the noise.

The received signal at two-time slots is given by:

$$\begin{bmatrix} y_1 \\ y_2 \end{bmatrix} = \begin{bmatrix} h_1 & h_2 \end{bmatrix} \begin{bmatrix} p_1 & -p_2^* \\ p_2 & p_1^* \end{bmatrix} + \begin{bmatrix} n_1 \\ n_2 \end{bmatrix} \quad (2)$$

Received signal at time t1 is given by:

$$[y_1] = [h_1 \ h_2] \begin{bmatrix} p_1 \\ p_2 \end{bmatrix} + [n_1] \quad (3)$$

Received signal at time t2 is given by:

$$[y_2] = [h_1 \ h_2] \begin{bmatrix} -p_2^* \\ p_1^* \end{bmatrix} + [n_2] \quad (4)$$

Where

y1 and y2 are the received signals at different time

P1\* is the conjugate of p1 symbol

P2\* is the conjugate of p2 symbol

n1 and n2 are noise

Simplifying the equation (4) to obtain  $y_2^*$

$$y_2^* = [h_2^* \ -h_1^*] \begin{bmatrix} p_1 \\ p_2 \end{bmatrix} + n_2^* \quad (5)$$

Combining the equations (3) and (5) to get the orthogonal channel matrix as:

$$\begin{bmatrix} y_1 \\ y_2^* \end{bmatrix} = \begin{bmatrix} h_1 & h_2 \\ h_2^* & -h_1^* \end{bmatrix} \begin{bmatrix} p_1 \\ p_2 \end{bmatrix} + \begin{bmatrix} n_1 \\ n_2^* \end{bmatrix} \quad (6)$$

c1 and c2 are the first and second columns of the channel matrix.  $c_1^H$  represents transpose conjugate of c1. When multiplying  $c_1^H$  with c2, if the result is zero then c1 is orthogonal to c2. This is called an orthogonal channel matrix and is represented as:

$$c_1^H c_2 = [h_1^* \ h_2] \begin{bmatrix} h_2 \\ -h_1^* \end{bmatrix} = 0 \quad (7)$$

To retrieve the transmitted symbols, weight vectors are used that are denoted as  $w_1$  and  $w_2$

$$w_1 = \frac{c_1}{\|c_1\|} = \frac{1}{\|h\|} \begin{bmatrix} h_1 \\ h_2^* \end{bmatrix} \quad (8)$$

$$w_2 = \frac{c_2}{\|c_2\|} = \frac{1}{\|h\|} \begin{bmatrix} h_2 \\ -h_1^* \end{bmatrix} \quad (9)$$

Equation (8) multiplied with the equation (5) to retrieve p1 symbol as:

$$w_1^H \vec{y} = \frac{1}{\|h\|} [h_1^* \ h_2] \begin{bmatrix} h_1 & h_2 \\ h_2^* & -h_1^* \end{bmatrix} \begin{bmatrix} p_1 \\ p_2 \end{bmatrix} + w_1^H \vec{n}_1 \quad (10)$$

$$= \frac{1}{\|h\|} [(h_1^* h_1 + h_2 h_2^*) \ (h_1^* h_2 - h_1^* h_2^*)] \begin{bmatrix} p_1 \\ p_2 \end{bmatrix} + \tilde{n}_1 \quad (11)$$

$$= \frac{1}{\|h\|} p_1 + \tilde{n}_1 \quad (12)$$

Equation (9) multiplied with the equation (5) to retrieve the p2 symbol as:

$$w_2^H \vec{y} = \frac{1}{\|h\|} [h_2^* \ -h_1] \begin{bmatrix} h_1 & h_2 \\ h_2^* & -h_1^* \end{bmatrix} \begin{bmatrix} p_1 \\ p_2 \end{bmatrix} + w_2^H \vec{n}_1 \quad (13)$$

$$= \frac{1}{\|h\|} (h_1^* h_2 - h_1^* h_2) \ (h_1^* h_1 + h_2 h_2^*) \begin{bmatrix} p_1 \\ p_2 \end{bmatrix} + \tilde{n}_2 \quad (14)$$

$$= \|h\| p_2 + \tilde{n}_2 \quad (15)$$

For a 2x2 MIMO, the same process is used to retrieve the transmitted symbols using the OSTBC code, but complexity is increased due to an increase in one more antenna at the receiver [12], [13].

### III. IMPLEMENTATION OF 2 X 2 MIMO OFDM SYSTEM

MIMO-OFDM system setup consists of 4-USRP's, 2 for transmitting and the other 2 for receiving signals. LabVIEW is a software in which block diagram is constructed with the inbuilt blocks of communication tools. To interface LabVIEW with USRP's Gigabit Ethernet router is used.

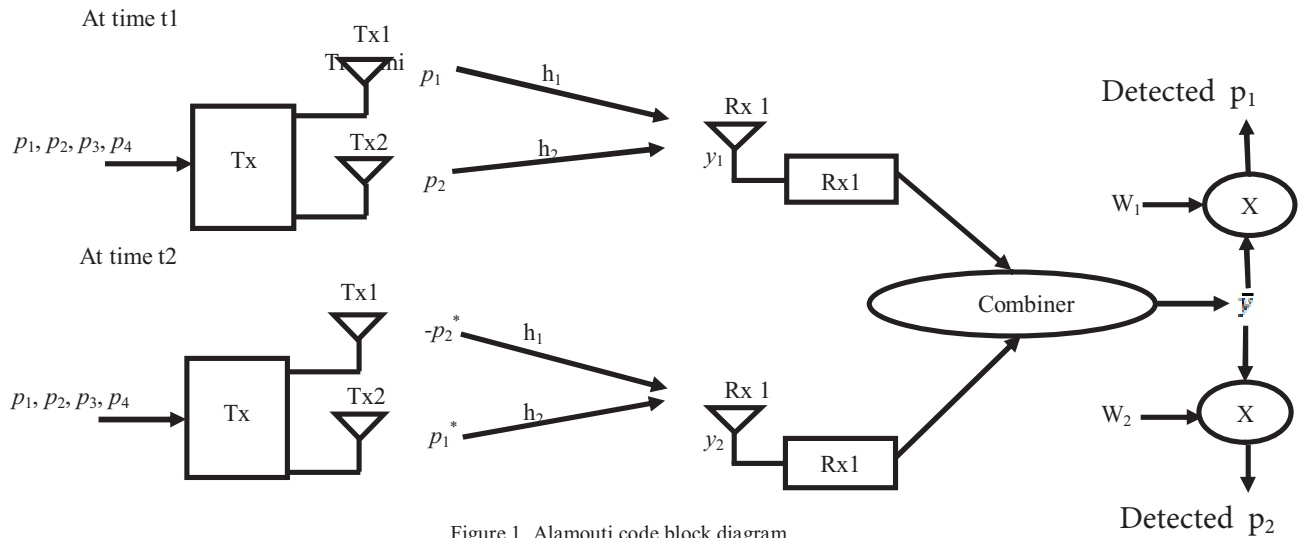


Figure 1. Alamouti code block diagram



Figure 2. Experimental 2x2 MIMO setup

In MIMO system, the data is transmitted from two transmitters at the same time. For that, an octa-clock is used for synchronization between the transmitter and receiver. The physical connection between the devices is shown in Fig. 2. The signal is transmitted with a bandwidth of 30 MHz and a frequency of 2.4 GHz. In 2x2 MIMO-OFDM system implementation, the PN sequence is used to generate a random sequence as a message signal. The generated bits are modulated using M-QAM (4, 16, 64 QAM) and modulated symbols are feed to the MIMO encoding block that results in transmitted signals in two channels, for each channel OFDM technique is applied as shown in Fig. 3. In OFDM, the wideband of serial data is converted into narrowband of N parallel data. Each narrowband is modulated with N subcarriers. Before the serial to parallel conversion of data, a training sequence (length 11 frank sequence) 0 is added for the channel estimation. The modulated subcarriers are passed through IFFT and the resultant OFDM signal is represented as follows:

$$x_n = \frac{1}{\sqrt{N}} \sum_{k=0}^{N-1} X_k e^{j\frac{2\pi kn}{N}}, 0 \leq n \leq N$$

The pulse shaping filter is used to reduce the bandwidth usage by clipping the edges and fit the signal into a transmitting channel.

The data is transmitted and received with the help of ADC in USRP. A maximum likelihood estimator is used for channel estimation. Schimidi cox algorithm is used for symbols timing recovery. The demodulation is used to recover the transmitted signal.

Fig. 4 shows the receiver of MIMO-OFDM in which a pulse shaping filter is used to receive the signal below the threshold level. The symbols in a signal get synchronized in symbol synchronization and the channel is estimated such that each channel constellation plot is obtained. To retrieve the Signal, the demodulated process is done.

#### IV. EXPERIMENTAL RESULTS AND DISCUSSIONS

In LabVIEW front panel the results of 2x1 MIMO, 2x2 MIMO and 2x2 MIMO-OFDM are shown in figures 5-7. By using M-QAM modulation techniques, incoming bits are demodulated and an approximate constellation plot for two transmitting channels at the receiver is obtained. BER is calculated for the received signal and shown in Table II. The BER is estimated for 2x1 and 2x2 MIMO system with different M-ary QAM modulations and is given in Table II. From Table II, the 2x2 MIMO system BER is less. In the 2x2 MIMO system, 2 receivers receive the transmitted signals obtained from multiple paths and retrieve their respective transmitted signals. In a 2x1 MIMO system, a single receiver can receive both the transmitted signals. The signals obtained at different delays cause interference, this results in high BER.

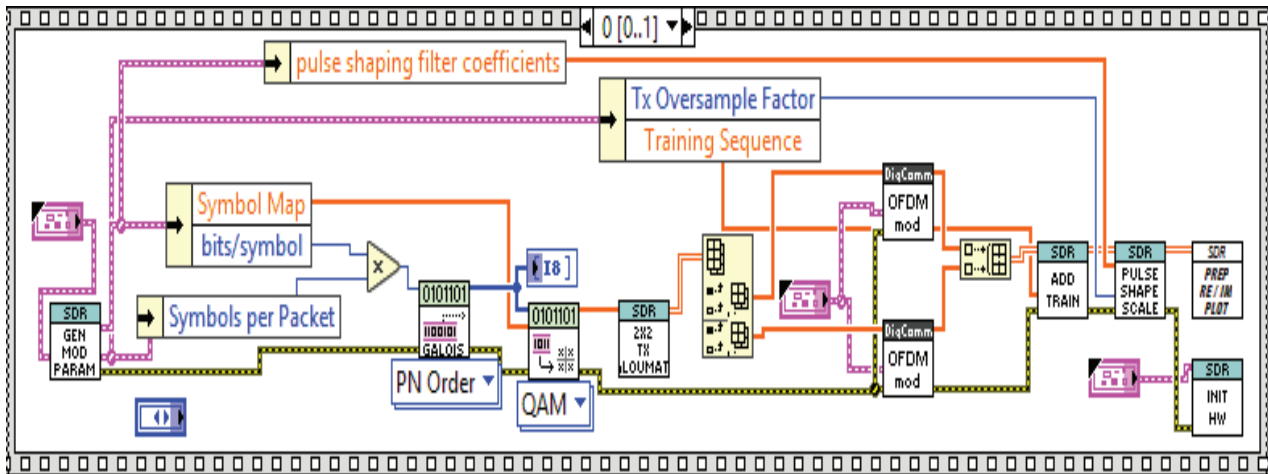


Figure 3. Implementation of 2x2 MIMO-OFDM transmitter

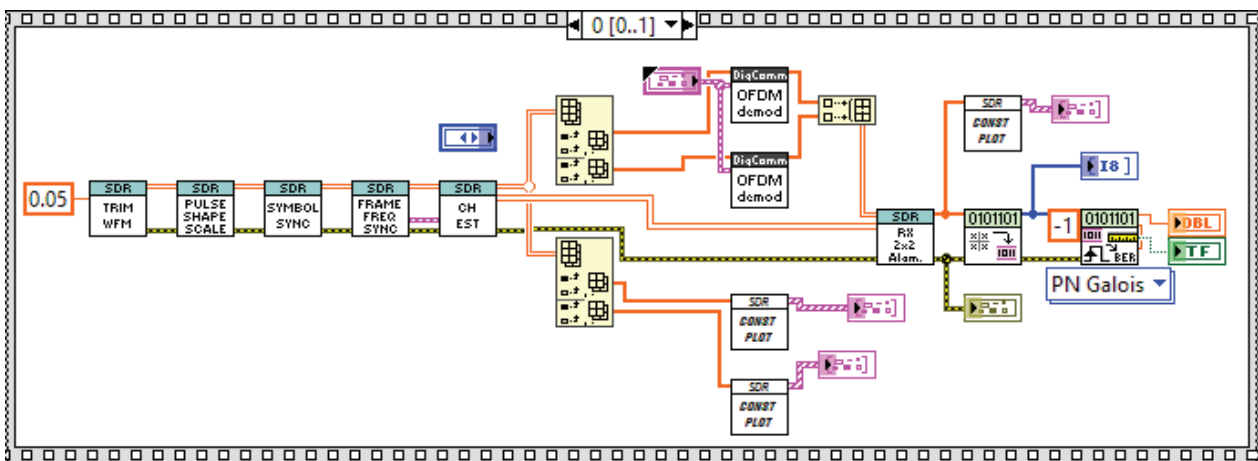


Figure 4. Implementation of 2x2 MIMO-OFDM receiver

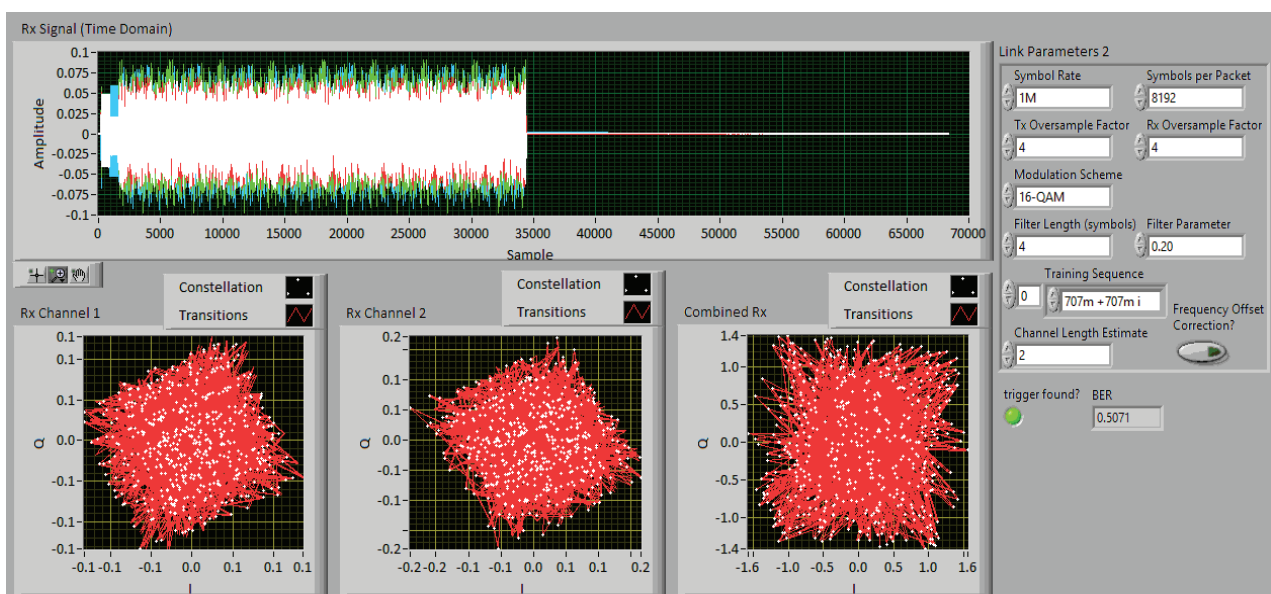


Figure 5. Front panel of 2X1 MIMO system

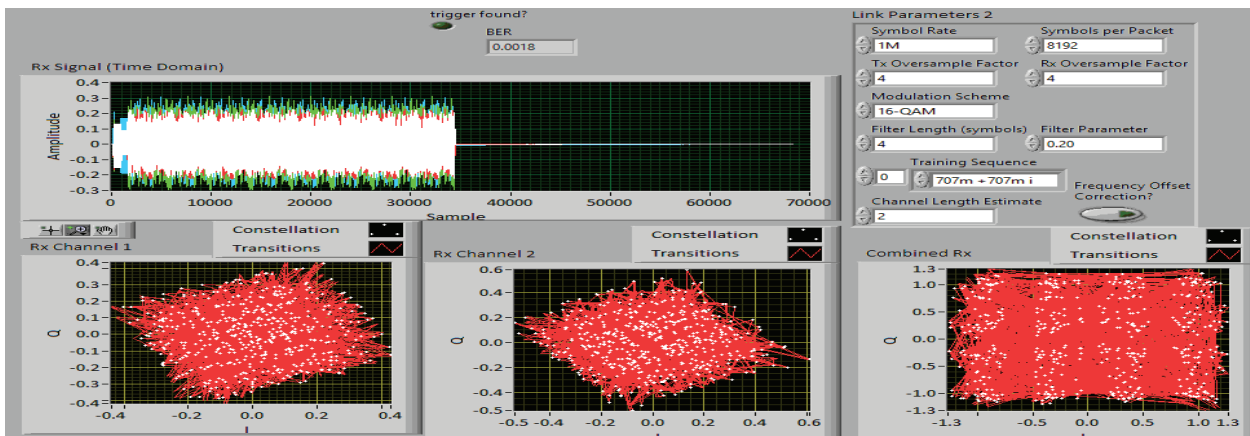


Figure 6. Front panel of 2x2 MIMO system

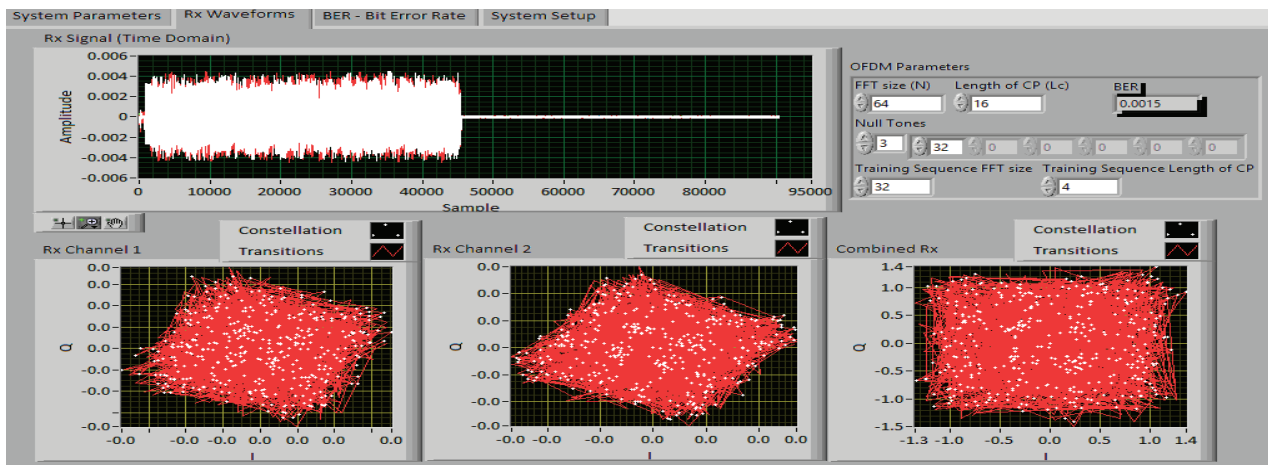


Figure 7. Front panel of 2x2 MIMO-OFDM system

TABLE II.  
COMPARISON OF BER PERFORMANCE OF 2x1 AND 2x2

QAM	BER	
	2x1	2x2
4	0.0160	0.0000
16	0.5071	0.0018
64	0.9010	0.0701

TABLE III.  
COMPARISON OF BER PERFORMANCE AT DIFFERENT IFFT SIZES

2 X 2 MIMO-OFDM			
QAM	BER with different IFFT		
	32	64	128
4	0.0002	0.0000	0.0008
16	0.0039	0.0015	0.0028
64	0.0593	0.0456	0.0818

In order to increase spectral efficiency, the OFDM system is combined with the MIMO system to obtain better BER performance such that channel estimation of 2x2 MIMO-

OFDM system constellation is shown in Fig. 7 and resultant information about M-QAM with BER Performance is shown in Table III.

From Table III, BER for 64 IFFT is reduced, when compared to 128 IFFT because with increasing the number of IFFTs the Peak to Average Power Ratio (PAPR) gets increases. PAPR is calculated as the average peak of signal to maximum power. As increasing M-ary QAM modulation, the constellation points increase, and this causes interference between symbols and reduces the BER performance.

## V. CONCLUSIONS

This paper includes the implementation of MIMO systems and their advantages. The main advantage of MIMO is high data rates and OFDM is high spectral efficiency. To capture this advantage, MIMO is combined with OFDM and MIMO-OFDM is implemented in LabVIEW using USRP. The BER of the MIMO-OFDM system is estimated as 0.0456. With increase in the FFT size, BER also increases due to the increase in PAPR of the OFDM signal. 2x2 system is used in many applications includes IEEE 802.11n, IEEE 802.11a/g WLAN, Digital

Video Broad Casting - Terrestrial 2<sup>nd</sup> Generation (DVB-T2), 3<sup>rd</sup> Generation Partnership Project (3GPP). It is also used in WiMAX which is the standard of IEEE 802.16, 5G and upcoming 6G technologies.

#### REFERENCES

- [1] G Foschini, D Chizhik, M Gans, C Papadias and R Valenzuela, "Analysis and performance of some basic space-time architectures", IEEE Journal on Selected Area in Communications, Volume. 21, number. 3, pp.303-302, Apr. 2003.
- [2] C F Ball, E Humburg, S Eder, L Lacinak, "WiMax Capacity Enhancements introducing MIMO 2x2 Diversity and Spatial Multiplexing", 2007 16<sup>th</sup> IST Mobile and Wireless Communications Summit, Sep 2007.
- [3] S. M. Alamouti, "A simple transmit diversity technique for wireless communications", IEEE Journal on Selected Areas Communications, Volume. 16, number. 8, pp. 1451– 1458, Oct. 1998.
- [4] Yong Soo Cho, Jaekwon Kim, Won Young Yang, and Chung G Kang, "MIMO-OFDM wireless communications with MATLAB", John Wiley & Sons, 2010.
- [5] Claude Oestges and Bruno Clerckx, "MIMO wireless communications: from real-world propagation to spacetime code design". Academic Press, 2010.
- [6] A. Paulraj and T. Kailath, "Increasing capacity in wireless broadcast systems using distributed transmission/directional reception", Feb. 21, 1992, U.S. Patent 5 345 599.
- [7] Yu Wei lin, Chen Yi Lee, "Design o an FFT/IFFT Processor for MIMO OFDM Systems", IEEE Transactions on Circuits and Systems, I: Regular Papers, Volume. 54, number 4, pp. 807-815, 16 April 2007.
- [8] V Tarokh, H Jafarkhani, A R Calderbank, "Space-time block codes from orthogonal designs", IEEE Transactions on Information Theory, Volume. 45, number 5, pp. 1456-1467, July 1999.
- [9] Pavan Kumar, Amita Kumari "BER Analysis of BPSK, QPSK, 16QAM & 64-QAM based OFDM System over Rayleigh Fading Channel", IOSR Journal of Electronics and Communication Engineering, Volume. 11, number. 4, pp. 6674, Jul-Aug 2016.
- [10] Malleswari Akurati, Yedukondalu Kamatham, Sathish Kumar Pentamsetty and Satya Prasad Kodati, "PAPR Reduction in OFDM using Hybrid Companding for 5G Wireless Communications", IEEE Global Conference for Advancement in Technology – GCAT 2019, Bengaluru, India, 18-20 October 2019.
- [11] Malleswari Akurati, Yedukondalu Kamatham, Satish Kumar Pentamsetty and Satya Prasad Kodati, "Reduction of PAPR in OFDM USING Hybrid SLM-Companding for future Wireless Communications", IEEE Global Conference for Advancement in Technology- GCAT 2019, Bengaluru, India, 18-20 October 2019.
- [12] Sravanti Thota, Yedukondalu Kamatham and Chandra Sekhar P, "Reduced Complexity Hybrid PAPR Reduction Schemes for Future Broadcasting Systems", International Conference on Emerging Trends in Engineering (ICETE), pp.69-76,22-23 March 2019.
- [13] Sravanti Thota, Yedukondalu Kamatham and Chandra Sekhar P, "Performance Analysis of Hybrid Companding PAPR Reduction Method in OFDM Systems for 5G Communications", The 9<sup>th</sup> International Conference on Computing, Communication and Networking Technologies (ICCCNT), pp. 1-5, July 10-12, 2018.

# Exploring Gender Classification from Speech Signal using Java-DSP Tool

Dr. G. Sasi

Professor, CVR College of Engineering/ECE Department, Hyderabad, India.  
Email: gsasikumar75@gmail.com

**Abstract:** More than a century, speech and audio processing play a crucial role in the entertainment and telecommunication systems. Due to the high demands, expecting more sophisticated features, still audio and speech processing require advanced techniques to serve better. This article focuses mainly on the gender classification from speech signals based on pitch period and pitch frequency analysis. To achieve the required tasks, the online graphical simulation, such as Java-DSP, is used here. J-DSP environment blocks can be dragged and placed in the editor easily, which helps to reduce the time required to complete the design issues. Also, the pitch period estimation is done using autocorrelation and cepstrum methods. The zero-crossing detection is used to focus on the identification of the voiced/unvoiced portion of the speech. The survey results from the participants who attended the training program on speech and audio processing course were obtained as feedback.

**Index Terms:** Autocorrelation, gender classification, J-DSP, on-line DSP simulator, pitch estimation.

## I. INTRODUCTION

The eminent faculty and students developed Java-DSP (J-DSP) at Arizona State University to teach the Digital Signal Processing course and related subjects through Internet-based labs and simulations. Students who are using J-DSP Tools do get benefit to understand, analyze, and realize the DSP concepts via online lab exercises [1–4]. Internet-based simulations, drag-and-drop facility, interactive approach, outreach functions support, interface to DSP hardware, and iPhone/iPad compatibility, basic and advanced functions of DSP are the major key features of the J-DSP tool [5–7].

This article mainly focuses on the usage of J-DSP tool on speech signals, especially with the male and female voice. In the last century and even today, audio signal and speech processing play a vital role in the telecommunication and entertainment systems. The main techniques behind audio and speech processing are as follows [8,9]:

- Quantization
- Entropy coding
- Transform coding
- Filter banks and transforms
- Subband coding
- Linear prediction
- Time-frequency analysis
- Lossless coding

Fig. 1 shows a few primary techniques and methods used in the audio and signal processing domain. Also, the multi-rate

digital signal processing applications are depicted in Fig. 2. Fig. 3 shows a simple J-DSP module on plotting Fast Fourier Transform (FFT) results for the given speech signal.

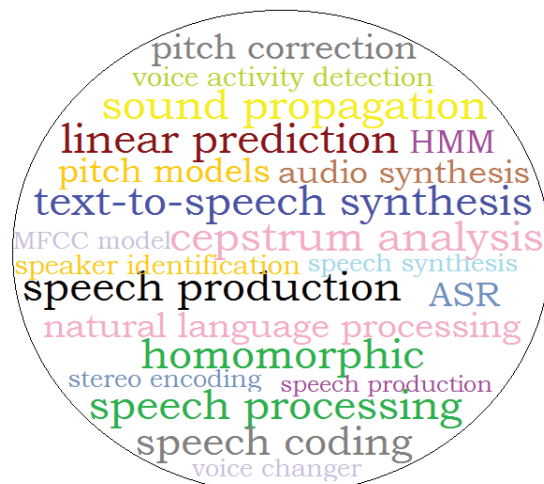


Figure 1. Techniques used in Speech and Audio Processing.

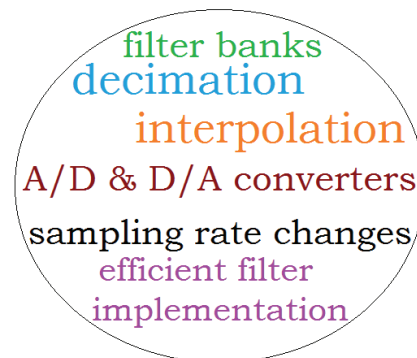


Figure 2. Applications of Multi-rate Digital Signal Processing.

The essential applications related to audio and speech processing, such as gender classification, speech/music classification, voiced/unvoiced classification, text-to-speech synthesis, audio hacking, and MP3 algorithms, can be worked out easily from students’ perspectives [10].

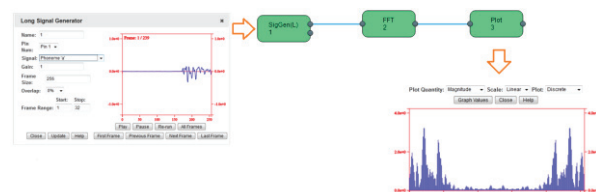


Figure 3. The FFT plot of a speech signal.



Speech is a comfortable medium or communication among people. Obviously, speech is the most powerful and easiest mode to communicate not only among human beings, also among human-animals and human-machines. A speech signal gives lots of information such as emotional status, gender, accent, dialect, etc [11].

Due to the different sizes of vocal cord, gender type, emotional status and dialect, the properties of each speaker vary enormously. Naturally, human beings identify the speaker from speech signals. But, for the automated applications, machines need to recognize the speech or a speaker, which would be the demanding task in modern computer technology. For the past decades, data mining and machine learning models have mostly used gender identification using voice signals. Features of the voice such as the vocal fold length, energy, formant and gait can be used for the machine learning models [12].

This article is organized as follows. Section 2 contains the materials and methods, which include pitch analysis on male and female speakers using both time and frequency domains. Part 3 includes an appraisal result of 30 students who participated in a two-day workshop on speech and audio processing course. Lastly, the conclusions are described in Section 4.

## II. MATERIALS AND METHODS

### A. Classification based on Pitch frequency

In common, the pitch frequency of the female speaker is much higher (almost double) than the male speaker. The vocal tract length is higher for males (approx. 17.5 cm), smaller for females (approx. 13 cm), and much smaller for children (approx. 9 cm). Hence, the pitch frequency of children is much higher than females and males. The variations among different speakers occur due to the age, gender, larynx, and vocal tract properties (physical), articulation habits, and the rate of speaking [13,14]

Fig. 4 shows the male speech signal and a voiced portion of the male speech. The sampling frequency of the speech signal is 8 kHz. The spectral analysis is done here on the 10th frame, which contains 256 samples. Hence, a 256-point Discrete Fourier Transform (DFT) is applied to the frame to view the spectral contents (see Fig. 5). As from Fig. 5, since there are four samples in between the spectral peaks, the peak-to-peak frequency resolution is calculated as follows:

$$\frac{4F_s}{N} = \frac{4 \times 8000}{256} = 125 \text{ Hz} \quad (1)$$

The result confirms gender as a male speaker. Similarly, the female speech signal and a voiced portion of the female speech are shown in Fig. 6. The spectral analysis using DFT and the results are shown in Fig. 7. As from Fig. 7, since there are eight samples in between the spectral peaks, the peak-to-peak frequency resolution is calculated as follows:

$$\frac{8F_s}{N} = \frac{8 \times 8000}{256} = 250 \text{ Hz} \quad (2)$$

The result confirms gender as a female speaker.

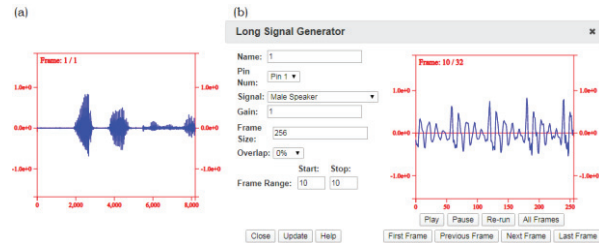


Figure 4. J-DSP environment blocks: (a) male speech signal; (b) the voiced portion of the male speech.

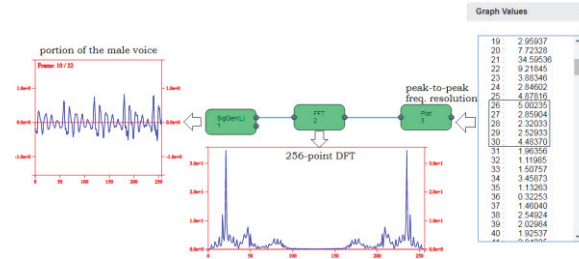


Figure 5. Spectrum analysis on the portion of the male voice.

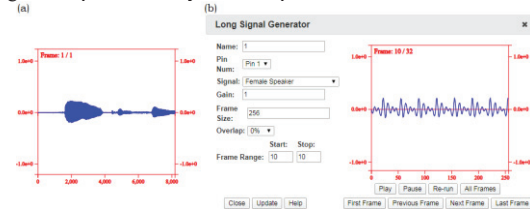


Figure 6. J-DSP environment blocks: (a) female speech signal; (b) the voiced portion of the female speech.

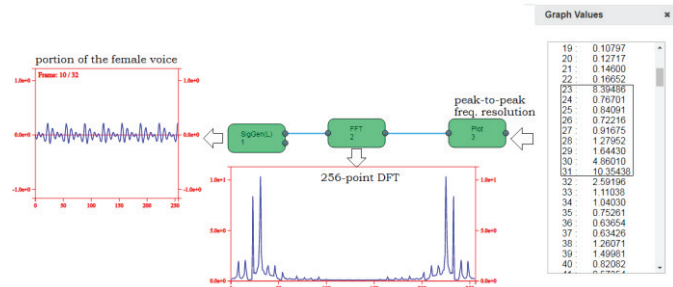


Figure 7. Spectrum analysis on the portion of the female voice.

### B. Classification based on Pitch period

Also, gender classification can be done using a pitch period. Fig. 8 shows the portion of the male speech signal, which contains the peaks in between 58 to 128 (total 62 of samples). Hence, the pitch period can be calculated as,

$$\frac{62 \text{ samples}}{8000 \text{ samples per second}} = 7.7 \text{ ms} \quad (3)$$

In general, the pitch period range for a male speaker is 4 to 20 ms, and for a female speaker is 2 to 8 ms. The above result confirms that the speaker is a male speaker. Similarly, Fig. 9 shows the portion of the female speech signal, which contains the peaks in between 55 to 88 (total 33 samples). Hence, the pitch period can be calculated as,

$$\frac{33 \text{ samples}}{8000 \text{ samples per second}} = 4.1 \text{ ms} \quad (4)$$

The above result confirms that the speaker as a female speaker.

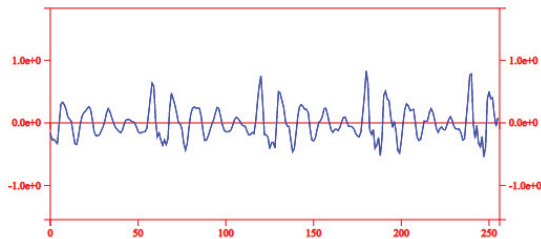


Figure 8. Pitch period analysis on a male speaker.

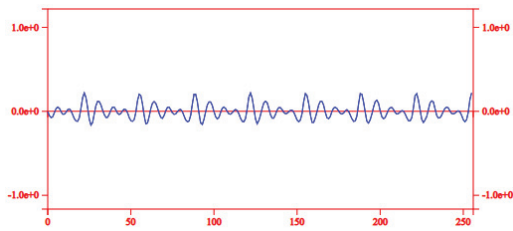


Figure 9. Pitch period analysis on a female speaker.

**C. Pitch period using autocorrelation**

Also, the autocorrelation technique can be used to determine the pitch period of a voice. Fig. 10 shows the autocorrelation results of a male speaker (lag with 61 samples), and Fig. 11 shows the results of the autocorrelation of a female speaker (lag with 33 samples). These results match the results obtained using pitch estimation using time-domain analysis for both the male and female speakers.

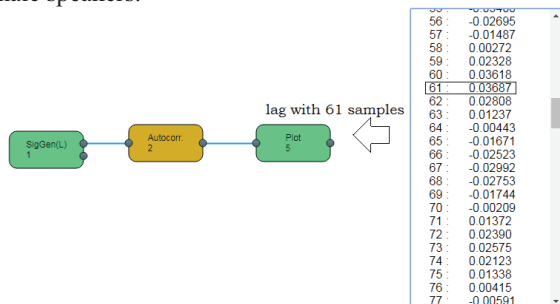


Figure 10. Pitch period estimation using autocorrelation on a male speaker.

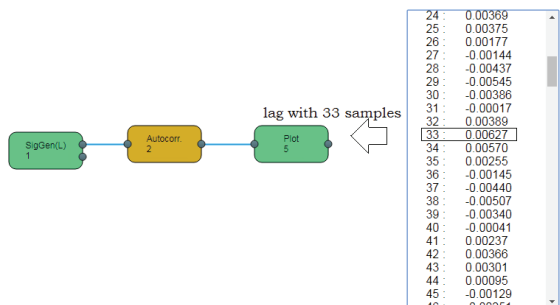


Figure 11. Pitch period estimation by autocorrelation on a female speaker.

**D. Other Experiments**

During the two-day workshop on speech and audio processing course, the participants did a few other experiments which are as follows,

- Gender classification using Matlab

- Voice activity detection
- Pitch correction
- Voice detection using zero-crossing rate detection
- Pitch estimation using Cepstrum analysis

**III. RESULTS AND DISCUSSION**

The thirty students who participated in a two-day workshop on speech and audio processing course were surveyed to identify the required time (minutes) per task (see Fig. 12). Since the J-DSP tool works fully on the drag-and-drop facility, almost all tasks require less time (except the cepstrum analysis). Also, the students were inspected to specify their interest in which exercise they experimented. The survey had the participants’ judge on a scale of 1 to 5, where one was “Boring”, two was “Not Interested”, three was “Interested”, four was “Very Good”, and five was “Highly Impressive”. Fig. 13 shows the average score (out of 30 scholars) for each task. On average, most of them were inspired by exploring digital filters (systems) using the J-DSP tool.

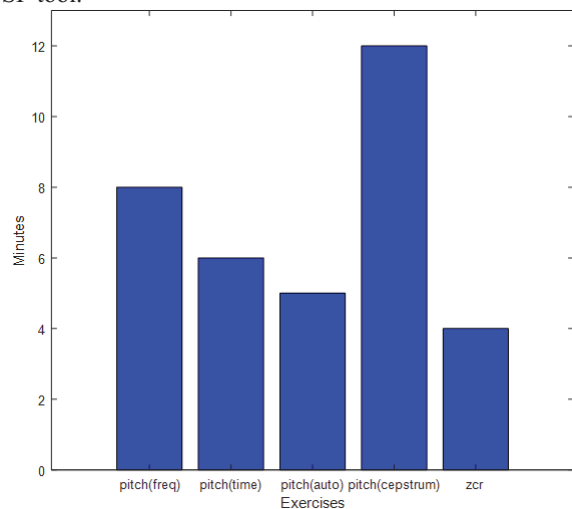


Figure 12. Results on time required per task.

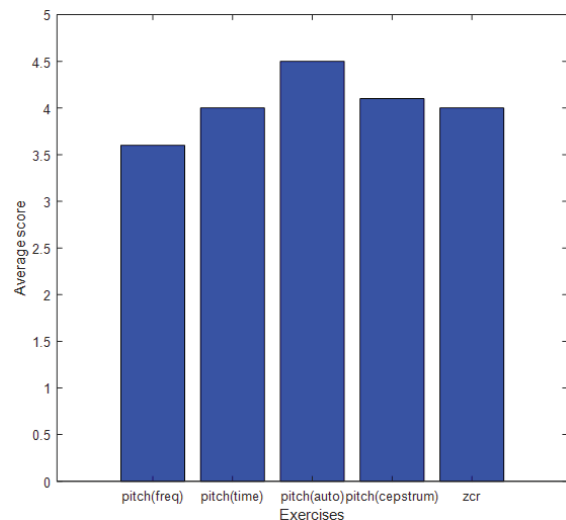


Figure 13. Survey results.

#### IV. CONCLUSIONS

The online based simulation software tools are much handy in teaching subjects such as linear systems, signals and systems, digital signal and image processing, audio and speech processing, control systems, etc. This sort of pedagogical method is comfortable for better analyzing the theoretical concepts with hands-on demonstrations. One such easy tool is J-DSP, the user-friendly tool, is used here to analyze speech signals, especially male and female speaker voices. Moreover, the pitch period is estimated using time domain, frequency domain, autocorrelation, and cepstrum methods. Also, the zero-crossing rate is used to identify the voiced/unvoiced portion of the speech. Conflicts of Interest: The authors declare no conflict of interest.

#### REFERENCES

- [1] Abhinav Dixit, Sameeksha Katoch, Photini Spanias, Mahesh Banavar, Huan Song, and Andreas Spanias, “Development of Signal Processing Online Labs using HTML5 and Mobile platforms”, Proceedings of the IEEE Frontiers in Education Conference (FIE), Indianapolis, IN, USA, pp.1–5,2017.
- [2] G.Sasi, P. Thanapal, R.K. Arvind Shriram, V.S. Balaji, V. and V. Elamaran, “Exploring digital signal processing concepts using on-line graphical DSP simulator”, International Journal of Advanced Science and Technology, 29: 410–421.
- [3] Andreas Spanias, Ted Painter, and Venkatraman Atti, “ Audio Signal Processing and Coding”. Wiley India,2013.
- [4] Suhas Ranganath, Jayaraman J. Thiagarajan, Deepta Rajan, Mahesh K. Banavar, Andreas Spanias, Jie Fan, Kristen Jaskie, and Cihan Tepedelenlioglu, “Interactive Signal Processing Education Applications for the Android Platform,” Computers in Education Journal, 10: 1–10, 2019. .
- [5] W. Wang, G. Zhang, L. Yang, V.S. Balaji, V. Elamaran, N.Arunkumar, 2019. Revisiting signal processing with spectrogram analysis on EEG, ECG and speech signals. Future Generation Computer Systems, 98: 227–232.
- [6] A. Dixit, U.S. Shanthamallu, A. Spanias, V. Berisha, and M. Banavar, “Online Machine Learning Experiments in HTML5,” Proceedings of the IEEE Frontiers in Education (FIE), San Jose, California, pp. 1–5, October 2018.
- [7] Uday S. Shanthamallu, SunilRao, Abhinav Dixit, Vivek S. Narayanaswamy, Jie Fan, and Andreas Spanias, “Introducing Machine Learning in Undergraduate DSP Classes,” Proceedings of the IEEE International Conference on Acoustics, Speech and Signal Processing (ICASSP), Brighton, United Kingdom, pp. 1–5, May 2019.
- [8] V. Elamaran, A. Aswini, V. Niraimathi, and D. Kokilavani, “ FPGA implementation of audio enhancement using adaptive LMS filters”, Journal of Artificial Intelligence, 5,pp. 221–226,2012.
- [9] Alison Behrman, “Speech and Voice Science”, Third Edition, Plural Publishers,2017.
- [10] B. Sindhura, S. Ashwin, G. Rajkumar, V. Elamaran, and M. Sankar, “Useful Tips and Tricks on Digital Data Processing with Discrete Fourier Transform”, Proceedings of the 2nd International Conference on Computing Methodologies and Communication (ICCMC 2018), Erode, India, pp. 738–742, 2018.
- [11] Manish Gupta, Shambhu Shankar Bharti, and Suneeta Agarwal, “Gender-based speaker recognition from speech signals using GMM model,” Modern Physics Letters B, 33: 1–23, 2019.
- [12] Ioannis E. Livieris, Emmanuel Pintelas, and Panagiotis Pintelas, “Gender recognition by voice using an improved self-labeled algorithm,” Machine Learning & Knowledge Extraction, 1: 492–503, 2019.
- [13] E. Abdulhay, V. Elamaran, M. Chandrasekar, V.S. Balaji, and K. Narasimhan, “Automated diagnosis of epilepsy from EEG signals using ensemble learning approach”, Pattern Recognition Letters, 28,pp. 5247–5251, 2017.
- [14] V. Elamaran, A. Praveen, M.S. Reddy, L.V. Aditya, and K.Suman, “FPGA Implementation of Spatial Image Filters using Xilinx System Generator”, Proceedings of the International Conference on Modeling Optimization and Computing (ICMOC-12), Procedia Engineering, 38,pp.2244 – 2249, 2012.
- [15] R. Naveena, V. Dorthy Rabecka, G. Rajkumar, and V. Elamaran, “Understanding Digital Filters from Theory to Practice using Matlab and Simulink”, International Journal of Pharmacy and Technology, 7,pp.9923–9934,2015.
- [16] V. Elamaran and G. Rajkumar, “ FPGA implementation of point processes using Xilinx System Generator”. Journal of Theoretical and Applied Information Technology, 41,pp. 201–206,2012
- [17] K. Narasimhan, V. Elamaran, S. Kumar, K. Sharma, and P.R. Abhisek, “Comparison of satellite image enhancement techniques in wavelet domain”. Research Journal of Applied Sciences, Engineering, and Technology, 4,pp. 5492 – 5496, 2012.

# A Cluster Head Routing Protocol for Improving Network Lifetime in Wireless Sensor Networks

Dr. Gaurav Sharma

Asst. Professor, CVR College of Engineering/ECE Department, Hyderabad, India

Email: [ergaurav209@yahoo.co.in](mailto:ergaurav209@yahoo.co.in)

**Abstract:** The energy efficiency in wireless sensor networks (WSNs) is a fundamental challenge. Cluster based routing is an energy saving method in this type of networks to reduce energy consumption in WSNs. A new Energy Efficient Cluster Head Routing protocol for heterogeneous WSN, which is called CHRP is proposed and evaluated which works on sleep-awake policy that helps in prolonging lifetime of the network. In CHRP, the cluster head is elected if its residual energy is more than system average energy of the network. Node pairing mechanism is also employed in CHRP. The nodes with high initial and residual energy will have more chances to become cluster head. Finally, the simulation results show that CHRP enhances lifetime of heterogeneous sensor network as compared to other protocols i.e., Distributed Energy Efficient Clustering (DEEC) and Threshold Sensitive Stable Electron Protocol (TSEP).

**Index Terms:** Clustering, Routing Protocol, Energy Efficient Algorithms, Wireless Sensor Networks.

## I. INTRODUCTION

Wireless Sensor Networks (WSNs) have gained worldwide attention in recent years, particularly with recent advances in microelectromechanical systems (MEMS) technology, wireless communications and digital electronics which have enabled the development of low-cost, low-power and multifunctional sensor nodes. A WSN consists of many small and low-cost sensor nodes capable of detecting physical phenomena such as temperature, light, heat, sound, etc. [1, 2]. WSNs have many applications including military, monitoring, home applications, traffic control, etc. Since the sensor nodes may be applied in dangerous and inaccessible environments, replacing or recharging their power supplies is not possible and economic. Therefore, optimizing energy consumption for prolonging the network lifetime is a critical issue in WSNs. In order to prolong the lifetime of sensor network, energy efficient routing protocols are designed based on clustering techniques.

Clustering has been proved an effective routing method for reducing the energy dissipation of nodes, balancing the energy consumption among nodes and prolonging the network lifetime [3, 4]. In clustering methods, nodes are divided into groups called clusters. Each cluster has a leader node named cluster head (CH) and the rest of the nodes are called member nodes. Member nodes transmit their data to the corresponding CH and then the CH, after collecting the received data, aggregates their data together with its own data and transmits them to the base station (BS).

In general, the clustering process consists of two phases: the setup phase and the steady state phase. The setup phase includes the selection of CHs and forming the clusters. In

the steady state phase, member nodes transmit their data to their corresponding CH, and CH sends the aggregated data to BS. Since most of the cluster-based routing protocols do not consider the consumed energy due to the clusters formation in the setup phase, the energy dissipation is not properly optimized.

In this paper, the performance of CHRP algorithm in saving energy for heterogeneous WSNs is studied. In the sensor network considered in this paper, each node transmits data either directly to base station or via cluster head which is elected by certain clustering algorithm, fuses the data collected from their cluster members and sends it to the “sink node”.

Here in this protocol, all the sensor nodes with different amounts of energy which leads to heterogeneous sensor network is considered [5]. The addition of new nodes in the networks prolongs the lifetime of the network. Currently in most of the protocols, such as DEEC [1], TSEP [6], heterogeneous network is assumed. In TSEP [6] three levels of heterogeneous sensor network is taken which is composed of normal nodes, intermediate nodes and advanced nodes. The advanced nodes are equipped with more energy nodes than normal nodes. Also, cluster heads are selected depending on probability of each type of node. However, it is not fit for multilevel heterogeneous WSN that includes more than two types of nodes.

In DEEC [1], each node spends its energy uniformly by rotating the role of cluster head among all nodes. Basically, CHs are elected based on the ratio between residual energy of each node and average energy of the network. Thus, DEEC can improve the stability period and hence prolong the network lifetime by heterogeneous clustering approach.

In this paper, a new energy efficient cluster head routing algorithm for heterogeneous WSN composing three different types of nodes i.e. normal nodes, super nodes and advanced nodes is proposed and evaluated. In CHRP, basically sleep-awake policy is used in which some nodes put to sleep to conserve energy and hence prolongs the lifetime of the network. Utilizing the concept of node pairing among sensor nodes and threshold energies, energy utilization of the network is optimized. The remainder of the paper is organized as follows. Section II describes the proposed algorithm. Section III shows the performance of CHRP by simulation and compares it with DEEC and TSEP. Finally, section IV gives concluding remarks.

## II. PROPOSED WORK

This section describes a new Algorithm CHRP (Cluster Head Routing Protocol) which has two main characteristics:

1. Direct Communication
2. Transmission via Cluster Head

It is reactive routing protocol, as transmission consumes more energy than sensing and it is done only when a precise threshold is reached [8, 9].

To describe whole protocol clearly particularly discussion about energy model and how optimum number of clusters can be computed is done. For three levels of heterogeneity, nodes with different energy levels are:

- 1) Normal Nodes
- 2) Advance Nodes
- 3) Super Nodes

Advance nodes having energy greater than normal nodes, super nodes with the highest energy. Super nodes can be chosen by using  $b$ , where  $b$  is proportion of super nodes and using the relation that energy of normal nodes is  $\mu$  times more than that of normal nodes. Energy for normal nodes is  $E_o$ , for advance nodes it is  $E_{ADV} = E_o(1+a)$  and energy for super nodes can be computed as  $E_{SUP} = E_o(1 + \mu)$ , where  $\mu = a/2$ .

So total energy of normal nodes, advance nodes and for super nodes will be,  $n.E_o.(1 - m - b)$ ,  $n.m.E_o.(1 + a)$ , and  $n.b.E_o.(1 + \mu)$  respectively.

Therefore, the total Energy of all the nodes will be,  $n.E_o.(1-m-b) + n.m.E_o.(1 + a) + n.b.E_o.(1 + \mu) = n.E_o.(1 + ma + b\mu)$ .

where  $n$  is number of nodes,  $m$  is proportion of advanced nodes to the total number of nodes  $n$  with energy more than rest of nodes and  $b$  is proportion of super nodes.

Starting of a round, BS broadcasts HELLO packets among the sensors periodically. If the RSSI of the received signal is greater than clustering threshold then no need to form clusters [10, 11, 12]. Based on stronger RSSI (Receiving Signal Strength Indicator) nodes closer to the BS are selected to send their data directly to BS. This region is called direct communication region. Remaining nodes follow dynamic clustering technique.

In WSN, sensors are deployed with high density due to limited resources and vulnerable nature of individual sensor. As a result the same area is covered by many sensor nodes. This causes a lot of redundancy because multiple sensor nodes consume energy to sense the same area and also to trans-receive the identical data. For this reason, redundant information will increase at the BS and also there will be wastage of transmission energy among the nodes. The solution to avoid this redundancy is to turn off the redundant nodes, as turning off some nodes does not affect the overall system as long as there are enough working nodes to provide the service. Turned-off sensor nodes save a significant amount of energy and this addresses one of the important constraints of WSN i.e. limited energy [13]. Therefore, if sensor nodes are scheduled to perform alternately, more energy can be saved and system lifetime can be prolonged effectively. So, in the proposed technique, at any moment, only some of the members perform i.e. they become active nodes and rest of the nodes remain in sleep mode i.e. they are passive nodes. The decision of choosing i.e. which node

will be active and which will be passive is taken on the basis of RSSI. The proposed approach is explained using these three phases:

#### A. Node Pairing

Before performing clustering, a node has to select its nearest node. A node sends a request message to find nearest neighbor. The 1-hop neighbor nodes which are closer to that node send a reply with their distances from that particular node and they are included in eligible neighbor list. Then the node in the Eligible Neighbor List which has maximum RSSI is selected as next node [14, 15]. The two nodes are added as coupled and then Node Paired ID message is broadcast in the network.

After performing the node pairing mechanism as shown in Fig.1, each node checks its remaining energy with its paired neighbor. In a pair, a node switches into Active mode if its residual energy is greater than its paired node. Thus, node having more residual energy in a pair will participate in clustering technique and the other one will remain in sleep mode for that round. During a sleeping period, the node ceases to perform any communication with the environment [14, 16, 17].

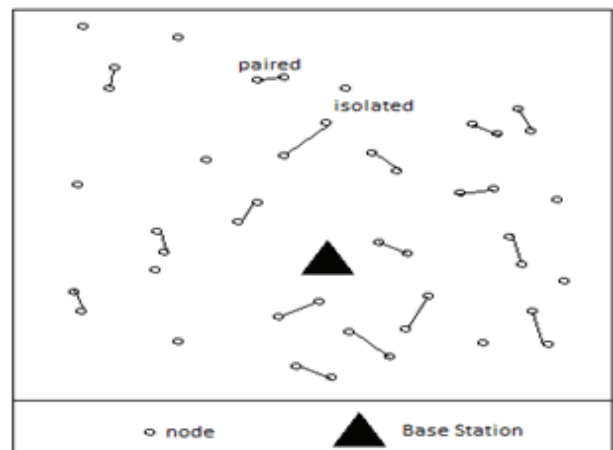


Figure 1. Node Pairing

Thus, power consumption is assumed to be minimal, whereas when a sensor is awake, it consumes regular amount of energy. In next communication period, nodes in Active-mode switch into Sleep-mode and Sleep-mode nodes switch into Active mode if and only if Sleep-mode node's residual energy is above Active-mode node's energy level. In this way, it is able to minimize energy consumption as nodes in Sleep-modes save their energy by not communicating with the CHs. Nodes in Sleep-mode also save their energy by avoiding idle listening and overhearing [10, 18, 19]. If coupled partner of a node is dead, then it will become active for rest of the round. Isolated nodes remain in Active-mode for every round till their energy resources depleted.

#### B. Cluster Heads Selection

At the starting of cluster head selection phase BS receives the status of the current energy level from all sensor nodes

in the network. Then selection of powerful nodes is done based on the received energy values. The BS computes the average energy level of the active nodes as follows:

$$E_{avg} = \sum \frac{E_{resi}}{m} \quad (1)$$

where  $m$  is the total number of active nodes;  $E_{resi}$  is nodes residual energy.

So, CHRP protocol uses  $E_{avg}$  to be the main parameter for selecting CHs and handle well the heterogeneous energy capacities among the sensor nodes considering system average energy in each round. After BS broadcasts average energy of the network, nodes having remaining energy greater than or equal to the system average energy include themselves in the set of eligible cluster heads. If a node finds its  $E_{resi} \geq E_{avg}$  then it sends a request message to find eligible neighbors [7, 12]. The 1-hop neighbor nodes which are closer to that node send a reply with their Energy Consumption Rate  $E_{ecr}$  in previous round. The node which has minimum energy consumption rate in previous round and with  $E_{resi} \geq E_{avg}$  is selected as CH node, where energy consumption rate is as follows:

$$E_{ecr} = \frac{E_o - E_{resi}}{m - 1} \quad (2)$$

The optimal probability of nodes, which are divided on the basis of energy, to be chosen as a CH can be calculated by using following formulas:

$$p_{nrm} = \frac{p_{opt}}{1 + m \cdot \alpha + b \cdot \mu} \quad (3)$$

$$p_{adv} = \frac{p_{opt}(1 + \alpha)}{1 + m \cdot \alpha + b \cdot \mu} \quad (4)$$

$$p_{sup} = \frac{p_{opt}(1 + \mu)}{1 + m \cdot \alpha + b \cdot \mu} \quad (5)$$

Now to ensure that CH selection is done in the same way as it is assumed, another parameter is taken into consideration, which is threshold level. Each node generates a number randomly inclusive of 0 and 1, if generated value is less than threshold then this node becomes CH [4, 7]. For all these type of nodes different formulas for the calculation of threshold depending on their probabilities are given below:

$$T_{nrm} = \begin{cases} \frac{p_{nrm}}{1 - p_{nrm} \left[ r \cdot \text{mod} \frac{1}{p_{nrm}} \right]}, & \text{if } n_{nrm} \in G' \\ 0, & \text{otherwise} \end{cases} \quad (6)$$

$$T_{adv} = \begin{cases} \frac{p_{adv}}{1 - p_{adv} \left[ r \cdot \text{mod} \frac{1}{p_{adv}} \right]}, & \text{if } n_{adv} \in G'' \\ 0, & \text{otherwise} \end{cases} \quad (7)$$

$$T_{sup} = \begin{cases} \frac{p_{sup}}{1 - p_{sup} \left[ r \cdot \text{mod} \frac{1}{p_{sup}} \right]}, & \text{if } n_{sup} \in G''' \\ 0, & \text{otherwise} \end{cases} \quad (8)$$

where  $r$  is number of rounds.

$G'$ ,  $G''$  and  $G'''$  are the set of normal nodes, advanced nodes and set of super nodes that has not become CHs in the past respectively, so ensuring that the equations (3), (4) and (5) are working.

Average total number of CHs per round will be:

$$n \cdot (1 - m - b) \cdot p_{nrm} + n \cdot b \cdot p_{sup} + n \cdot m \cdot p_{adv} = n \cdot p_{opt}$$

Although, average number of CHs is same as that of DEEC and TSEP, however, here a good aspect of CHRP is that energy dissipation is condensed due to energy heterogeneity and node pairing.

### C. Data Transmission and Data Aggregation

At the start of each round, the phenomenon of cluster change takes place. In case of CHRP, at cluster change time, the CH broadcasts the following parameters.

Hard Threshold (HT): It is an absolute value of sensed attribute beyond which node will pass on data to CH. As if sensed value becomes equal to or greater than this threshold value, node turns on its transmitter and transmits.

Soft Threshold (ST): It is the smallest sensed value at which the nodes switch on their transmitters and sends that information to CH.

All nodes keep on sensing the environment continuously. When parameters from attribute set reaches hard threshold value, transmitter is switched on and data is transmitted to CH, however this is only for the first time when this condition is met.

This sensed value is stored in an internal variable in the node, called Sensed Value (SV). Then for the second time and the other, nodes will transmit data if and only if sensed value is greater than hard threshold value or if the difference between currently sensed value and the value stored in SV variable is equal to or greater than the soft threshold [12, 20]. So, by keeping these both thresholds in consideration, the number of data transmissions can be decreased, as transmission will only take place when sensed value reaches hard threshold. And further transmissions are narrowed by soft threshold, as it will eliminate transmissions when there is a small change in value, even smaller than interest. Some of the important features are described below:

1) Time with which critical data reaches the user almost instantaneously.

2) Nodes keep on sensing continuously, but transmission is not done frequently, so energy consumption is much lesser than that of proactive networks.

3) At time of cluster change, values of soft threshold, TR is transmitted afresh and so, user can decide how often to sense and what parameters to be sensed according to criticality of sensed attribute and application.

4) The user can change the attributes depending on requirement, as the attributes are broadcasted at the cluster change time.

The significant trade off of this scheme is that if threshold is not reached, user will not get any information from network and even if any or all the nodes die, system will not

come to know about that. So, it is not useful for those types of applications where a data is required continuously.

**D. Algorithm Process**

**Step 1:** For a given simulation time  $T$ , the Base Station broadcasts HELLO packets periodically. If a sensor node listens HELLO packet then it replies with residual energy. If the RSSI of the received signal is greater than that of any other cluster head then no need to form clusters. Else Clustering occurs.

**Step 2:** If any node is alive then node pairing is done with closest neighbor. Follow step 4 to decide about the active nodes. If node is active then for each round the Base Station chooses CHs. If a node is Cluster Head then it broadcasts its advertisement message and all non-CHs active nodes, send joining request message to that CH, from which it received the highest RSSI [6, 17]. Cluster head accepts the joining request. Thus forming respective clusters.

**Step 3:** A node broadcasts a request message to find the closest neighbor. The neighbors respond reliably. The neighbor with the strongest RSSI is selected as the next node. The node status will be PAIRED and it broadcasts Node\_Paired\_ID message.

**Step 4:** Get  $N$  paired node sets in the network. If node is paired then for each pair set, node broadcasts an Energy\_Msg message to its neighboring node [1, 14, 16]. Receiving Energy\_Msg from its neighboring node, the node updates its own Neighbor\_Table. If  $E(r)_{node} > E(r)_{neighbor}$  then node is active else the node sleeps. If neighbor node is dead then another node of that pair is awake for remaining rounds else node is active for whole network life time.

**Step 5:** Base Station receives the status of the residual energy from all nodes. Then based on this, the Base Station computes average energy of the active nodes. For each node having residual energy more than average energy include in the set of eligible Cluster Heads. If a node finds its residual energy more than average energy then it sends a request message to find eligible neighbors. The 1-hop neighbor nodes closer to that node send a reply with their energy consumption rate [21]. The node which has minimum energy consumption rate and with residual energy more than average energy is selected as Cluster Head node.

**Step 6:** If current value is greater than or equal to the hard threshold then test = current value – sensed value [8]. If test is greater than or equal to the sensed value and the distance between the sensed region is more than threshold then:

Energy = Energy – less transmission energy

else

Energy = Energy – more transmission energy

**III. SIMULATION RESULTS**

For performance evaluation MATLAB is used. The goals in doing simulations were to compare performance of CHRP with TSEP [6] and DEEC [1] protocols on the basis of energy dissipation with longevity of the network [5, 13].

Performance attributes used in the simulations are:

- 1) Stability period, the period from starting of the network operation and the first dead node.
- 2) Instability period, the period between the first dead node and the last dead node.
- 3) Number of nodes alive per round.
- 4) Number of nodes dead per round.
- 5) Throughput, number of packets sent from the cluster heads to the base station per unit time.

A network consisting of 100 nodes, placed randomly in a square region,  $100m \times 100m$  and a BS located in the center is considered. Simulations for different values of  $\alpha$  and  $m$  while keeping  $b$  constant i.e., 0.3 are performed. For the first case  $\alpha = 1, m = 0.2$ , for second case  $\alpha = 3$  and  $m = 0.2$ . This is done to observe the change in network’s stability, life and throughput relative to increase the number of advance nodes and corresponding energies. Since  $p_{opt} = 0.1$ , is optimal probability of CHs, by using equations (3), (4) and (5) different probabilities for every type of node in accordance with different values of  $\alpha$  and  $m$  are obtained. All the parameters used in simulations are shown in Table I.

TABLE I.  
PARAMETER SETTINGS

Parameters	Value
$E_{elect}$	50nJ/bit
$E_{DA}$	5nJ/bit/message
$\epsilon_{fs}$	10pJ/bit/m <sup>2</sup>
$\epsilon_{mp}$	0.0013pJ/bit/m4
$E_o$	0.5J
$K$	4000
$p_{opt}$	0.1
$N$	100
$\alpha$	1
$m$	0.2

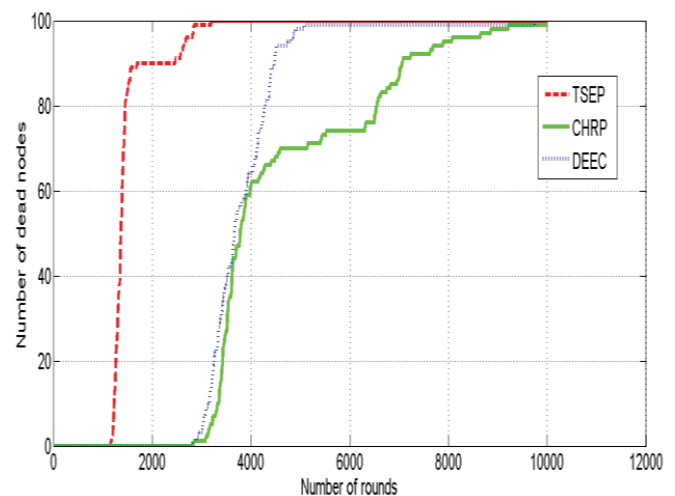


Figure 2. Number of dead nodes per round for  $\alpha = 1$  and  $m = 0.2$

By using the equations (6), (7) and (8), CHs election for normal, advance and super nodes respectively, can be determined.

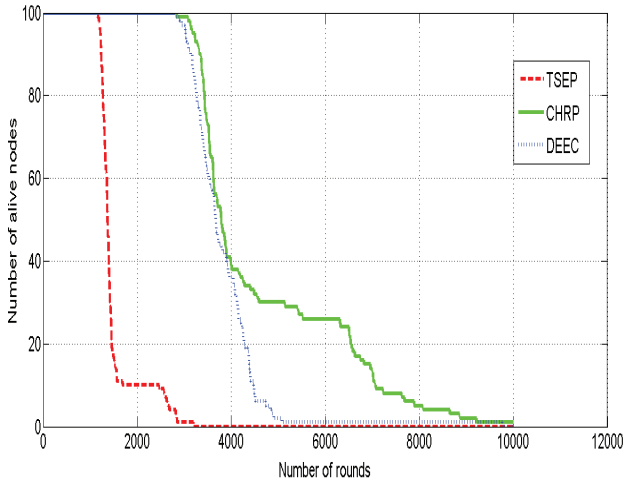


Figure 3. Number of alive nodes per round for  $\alpha = 1$  and  $m = 0.2$

Fig.2 and Fig.3 show comparison of protocols DEEC, TSEP and CHRP regarding dead and alive nodes, relative to the number of rounds. As it can be seen, CHRP has completely dominated the other two protocols because of heterogeneity, threshold consideration and node pairing.

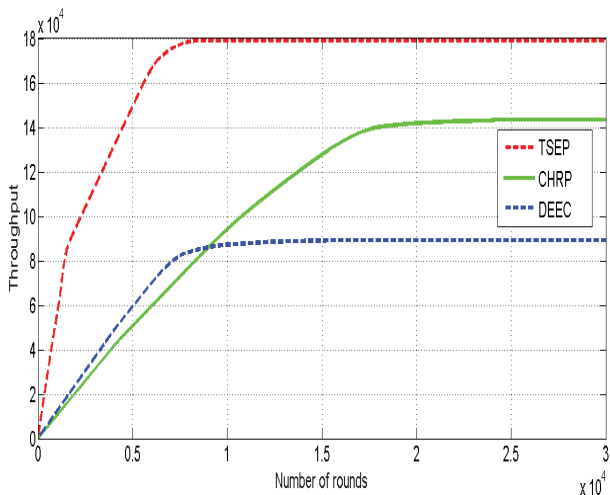


Figure 4. Number of packets sent from CHs to BS for  $\alpha = 1$  and  $m = 0.2$

Fig. 4 shows throughput, data sent from CHs to the BS. CHRP being threshold sensitive protocol and sleeping protocol, shows better result than DEEC and TSEP, as here transmission rate is less so energy consumption will be less than others.

From Fig. 2, Fig. 3 and Fig. 4, it can be concluded that stability period and the network life time are greater in CHRP, than all other protocols. Nodes tend to die out slowly in CHRP, as in CHRP a huge part of energy is consumed in sensing; while transmission of data is done only at the conditions when HT value is achieved by sensed node or is exceeded.

The number of rounds is more in CHRP when percentage of dead nodes is 50% and the number of rounds becomes huge in CHRP when percentage of dead nodes is 100%. So, CHRP is a lot better than the existing techniques when  $\alpha = 1$  and  $m = 0.1$  as shown in Table II.

TABLE II.

AVERAGE LIFETIME OF NODES IN NUMBER OF NODES FOR  $\alpha=1$  AND  $m = 0.1$

% of dead nodes	Number of rounds		
	DEEC	TSEP	CHRP
1	1020	2187	3104
10	1038	3124	3154
50	1201	3297	3472
100	3211	7601	9304

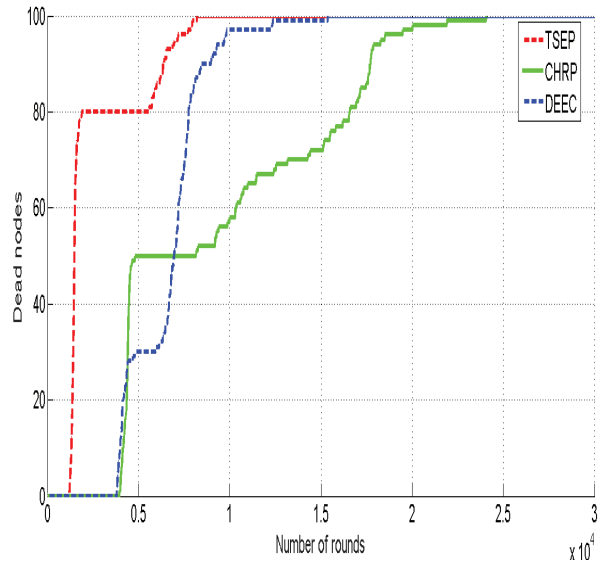


Figure 5. Number of dead nodes per round for  $\alpha = 2$  and  $m = 0.3$

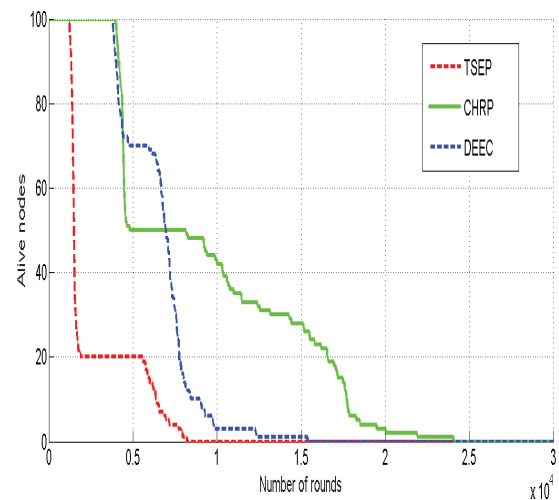


Figure 6. Number of alive nodes per round for  $\alpha = 2$  and  $m = 0.3$

Same is the case for results shown in Fig. 5, and Fig. 6, where  $\alpha = 2$  and  $m = 0.3$ . In this case, energy of nodes as well as packets to BS is also increased. Therefore, more number of nodes will be available with an extra energy. As shown in Fig. 5, Fig. 6, by increasing number of advanced nodes and  $\alpha$  stability period and the network lifetime are increased. It happens because of three level heterogeneity. So, it can be clearly seen that there are noticeable differences among the protocols in accordance with alive nodes, dead nodes and throughput. Throughput of DEEC is found to be better but redundant information is reduced in packets sent by CHRP.



By performing simulations in MATLAB, it is observed that:

- CHRP has enhanced stability period compared to all other protocols. This is shown in Fig. 2, Fig. 3 and Fig. 5, Fig. 6.
- The network life time for CHRP was increased as compared to others.
- Decrease and increase in number of dead and alive nodes respectively with increase in  $\alpha$  and  $m$ .
- Throughput is increased due to three level heterogeneity and there is decrease in throughput due to threshold sensitivity as can be observed in Fig.4.

In Table III, the number of rounds is more in TSEP than that of CHRP when percentage of dead nodes is 50% but the number of rounds becomes huge in CHRP when % of dead nodes is 100%. So, CHRP is a lot better than the existing techniques when  $\alpha = 2$  and  $m = 0.3$ .

TABLE III.

AVERAGE LIFETIME OF NODES IN NUMBER OF NODES FOR  $\alpha = 2$  AND  $m = 0.3$

% of dead nodes	Number of rounds		
	DEEC	TSEP	CHRP
1	1074	4122	4127
10	1098	4159	4182
50	1192	6421	4306
100	7967	15620	25098

#### IV. CONCLUSIONS

A reactive cluster head routing protocol viz. CHRP is proposed in this paper which is composed with three different levels of energies and node pairing. From the simulations results it is concluded that the proposed routing protocol is more energy efficient and hence there is enhancement in the sensor network lifetime, there are more alive nodes in the network if the results of TSEP and DEEC to the proposed protocol are compared. In the existing system transmission of data depends on current energy of nodes and distance between the nodes whereas TSEP algorithm works only on three different levels of energies. The sleeping algorithm improves lifetime of the network. Selection of CHs is based on threshold value which depends on three levels of heterogeneity and being a reactive routing network protocol causes increase in stability period and network life. As it can be seen from simulation results the throughput has increased so much. In comparison with DEEC and TSEP it is concluded that the protocol will perform well for long time. In the future, intermediate nodes can be introduced in this protocol for increasing the levels of heterogeneity, results in further increase the network lifetime.

#### REFERENCES

[1] "An application-specific protocol architecture for wireless microsensor networks," IEEE Transactions on Wireless Communications, vol.1, no. 4, pp. 660670, October 2002.

[2] W. R. Heinzelman, A. P. Chandrakasan, and H. Balakrishnan "An application-specific protocol architecture for wireless microsensor networks," IEEE Transactions on Wireless Communications, vol. 1, no.4, pp. 660-670, October 2002.

[3] F. Akyildiz, W. Su, Y. Sankarasubramaniam, E. Cayirci, A survey on sensor networks, IEEE communications magazine 40 (8) (2002) 102–114.

[4] Sarkar, A., & Murugan, T. S. (2019). Cluster head selection for energy efficient and delay-less routing in wireless sensor network. *Wireless Networks*, 25(1), 303-320.

[5] B. Meenakshi, P. Anandhakumar, "Lifetime extension of wireless sensor network by selecting two cluster heads and hierarchical routing", IEEE International Conference on

Advances in Computing, Communications and Informatics, 2012.

[6] Babar Nazir, Halabi Hasbullah, "Energy Balanced Clustering in Wireless Sensor Network", IEEE International Conference on Information Technology, 2010.

[7] Sharma, G., & Kumar, A. "Improved range-free localization for three-dimensional wireless sensor networks using genetic algorithm" *Computers & Electrical Engineering*. Vol. 72, no. 11, pp. 808-827, Nov. 2018.

[8] W. Heinzelman A. Chandrakasan and H. Balakrishnan. An application-specific protocol architecture for wireless microsensor networks. *Proc. 33rd Hawaii Int'l. Conf. Sys. Sci.*, pages 660--670,2000.

[9] Singh, M., Soni, S., & Kumar, V. G. Sharma, (2016, March). Clustering using fuzzy logic in wireless sensor networks. In 2016 3rd International Conference on Computing for Sustainable Global Development (INDIACom) (pp. 1669-1674). IEEE.

[10] G. Smaragdakis I. Matta and A. Bestavros. SEP: A stable election protocol for clustered heterogeneous wireless sensor networks. In *Second International Workshop on Sensor and Actor Network Protocols and Applications (SANPA)*, 2004.

[11] Q. Nadeem M.B. Rasheed N. Javaid Z.A. Khan Y. Maqsood and A. Din. M-GEAR: Gateway-based energy-aware multi-hop routing protocol for wsns. *Broadband and Wireless Computing, Communication and Applications (BWCCA) of IEEE*, pages 164--169, July 2013.

[12] G. Sharma and A. Kumar, "Modified Energy-Efficient Range-Free Localization Using Teaching-Learning-Based Optimization for Wireless Sensor Networks," *IETE Journal of Research*, vol. 64, no. 1, pp. 124–138, Jul. 2017.

[13] Sharma, G., & Kharub, M. (2019). Enhanced Range Free Localization in Wireless Sensor Networks. *CVR Journal of Science and Technology*, 16(1), 26-31.

[14] G. Sharma, & A. Kumar, "Improved DV-Hop localization algorithm using teaching learning based optimization for wireless sensor networks". *Telecommunication Systems*, vol. 67, no. 2, pp. 163-178, 2017.

[15] R. Mitra and D. Nandy. A survey on clustering techniques for wireless sensor network. *Int. J. of Research in Computer Science*, 2(4):51--57,2012.

[16] Prasad, A. Y., & Balakrishna, R. (2019). Implementation of optimal solution for network lifetime and energy consumption metrics using improved energy efficient LEACH protocol in MANET. *Telkomnika*, 17(4), 1758-1766

[17] G. Sharma and A. Kumar, "Fuzzy logic based 3D localization in wireless sensor networks using invasive weed and bacterial foraging optimization," *Telecommunication Systems*, vol. 67, no. 2, pp. 149–162, May 2017.

[18] A. Kashaf, N. Javaid, Z. A. Khan and I. A. Khan. TSEP: Threshold-sensitive Stable Election Protocol for WSNs, Cornell University Library, 2012.

[19] W. R. Heinzelman, A. P. Chandrakasan, and H. Balakrishnan, "Energy Efficient communication protocol for wireless microsensor networks," in *Proceedings of the 33rd Hawaii International Conference on System Sciences (HICSS-33)*, January 2000.

[20] G. Sharma, & A. Kumar, "Dynamic Range Normal Bisector Localization Algorithm for Wireless Sensor Networks". *Wireless Personal Communications*, vol. 9, no. 3, pp. 4529-4549, 2017.

[21] Wang, Q., Lin, D., Yang, P., & Zhang, Z. (2019). An Energy-Efficient Compressive Sensing-Based Clustering Routing Protocol for WSNs. *IEEE Sensors Journal*, 19(10), 3950-3960.

# Low Power PCI Controller using Design Compiler

T. Subha Sri Lakshmi

Asst. Professor, CVR College of Engineering/ECE Department, Hyderabad, India

Email: rupashubha@gmail.com

**Abstract:** As the technology is shrinking, industries are facing many challenging issues due to the design complexities involved in it. The three main factors that drive the digital design industries are speed, power and area. This paper explains the different steps to generate a technology specific gate level net list from the Hardware Description Languages (HDL), using the Design Compiler Synthesis tool of Peripheral Component Interconnect (PCI) Controller along with the use of four masters i.e., Video Data set, Video Codec, IEEE 1394 bus and Personal Computer (PC). It also explains about the different low power checks along with power and area reports when the design operates at different Process-Voltage-Temperature (PVT) corner. Apart from above the above details, it also describes Low-Vt (LVT), High-Vt (HVT) cells and their impact on power consumption in a design along with the special management cells like isolation and level shifter cells etc.

**Index Terms:** Peripheral Component Interconnect (PCI) Arbiter, Register Transfer Logic (RTL), Unified Power Format (UPF), Application Specific Integrated Circuits (ASIC), Design Compiler (DC), Synopsys Low Power Signoff Verification (VCLP).

## I. INTRODUCTION

Now a days, the speed and integration density of Integrated Circuits (ICs) have drastically been improved. In today's Very Large Scale Integrated Circuits (VLSI) chip designs [12], nearly 50-60 million transistors can be packed on a single die. As the design complexity increases, meeting the timing requirement (timing closure) and consuming less power becomes extremely complex. As the process technology shrinks, designer can place the larger number of transistors on a single silicon chip. However, the major concerns of a VLSI designer were power, area, cost, performance and reliability in the past but now, the parameters power, area, cost, reliability and speed. It is because they are crucial and have begun to change drastically in the Asic design flow while yielding at the issues that are being given comparable weight to power, area and performance considerations [1,3]. So, in the low power technologies special management cells like isolation cells, level shifters and retention cells are playing an important role in reducing the power consumption in the design using different EDA tools. [12]

This paper is organized as follows. Section II gives an basic introduction of PCI Controller. Section III presents design of PCI Controller. Section IV presents the Synthesis of PCI Controller. Section V presents the experimental results in terms of Timing, Area, Power analysis at different

PVT Corners and error check control word. Finally the conclusion is drawn in Section VI.

## II. PCI CONTROLLER

A general computer system with two or more central processing units is defined as a multiprocessor in which all the processing units share a common resource bus structure it is called as Peripheral Component Interconnect (PCI) bus. In this paper Peripheral Component Interconnect (PCI) controller [11] is discussed for four processors in which few are considered as master devices and other few are target devices. A video compression system is taken into consideration for bus arbitration and finally the design can be modified & used for further multi processor applications. Peripheral Component Interconnect (PCI) bus [11] is connected with the use of four masters they are video data set (raw data or original data collection of a motion picture in Red Green Black (RGB) format which will be given in the form of no. of frames per second), video codec (this performs the compression and reconstruction and codec circuit which can be designed with the help of simple encoder and decoder blocks. These blocks can be coded using Verilog Hardware Description Language (HDL)/ Very High Speed IC Description Language (VHDL) [11] and can implemented either on FPGA or ASIC) and finally the collected raw or original data will be given to codec block via PCI bus/ IEEE 1394 bus (One type of serial bus which can connects up to 64K nodes. It mainly arrange the merged data in serialized manner and will be given to the decoder block of codec for reconstruction purpose) and a Personal Computer (PC) (which build up and synchronize all the system devices with the help of a bridge).

## III. DESIGN OF PCI CONTROLLER

Four masters of PCI bus such as video data set, video codec, fire wire and PC are requested the PCI [11] serial bus by using request signals (i.e. REQ0, REQ1 and soon). Depends on the priority of the request made, the arbiter will assign the grant signals i.e. GNT0, GNT1 etc. The serial order in which all the masters can get access of PCI bus are video dataset named as VG, video codec named as VC, fire wire (FW) and finally the host nothing but PC or central processing unit. Generally the PC access the PCI bus, in which the priority sequences, repeats for the multiple times from the original data collection. Video data set and codec blocks will access the bus more frequently to get the merged data which can be used for further decompression. The transaction will be taken place in between

Video data set => Codec (Original Data)  
Codec => IEEE 1394 bus (Merged Data)

IEEE 1394 bus => Codec (Merged Data)

Codec => Accelerated Graphics Port (Display Monitor)  
(Reconstructed video data)

As shown in figure 1 (a, b) the Verilog code has been developed based on ASM chart. In this code/process, initially controller will be in hang around/wait state and later will be represented by a decimal value which will be very easy to code in using Verilog. During the hang around state, the controller will check for request signal in the priority order. If the request becomes true, then controller will issue the grant signal to the device. If request signal is in false condition, then it will check for another priority request and so on. In general when hang around state is "0" all the requests from 0 to 3 will assert the grant signal 0 and 1 to the next state of the device due to video data set is located at top priority when it uses PCI bus. If any masters have not made the request, then the controller will be in the same hang around state. In video data set state 1, if request 0 is still in assertion state, then controller also will be in the state only. When the video data set give up the bus then video codec will get a chance to use the device by issuing the grant signal 1. IEEE1394 and PC will get the chance when all the masters of video data set release or do not use the bus. Suppose in the state 1 the video codec, IEEE 1394 and PC do not access the bus the iteration takes place and again start with the video data set. In this scenario PC can get a one more chance to access the bus since video data set block had give up to access the bus. Based on the priority in state 2 the video codec get the access of bus by using the request 2 signals and grants the device by using the grant 2 signal. When video codec uses the bus, the voucher passes to IEEE 1394 and to PC. In IEEE 1394 state 3, the controller grants the grant 2 signal because as long as it is present on request 2 signal. As mention earlier once it is completed it goes back to video data set block. Finally PC is overhaul in state 4 the controller grants the signal 3 for request signal 3. Once PC completes its operation the voucher passes to video data set.

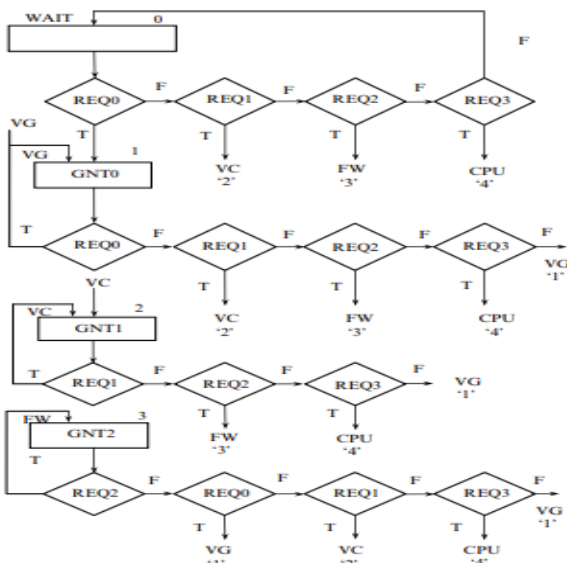


Figure 1a. ASM Chart of PCI Controller

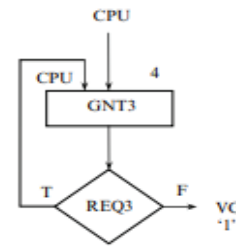


Figure 1b. ASM Chart for Controller Design

#### IV. SYNTHESIS OF PCI

In Asic design flow [1,3], logic synthesis is one of the crucial stage where the entire design in HDL is converted to the technology specific gate level net list. Converting of RTL to technology specific gate level net list includes three steps. They are translation, optimization and technology mapping. Input files required to generate a technology specific gate level net list are HDL files (verilog or VHDL or system verilog), Synopsys Design Constraints (SDC), logical libraries (.LIB) and Unified Power Format (UPF) file.

##### A. Translation

This is the first stage in synthesis, where RTL [1] code is translated to the technology independent net list. Now, this translated logic is accessible in the Boolean equation form.

##### B. Optimization and Technology Mapping

In this stage, the entire design is optimized using the optimization techniques and also the technology independent logic is mapped to the technology dependent library logic gates based on the design constraints, library of available technology gates. Figure 2 briefly explains about the RTL code which is converted to technology specific gate level net list. There are few steps involved in generating the gate level net list. [1-3]

#### Synthesis = Translation + Optimization + Mapping

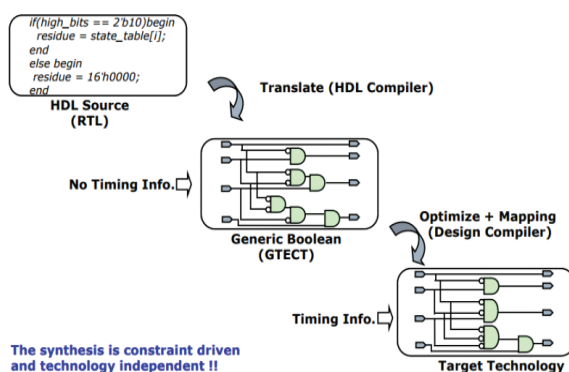


Figure 2. Synthesis Flow in Design Compiler

### C. Specify the Logic Libraries Provided by the ASIC Vendor

A designer must define the logic libraries provided by the vendors. Under the `target_library` variable, specify the technology library file path such that the synthesis tool chooses only those cells that are present in the mentioned technology library. Similarly, `link_library` variable [2] is used to pick the cells from the library, according to the functionality of a design. For example consider the figure 1 in which (AND, EXOR) gates are required to generate a net list. So, specify

```
Set link_library project/standardcell.lib
```

From the above under project directory, a library file called standard cell is present. In this standard cell.lib file a designer can find all types of cells. So synthesis tool chooses the cells according to its requirement. So whatever the cells present in libraries mentioned under `link_library` variable are used as the references. These references can be seen in the output net list file and a designer can easily analyze connections to that particular reference cell. [1-3]

### D. Read the Design

After setting the logical libraries, design must be read using the `read_file` command. Here, file can be a verilog or VHDL (Very High Speed Description Language). [3]

### E. Define Design Environment

Before generating the technology specific gate level net list, a designer should ensure operating condition the design in which must run. Here, operating condition includes the PVT corners. PVT stands for Process, Voltage and Temperature. In real time scenarios, a designer can set the operating condition according to requirement using the `set_operating_condition` variable. [1]

### F. Defining The Design Constraints

Usually, design constraints are classified into two types. They are Design Rule Constraints and optimization constraints. Design Rule Constraints are called as the implicit constraints which are already defined in the logical libraries provided by the asic vendor [4]. Maximum and minimum capacitance values, transition time and maximum fan-out are defined as design rule constraints. These constraints should never violate. For example, the maximum capacitance range is not specified in the libraries then a designer may use the maximum capacitance value which leads to high power consumption. Hence a certain range is provided. So these Design Rule Constraints that are provided by the vendor in the (.LIB) file [3-4] ensure that the product should meet the specifications and work as intended.

### G. Compiling and Optimizing the Design

When `compile` or `compile_ultra` command is used, there are three types of optimizations performed on the design. They are architectural optimization, logic level optimization

and gate level optimization. In the architectural optimization, resource sharing and arithmetic optimization techniques are used to optimize [8] the design. Whereas, in the logic level optimization stage flattening and structuring techniques are used to optimize the entire design. In the gate level optimization, the stage a technology independent net list is converted to the technology specific gate level net list.

### H. Analyze and Resolve Design Problems

Here, the design compiler tool generates the numerous reports on the results. Examples are area, power and timing reports. The Designer uses these reports to analyze and resolve any design problems or to improve the results i.e., better QOR. [1]

### I. Save the Design Database

By using the `write_file` command, a designer can save the synthesized design.

#### Synthesis Report of PCI

```
I/O Primitives:
  IBUF           : 5
  OBUF           : 4
  BUFGP          : 1
I/O Register bits : 4
Global Clock Buffers : 1
Total LUTs       : 10
```

### J. Low Power Checks

An IEEE standard for specifying the power intent of a design is specified as upf file. As (.upf) file is one of the input files for power aware synthesis, a brief explanation about the Upf is explained in detail. The entire design has been divided into the power domains. Supply nets and supply ports were declared using the `create_supply_net`, and the `create_supply_port` commands. Then connect these nets using `connect_net`, `connect_port` commands. Special management cells like Isolation cells, level shifters were used to reduce the amount of power in the design. These special management cells were inserted by the design compiler tool according to the strategies mentioned in the Upf file [5-7]. If these cells were not inserted or connected properly, the design would have shown up some errors at in the implementation stage itself. So, these kinds of checks will be performed by the Vc lp tool [6]. Therefore, some of the low power checks were performed on the design functional checks, structural checks and signal corruption checks etc.

## V. EXPERIMENTAL RESULTS

### A. Timing Analysis

To analyze the timing report of a PCI design. Using the `report_timing` command a designer can analyze the timing path and view whether the timing [2] is met or not. Worst slack of PCI Controller is 15.864 ns. If `slack>0` then timing is met. If `slack<0` then the timing requirement is adjusted by making the slack value positive.

Worst Slack of PCI Design – 15.864ns

Timing Constraints of PCI

Requested Frequency – 50.0 MHz  
Estimated Frequency – 241.8 MHz  
Requested Period – 20.000  
Estimated Period – 4.136

Timing Summary of PCI

Minimum Period – 3.401ns  
Maximum Frequency – 294.031 MHz  
Minimum input arrival time before clock – 2.671ns  
Minimum output required time after clock – 5.419ns

*B. Area and Power Analysis at Various PVT Corners*

The area report can be obtained by using the report\_area command. When the design is run at two different PVT corners, the area reports obtained are shown in the figure 3a and 3b. When the designer reduces the amount of voltage from 0.8 V to 0.72 V the design area is increased [5, 6]. When a design works at low voltage, it requires higher drive strength cells to pass the logic. So, the cells with higher drive strength occupy more amount of area on the die compared to the cells with less drive strength. [7]

Theoretically, when the voltage value is increased the power consumption also increases. But, coming to the practical scenarios the power consumption [7] entirely depends on the number of cells utilized in the design. From the above example, observe that at 0.8 volts the power consumed by the design is less compared to the design operating at the 0.72 V. This is because, the number of cells utilized by the design at 0.8 V is less compared to the cells at 0.72 V. Hence, the below table 1 summarizes that the more optimization [7, 8] performed on the design lesser will be the power consumption. Because the optimized design contains lesser number of cells compared to the unoptimized design. A designer can use the report\_cells command to determine the number of cells utilized by the design.

TABLE I.  
POWER ANALYSIS REPORT

PVT Corner	Power (mW)
Process-slow Voltage-0.8 V Temperature-0	87.88
Process-slow Voltage-0.72 V Temperature-0	88.567

From table 2, as the frequency increases the power consumption also increases. But the threshold voltage plays a crucial role in the power consumed by the design. In the technology libraries different flavors of cells are available

with different strength and threshold voltage levels like (LVT, SVT and RVT cells) [9]. If a design contains majority of LVT cells then the leakage power consumption is more and the timing is also met very easily. If the design contains majority of HVT cells, then the power consumption will be less but HVT cells' delay will be high compared to the delay of LVT cells. Hence a designer can use the LVT cells on the critical path to meet the timing easily. However, HVT cells are used on the non critical paths to reduce the amount of power consumption in a design. Now a day, designer is using the multi V<sub>th</sub> libraries provided by asic vendor to reduce the amount of power consumption in a design.

TABLE II.  
POWER CONSUMED BY THE DESIGN BASED ON FLAVORS MAJORITY OF V<sub>TH</sub> CELLS

Freq. (MHz)	Switching power (mW)	Leakage power (mW)	Internal power (mW)	Total Power (mW)
250 (LVT)	8.521	5.564	98.006	112.0
500 (LVT)	10.33	5.57	128.59	144.5
250 (HVT)	8.22	2.51	80.147	90.88
500 (HVT)	9.89	2.61	105.5	118.0

When report\_lp command is used it shows different types of errors and warnings that occur during the net list implementation stage. From the figure 3, UPF\_CSN\_MACRO warning says that, a supply net is missing for a macro in the design at the UPF stage. Hence, a designer can prevent this kind of warning by connecting a supply net to that macro in the UPF file [2, 10]. Similarly, ISO\_OUTPUT\_UNCONN and LS\_OUTPUT\_UNCONN tell that both isolation and level shifter cells outputs are unconnected.

```

-----
Tree Summary
-----
Severity Stage Tag Count
-----
error Design CORR_CONTROL_STATE_WITHISO 53
warning UPF UPF_CSN_MACRO 21
warning UPF UPF_SUPPLY_MISSING 1
warning Design ISO_OUTPUT_UNCONN 1
warning Design LS_OUTPUT_UNCONN 1
-----
Total 77
-----

```

Figure 3. Low Power Check Report

The above error occurs when the signal passes through corrupting objects in the design and at the same time passes through an isolation cell which guards the corrupting objects. In this way different types of power checks are

performed on the design and errors are analyzed as shown in the figure 4.

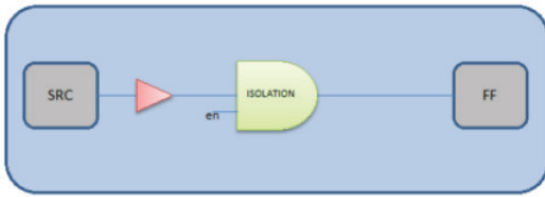


Figure 4. Corr\_Control\_State\_Withiso

## VI. CONCLUSIONS

Analysis of area and power factors of PCI controller at different PVT corners along with fixing of timing violations by considering the scenarios has been presented. Various low power checks are performed at different frequencies i.e., 250MHz and 500MHz with the help of LVT & HVT cells. 15.86ns is observed as worst slack for the maximum timing. By inserting level shifter cells at implementation stage power and timing can be improved by 20%. Leakage power is observed very less when it is operated at High-Vth range. In future, the design undergoes physical design work where, floor planning, placement, CTS and routing must be done and finally tape out.

## REFERENCES

- [1] Himanshu Bhatnagar, "Advanced Asic chip synthesis using Design Compiler physical compiler and prime time second edition conexant systems" (2002).
- [2] Bhasker, J., Rakesh Chaddha," Static timing analysis for nanometer designs a practical approach" (2009).
- [3] Jan Rabaey, M., Anantha Chadrakasan, Borivoje Nikolic, "Digital Integrated circuits a design perspective", second edition.
- [4] Ghosh, A., Devdas, S., Keutzer, K., White, J., "Estimation of average switching activity in combinational and sequential circuits", ACM/IEEE Design Automation Conf (1992).
- [5] Chandrakashan, A.,P., Sheng, S., Brodersen, R., "Low power CMOS digital design", IEEE Trans. On Solid State Circuits, vol. 27, no.4,pp. 473-483, April (1992).
- [6] Roy, K., Roy, R., Tan-Li Chou, "Design of low power digital systems, Designing Low Power Digital Systems Emerging Technologies" (1996),pp. 137-204,1996.
- [7] Patil, P., Roy, R., Roy, K., "Low power driven logic synthesis using accurate power estimation technique, VLSI Design" 1997. Proceedings. Tenth International Conference on, pp. 179-184, 1997.
- [8] Dey, S., Brglez, F., Kedem, G.,"Partitioning sequential circuits for logic optimization, Computer Design: VLSI in Computers and Processors" 1991. ICCD '91.Proceedings 1991 IEEE International Conference on, pp. 70-76,1991.
- [9] Brayton, Khatri, "Multi valued logic synthesis", 12th International Conference on VLSI Design (VLSI-99),PP 196-205,Goa,India,pp. 196-205.
- [10] Khatri, Gulat, "Advanced Techniques in Logic Synthesis, optimizations and Applications", Springer Publishers, 1st edition 2011. 240p.
- [11] [https://www.xilinx.com/support/documentation/ip\\_documentation/pci\\_arbiter.pdf](https://www.xilinx.com/support/documentation/ip_documentation/pci_arbiter.pdf)

- [12] Ganesh. R, "Design Procedure for Digital and Analog ICs using Cadence Tools", CVR Journal of Science & Technology, Vol. No. 9, December 2015, pp. 56-60.

# Implementation of Pilot Channel Estimation Techniques for OFDM System with Low Mean Square Error

T. Padmavathi<sup>1</sup>, Dr. Kusma Kumari Cheepurupalli<sup>2</sup> and Dr. R. Madhu<sup>3</sup>

<sup>1</sup>Sr.Asst. Professor, CVR College of Engineering /ECE Department/Hyderabad, India  
Email: padmatp41@gmail.com

<sup>2</sup>Assoc. Professor, GVP College of Engineering, (Autonomous), /ECE Department, Visakhapatnam, India  
Email: chkusumasrinivas@gmail.com

<sup>3</sup>Asst. Professor, University College of Engineering, JNTUK/ECE Department, Kakinada, India  
Email: madhu\_ramarkula@rdiffmail.com

**Abstract:** Orthogonal Frequency Division Multiplexing (OFDM) has grown to be the most popular multi carrier communication system in high speed data communications. The available bandwidth is utilized efficiently, and more data rates can be achieved because of orthogonal carriers in OFDM system. OFDM system requires precise channel estimation and synchronization to reduce Mean Square Error (MSE). In this work, various Pilot Channel Estimation (PCE) techniques are used to compute CSI (Channel State Information). Pilots are transmitted along with the data and channel response is computed with various interpolation techniques such as linear, spline, cubic Interpolation techniques by extracting the pilots at the receiver. The performance metrics like Mean Square Error (MSE) and computation time are computed and compared for different PCE techniques. Discrete Fourier Transform (DFT) based channel Estimation is combined with interpolation techniques and channel response is computed and compared with Least Squares (LS) and Minimum Mean Square Error (MMSE) approaches. LS, MMSE, LMMSE (Linear MMSE) methods are combined with Time Division(TD) and Time Division Duplexing(TDD) techniques to compute MSE. TD-LMMSE approach achieves least MSE with more computation time.

**Index Terms:** OFDM, channel estimation, interpolation, CSI, MSE, computation time.

## I. INTRODUCTION

OFDM (Orthogonal Frequency Division Multiplexing) divides the entire channel bandwidth into subchannels, which increases the symbol duration. OFDM eliminates the Inter Symbol Interference (ISI) caused by multipath environment due to increased symbol duration [1]-[3]. Wireless LAN such as IEEE802.11a and HIPERLAN/2 and multimedia communications are implemented with OFDM.

Multipath propagation introduces constructive and destructive Interference at the receiver. Since the wireless channel is time varying and frequency selective, a dynamic Channel estimation is necessary before demodulation of OFDM signal [4]. Channel estimation can be done with two approaches. Blind channel estimation requires less bandwidth but it depends on only the statistical information of received symbols [5]. Pilot Channel Estimation inserts the pilots in the data sequence and consumes more bandwidth. In OFDM, either entire OFDM symbol is used for pilot transmission or pilot symbols may be inserted periodically after group of OFDM symbols [6]. The first method is,

block type pilot channel estimation and it has been developed for slow fading channel. Least Squares (LS) and Minimum Mean Square Approaches (MMSE) has been used for Block-Type pilot arrangement to compute Mean Square Error (MSE). Performance of MMSE Method is better in terms of MSE than the LS but is more complex. [7]. Comb-type pilot channel estimation has been introduced to equalize the fast fading channel. The algorithms have been implemented for Comb-Type channel estimation is based on interpolation since the pilots are characterized in the frequency domain. In comb-Type channel estimation, channel can be estimated at the pilot frequencies based on LS, MMSE. The performance of MMSE is better than LS[8,9], and the complexity of MMSE is reduced by singular Value Decomposition low rank estimator. Low rank channel estimators proposed for comb-type pilot arrangement reduces computational time but it requires memory [10]. In the spectrum of OFDM system, the subcarriers of symbol carries data and pilots, these pilot carries are interpolated in time domain to estimate the channel. But time domain interpolation fails to keep track of quick channel variation caused by fast moving receiver. Even though channel estimation without time-axis interpolation enables fast estimation, the performance of channel estimation degraded for a long delay spread channel in a single carrier networks (SCNs) because of inadequate pilot sub-carriers [11]

Channel estimation can be done with the help of Wavelets to reduce the MSE. It improves Transmission efficiency and Data rate because channel coefficients will be estimated in time domain effectively. But the accuracy of proposed Haar wavelet based channel estimation need to be improved [13].

In frequency domain, OFDM signal can be represented with group of subcarriers. Each subcarrier frequency response can be obtained by interpolation techniques. In comb-type channel estimation, Channel can be interpolated with linear interpolation, spline Interpolation, Cubic interpolation and time domain interpolation. Performance of the interpolation techniques are compared in terms of MSE by including different modulation techniques like BPSK, QPSK. OFDM System model and its mathematical representation are described in Section II. In section III pilot channel estimation with various interpolation techniques are discussed. Simulation Results are discussed in Section IV.

**II. SYSTEM MODEL**

The pilot channel estimation based OFDM system given in Figure.1. The binary data is mapped to constellation points using BPSK/QPSK modulations. Pilots are inserted

$$Y(k) = FFT\{y(n)\} \text{ for } k = 0,1,2 \dots \dots N - 1$$

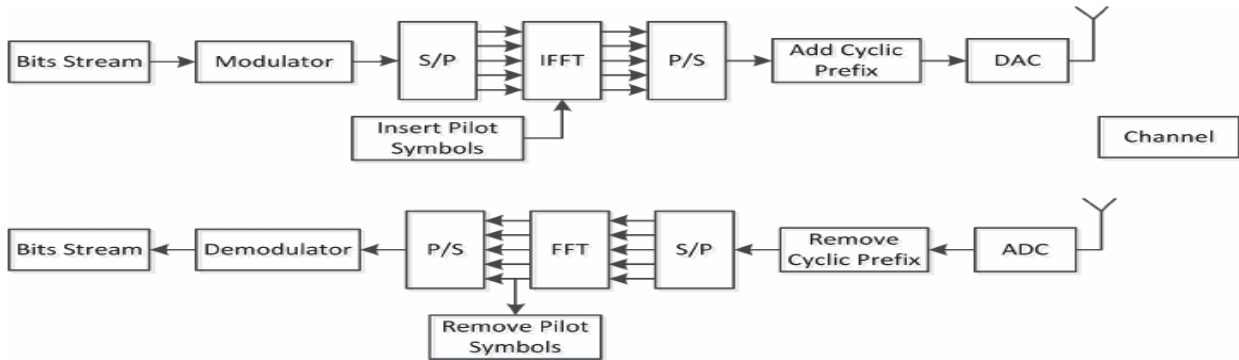


Figure.1 OFDM System

either to all OFDM Symbols periodically or only for specific symbols. The resulting data converted from frequency domain to time domain using IFFT with the following equation

$$x(n) = IFFT(X(K)) \text{ for } n = 0,1, \dots \dots N$$

$$= \sum_{K=0}^{N-1} X(K) e^{j\frac{2\pi kn}{N}}$$

(1)

Where N is the FFT length. Guard time is added to x (n) which is to be larger than the expected delay spread, so that Inter-Symbol Interference is removed. Part of OFDM symbol is cyclically extended with the guard time, to remove Inter Carrier Interference (ICI). Then resulting signal is given by

$$x_f(n) = \begin{cases} x(N+n), & n = -N_g, N_g + 1, \dots \dots, 1 \\ x(n) & n = 0, 1, 2 \dots \dots N - 1 \end{cases}$$

(2)

Where Ng is the guard time interval. The signal from transmitter is passed through the frequency selective fading channel with Additive White Gaussian Noise (AWGN). In this paper frequency selective fading channel is modelled with Rayleigh fading. The signal at the receiver is given by

$$y(n) = x_f(n) \otimes h(n) + w(n)$$

(3)

Where y(n) is the received signal, h(n) is the Impulse response of the channel, w(n) is the AWGN Noise. Channel Impulse Response (CIR) h is given by

$$h(n) = \sum_{r=0}^{m-1} h_r e^{j\frac{2\pi}{N} f_{Dr} T_n \delta(\lambda - \tau_r)} \text{ for } 0 \leq n \leq N-1$$

(4)

where m is the total propagation paths, h<sub>r</sub> is the complex impulse response of the r<sup>th</sup> path, f<sub>D</sub>r is the Doppler frequency shift, λ is the delay spread index, T is the sample period and τ<sub>r</sub> is the r<sup>th</sup> path delay. The signal received at the receiver after passing through the A/D converter and low pass filter, guard time is eliminated then

$$y(n) = y_f(n) \text{ for } -N_g \leq n \leq N - 1$$

(5)

Y(k) is obtained by sending y(n) to the FFT block,

$$1/N \sum_{n=0}^{N-1} y(n) e^{-j\frac{2\pi kn}{N}}$$

(6)

Assume there is no ISI [8], then H (k) can be obtained from the relation

$$H(k) = IFFT(h(n))$$

(7)

After IFFT block, in the channel estimation block pilots are extracted and estimated for data sub-channels. Then the estimate of data is given as

$$X_s = \frac{Y(k)}{H_s(k)} \quad k = 0,1, \dots \dots N - 1$$

(8)

**III. IMPLEMENTATION OF PILOT CHANNEL ESTIMATION TECHNIQUES**

Pilots symbols are transmitted periodically and all subcarriers carries pilot symbols in PCE. The channel is assumed to be constant during the pilot transmission, resulting no error in the channel estimation. PCE can be performed by either LS or MMSE approach [7], [9]

The signal at the receiver can be given by the following equation in the absence of ISI

$$Y(k) = X(k)H(K) + W(n)$$

(9)

In the matrix form above equation can be represented as

$$Y = XFh + W$$

(10)

Where

$$X = \text{diag}(X(0), X(1), \dots \dots, X(N - 1))$$

$$Y = [Y(0), Y(1), \dots \dots Y(N - 1)]^T$$

$$W = [W(0), W(1), \dots \dots W(N - 1)]^T$$

$$H = [H(0), H(1), \dots \dots H(N - 1)]^T = IFFT(h)$$

$$F = \begin{bmatrix} W_N^{00} & \dots & W_N^{0(N-1)} \\ \vdots & \ddots & \vdots \\ W_N^{(N-1)0} & \dots & W_N^{(N-1)(N-1)} \end{bmatrix}$$



$$W_N^{nk} = \frac{1}{N} e^{-j2\pi\left(\frac{n}{N}\right)k} \quad (11)$$

If the channel vector  $h$  and noise vector  $W$ , are uncorrelated then the channel estimate  $h$  using MMSE approach in the frequency domain [11] is given by

$$H_{MMSE} = FR_{hY}R_{YY}^{-1}Y \quad (12)$$

Where  $R_{hY} = E\{hY\} = R_{hh}F^HX^H$

is the Cross correlation matrix between  $h$  and  $Y$

$$R_{YY} = E\{YY\} = XFR_{hh}F^HX^H + \sigma^2I_N$$

is the auto correlation matrix, and  $\sigma^2$  represents the noise Channel estimate  $h$  using LS approach in the frequency domain is given by

$$H_{LS} = X^{-1}Y \quad (13)$$

Which minimizes

$$(Y - XFh)^H(Y - XFh)$$

In pilot channel estimation, the data can be estimated at data-subcarriers using channel information at pilot subcarriers. This can be done with efficient interpolation techniques. [7]

#### A. LINEAR INTERPOLATION

In this method two successive pilot subcarriers are used to find the channel response for data carriers. The channel estimation of data carriers is given by

$$\begin{aligned} H_g(k) &= H_g(mD + l) \quad 0 \leq l < D \\ &= (H_p(m+1) - H_p(m)) \frac{l}{D} + H_p(m) \end{aligned} \quad (14)$$

where  $D$  is the spacing between two adjacent pilot subcarriers and  $H_p(m)$  is the value of the received pilot subcarrier at frequency  $m$ . The frequency response of the channel is considered as a straight line between two adjacent pilot carriers.

#### B. CUBIC INTERPOLATION

The third degree polynomial can be obtained in the cubic interpolation using four known points. The values between reference values can be obtained with the following expression

$$P_1(k) = a_3K^3 + a_2K^2 + a_1K + a_0 \quad (15)$$

where  $a_k$  are the coefficients of the polynomial and  $k$  is the frequency index.

When the range of interpolation is larger than the range enclosed by first four reference points, then it is essential to obtain a second polynomial, using the subsequent four points. It is significant to assure that the first and second order derivative must be considered in the computation of the coefficient in the interpolation.

#### C. CUBIC-SPLINE INTERPOLATION

The transfer function of each subcarrier is approximated to the third order polynomials with respect to  $1/L$ . Estimation is done by obtaining coefficients of the polynomials by means of four adjacent reference signals and their second order derivatives. Hence, the estimate of a subcarrier is

$$H^{\wedge}(k) = A\left(\frac{1}{L}\right)H_r(m) + B\left(\frac{1}{L}\right)H_r(m+1) + C\left(\frac{1}{L}\right)z(m) + D\left(\frac{1}{L}\right)z'(m) \quad (16)$$

Where  $A\left(\frac{1}{L}\right), B\left(\frac{1}{L}\right), C\left(\frac{1}{L}\right)$  and  $D\left(\frac{1}{L}\right)$

are constants determined by  $\left(\frac{1}{L}\right)z(m) = H_r(m)$

$H_r(m)$  is the second order derivative of the transfer function of the  $m^{\text{th}}$  reference signals, then all the second order derivatives can be given by

$$Z = K^{-1}V$$

Where

$$Z = [z(m - (K/2) + 1), \dots, z(m_0), \dots, z(m - K/2)]$$

$X$  and  $V$  are numerator and denominator matrix of the second order derivatives, respectively. Therefore, additional computations to find the second order derivatives of the transfer function are required

#### D. DFT BASED CHANNEL ESTIMATION

The DFT-based channel estimation [12] technique has been derived to increase the performance of LS or MMSE channel estimation by removing the effect of noise outside the maximum channel delay. Let  $H[k]$  denotes the estimate of channel gain at the  $k^{\text{th}}$  subcarrier, obtain by either LS or MMSE channel estimation method. Taking the IDFT of the channel estimate

$$IDFT\{\hat{H}[k]\} = h(n) + z(n) \sim \hat{h}(n), \quad n = 0, 1 \dots N - 1 \quad (17)$$

Where  $z(n)$  denotes the noise component in the time domain. Ignore the coefficient  $h^{\wedge}(n)$  that contain the noise only, then the coefficients for the maximum channel delay  $L$  is given as

$$\begin{aligned} \hat{h}_{DFT}(n) &= h(n) + z(n), n = 0, 1 \dots L - 1 \\ &= 0, \text{ Otherwise} \end{aligned} \quad (18)$$

and transform the remaining  $L$  elements back to the frequency domain as follows

$$\hat{H}_{DFT}(K) = DFT\{\hat{h}_{DFT}(n)\} \quad (19)$$

## IV. RESULTS

In the OFDM system, the transmitted bits have been modulated by different modulation techniques like BPSK or QPSK.

TABLE I.  
SIMULATION PARAMETERS

Parameters	Specifications
FFT length	1024
Number of subcarriers(active)	64
Number of data carriers	48
Number of pilot carriers	4
Sampling frequency	20MHZ
Number of carriers for cyclic prefix	16
Modulation	BPSK,QPSK
Channel Model	Rayleigh fading

Modulated data will be converted into parallel form where each bit is being multiplied with the carrier in the IFFT block, so that the output of the IFFT block (i.e. Parallel data) is converted into serial form. Then by adding cyclic prefix the required signal can be obtained. Simulation parameters considered to implement OFDM system are shown in Table I.

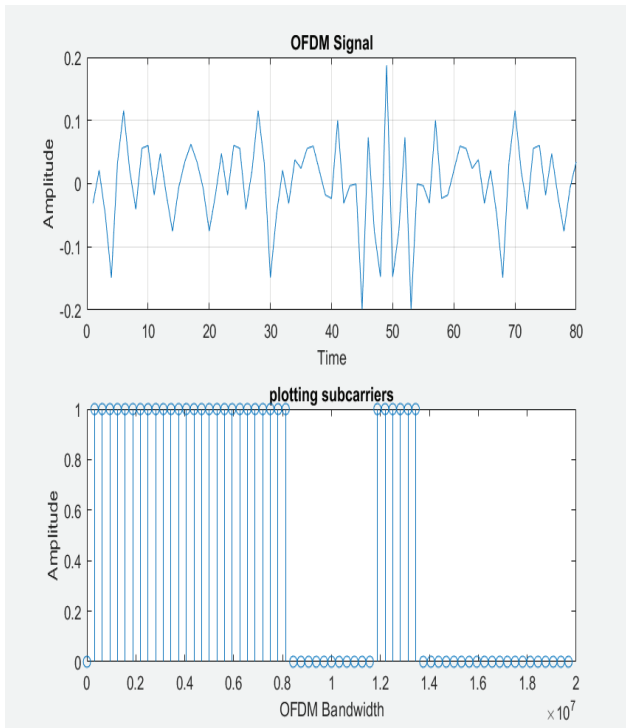


Figure 2. Generation of OFDM signal with 64 subcarriers

According to the WLAN standards, 64 subcarriers are considered as data carriers, according to the 4 pilot subcarriers are transmitted. Each symbol on subcarrier indices can be represented as shown in the figure 4.1 where Y axis represents the no of subcarriers i.e., from 0 to 63 and X axis represents the time taken by each subcarrier to be on the frame (frame time ). The bandwidth of the OFDM signal is 20MHz which is divided by each subcarrier (0.3125MHz). Each symbol duration will be 3.2μs.

Various Pilot Channel Estimation techniques are implemented for OFDM system and channel estimates are evaluated using interpolation techniques. The performance metrics such as MSE, BER and Computation time are calculated and discussed in sections A, B and C.

**A. Performance Analysis of Different Channel Estimation Techniques using Linear / Spline Interpolation:**

The channel estimates obtained by using the various channel estimation methods with and without DFT technique are compared and plotted at various subcarrier indices are shown in the Figure.3..and Table.2.

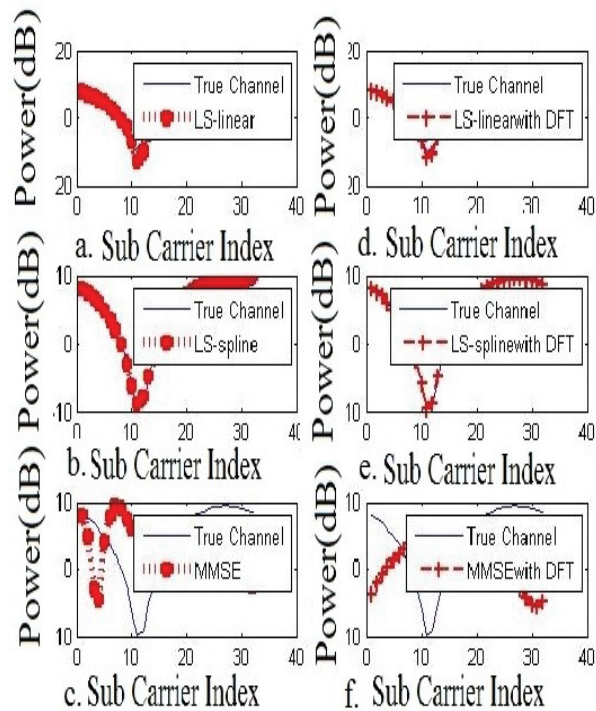


Figure 3. Performance analysis of different channel estimation techniques using Linear/Spline interpolation

TABLE II.  
POWER (DB) AT VARIOUS SUBCARRIER INDICES WITH AND WITHOUT DFT

Sub carrier index	True channel	LS Linear (without DFT)	LS Spline (with DFT)	MMSE Linear (without DFT)	MMSE Linear (with DFT)
5	4	4	4	2.5	-2
15	4.5	4.5	4.5	5.5	4
25	-10	-11	-10	1	-1
27	-15	-13	-15	1	1
30	-5	-5	-4	1	-5

The channel response is computed for LS-Linear, LS-Spline and MMSE approach then compared with true channel response and plotted in in Figure.3.a, b, c. Figure3.a. depicts that LS-linear channel response is close to True channel response. DFT is combined with LS-Linear, LS-Spline, MMSE techniques and channel response is plotted in Figure 3.d, e, f. The Figure 3. and Table. II. Shows that the DFT-based channel estimation method improves the performance of channel estimation since it is close to the true channel response.

**B. MSE Vs EbNo CHARACTERISTICS OF PCE TECHNIQUES**

MSE is calculated for LS, MMSE & LMMSE (Linear MMSE) approaches and MMSE technique is combined with TD (Time Duplexing) & TDD (Time Division Duplexing)

techniques. MSEs of various techniques are compared and plotted MSE vs EbNo characteristics shown in Figure.4.

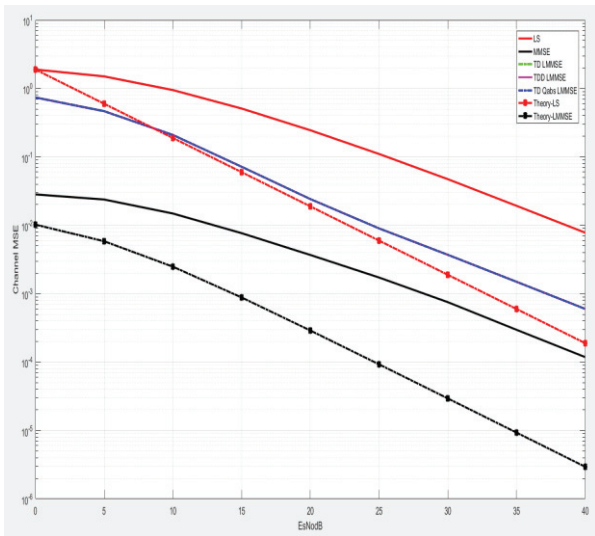


Figure 4. MSE vs EbNo Characteristics for different Pilot Channel estimation techniques

The MSE vs EbNo characteristics shows that LMMSE with TD approach gives minimum MSE.

depends on the channel estimate equations, transfer function, impulse response, cross correlation, and channel energy.

The time required to compute Mean Square Error (MSE) is calculated for various Pilot Channel Estimation techniques and shown in Table III. are computed based on the time required for matrix multiplications, matrix inversions, DFT Computation.

### V. CONCLUSIONS

PCE Estimation method is implemented for OFDM system. At the transmitter, equispace and equipower pilots are inserted in the data. The pilots have been designed and inserted in the data. The modulated signal and pilots are transmitted through Rayleigh fading Channel. At the receiver these pilots are extracted, and extracted pilot s are used to estimate the channel using various techniques like Linear, cubic interpolations.

TABLE III.  
COMPARISON O COMPUTATION TIME(NS)

SNR (db)	LS	Theory LS	MMSE	Theory MMSE	TD MMSE	TDD MMSE	TDQabs
0	$192 \times 10^{-2}$	$195 \times 10^{-2}$	$433 \times 10^{-2}$	$404 \times 10^{-2}$	$430 \times 10^{-2}$	$476 \times 10^{-2}$	$453 \times 10^{-2}$
5	$168 \times 10^{-2}$	$177 \times 10^{-2}$	$413 \times 10^{-2}$	$399 \times 10^{-2}$	$380 \times 10^{-2}$	$465 \times 10^{-2}$	$425 \times 10^{-2}$
20	$170 \times 10^{-2}$	$172 \times 10^{-2}$	$394 \times 10^{-2}$	$386 \times 10^{-2}$	$419 \times 10^{-2}$	$438 \times 10^{-2}$	$417 \times 10^{-2}$
30	$169 \times 10^{-2}$	$173 \times 10^{-2}$	$351 \times 10^{-2}$	$403 \times 10^{-2}$	$400 \times 10^{-2}$	$434 \times 10^{-2}$	$424 \times 10^{-2}$
40	$171 \times 10^{-2}$	$171 \times 10^{-2}$	$371 \times 10^{-2}$	$297 \times 10^{-2}$	$416 \times 10^{-2}$	$460 \times 10^{-2}$	$422 \times 10^{-2}$

For a given SNR, MMSE estimation performs better because of the mean square error for particular values of SNR [Decibels] decreases quickly in the required elapsed time when compared to the other estimation techniques. The complexity of MMSE estimator is large than LS estimator but gives better performance in comparison to LS estimation.

### C. COMPUTATIONAL TIME

The pilot channel estimation technique performance can also be expressed in terms of computational complexity. In this section all estimators' computational complexities are evaluated. The computational complexity for LS, MMSE algorithm

The resulting MSE for MMSE with TD approach is reduced by 3.16% at 0db SNR which is better with the existing techniques. Finally, the time required to compute MSE is also evaluated for LS and MMSE approaches and MMSE technique computationally complex with least MSE for OFDM system.

### REFERENCES

- [1] L. J. Cimini, Jr., B. Daneshrad, and N. R. Sollenberger, "Clustered OFDM with transmitter diversity and coding," in Proc. 1996 IEEE Global Telecommunications Conf., London, U.K., pp. 703–707.
- [2] L. J. Cimini, Jr., "Analysis and simulation of a digital mobile channel using orthogonal frequency division multiplexing," IEEE Trans. Commun., vol. COM-33, pp. 665–675, July 1985.

- [3] Theodore S. Rappaport, “Wireless Communications: Principles and Practice”, 2<sup>nd</sup> Edition,
- [4] Prentice Hall, 2002. A. R. S. Bahai and B. R. Saltzberg, Multi-Carrier Digital Communications: Theory and Applications of OFDM: Kluwer Academic/Plenum, 1999.
- [5] Sinem Coleri, Mustafa Ergen, Anuj Puri, and Ahmad Bahai, ‘Channel Estimation Techniques Based on Pilot Arrangement in OFDM Systems’ IEEE Transactions On Broadcasting, Vol. 48, No. 3, September 2002..
- [6] Chengyang Li, Sumit Roy, ‘Subspace-Based Blind Channel Estimation for OFDM by Exploiting Virtual Carriers’ IEEE Transactions On Wireless Communications, Vol. 2, No. 1, January 2003.
- [7] J.-J. van de Beek, O. Edfors, M. Sandell, S. K. Wilson, and P. O. Borjesson, “On channel estimation in OFDM systems,” in Proc. IEEE 45th Vehicular Technology Conf., Chicago, IL, Jul. 1995, pp. 815–819.
- [8] M. Hsieh and C. Wei, “Channel estimation for OFDM systems based on comb-type pilot arrangement in frequency selective fading channels,” IEEE Trans. Consumer Electron., vol. 44, no. 1, Feb. 1998.
- [9] O. Edfors, M. Sandell, J.-J. van de Beek, S. K. Wilson, and P. O. Borjesson, “OFDM channel estimation by singular value decomposition,” *IEEE Trans. Commun.*, vol. 46, no. 7, pp. 931–939, Jul. 1998.
- [10] Meng-Han Hsieh, Che-Ho Wei “Channel Estimation For OFDM Systems Based On Comb-Type Pilot Arrangement In Frequency Selective Fading Channel” IEEE Transactions On Consumer Electronics, Vol. 44, No. 1, February 1998
- [11] Y. Zhao and A. Huang, “A novel channel estimation method for OFDM Mobile Communications Systems based on pilot signals and transform domain processing,” in Proc. IEEE 47th Vehicular Technology Conf., Phoenix, USA, May 1997, pp. 2089–2093.
- [12] A. V. Oppenheim and R. W. Schaffer, Discrete-Time Signal Processing, New Jersey: Prentice-Hall Inc., 1999.
- [13] Tang, R.G.; Zhou, X.; Wang, C.Y. A Haar wavelet decision feedback channel estimation method in OFDM systems. *Appl. Sci.* 2018, 8, 877. [CrossRef]

# ARM Based Smart Living System using Brain Computer Interface

K. Arun Kumar<sup>1</sup>, R. Satya Prakash<sup>2</sup>, and M. Vinod Kumar Reddy<sup>3</sup>

<sup>1</sup>Asst. Professor, CVR College of Engineering/ ECE Department, Hyderabad, India  
Email: arun.katkoori@gmail.com

<sup>2</sup>Asst. Professor, CVR College of Engineering/ CSE Department, Hyderabad, India  
Email: prakashscits@gmail.com

<sup>3</sup>Asst. Professor, CVR College of Engineering/ECE Department, Hyderabad, India  
Email: vinodreddy.488@gmail.com

**Abstract:** As of late, numerous ecological control systems have been proposed to improve human personal satisfaction. In any case, little research has concentrated on environmental control directly using the human physiological state. The primary point of this paper is to control the physical gadgets like home machines utilizing EEG signals and to assist the physically disabled persons with controlling the home apparatuses, so they become autonomous in their everyday life. This methodology offers an elective correspondence and the control framework and is referred as an artificial system that evades the human body's typical enough pathways, which are neuromuscular yield channels. In this paper, a non-obtrusive Brain Computer Interface is utilized. The brainwave sensor is utilized to detect the brain signals and eye blink. As per the eye blink values and the brain attention values, the gadgets will be chosen and through transfers the turning ON and OFF the home apparatus are done as needs be. The experimental results show how to operate the modules like fan/bulb by blinking the eyes with help of ARM7 processor. It is observed that the mean response time of the system for bulb was found to be 15.6 sec with accuracy of 84.6% for ON state, and 21 sec with accuracy of 72.4% for OFF state.

**Index Terms:** Brain wave sensor, Brain computer Interface, Electroencephalogram (EEG), ARM processor.

## I. INTRODUCTION

Recently, with the development in sensor innovation and data technology, numerous examinations are attempting to create business products to acquire the comfort to individuals their standard life. In this manner, the fast development of research on smart houses is proposed and created as a standard to give different sorts of environmental control systems. RFID, outside sensor modules, and voice recognition are used as control signals in some of the environmental control systems [1]. For automatic detection of person's motion, the RFID tags or external sensors are placed in different regions in advance. By combining with universal plug and play home systems, a person can send a request from his cell phones, a wearable machine, or outside sensors to the home server either motion, GUI, or voice. Brain Computer Interface is an alternative technique to apply the physiological signals as the stimulus of ecological control system in smart home [2][3].

In any case, the greater part of current BCI based system requires the person's dynamic mental order to control outside devices [4][5] [6]. Subsequently, these systems can't

control peripherals consequently and adaptively as indicated by the client's present intellectual state. Besides, most of the flow BCI-based environmental systems are inconvenient because of their complexity and expensive.

Therefore, the goal of this paper is to propose a low cost and flexible brain computer interface-based system to control devices based on the user's psychological state (languor or readiness). In this method, an embedded processor like ARM processor and signal acquisition module like brain wave sensor are proposed. Not quite the same as other BCI frameworks, which are generally massive and need to transmit EEG signals to a backend PC to process the EEG signal, our proposed method is having the advantages of low power, small size and are suitable for practical applications.

## II. PROPOSED MODEL

### A. EXISTING METHOD

In a normal system, to control electronic home appliances a manual method of operating is required and there is no means of data transfer. The data transfer is done through cables and individual must depend upon others to operate the devices. And, there is no muscle contraction in existing systems where as BCIs use brain signals to gather information on user intentions[7]. To that effect, BCIs rely on recording state that measures brain activity and translates the information into tractable electrical signals and requires direct personal computer interaction.

In the proposed system, the basic method adapted is Brain wave analysis, where the signals generated from the brain are directly analyzed. A thought generated by the brain can make certain muscular contractions, by this an automated robot could be controlled by using human thoughts[8]. The proposed system provides self-controlled and operating facility. A most of newly developed devices are features with Bluetooth which is easy to access and transfer files in the proposed system Bluetooth communication plays a major role in transferring the data for analysis[9]. The architecture of Brain Computer Interface is shown in Figure 1. It contains three stages- i) signal acquisition and preprocessing, ii) Signal processing, iii) commands/ control.

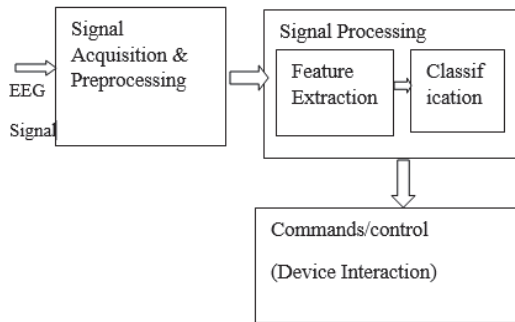


Figure 1. BCI Structure

**B. EEG-ELECTROENCEPHALOGRAM**

The EEG is a chronical of the electrical movement of the brain from the scalp. The principal recordings were made by Hans Berger in 1929 although comparative investigations had been completed in creatures as ahead of schedule as 1870.

The waveforms recorded are thought to mirror the movement of the outside of the brain, the cortex. This movement is impacted by the electrical action from the mind structures underneath the cortex. EEG follows are appeared in figure 2. Each electrode is marked with a letter followed by a number, the letter refers to the zone of cerebrum basic the electrode and the number is even or odd. Odd number indicates left half of the head and even indicates the correct side of the head.

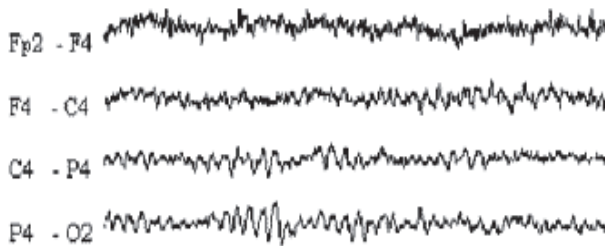


Figure 2. EEG traces

The nerve cells in the mind produce a signal that is called activity over possibilities. These active possibilities move to start with one cell then onto the next over a hole called the neural connection. Unique synthetic compounds called synapses help the signal to move over the gap. There are two kinds of synapses; one will help the active potential to move to the following cell, the other will stop it moving to another nerve cell. The brain ordinarily strives to keep an equivalent measure of every one of these synapses in the mind. EEG action is very little, estimated in microvolts with the primary frequencies of interest up to around 30Hz.

To examine the EEG signal, a ‘Thinkgear’ brainwave sensor is utilized. Brain-Computer-Interface is an immediate correspondence pathway between human brain and the external component. As per the human contemplations i.e., the brain consideration esteems the physical components are worked [10]. The signal acquisition unit receives the brain wave raw data and processes the signal utilizing MATLAB. Along with MATLAB, Visual Basic software is used because, a large amount of data is receiving from the brain sensor and sending these data to the MATLAB in signal processing unit [11][12]. Meanwhile the attention and eye blink values are sent to the hardware side. So, the data transmission rate in Visual Basic is relatively more prominent than that of the MATLAB. The following figure 3 shows the block diagram of BCI.

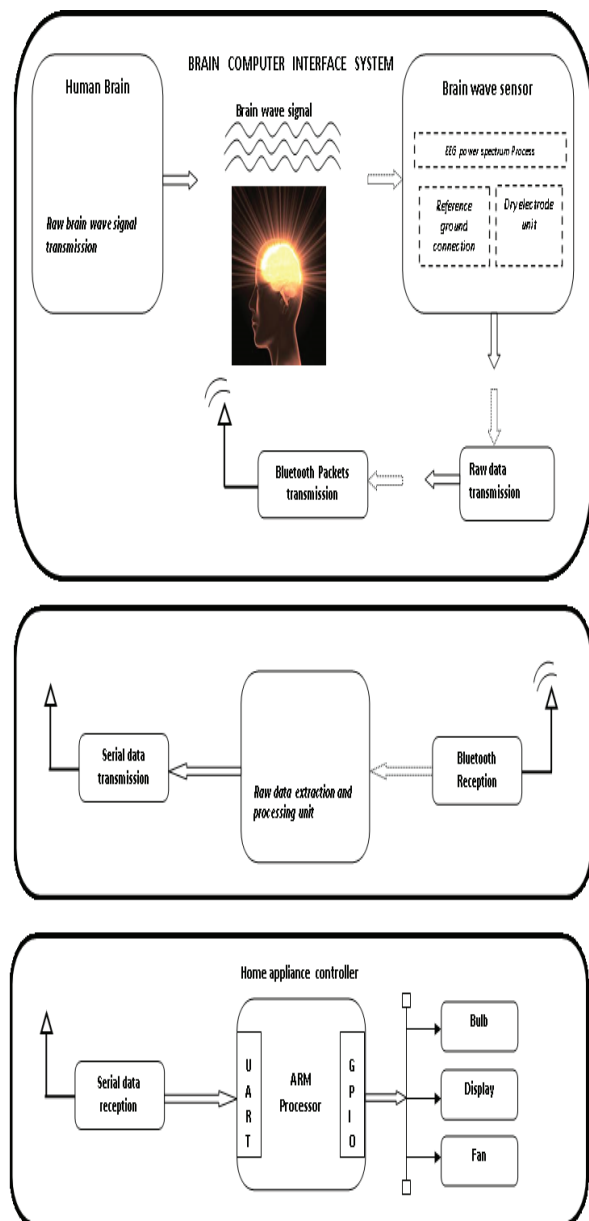


Figure 3. Proposed BCI system Block diagram

The brain wave data is sent to the controller unit. This data is sent serially using UART. Then the instructions will be sent to the home appliances to control the devices like bulb, fan, display, etc. as shown figure 3. In the controller unit, ARM controller receives serial data and send commands to the physical devices through GPIO bus.

### C. ARM PROCESSOR

The abbreviation of ARM is Advanced RISC Machine, is widely used in the field of embedded system. The following are the features of ARM3 module—

- It's Operating clock frequency varies from 156MHz to 320MHz.
- Contains two 16-bit MAC (multiply-and-accumulate) units to execute 1200 lines multiplication and addition operations.
- It has four independent DMA (Direct Memory Access) mechanisms. The processing time was reduced.
- It contains Serial peripheral interface Flash is used (to reduce the module size).
- It also contains wireless transmission unit via universal asynchronous receiver/ transmitter (UART) interface.
- This module can be operated with a 3.7 V DC power supply, and it can continuously operate for more than 45h operations with a 1100mAh Li-ion battery.

Cognitive state detection algorithm was implemented in this embedded module. Then got EEG information is processed, analyzed and displayed by this module [13]. At this point when the difference is subjective condition of the client is identified, the corresponding instruction will be sent either by RF module or by Ethernet through Universal plug and play protocol. A RS232 to Ethernet adapter module is required to do this.

### D. BRAIN SENSE-BRAIN WAVE SENSOR

Brain wave is a Brain-Computer Interface (BCI) device transforms person's brainwaves into activities, opening new worlds of intuitiveness [14]. By using proprietary Attention and Meditation eSense algorithms, the brain wave sensor reports the wearer's mental state. The head set of brain wave sensor is shown in figure 4. Implanted inside the TGAM, is the TGAT chip, a ground-breaking, completely coordinated single chip EEG sensor. The chip comes modified with Neurosky eSense, Analog-to-Digital Converter, enhancement off head recognition, and noise filtering for EMG and 50/60 Hertz AC powerline impedance. The TGAM is evaluated to control mass reception in toys, cell phones, instructive apparatus and different items.

To power ON the Brainwave sensor, plug the battery terminal to the terminals. To turn the Brainwave sensor OFF, remove the terminals plugged to the battery. [15] While the Brainwave is powered on, the LED light on the side of the headset will be turned on.

Brainsense is more than an average headset. It can use person's brainwaves for exciting new applications. In order to take full advantage of these functions and features of the Brainsense, the Brainsense must be properly worn.



Figure 4. Brain wave sensor headset

### Features and functions of Brain wave sensor:

It allows the ear band to rest behind the left ear, and afterward clip the ear clip onto individual's ear cartilage.

Make sure the two metal contacts within the two sides of the ear clip make skin contact with ear. Move any hair or obstructions such as jewelry out of the way. Read just the ear clip as necessary to make proper contact with the skin of ear. The figure 5 shows the brain sense earlobe. It may need to squeeze the ear clip against human's ear for a few moments.



Figure 5. Brainsense Earlobe

Adjust the forehead Sensor Arm of the headset so that the Sensor Tip contacts the skin of forehead. Sensor Tip must maintain steady skin contact in order to properly measure your brainwaves.

Sensor Tip should be comfortable yet stay normally in position. Keep hair away from the sensor – the sensor must always be able to directly contact the skin. Make up, dead skin, or debris can interfere with the connection. Scratch or wipe the obstruction away if the person has trouble obtaining a clean signal.

The Brainsense should look when properly worn. During usage, if person is not receiving a signal, repeat the steps above to make minor adjustments to ensure the sensor and contacts have proper skin contact. Figure 6 shows the brain sense forehead sensor tip contact.



Figure 6. Brain sense forehead sensor tip contact

**E.FLOWCHART:**

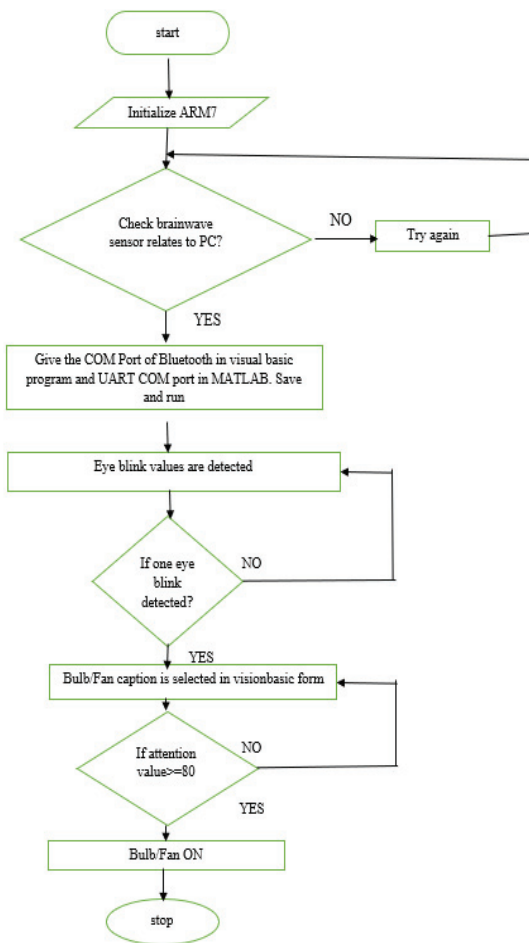


Figure 7. Flowchart of proposed method

**F. HARDWARE CONNECTIONS**

- Establish a connection between the board to the power supply.
- Connect the adapter to the DC voltage and plug it to the LPC2148 board and switch on the power supply.
- Switch on the thinkgear Brain wave sensor by plugging the battery, check whether the LED is turned on and blinking.
- Check whether the dry electrode is properly in contact with the forehead and the ear plug is properly attached to the ear lobe with proper contact.
- Check whether the COM port and Bluetooth is properly paired with the PC and sensor. These are shown in figure 8.

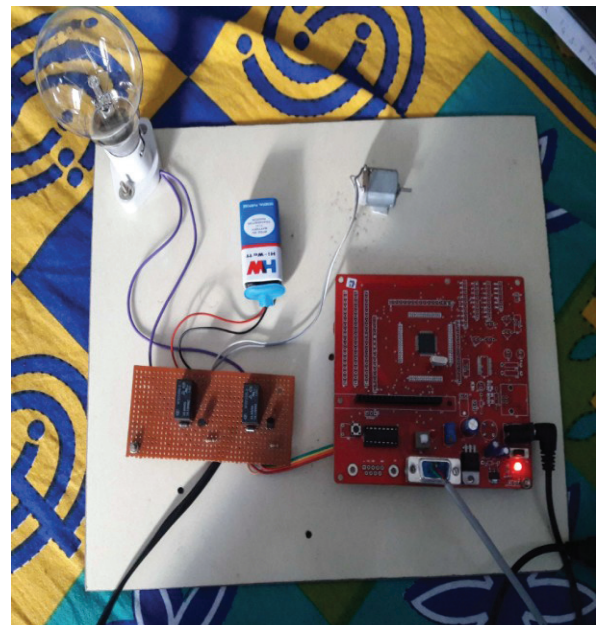


Figure 8. Hardware connections

**G. RESULTS**

- In order to make the application run, Open the Matlab M-File.
- Click the run button in the editor toolbox.
- After clicking the run button, a new command window opens, The thinkgear is loaded and the attention and meditation values are plotted
- These signals are plotted and analyzed by the brainwave sensor.
- The muscle contraction occurs because of blinking of the eyes and the bulb turns on and off accordingly.
- In the figure 9, the red line in the graph represents the attention value and the black color dots represent the number of times the blink is plotted. The form of Visual Basic is displayed when the



value of eye blink detected is 80. A device is selected depending on number of eye blinks (one or two eye blinks) and that device is tuned ON or OFF depending on the attention value.

After connecting all the components switch ON the power supply. In a few seconds thinkgear brainwave sensor establishes a connection to the personal computer via Bluetooth. The signal generated is analyzed by using the MATLAB GUI platform. Then the instructions will be sent to the home section to operate the modules like bulb and fan, etc. The ON-OFF condition of electrical gadgets is based on changing the muscle movement with eye blinking.

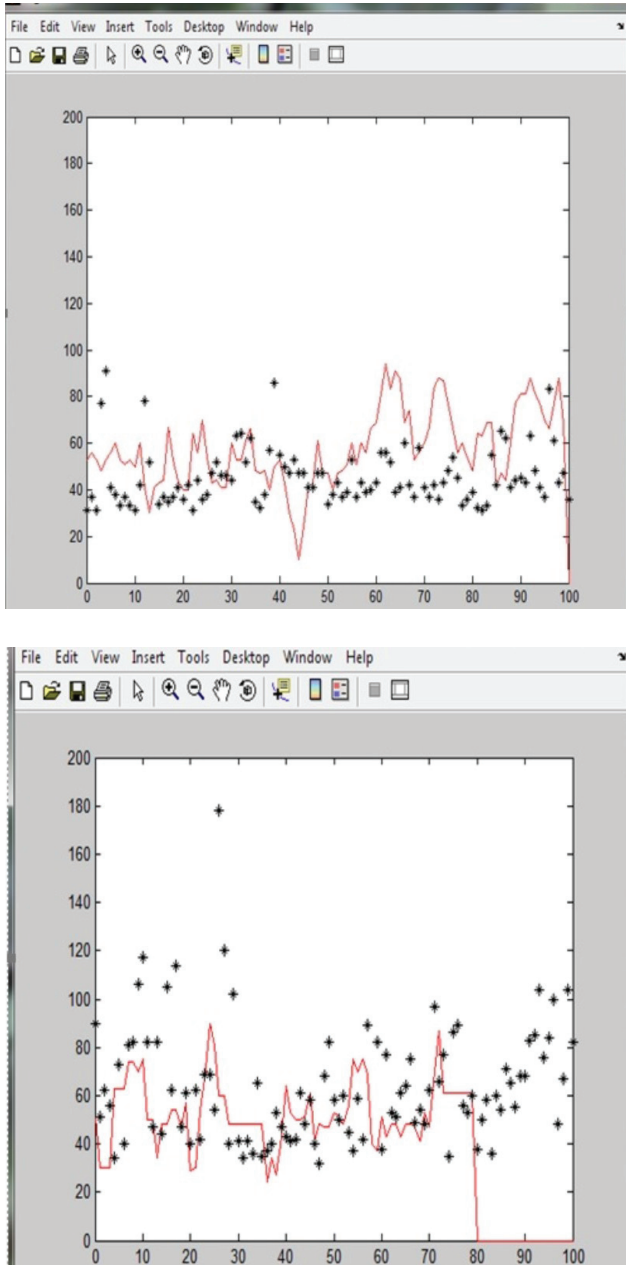


Figure 9. Graphical plotting for different number of trials

Vision Basic is a Field Device Tool frame application with a modern & uncomplicated GUI. It gives powerful essential usefulness to setup, diagnostics and support of intelligent field gadgets.

Different patterns of neural interaction lead to different waveforms. These waves are having different amplitudes and frequencies. This neural cooperation is finished with different neurons. Each collaboration between neurons makes a tiny electrical release.

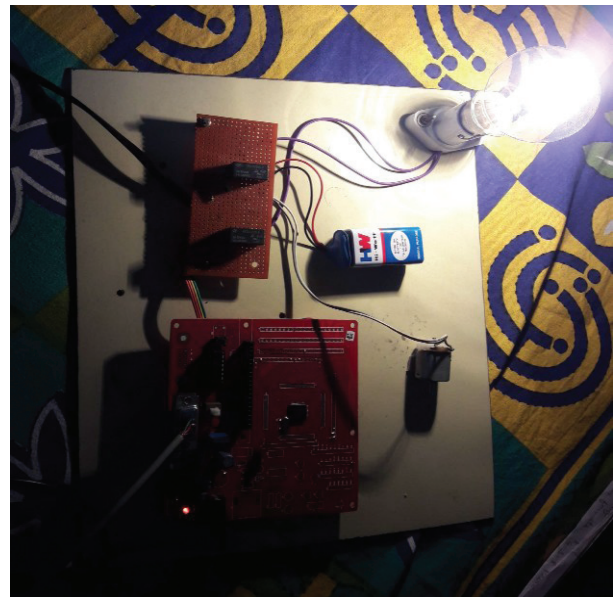


Figure 10. output of the module

TABLE I.  
MEAN RESPONSE TIME FOR BULB FOR TWO STATES

Number of trials	ON state(sec)	OFF state(sec)
Trial 1	14	19
Trial 2	11	24
Trial 3	16	13
Trial 4	23	19
Trial 5	16	30
<b>Mean time(sec)</b>	<b>15.6</b>	<b>21</b>

TABLE II.  
MEAN ACCURACY FOR BULB FOR TWO STATES

Number of trials	ON state(sec)	OFF state(sec)
Trial 1	75.6%	68.4%
Trial 2	99%	95%
Trial 3	75%	68%
Trial 4	84%	79%
Trial 5	88%	52%
<b>Mean Accuracy</b>	<b>84.6%</b>	<b>72.4%</b>

Above Table I gives the mean response time for bulb for turn ON and turn OFF states. It is observed that, for five

trials, the mean time for bulb's ON time is 15.6 seconds and bulb's OFF time is 21 seconds. OFF state takes more time than ON state.

Table II shows the mean accuracy for bulb for two states i.e. turn ON and turn OFF states for five trials. For ON state, the accuracy is 84.6% and for OFF state, the accuracy is 72.4%.

### III. CONCLUSIONS

Human brain sends signals to brain wave sensor (via Bluetooth channel). By using wave measuring unit converts raw data into suitable signals using MATLAB GUI platform. Then Commands are sent to control the devices like fan, bulb etc... By blinking the eyes there will be a change in the muscle movement, this is sensed by the Brainwave sensor and given to a MATLAB program via bluetooth, using highly Advanced RISC Machine(ARM) board and with the help of growing technology has been successfully implemented.

BCIs can have various applications over an assortment of fields, clinical and non-clinical. BCIs can give remote control in situational inability conditions, for example, space travelers and specialists, improve intellectual capacities, for example, improving consideration, official capacities, working memory, and also in non-medical applications like smart home controlling, robots controlling, security and health.

### REFERENCES

- [1] Anirudh Vallabhaneni et al., "Brain—Computer Interface", 1<sup>st</sup> ed.: Springer US, 2005, pp 85-121
- [2] L. Zhang, H. Leung, and K. C. C. Chan, "Information fusion based smart home control system and its application," *IEEE Trans. Consumer Electron.*, vol. 54, no. 3, pp. 1157–1165, Aug. 2008.
- [3] Ghodake, A. Brain Controlled Home Automation System. [PDF] San Diego, CA, USA: 2016 10th International Conference on Intelligent Systems and Control (ISCO), 2016, pp.1-4.
- [4] S. Helal, W. Mann, H. El-Zabadani, J. King, Y. Kaddoura, and E. Jansen, "The gator tech smart house: A programmable pervasive space," *IEEE Comput.*, vol. 38, no. 3, pp. 50–60, Mar. 2005.
- [5] W.-H. Liao, C.-L. Wu, and L.-C. Fu, "Inhabitants tracking system in a cluttered home environment via floor load sensors," *IEEE Trans. Autom. Sci. Eng.*, vol. 5, no. 1, pp. 10–20, Jan. 2008.
- [6] Alrajhi, W., Alaloola, D. and Albarqawi, A. (2017). Smart Home: Toward Daily Use of BCI-Based Systems. [PDF] San Diego, CA, USA: IEEE Conference Publications, pp.1-5.
- [7] Goel, K., Vohra, R. and Baths, V. (2014). Home Automation Using SSVEP & Eye-Blink Detection Based Brain-Computer Interface. [PDF] San Diego, CA, USA: IEEE International Conference on Systems, Man, and Cybernetics, pp.4035-4036.
- [8] D. H. Stefanov, Z. Bien, and W.-C. Bang, "The smart house for older persons and persons with physical disabilities: Structure, technology arrangements, and perspectives," *IEEE Trans. Neural Syst. Rehabilitation Eng.*, vol. 12, no. 2, pp. 228–250, Jun. 2004.
- [9] S. H. Kim, J. S. Kang, H. S. Park, D. Kim, and Y.-J. Kim, "UPnPZigBee internetworking architecture mirroring a multi-hop zigbee network topology," *IEEE Trans. Consumer Electron.*, vol. 55, no. 3, pp. 1286–1294, Aug. 2009.
- [10] C.-S. Li, Y.-M. Huang, and H.-C. Chao, "UPnP IPv4/IPv6 bridge for home networking environment," *IEEE Trans. Consumer Electron.*, vol. 54, no. 4, pp. 1651–1655, Nov. 2008.
- [11] T.-W. Jo, Y.-D. You, H. Choi, and H.-S. Kim, "A bluetoothUPnP bridge for the wearable computing environment," *IEEE Trans. Consumer Electron.*, vol. 54, no. 3, pp. 1200–1205, Aug. 2008.
- [12] C. Rus, K. Kontola, I. D. D. Curcio, and I. Defee, "Mobile TV content to home WLAN," *IEEE Trans. Consumer Electron.*, vol. 54, no. 3, pp. 1038–1041, Aug. 2008.
- [13] B. A. Miller, T. Nixon, C. Tai, and M. D. Wood, "Home networking with universal plug and play," *IEEE Commun. Mag.*, vol. 39, no. 12, pp. 104–109, Dec. 2001.
- [14] T. Hwang, H. Park, and E. Paik, "Location-aware UPnP AV session manager for smart home," in *Proc. IEEE 1st Int. Conf. Networked Digit. Technol.*, Jul. 2009, pp. 106–109.
- [15] B. Rebsamen, C. Guan, H. Zhang, C. Wang, C. Teo, M. H. Ang, and E. Burdet, "A brain-controlled wheelchair to navigate in familiar environments," *IEEE Trans. Neural Syst. Rehabil. Eng.*, vol. 18, no. 6, pp. 290–298, May 2010.

# Flood Inundation Warning and Relief System Based on GIS and Remote Sensing

B. Teena<sup>1</sup> and Dhruva R. Rinku<sup>2</sup>

<sup>1</sup>PG Scholar, CVR College of Engineering/ECE Department, Hyderabad, India  
Email: teenapaul23@gmail.com

<sup>2</sup>Assoc. Professor, CVR College of Engineering/ECE Department, Hyderabad, India  
Email: rinkudhruva.ravi@gmail.com

**Abstract:** Due to climate change and uncontrolled urbanization, frequencies of floods are increasing these years. In a developing country like India, flood creates a great havoc which takes many years to get restored. To mitigate the affect of flood disaster, an accurate flood inundation warning is required.

In this system, a geographic information system (GIS) model is developed on the basis of Digital Elevation Model (DEM) and the shapefile of buildings. They accurately analyze the land behavior in presence of flood and identify the flood inundation risk of different places. This would be helpful to take active measures to mitigate the destruction caused by flood, in time being. Global Precipitation Measurement's (GPM) half-hourly rain data is used to find the impact of rain on current flood conditions in various areas; this helps to warn the people living in nearby places, as they also may have threat of life and property.

This system also contains the flood relief system which is a web-based system (developed using PHP) having web application and MySQL database, to create a platform that provides a foundation that prepares the donors to help the victims of flood with various kinds of donations. This system informs the donors by sending an SMS using a GSM module. This is done to prepare the donors with their donations, immediately after the flood warning is released. These donations would equip the authorities to provide essential needs of the flood victims. This system is developed for Mumbai city, India's largest city as it is a city affected by flood almost every year causing great destruction of property and life.

**Index Terms:** GIS, remote sensing, DEM, Arduino, MySQL, PHP, GSM

## I. INTRODUCTION

Temporary overflow of water to a normally dry area due to entrance of large amount of water which cannot be drained at the same rate and gets accumulated is called flood. The source of this large amount of water can be heavy rainfall, precipitation, rise in water level of river, broken dams which may be caused due to levees failure, improper drainage basins, natural disasters like storm surges and earthquake in water, known as Tsunami. Whatever may be the source of flood water but it has the potential to destroy the life and property in huge amounts, that too without warnings or signs which makes people, authorities and government powerless and helpless to avoid the havoc it creates.

Flood is the deadliest natural disaster which affects millions of people every year. Various technologies are being developed to warn people for flood and mitigate the

damage, yet many millions of people are affected by flood. International disaster database declares that in 2018, 109 floods occurred throughout the world which devastated the lives of many people as shown in "Figure 1" [1]. India is a developing country which is affected by flood every year especially in its monsoon season which is from June to September. The southern and north-western India receives 50%-75% of their total annual precipitation in this season. India receives average rainfall of 200-300 mm [2].

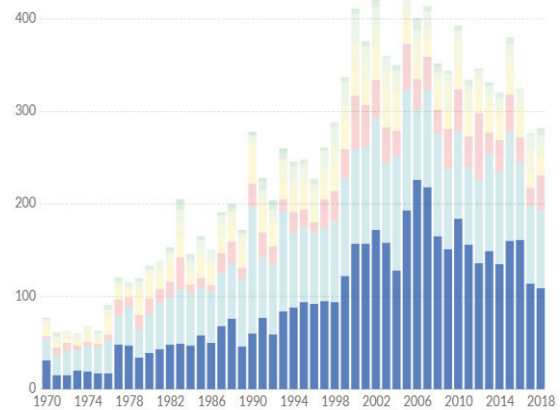


Figure 1. Statistics of floods occurred in 1970-2018.

Mumbai is taken as study area for this work because Mumbai is the largest city on India's Konkan coast in west coast and it is the financial capital of India. Mumbai is the most densely populated metropolitan city of India with population of 18,394,912 as of 2011. Mumbai generates 6.160% of India's GDP, accounts for 25.0% of industrial output from India and brings 70.0% of capital transactions to India's economy. The ports of Mumbai execute 70.0% of India's maritime trade. This city provides a lot of employment opportunities, for instance, the factories in Mumbai produces 10.0% of total factory employments in India. The industries in Mumbai produce 25.0% of total industrial outputs for India. Mumbai benefits the Indian government's revenue as the citizens of Mumbai pay 33.0% of total income tax collections, 60.0% of total customs duty collections, and 20.0% of total central excise tax collections in India. The companies of Mumbai play a vital role in foreign trade as 40.0% of India's foreign trade is done in Mumbai [3]. These factors get disturbed when Mumbai is hit by floods every monsoon and produce a very negative impact on the economy of its state and that of the nation.

In monsoon season western and central India receives more than 90% of their total annual precipitation. India has coastline of 7516.6 km which cross through Mumbai, this makes it more prone to flood due to water overflow from coastal seas. Apart from this uncontrolled construction, antiquated drainage system and ruination of Mangrove ecosystems due to aquaculture expansion increase the damage cause by floods in Mumbai [4].

In 2017 Mumbai was flooded due to 468 mm of rainfall within 24 hours and two to three days of heavy rainfall over central India; this killed 14 people. This flooding caused a building to collapse, killing at least 21 people [5]. The transport system of trains and roadways was collapsed.

In 2005 Maharashtra floods, which were caused due to 944 mm (37.17 inches) of rainfall within 24 hours, 644mm (25.35 inches) within 12 hours which killed 1,094 people [6]. The loss incurred was about Rs. 550 crores (US\$100 million). The damage caused to transport was very huge.

In these ways Mumbai floods are bringing a huge damage of life and property. So, it is very crucial for the nation to preserve its financial capital Mumbai from frequent flood damage [7]. In this work, a GIS based model is developed which identifies the blue-spots (place where the water gets in and accumulates because it has no outpour) which makes the buildings of this area more prone to flood, those buildings are identified using ArcGIS [8], a GIS based software.

The amount of rain water, which totally inundates an area that is prone to flood, is calculated and is known as the fill-up value; later this value helps to identify when the flood water will flow out to its nearby places. The near-real time precipitation data generated through remote sensing is processed to identify the present condition of flood through which a flood warning can be released for the people living nearby. A flood relief system is developed which contains a website based on PHP, this enables the donors to get registered and it stores their information in a database. These donors are informed about the potential flood victims who may suffer, when the flood warning is generated so that they can send their donations to the flood victims.

## II. LITERATURE SURVEY

There are many existing flood warning systems such as, Central Water Commission (CWC) of government of India. It monitors the flood situation by observing discharges along the major rivers in the country and issues a flood warning. This Flood warning Network has 325 stations which covers 197 low lying cities and towns. This system is able to mitigate low to moderate level of floods, but it fails to be accurate in case of Mumbai which have only four rivers and which is mainly hit by pluvial flood almost every year.

Dadasaheb K. Mane [9] proposed a flood warning system which uses ultrasonic sensor, deployed by the river side to monitor the water level of the river, this system monitors flood but any disturbance caused due to wind or sound of water alters the data. Moreover, the ultrasonic sensor has lesser range, which is up to 3 meters. Hence, it is not much reliable. Barometric Pressure sensor is implemented to identify the water level of the river as it avoids all the

disturbances using a pipe and generates an alert, as proposed by Azid et al. [10]. But it is limited only for fluvial flood where flood occurs mainly due to river overflow and it views the incoming flood only from one region i.e. where the sensor is deployed in case of a large river, multiple sensors can help to understand all the flood sources. Moreover, this can warn only the people residing by river side, which is not the exact case of Mumbai.

According to Khalaf et al. [11] and Devaraj et al. [12], water level sensor can be used to sense the water level in rivers; forming a network of these sensors can produce a flood warning but fails to give information of the direction in which flood water is flowing, especially in a residential area. The information about the direction of flow of flood water would help much more accurately. Hence it produces a flood warning but not accurate enough to help people of Mumbai due to inadequate sensors in the network which would tell the direction of flow of flood water. Moreover, the rain data must also be considered to track the current flood condition.

Dense number of rain gauges that form a network can help to track the precipitation rate and identify flood risk as proposed by Carbone et al. [13], but it is not economically feasible for India, moreover it should be setup in a flat area, a place which has no blockage towards sky and must be away from any kind of blockages such as buildings, trees, etc. Moreover, this network requires maintenance of the rain gauges, as damage of a single rain gauge can diminish the accuracy. This is hard to implement in Mumbai city which has very dense population that makes this approach inappropriate.

To get accurate precipitation data for flood warning in addition to number of rain gauges, optimal locations to setup rain gauge is also vital, Kriging technique is used for this purpose, according to Sajal Kumar Adhikary et al. [14], this technique provides good quality rainfall estimates to release accurate flood warning, but it takes a lot of effort to practically implement it, satellite data can be used as a substitute to get rainfall information in flood-plain. In addition to this the study of terrain's surface and hydrology helps better to build an accurate flood warning system as it tells where the flood water is going to get accumulated and where inundation will occur.

Flood-plain mapping helps to understand the direction of flow of flood water, which can be implemented by DEM. It is the raster data set which provides the information of elevation at every location. This is used to compute the structural properties of watershed area to plot the susceptibility to floods according to Keighobad et al. [15]. This data provides the information of flood risk in an area, but it is a static topographic model, a dynamic model helps better.

In this work, DEM map of Mumbai is used to identify the areas of sinks. All the sinks belonging to the same group are identified and grouped together. The buildings which fall under the sink regions are identified and declared as the region having risk of floods. Moreover, remotely sensed precipitation data is processed to release flood warning. The objective of this work is to develop a customized flood warning for Mumbai, improve the accuracy of flood

warning using sinks, release timely warnings and develop a flood relief system.

### III. FLOOD WARNING SYSTEM BASED ON SINKS

#### A. Identification of flood-risked Buildings

To understand the affect of flood in different areas, the elevation data of the affected area is to be studied. A Digital Elevation model (DEM) map provides the elevation data of earth's surface. The DEM data of Mumbai used for this work is taken from NASA's STRM DEM data. This DEM data has to get geo-processed, in order to understand the flood dynamics.

GIS is a framework used for gathering, managing, and analyzing geological data. It integrates many types of data and performs various operations on them. The output of processed information is shown in the maps; they have specific geographical coordinates in reference to the actual geographical coordinates. The basic unit of a map is pixel or cell. ArcGIS is the software that provides a platform to perform geo-processing on the input data.

For this work DEM map is taken as input of the flood warning system. It has 90 meters horizontal resolution. It also has a vertical resolution or accuracy. The elevation shown in DEM map, which is less than vertical accuracy, might be an error. These errors should be removed before geo-processing the data to obtain flood warning. The DEM map is made error free and is used to identify sinks in the flood plain area that is shown in DEM map. All the cells having elevation less than zero are identified as sink cells, where as zero is considered as the normal ground elevation.

All the pixels having sinks and the pixels which have continuous sinks are grouped to find out the whole region of sink. These regions are dissolved to identify the sinks as whole which gives us the information about the inundation areas as the flood water gets accumulated in these regions.

Vector map is a map consisting of points, lines or polygons used to represent a delineation of three-dimensional data, such as parks, buildings or water bodies. The collection of vector data is called a shape-file as shown in "Figure 2". A shape-file contains a table attached to it, called as attribute table which stores the data of the vectors drawn in the shape-file. A shape-file is required to draw the delineation of the shape of raster (a 3-D object).

In order to have more accuracy of flood warning i.e. up to building's level, the shape-file of buildings is superimposed on the sink's map. To exactly super-impose a map on other map, it must be geo-referenced in order to get the information without any errors of direction. To match a digital map to real world 'geo-referencing' is done. Geo-referencing is the assignment of a real world geographical coordinate system to a digital map, which specifies each location as a set of latitude (horizontal) and longitude (vertical).

Latitude is a point formed by the angle between the plane of equator and the centre of the Earth. Longitude is the angle formed by a reference meridian to another meridian, from east to west. Geo-referencing is done to precisely match different layers over a base layer on a map, in this case the

geo-referencing is used to map the buildings over sinks map, and this is done to get building level accuracy. Geo-processing is done to identify the buildings which have the risk of flood, and to warn them.



Figure 2. The Mumbai city buildings Shape file.

The flood risked buildings are pin-pointed by implementing the algorithm shown in the flow chart of "Figure 3". This is implemented by creating the model in ArcGIS and automating the model by a python script which takes in the inputs, automatically processes it and provides the flood risked buildings as output.

This provides us with a static model of area having sinks, where the flood water gets accumulated. To get more accurate flood warning system, we have to make the flood warning dynamic, for that the hydrological aspects of this area must be considered, such as flow direction of water.

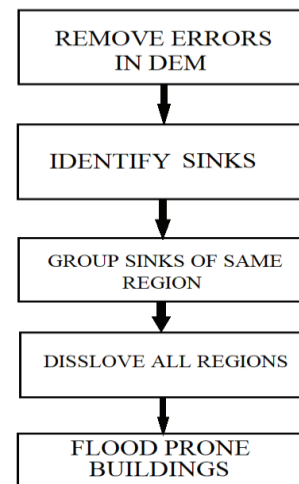


Figure 3. Flood-risked buildings Identification Flow chart.

#### B. Identification of fill-up value of sinks

To identify situation when the accumulated flood water will flow out to its neighboring places, the fill-up value is to be identified. For this purpose the volume of sinks can be identified by adding the elevation of all pixels; this addition will provide the height. The area of sinks is identified by

finding the area of pixels of different regions of sinks. The inundation in an area can be caused by two reasons; first reason is due to precipitation and another is due to water flowing from higher elevation to lower elevation area. To identify the water accumulated in an area besides that which is due to precipitation, the flow direction must be considered. The flow direction of water is calculated by identifying the steepest continuous neighbor pixel for a given pixel, from the eight surrounding pixels, this provides the flow direction map.

Inundation mainly occurs in the area where the water flows in but does not flow out (which means the region formed by combination of continuous pixels where none of surrounding pixels is having steepest elevation, from which the water can flow through), this region is called a watershed. A watershed is an area on the top of the slope which has a common point for concentrated drainage flow known as pour point. Pour point is the lowest point in the boundary of watershed. A watershed may contain many watersheds which are called as sub-basins. The watershed area is described from the flow direction, which is derived from the DEM. Watershed area is used to determine the catchment area for precipitation data, as the affect of rain in any part of a region is same as that of whole region because the water doesn't flow out till it reaches the fill-up value. The fill-up value gives the information when the water will start flowing out of the watershed area and will make the nearby areas inundated and it is derived from "Eq. (1)".

$$\text{Fill-up value} = \text{Sink volume} / \text{Watershed area} \quad (1)$$

### C. Finding current situation of flood using Near-Real time precipitation data

The volume of sink and the watershed area is used to determine the fill-up value of the sink. After determining the fill-up value the near real-time precipitation data is used to dynamically check whether the sink is filled or not, this is done by identifying whether the current rainfall has exceeded the height of pour-point of sink, which gives the information of inundation for that area. This information can be used to warn the people living in a watershed region and nearby places and helps the authority to evacuate the people residing there.

### D. Web-Based Flood relief system

The flood relief provided by the government is not available soon and not sufficient. To meet this lack, a large group of donors are required to be prepared well before, who can send relief to the flood victim's for the time being and can help them. To prepare this system the donors are made to sign up for donations through a web-page, especially the donors residing in the nearest unaffected regions. So that when a flood warning is released, donors are sent an SMS which gives them the information of flood victims suffering in a particular place, and encourage them to come forward and send donations to help the flood victims. These donors are informed to get prepared well before for the donations and when need arises the victims can receive their help from them.

PHP is a server-based backend language used to develop dynamic web pages. It is used here to develop registration webpage. HTML is used to develop static web-pages and CSS language is used to style the web-page. All these languages are used to develop a website where donors can sign-up, they have to give their information and phone number. All their data is stored in a database. When a flood warning is released this list of donors is retrieved from the database and the information of flood victims is given to them through SMS sent to their respective phone numbers.

### F. SMS containing donation information

GSM module is used to send SMS using its SIM 900A module, it basically contains a modem. It is controlled by Arduino Nano which contains Atmel ATmega328 microcontroller; it operates on 5V and at the clock Speed of 16 MHz. AT commands are used to control the modem. There are various commands for different operations such as AT+CGDAT for establishing a connection, ATD for dialing up a connection or AT+CMGS for sending SMS to a receiver. Flow chart as shown in "Figure 4" shows the process to send SMS which would inform the donors about the flood victims and would encourage them to help these people.

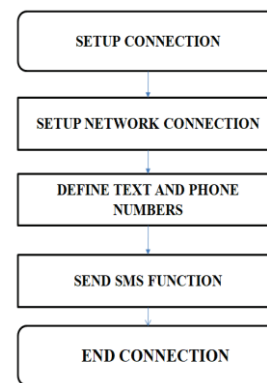


Figure 4. SMS over GSM communication Flow chart.

## IV. IMPLEMENTATION & RESULTS

ArcGIS 10.5 is used to develop the sink based flood model. It is GIS based software which provides infrastructure to generate maps and manage geographic information. Shuttle Radar Topography Mission (SRTM) by NASA is used to get the remote sensed DEM data which determines the flow and displacement of the flood water over the land. It consists of 176 orbits, acquiring the Digital Elevation Model (DEM) of 80% of the land from between 60 degree North and 56 degree south latitude, except some areas where the hills block to measure the actual height. It has pixel size of 3 arc second (approx. 90 meters). It is arranged in the form of tiles of one degree each. This means each pixel of DEM map of Mumbai used in this work is of 90 meters as shown in "Figure 5".

In ArcGIS various geo-processing tools are used to develop this flood warning system such as, spatial analyst tool-set; it contains the tools required to process the data on

the basis of its space. It is used to make the DEM map error free, identify the sinks, group the sinks and dissolve them to get overall sinks. Moreover, ArcGIS contains conversion toolset, which contains the tools used to convert the raster (3-D) data to vector data (2-D) for certain operations which operate only on a vector data. The output of first model has a map showing the risked buildings along with the table containing the data of regions having sinks with their depths. The model is scripted to get automated using the python plug-in called as arcpy.



Figure 5. Mumbai DEM map.

The DEM map is made error free and the sinks are identified as shown in “Figure 6”. The sink pixels give information about the inundated regions, all non-blue pixels show sink pixels of different depths, where the reddish pixels show the more depth sinks and light-colored pixels show less depth sinks.

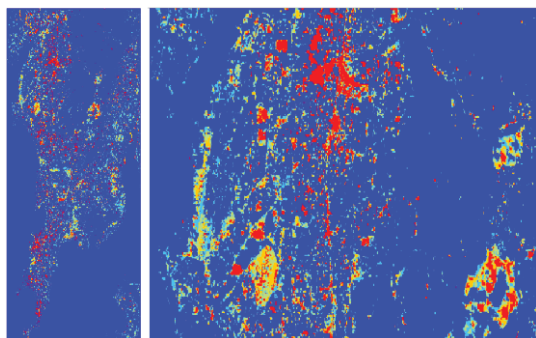


Figure 6. Sink pixels showing inundated regions.

The continuous sink pixels are grouped into a region as shown in “Figure 7”. Different colors of groups distinguish the different depths of sink regions. The dark-colored ones reveal the deep sink regions whereas the light-colored reveal the less deep sink regions.

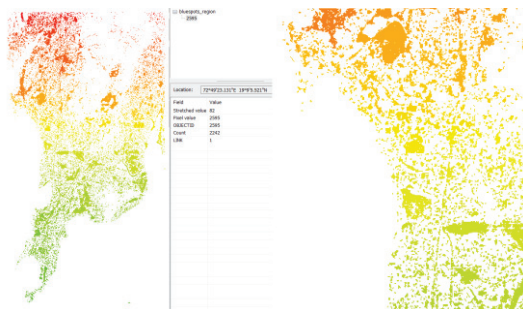


Figure 7. Grouped region's of sinks.

The grouped sinks are dissolved to identify the sinks in the entire Mumbai city. This will give us the information of the areas having inundation risks. The shape-file of buildings is mapped onto the map of dissolved sinks by ge-referencing them, then the buildings having flood risk are identified. The pink colored region is the region of sink and the buildings within these sinks are having flood risk as they lie in sink region as shown in “Figure 8” the output also contains a table listing the buildings having flood risk.

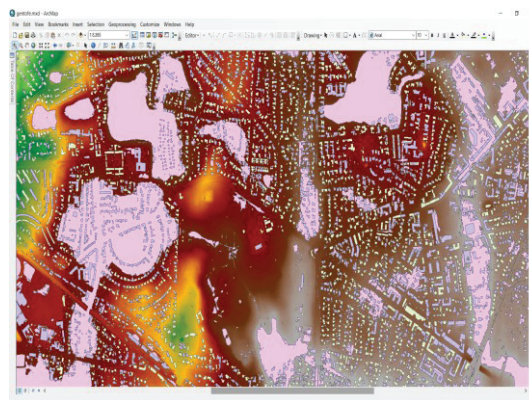


Figure 8. The buildings having flood risk are displayed.

The direction of flow of the flood water is determined by identifying the neighbor pixel having the least elevation, through which the water gets to flow, from the flow direction map the watershed area is derived as shown in “Figure 9”. The different color regions display the different outpour points into different watershed areas.

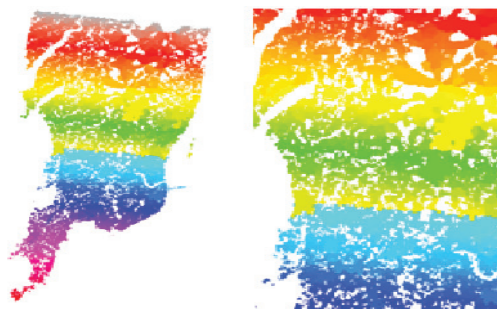


Figure 9. Various Watershed areas are displayed.

The fill-up value is calculated using the sinks volume and the watershed area. The sink volume is identified by subtracting the average height of normal elevation from the elevation of sinks, this gives the height a sink when multiplied by the sink region's area it gives the volume of sinks. The volume of sinks and watershed area provides the fill-up value of sink as few of them are shown in the attribute table of "Table 1".

The fill-up value of all sinks in millimeters, so it is easy to analyze on the basis of rainfall data as rainfall data is also in millimeters. The OBJECTID and Value fields specify the unique number for each sink region. Count Field gives information about the number of features each individual region contains in it.

TABLE I.

TABLE CONTAINING FILL-UP VALUES OF EVERY WATERSHED REGION

OBJECTID	Value	Count	LINK	Volume	SUM	SUM_1	WatershedArea	FillUp
1	1	7	1	0.691204	50.6199998	50.89	168.96	4.090931
2	2	9	1	0.691204	81.18	81.450002	89.6	7.714326
3	3	10	1	1.126399	23.0639999	23.4999999	266.24	4.230765
4	4	15	1	1.587202	26.83	27.450001	4762.08	0.331906
5	5	13111	1	642.1508	3223.309994	3474.150125	47580.16	13.49619
6	6	5	1	0.4864	8.51	8.7	125.44	3.877953
7	7	7	1	3.174399	37.68	38.92	1456.64	2.179261
8	8	6	1	0.5376	11.31	11.52	240.64	2.23404
9	9	33	1	3.148792	335.369997	336.599994	453.12	6.949135
10	10	82	1	23.0144	13.15	22.140001	550.4	41.81395
11	11	3	1	0.368483	29.17	29.310001	30.72	11.66677
12	12	21	1	1.459209	212.999998	213.570002	368.64	3.968358
13	13	6	1	0.537607	62.129999	62.340002	76.8	7.000096
14	14	13	1	1.510398	134.870002	135.460001	125.44	12.0408
15	15	20	1	1.638298	76.759998	77.399998	524.8	3.121948
16	16	7	1	1.587197	72.25	72.869999	235.52	6.739118
17	17	20	1	2.355205	187.48	188.400002	197.12	11.94888
18	18	28	1	2.432014	281.669999	282.520004	688.64	3.531619
19	19	50	1	35.22561	146.74	168.500002	565.76	62.26246
20	20	5	1	0.512004	41.499999	41.700001	189.44	2.702726
21	21	5	1	0.870401	5.61	5.95	2590.72	0.333969
22	22	5	1	0.384004	46.349999	46.500001	711.68	0.539574
23	23	6	1	0.435198	60.79	60.959999	258.56	1.683159

To make the flood warning system accurate, the NASA's GPM (Global Precipitation Mission) Integrated Multi-satellite Retrievals for Global Precipitation Measurement mission (IMERG) rain data is taken. This provides near-real time half-hourly rain data of the Mumbai city. This data is analyzed with respect to the nearby rivers and the watersheds.

A model is developed in ArcGIS and scripted which continuously monitors the rain data with respect to land hydrology to analyze how rain is causing the flood such as its behavior on the rivers and the watersheds. Finally all the models are combined to produce the accurate flood warning in form of a table containing the names of buildings which face the risk of being inundated and need to get evacuated.

This model was implemented on 2<sup>nd</sup> July 2019, when Mumbai received highest rainfall of that in last 10 years. The half-hour GPM IMERG data was constantly collected and implemented in the model of flood risked buildings and that of fill-up value which gave the result of buildings which were going to get inundated and need to get evacuated.

The result gave a huge list of buildings where were having flood risk and needed to get warned to be in their homes and the old houses were to get evacuated. Some of the buildings for which warning is given are shown in the table given in "Table 2",

TABLE II.  
TABLE CONTAINING LIST OF FLOOD RISKED BUILDINGS.

OBJECTID	Value	Count	name	type
1	722	1	Middle Ground Shoal	
2	1083	34	Siddhivinyak Mandir	place_of_worship
3	56	1748		
4	57	2090	Jayanti Jagannath Pendre Park	
5	75	4297		stadium
6	85	1444	Gateway of India	monument
7	107	2489	Taj Mahal Hotel	hotel
8	115	31163	Maharashtra Vidhan Bhavan	apartments
9	136	2646	Bombay Stock Exchange	
10	166	2585	International Cruise Terminal	
11	178	1444		
12	196	1767		roof
13	199	703	Mumbai CSMT (Suburban)	roof
14	211	11743	Gitanjali Garden	apartments
15	221	666	Wansingham House School	apartments
16	232	1444	Jamshed Bhabha Theatre	apartments
17	238	1425	Brij Kutir Shopping Centre	retail
18	246	722	Woodland Apartments	apartments
19	250	12999	Regency Hotel	apartments
20	261	3098	Danyal Mahal 3	apartments
21	270	2489	Sagar Kunj	apartments
22	275	1045	Hanuman Bhavan	apartments
23	295	703	Glenslogie	apartments
24	311	3533	Trade View	apartments
25	329	2109	Nehru Planetarium	apartments
26	335	1729	Madhu Kunj	apartments
27	355	4636		apartments
28	356	1406	Seva Sadan	apartments
29	365	1444	Bakhtawar	apartments
30	378	7809	Pleasant Palace	apartments
31	379	2489	Bharat Villa	apartments
32	383	4941	Symphony	apartments
33	384	703	WVAA Club	apartments
34	412	1083	Tulip	apartments
35	423	34602	Daisy Lea	apartments
36	436	722	Saint Elizabeth's Hospital	apartments

The website is created which displays the information of flood warning; it also contains the web-page where the donors can register themselves. To identify the website a domain name required and a server is needed to host the website. The web-page is created using PHP, which is connected to the phpMyAdmin database in backend, to store the donor's information as shown in "Figure 10". In order to send SMS to inform the donors about the flood victims and encourage them to come forward and help the flood victims by donating their donations, nearby donation centers were to be set up by non-government organizations. In this way this website acts as a mediator to connect the donors with the non-profit organizations and provides the facility to help the flood victims.

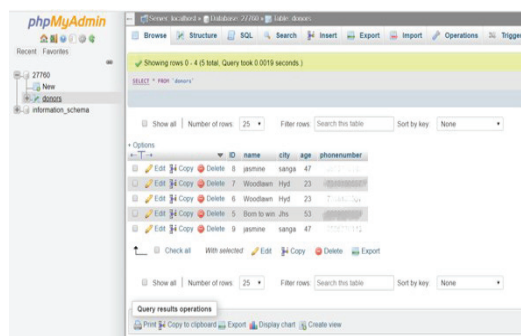


Figure 10. Donor's information is stored in the database.

When the flood warning is released the donors are send a personalized SMS asking them to help the flood victims by providing their donations to the victims. To automate this work as it is very time consuming manually, a device is created dedicated to send SMS by using Arduinio nano, which is used to send commands to the GSM module as shown in "Figure 11".



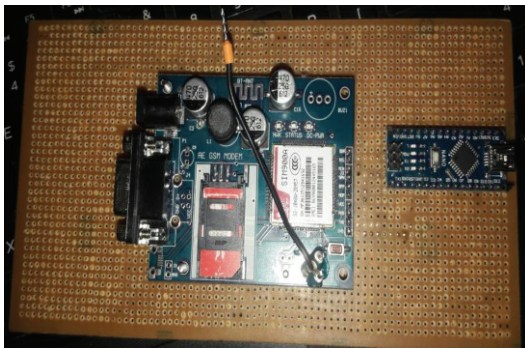


Figure 11. GSM based Device that sends SMS.

This flood warning system uses DEM of 90 meters accuracy to create a static model of sinks and identifies the buildings having inundation risk which is very accurate. It also takes GPM IMERG data having 0.1 arc seconds of accuracy i.e. 11 kilometers. This data helps to study the impact of rain on the Mumbai floods, the direction of flow of flood water, where the water gets accumulated and the pour points with respect to the falling rain. The models are automated using python script which takes very less time to execute as soon as the half-hourly averaged rainfall data is available as input.

The existing flood warning system by CWC releases flood warning, district wise [16] as it is accurate in providing the information regarding the districts only, but more accurate system helps the flood victims a lot more such as this work which produces flood warning as per buildings.

The existing rain gauge based flood warning system [17] has less accuracy than this work as it can produce flood warning up to street level, which is good but not much accurate. With rain gauge system the accuracy can be improved by deploying more number of rain gauges which is not much feasible. This work also overcomes the limitation of rain gauges as it takes the remote sensed rain data to monitor the formation of flood and produce a flood warning.

## V. CONCLUSIONS

Flood is the most devastating natural disaster in India. The flood inundation warning system should be capable of accurately mapping the effect of flood over a region. The GIS model is produced, which identifies the sinks in different regions and maps it according to the buildings constructed in that area. This gives us the information about affected buildings. Their fill up value is calculated based on the sink volume and the watershed area. The buildings constructed within the sink area are pronounced as buildings having flood-risk as these areas have no outpour till the flood water will reach the level of their pour-point. These kinds of buildings are determined. With the help of near-real time rain data through remote sensing the outpour time of the inundated areas are calculated and the flood warning is released to the nearby places. Hence, an accurate flood inundation warning up to buildings level is released.

The flood relief system is developed based on the website which registers the concerned donors for the flood relief and this data is stored in the database. From here the GSM module, controlled by Arduino nano sends the donors the flood information through SMS, even before the flood inundation starts the authorities are equipped with donations which are necessary for the victims.

In future this system can be improved by using the précised rainfall prediction data with this model to get more accuracy also more accurate DEM data and remote sensed data from aircrafts or satellite with high accuracy can be used.

## REFERENCES

- [1] EMDAT (2019): OFDA/CRED International Disaster Database, Université catholique de Louvain – Brussels – Belgium.
- [2] T.N. Krishnamurti."Indian monsoon" Encyclopædia Britannica. Encyclopædia Britannica, inc. October 12, 2015.
- [3] T Thomas."Mumbai a global financial centre? Of course!" Reddif. November 18, 2008.
- [4] Mangroves for coastal defence, 2014 Wetlands International and The Nature Conservancy.
- [5] The Times of India."Mumbai rains: Misery all around, BMC says the situation is 'exceptional'". August 30, 2017.
- [6] Millions Suffer in Indian Monsoon, BBC News, 1 August 2005.
- [7] Rain Brings Mumbai to a Halt, Rescue Teams Deployed, The Hindu, 5 July 2006.
- [8] ArcGIS for Developers."What is ArcGIS?".Esri <https://developers.arcgis.com/labs/what-is-arcgis/>
- [9] Dadasaheb K. Mane (2013). Disaster Flood Alert System Using Ultrasonic Sensor. International Journal of Engineering Research & Technology (IJERT). Vol. 2 Issue 1, January-2013.
- [10] Azid, S. & Sharma, Bibhya & Raghuiwaiya, Krishna & Chand, A. & Prasad, S. & Jacquier, A. (2015). SMS based flood monitoring and early warning system. ARPN Journal of Engineering and Applied Sciences. 10. 6387-6391.
- [11] Khalaf, Mohamed. (2011). Flood Detection using Sensor Network and Notification via SMS and Public Network.
- [12] E. Devaraj Sheshu, N. Manjunath, S. Karthik and U. Akash, "Implementation of Flood Warning System using IoT," 2018 Second International Conference on Green Computing and Internet of Things (ICGCIoT), Bangalore, India, 2018, pp. 445-448, doi: 10.1109/ICGCIoT.2018.8753019.
- [13] Carbone, Marco & Garofalo, Giuseppina & Tomei, G. & Piro, Patrizia. (2014). Storm Tracking based on Rain Gauges for Flooding Control in Urban Areas. Procedia Engineering. 70. 256–265. 10.1016/j.proeng.2014.02.029.
- [14] Sajal Kumar Adhikary, Abdullah Gokhan Yilmaz and Nitin Muttli Hydrol. Process. 29, 2582–2599 (2015) Hydrological Processes published by John Wiley & Sons Ltd. Optimal design of rain gauge network in the Middle Yarra River catchment, Australia DOI: 10.1002/hyp.10389.
- [15] Keighobad Jafarzadegan, Venkatesh Merwade A DEM-based approach for large-scale floodplain mapping in ungauged watersheds. <https://doi.org/10.1016/j.jhydrol.2017.04.053>.
- [16] Central Water Commission."Flood Forecasting/ Hydrological Observation"<http://cwc.gov.in/flood-forecasting-hydrological>.
- [17] E. B. Panganiban and J. C. Dela Cruz, "Rain water level information with flood warning system using flat clustering predictive technique," TENCON 2017 - 2017 IEEE Region 10 Conference, Penang, 2017, pp. 727-732, doi: 10.1109/TENCON.2017.8227956.

# Fast-Converging Speed and Zero Oscillation MPPT Method for PV system

Dr.G.Sree Lakshmi<sup>1</sup> and Dr. S. Harivardhagini<sup>2</sup>

<sup>1</sup>Professor, CVR College of Engineering/EEE Department, Hyderabad, India

Email: sreelakshmisampath@gmail.com

<sup>2</sup>Professor, CVR College of Engineering/EIE Department, Hyderabad, India

Email: harivardhagini@gmail.com

**Abstract:** This paper proposes Photovoltaic (PV) system with Maximum Power Point Tracking (MPPT). The DC-DC boost converter is used for DC loads. The PV panels are simulated in a circuit-based model and are proposed to evaluate and analyze the electrical behavior of a PV panel concerning the change in environmental conditions like irradiance and temperature. Different types of algorithms and switches are used in MPPT techniques depending on the operating conditions of the array. Perturb and Observe (P&O) is the basic MPPT method, Incremental Conductance Method is another MPPT method and Conventional Beta MPPT method is the one used in this paper. The Conventional Beta Method ensures higher efficiency in terms of tracking time, power loss, voltage and it can also further reduce the oscillations around the MPP of a PV panel under steady-state conditions. The improved Beta MPPT method achieves all the objectives of MPPT in eliminating the oscillations around the PV power systems. A DC-DC boost converter is used to get constant DC voltage output by changing DC panel voltage and hence duty cycle of the converter is calculated accordingly. The proposed method is simulated using MATLAB/SIMULINK and the results are presented.

**Index Terms:** DC-DC Boost Converter, Perturb and Observe Algorithm (P&O), Incremental Conductance Algorithm (INC), Conventional Beta Method, Maximum Power Point Tracking (MPPT), Photovoltaic (PV) system, Solar PV module, Zero oscillation, and fast converging speed.

## I. INTRODUCTION

Photovoltaic (PV) [1] frameworks have been used for a long time. Today, with the emphasis and prominence on greener wellsprings of intensity, PV has turned into a critical intensity for a wide-ranging variety of utilizations. Enhancement in changing over light vitality into electrical vitality and the cost decreases has made this development. Indeed, even with higher productivity and lower cost, the objective stays to amplify the power from the PV framework under different lighting conditions. Photovoltaic (PV) energy is gaining popularity and regarded as one of the most important sustainable energy sources in the recent times [2]. The photovoltaic energy is a spotless vitality, with a long life expectancy and a high firm quality. In this way, it can be considered as a standout amongst the most practical of sustainable power sources. Solar cells are the essential parts of photovoltaic panels. Most of them are produced by using

silicon even though various materials are additionally utilized. Solar-powered cells exploit the photoelectric impact: the capacity of a few semiconductors to change over electromagnetic radiation straightforwardly into electrical current. In other words, the Photovoltaic (PV) effect is the conversion of sunlight energy into electricity. The basic component of a photovoltaic system is the photovoltaic cell. These cells are designed to form a photovoltaic panel and are grouped to form a photovoltaic array [3]-[5].

The solar-powered cell V-I characteristics are nonlinear and alter with light and temperature. The output power of the PV system changes with changes in irradiation and temperature. Therefore, a maximum power tracking algorithm is needed to extract maximum output power from the PV system. There is a novel point on the V-I or V-P bend, called the Maximum Power Point (MPP), at which the whole PV framework works with most extreme ability [6]-[7]. The area of the MPP is not known, however, it can be found, either through figuring models or by seeking calculations. Accordingly, Maximum Power Point Tracking (MPPT) strategies are expected to keep up the PV working point at its MPP. Many maximum power point tracking techniques have been proposed, such as Perturb and Observe method, Incremental Conductance Method, Conventional Beta method, and proposed method. These methods vary in their simplicity, convergence speed, and hardware implementation. Depending upon the performance in steady and transient stages, the proposed method gives higher performance when compared to other methods [8]-[10]. In this paper, a PV array is modeled in MATLAB/ SIMULINK environment and peak power is tracked using the proposed MPPT technique. The proposed method is simulated in a circuit-based approach in addition to this a DC-DC boost converter is also simulated and the duty cycle of the converter is derived according to the maximum power point determined by the MPP tracker. The goal is to achieve a constant DC output voltage from the converter to feed the DC load.

## II. SYSTEM CONFIGURATION

A sun-powered cell essentially is a p-n semiconductor intersection. At the point when presented to light, a DC is produced. The produced current differs straight with the sun-powered irradiance. The amount of radiation falling on a Solar

based cell alters over daylight directly to DC control. Thus, the Photovoltaic cell present in the PV panel creates power from the sun. PV board work under the phenomenon of photoelectric impact. Figure 1 shows the cross-section of a PV cell. At a point where the sun-based cell is accessible to daylight, it changes over sun-powered vitality into electrical vitality. The framework arrangement for this theme is as indicated in Figure 2. Here the PV exhibit is a mix of arrangement and parallels sun powered cells. This exhibit builds up the power from the sun-oriented vitality straightforwardly and it will be switched by depending upon the temperature and sun-based irradiances.

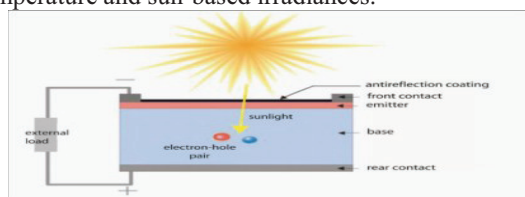


Figure 1. Cross-Section of a PV Cell

### A. Components of a Solar PV Panel

A typical solar PV system consists of a solar panel, charge controller, batteries, inverter, and the load. Figure 2. shows the block diagram of such a system.

### B. Charge Controller

At a point where the battery is combined into a framework, then there will be a need for a charge controller. A charge controller is used to control the unverifiable voltage developed in the system. On a fine bright day, the sunlight-based cells create more voltage which results in reducing the battery harm, and the power created doesn't run back to the solar panels overnight resulting in draining the batteries. Some charge controllers are available with additional capabilities, like lighting and load control, but managing the power is its primary job. A solar charge controller is available in two different technologies, PWM and MPPT. The performance in a system is very different from each other.

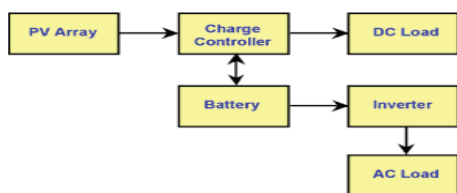


Figure 2. Components Grid

An MPPT charge controller is more expensive than a PWM charge controller, and it is often worth it to pay the extra money. A charge controller keeps up the adjust in charging the battery.

### C. Batteries

Batteries are used to store the charges. The stored chemical energy is directly converted into electrical energy by a battery that consists of one or more electrochemical cells. The electrons flow from the negative to the positive terminal,

which injects an electrical current when an external load is connected. To store the charges, batteries are utilized. Batteries are used to store energy when excessive generation is taking place and give back to grid during peak loads. They are playing a very important role in Smart Grid, as they can charge during periods of low demand and feed their stored energy into the grid when demand is high. There are abundant types of batteries available in the market. For the most part, utilized batteries are nickel/cadmium batteries.

### D. Inverter

An inverter is an electrical device that converts direct current (DC) to alternating current (AC); the converted AC can be at any required voltage and frequency with the use of appropriate transformers, switching, and control circuits. Solid-state inverters have no moving parts and are used in a wide range of applications, from small switching power supplies in computers, to large electric utility high-voltage direct current applications that transport bulk power. Inverters are commonly used to supply AC power from DC sources such as solar panels or batteries. Sun oriented board produce dc power, yet the greater part of the family unit and mechanical apparatuses require air conditioning current.

### E. Characteristics of a Solar Module

When the sunlight is incident on the cell of the solar panel, some of the photons present in that area are absorbed by the solar cells. Some of the absorbed photons will have energy greater than the energy gap between the valence band and conduction band in the semiconductor crystal. Hence, one valence electron gets energy from one photon and becomes excited and jumps out from the bond and creates one electron-hole pair. These electrons and holes of e-h pairs are called light-generated electrons and holes. The light-generated electrons near the p-n junction are migrated to the n-type side of the junction due to the electrostatic force of the field across the junction. Similarly, the light-generated holes created near the junction are migrated to the p-type side of the junction due to the same electrostatic force. In this way, a potential difference is established between two sides of the cell and if these two sides are connected by an external circuit current will start flowing from positive to the negative terminal of the solar cell. This was a basic working principle of a solar cell. While choosing a solar cell for a specific project, it is essential to know the rating of a solar panel. These parameters tell us how efficiently a solar cell can convert the light to electricity.

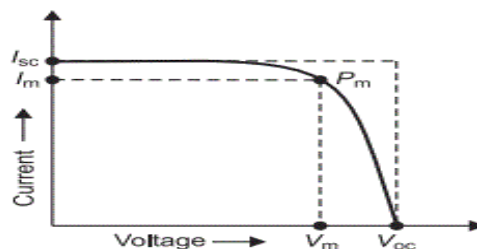


Figure 3. V-I Characteristics of Solar Cell

**F. Solar Module Parameters**

- Module type:user defined
- Maximum power:60W
- Voltage at maximum power:17.1V
- Current at maximum power: 3.5A
- Open-circuit voltage:21.1V
- Short-circuit current:3.8A
- Temperature coefficient of  $V_{oc}$ : $-0.1mV/^{\circ}C$
- Temperature coefficient of  $I_{sc}$ :  $0.065\%/^{\circ}C$

**III. ROLE OF MPPT IN SOLAR POWER SYSTEM**

Photovoltaic power generation is one of the major keys to resolve energy demand. Photovoltaic systems often use the MPPT technique to uninterruptedly pass on the most lifted possible capacity to the load whenever there is a change in the variation of division and temperature. The Power generated through the PV system has its advantages like pollution-free and cheap.

PV modules still have large low-change efficiency; in this way, controlling the most extraordinary power point following (MPPT) for the sun arranged show is essential in a PV structure. The Maximum Power Point Tracking (MPPT) is a methodology used as a part of electronic circuits used to isolate the most extraordinary essentialness from the Photovoltaic (PV) Systems. Nowadays, the PV control age has expanded more widely due to its different purposes of enthusiasm, to enhance the vitality productivity; it is authoritative to work the PV framework consistently at its most extreme power point. Abundant maximum extreme power point Tracking (MPPT) strategies are available and proposed different techniques for obtaining the greatest power point. In any case, among the accessible method’s adequate similar examination especially with variable ecological conditions is not finished. A sun-powered cell essentially is a p-n semiconductor intersection. At the point when presented to light, a direct current is produced. The produced current differs straight with the sun-powered irradiance.

**A. PV Equivalent Circuit**

Solar cells are connected in series and parallel to set up the solar array. Solar cells will produce dc voltage when it is exposed to sunlight. Solar cells can be regarded as a non-linear current source. Its generated current depends on the characteristic of material, age of solar cell, irradiation and cell temperature.

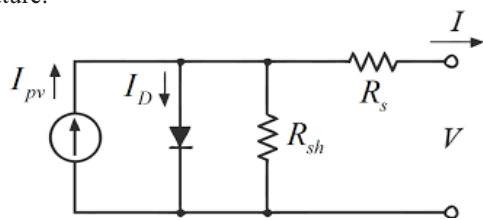


Figure4. Equivalent circuit of Solar Panel

The fundamental equation that describes the I-V characteristics of the PV model is given by the equation

$$I = I_L - I_0 \left( e^{\frac{q(V-IR_s)}{AKT}} - 1 \right) - \frac{V + IR_s}{R_{sh}}$$

This equation shows the dependence of PV current on temperature and hence the dependence of power drawn from the PV array.

**B.PV System with MPPT control**

The MPPT method is extensively used in order to maximize power control extraction irrespective of the environmental conditions. PV bodies exist in various configurations with respect to their relationship to inverter frameworks, outer lattices, battery banks, or other electrical burdens. Nevertheless, a definitive goal of the sun powered power; however, the crucial issue tended to MPPT is that the productivity of intensity exchange from the sun-based cell depends upon both the measure of daylight falling on the sun-oriented boards and the electrical characteristics of the mound.

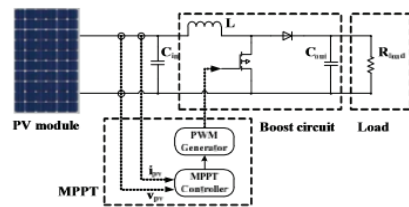


Figure 5. PV array with MPPT control

As the measure of daylight shifts, the heap trademark that is the characteristics of the load which gives the maximum energy transfer effectiveness changes, so the proficiency of the framework is upgraded when the heap trademark changes to keep the power exchange at most astounding productivity. This heap trademark is known as the greatest power point (MPP) and MPPT is the way toward discovering this point and keeping the heap trademark there. Electrical circuits can be intended to introduce self-assertive burdens to the photovoltaic cells and after that change over the voltage, current, or recurrence to suit different gadgets or frameworks, and MPPT takes care of the issue of picking the best load to be exhibited to the cells to get the most usable power out.

**C. Methodology of Peak Power Tracking**

MPP trackers are utilized to draw most extreme accessible power over the PV board for a given ecological condition. It can be Electro-Mechanical apparatuses or Electronics hardware. In this undertaking the MPP is followed by circuit-based re-enactment to guarantee the activity of the PV source at greatest power amid various natural conditions.

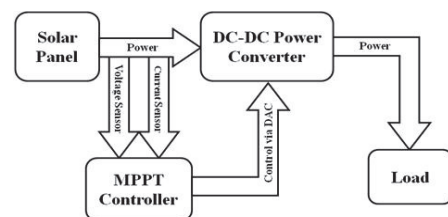


Figure 6. Proposed system for MPP Tracking with Boost Converter

The point of MPPT is to control the real working voltage of PV board to the voltage at MPP, for this reason, MPPT modifies the yield intensity of inverter or DC converter as per the heap for the framework. If the PV yield voltage is higher than MPP voltage, at that point exchanged capacity to the heap or system is expanded, else, it is decreased.

**D. Modelling of a DC-DC Boost Converter**

Boost converter steps up the input voltage magnitude to a required output voltage magnitude without the use of a transformer. The main components of a boost converter are an inductor, a diode and a high frequency switch. These in a coordinated manner supply power to the load at a voltage greater than the input voltage magnitude. The control strategy lies in the manipulation of the duty cycle of the switch which causes the voltage change. The circuit diagram for a lift converter is shown in Figure 7. At the point when switch q is shut, the information source charges up the inductor while diode D is turned around one-sided to give disengagement between the information and the output of the converter. At the point when the switch is opened, vitality is put away in the inductor and the power supply is exchanged to the heap.

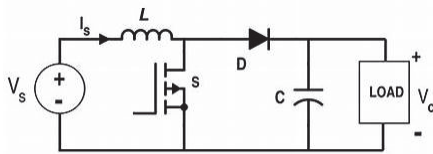


Figure 7. Circuit diagram for DC-DC Boost Converter

The output voltages are determined by the following equation

$$\frac{V_{out}}{V_{in}} = \frac{1}{(1 - D)}$$

Where,  $V_{out}$ : Output voltage of the converter

$V_{in}$ : Input voltage of the converter

D: Duty cycle of the switch 's'

The output current is given by the following equation assuming the converter as ideal.

$$I_{out} = I_{in} \times (1 - D)$$

From the above equations it deduced that:

$$\frac{V_{out}}{I_{out}} = \frac{V_{in}(1 - D)}{I_{in}(1 - D^2)}$$

**E. Effects of Temperature**

Another imperative differentiator in sun powered PV execution, particularly in hot atmospheres, is the temperature coefficient of intensity. PV cell execution decays as cell temperature rises. For instance, in brilliant daylight, cell temperatures in Singapore can reach more than 70°C, though PV modules are evaluated at a cell temperature of 25°C. The misfortune in influence yield at 70°C is in this manner estimated as  $(70 - 25) \times$  temperature coefficient. Most thin film innovations have a lower negative temperature coefficient contrasted with crystalline advancements. At the end of the

day, they have a tendency to lose less of their appraised limit as temperature rises.

**IV. MPPT TECHNIQUES**

**A. Perturb and Observe Method**

Perturb and Observe method results in top-level efficiency, provided that a proper predictive and adaptive hill climbing strategy is adopted. The perturb and observe (P&O) method is the most popularly used algorithm that goes to the period of the direct MPPT techniques; it is characterized by the addition of a slight perturbation into the system, whose properties are used to determine the operating point near the MPP. In the P&O method, the MPPT algorithm can be calculated by the PV output power and the power change obtained by sampling both the PV current and voltage. The tracker tracks by intermittently increasing or decreasing the solar voltage so that the MPP is tracked irrespective of the level of irradiance, changes in temperature, degradation, and aging, thus ensures high robustness and reliability.

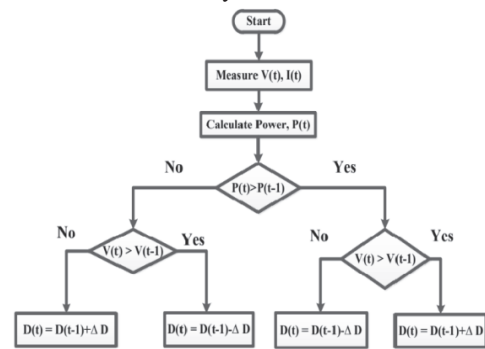


Figure 8. Flowchart for P&O Method

The P&O method can be implemented by the PV operating point which is perturbed periodically by the change in PV source voltage terminals. Subsequently before and after the perturbation each perturbation, the control algorithm compares the values of the power fed by the PV source. After each perturbation, the PV power has increased and the operating point has been moved towards the MPP; therefore, the successive perturbation imposed to the voltage will have the same sign as the previous one. If after a voltage perturbation the power drawn from the PV array decreases, then the operating point has been moved away from the MPP. Therefore, the sign of the subsequent voltage perturbation is reversed. The switching converter is used to drive the perturbation of the operating voltage of the PV generator. The input voltage and input current obtained from the PV array system can be used to compute the instantaneous power of the given system. The maximum power point (MPP) is known and the duty ratio of the converter varies in accordance with the MPPT algorithm. The duty ratio is varied in such a way that the input power delivered to the converter will almost be equal to the power delivered to the load. Other methods derived by the P&O approach are the incremental conductance(INC) and the conventional beta method. Such methods differ from the

P&O approach either for the variable observed or for the type of perturbation. All these algorithms have the advantage of being independent of the knowledge of the PV generator characteristics.

**B. Incremental Conductance**

Incremental conductance is one of the important techniques in the MPPT system because of its higher steady-state accuracy and environmental adaptability it is widely implemented tracked control strategy. The main disadvantage of the ‘Perturb and Observe Method’ is to track the peak power of the solar panel under the fast-varying atmospheric condition. This disadvantage can be overcome by using Incremental Conductance method.

In incremental conductance method the array terminal voltage is always adjusted according to the MPP voltage. It is based on the incremental and instantaneous conductance of the PV module. The IC can determine that the MPPT has reached the MPP and stop perturbing the operating point. If this condition is not met, the direction in which the MPPT operating point must be perturbed can be calculated using the relationship between  $dI/dV$  and  $-I/V$ .

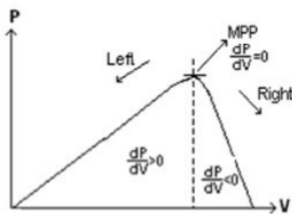


Figure 9. Incremental Conductance Method on a P-V Curve of Solar Module

$$dI/dV = -I/V \text{ at MPP} \dots (1)$$

$$dI/dV > -I/V \text{ left of MPP} \dots (2)$$

$$dI/dV < -I/V \text{ right of MPP} \dots (3)$$

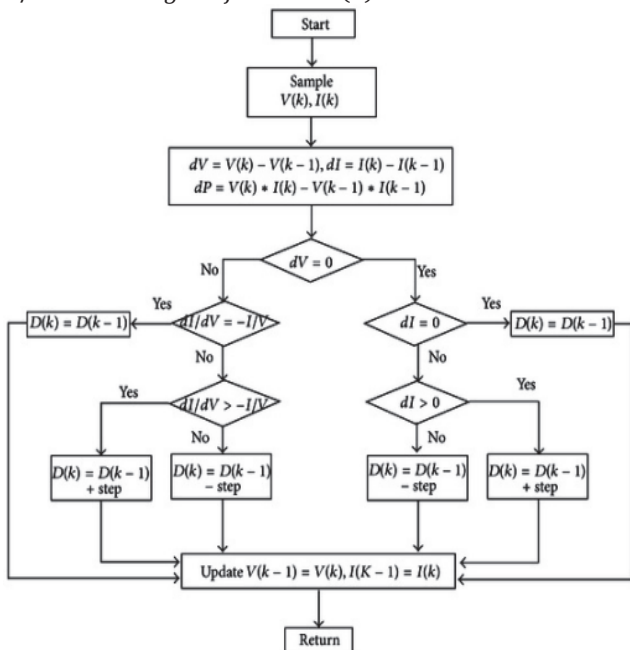


Figure 10. Flowchart for Incremental Conductance Method

This relationship is derived from the fact that  $dI/dV$  is negative when the MPPT is to the right of the MPP and positive when it is to the left of the MPP. This algorithm has advantages over P&O in that it can determine when the MPPT has reached the MPP, where P&O oscillates around the MPP. Also, incremental conductance can track rapidly increasing and decreasing irradiance conditions with higher accuracy than P and O.

**C. Conventional Beta Method**

The Conventional Beta method was first proposed by Jain and Agarwal the basic principle of conventional beta method is to track an intermediate variable  $\beta_a$  irrespective of the change in power. The intermediate variable  $\beta_a$  can be expressed by the following equation

$$\beta_a = \ln(I_{pv}/V_{pv}) - c \times V_{pv}$$

where  $V_{pv}$  are the PV module output voltage and  $I_{pv}$  are the output current respectively. There is a diode constant ‘c’ which can be expressed as

$$c = q/(N_s AKT)$$

where q is the electron charge  $1.602 \times 10^{-19}C$ , A is the diode ideality factor, K is Boltzmann constant  $1.38 \times 10^{-23}J/K$ , T (in Kelvin) is the temperature of the p-n junction, and  $N_s$  is cell number of the PV module.

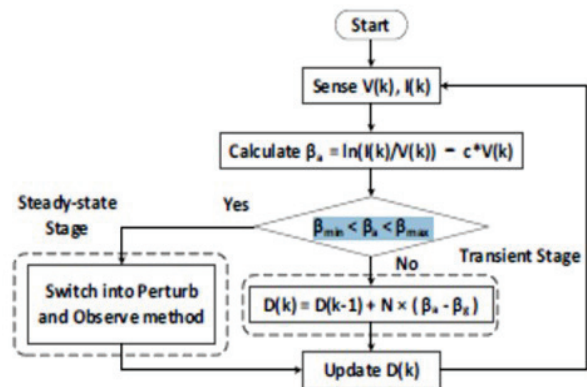


Figure 11. Flowchart of Conventional Beta Method

This method can be implemented in two stages: that is the transient stage and the steady-state stage. These two stages adapt to the variable step and fixed step respectively. In the implementation of the Beta method, the range of  $\beta_{min}$  and  $\beta_{max}$  must be identified and, the algorithm calculates  $\beta_g$  itself. Firstly, the voltage and current of a PV module output are measured, and then the actual values of  $\beta_a$  are calculated continuously. If the value of  $\beta_a$  is within the limits of  $(\beta_{min}, \beta_{max})$ , the Beta method switches into steady-state stage and the P&O method will be implemented, otherwise the Beta method switches into the transient stage. In the transient stage, a guiding parameter  $\beta_g$  is adopted which is used in calculating the variable step size  $\Delta D$ , which can be expressed as:

$$\Delta D = N \times (\beta_a - \beta_g)$$

where N is the scaling factor which indicates that the range of the parameter  $\beta$ ,  $(\beta_{min}, \beta_{max})$  and parameter  $\beta_g$ , needs to be

identified. The range of the parameter  $\beta$  depends on the environmental conditions of the PV module, such as the irradiance and temperature.

In the conventional Beta method, the converging speed for the rapid change in the environmental conditions depends on the scaling factor. The performance of this method can be optimized by identifying the range of the parameter  $\beta$  for various environmental conditions; furthermore, the scaling factor can be optimized through the parameter sweeping. Though, the optimal scaling factor subsequent from this process will be suitable for only limited operating conditions, additionally, the oscillations can still be observed in the steady state. Thus, there is a need for the potential of Beta method to further optimization for both steady-state and dynamic operations.

#### D. Proposed Beta Method

The Proposed MPPT method can be implemented by using two stages: 1) the Adaptive Scaling Factor Beta (ASF-Beta) which is used for transient state, and 2) the Zero Oscillations Perturb and Observe (ZOPO) which is used for the steady state. The flow chart of a proposed beta method is shown below. It consists of the Adaptive Scaling Factor Beta (ASF-Beta) as shown in branches from (A) to (D), and the Zero Oscillations Perturb and Observe (ZOPO) as shown in branches (E) to (H).

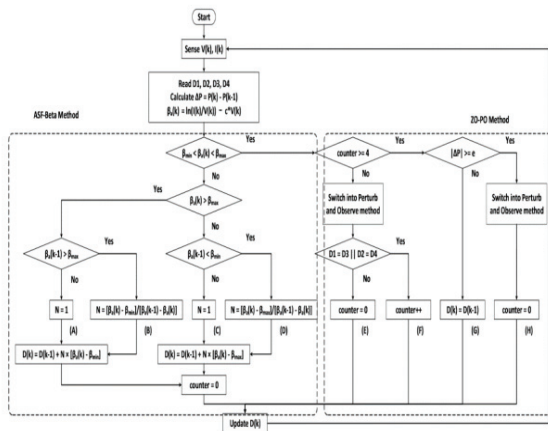


Figure 12. Flowchart of Proposed Beta Method

In the Conventional Beta method, the ASF-Beta method implements an adaptive scaling factor instead using the fixed scaling factor. The process to regulate the optimal scaling factor is removed and the guiding parameter  $\beta_g$  is eliminated in the practical implementation. Thus, the ASF-Beta becomes less dependent on the PV system. Also, the step size is automatically updated in the changes of parameter  $\beta$  due to the environmental changes. Thus, the proposed method can attain a faster tracking convergence speed when compared to the conventional Beta method. Under the steady-state operation The Zero Oscillations Perturb and Observe (ZOPO) method identifies the middle point of the three-level perturbations. Therefore, the steady-state oscillations can be eliminated,

which further helps in improving the tracking efficiency. By comparison with the P&O method and the variable step size incremental conductance (VSSINC) method, the main advantages of the proposed method are (1) By totally eradicating oscillations there will be high steady-state tracking efficiency; (2) by employing an adaptive scaling factor the dynamic efficiency of the system is improved; (3) the wrong step change instigated by the rapid change in the irradiance can be eliminated.

The PV system is modeled and simulated in MATLAB. In this model a PV panel of 10 cells per module having a maximum power of 59.85W has been simulated with employment of both the ASF-BETA method and ZOPO method for a quite efficient MPP track. The duty cycle pulses have been fed to the DC-DC boost converter in accordance with the MPP value.

By comparing the results of all MPPT the proposed method shows the fastest method results among these methods to locate the MPP while the P&O method is the slowest one in all cases. The VSSINC method is faster than the conventional Beta method when the irradiance is increased. Contrarily, the conventional Beta method is faster than the VSSINC method when the irradiance or resistance is decreased with these MPPT methods under the different irradiance levels. Due to a fixed step size, the power loss for the P&O method and the conventional Beta method are almost the same, which are higher than other methods. The power loss for the VSSINC method is reduced compared with P&O method and the conventional Beta method. Since the proposed method eliminates totally the oscillations, the power loss of this method is the smallest one under all irradiance levels.

## V. SIMULINK MODEL AND RESULTS

### A. Simulation results of P&O

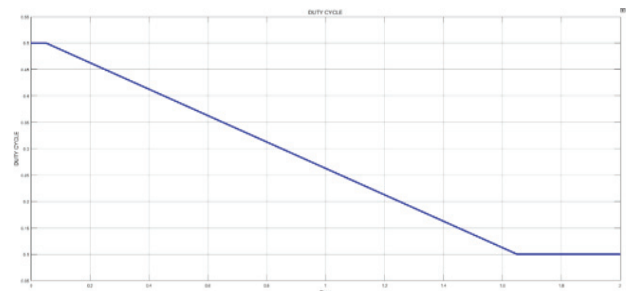


Figure 13. Simulation of P&O and its duty cycle (Secs)

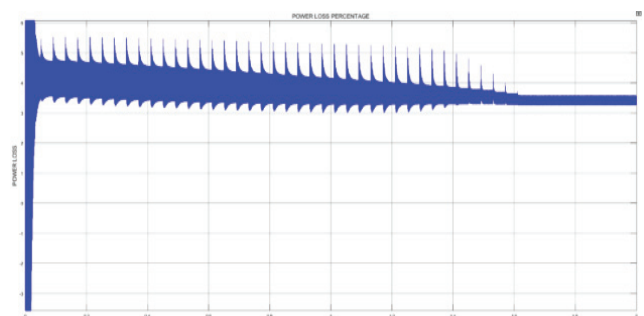


Figure 14. Simulation of MPPT P&O and their Power Loss (Watts)

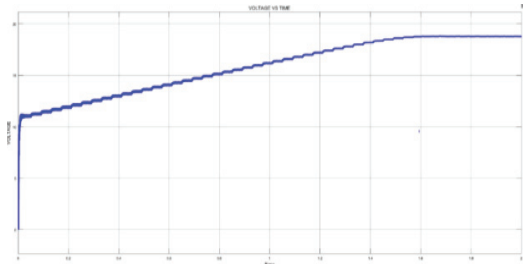


Figure 15. Simulation of MPPT P&O and Voltage vs Time

The P&O method simulation is done in MATLAB under various scenarios and has been analyzed including the variation of irradiance and different load variation conditions

At an irradiance of  $500\text{w/m}^2$  and a resistance of  $5\text{ohms}$  the power loss is 4% and the tracking time taken by the system is 1.6sec. At an irradiance of  $600\text{w/m}^2$  and a resistance of  $5\text{ohms}$  the power loss is 4.5% and the tracking time taken by the system is 1.65 sec. At an irradiance of  $800\text{w/m}^2$  and a resistance of  $5\text{ohms}$  the power loss is 6% and the tracking time taken by the system is 1.62 sec.

*B. Simulation results of INC*

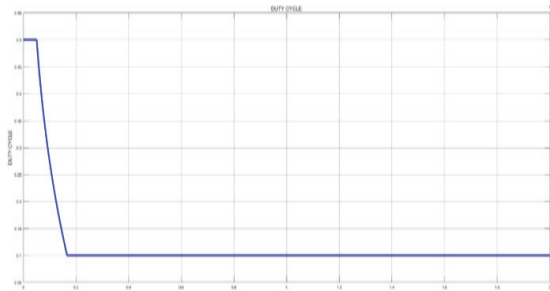


Figure 16. Simulation of P&O and its duty cycle

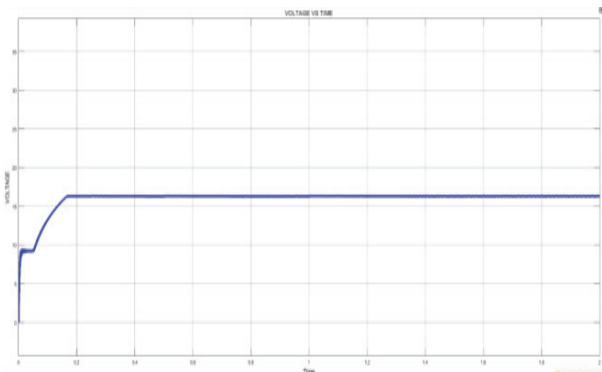


Figure 17. Simulation of MPPT INC and Voltage vs Time

The INC method simulation is done in MATLAB under Various scenarios and has been analyzed including the variation of irradiance and different load variation conditions

At an irradiance of  $500\text{w/m}^2$  and a resistance of  $5\text{ohms}$  the power loss is 3.1% and the tracking time taken by the system is 1.17sec. At an irradiance of  $600\text{w/m}^2$  and a resistance of  $5\text{ohms}$  the power loss is 3.5% and the tracking time taken by the system is 0.65 sec. At an irradiance temperature of

$800\text{w/m}^2$  and a resistance of  $5\text{ohms}$  the power loss is 3.5% and the tracking time taken by the system is 0.62 sec.

*C. Simulation results of Conventional Beta Method*

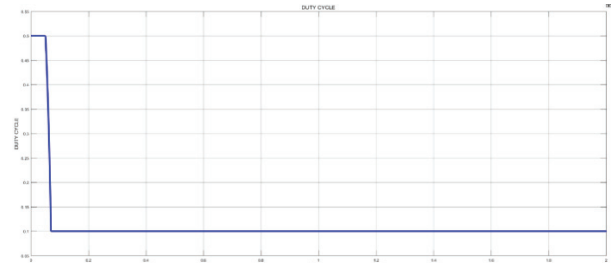


Figure 18. Simulation of Conventional Beta Method and its duty cycle

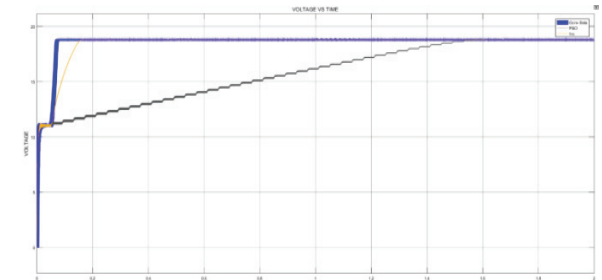


Figure 19. Simulation of Conventional Beta Method and Voltage vs Time

The conventional Beta method simulation is done in MATLAB under Various scenarios and has been analyzed including the variation of irradiance and different load variation conditions. At an irradiance of  $500\text{w/m}^2$  and a resistance of  $5\text{ohms}$  the power loss is 3.6% and the tracking time taken by the system is 0.08sec. At an irradiance of  $600\text{w/m}^2$  and a resistance of  $5\text{ohms}$  the power loss is 3.6% and the tracking time taken by the system is 0.76 sec. At an irradiance of  $800\text{w/m}^2$  and a resistance of  $5\text{ohms}$  the power loss is 3% and the tracking time taken by the system is 0.75 sec.

*D. Simulation results of Proposed Method*

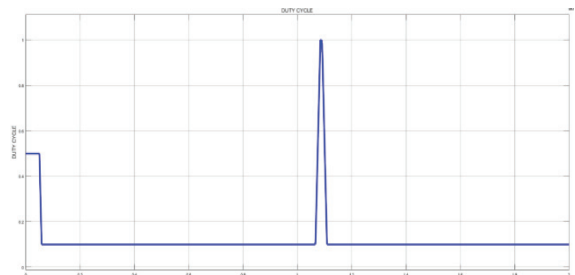


Figure 20. Simulation of Proposed Method and its duty cycle



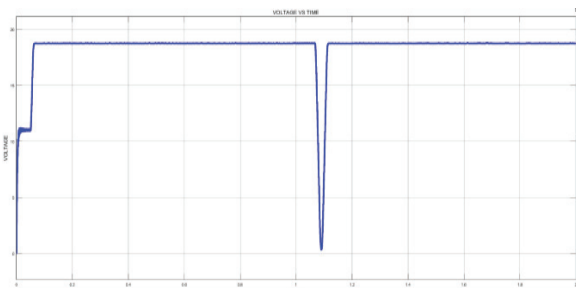


Figure 21. Simulation of Conventional Beta Method and Voltage vs Time

The Proposed Beta method simulations are done in MATLAB under Various scenarios and have been analyzed including the variation of irradiance and different load variation conditions. At an irradiance of  $500\text{w/m}^2$  and a resistance of  $5\text{ohms}$  the power loss is  $3.2\%$  and the tracking time taken by the system is  $0.07\text{sec}$ . At an irradiance of  $600\text{w/m}^2$  and a resistance of  $5\text{ohms}$  the power loss is  $3.3\%$  and the tracking time taken by the system is  $0.065\text{sec}$ . At an irradiance of  $800\text{w/m}^2$  and a resistance of  $5\text{ohms}$  the power loss is  $3.2\%$  and the tracking time taken by the system is  $0.065\text{sec}$ .

## VI. COMPARISON OF VARIOUS MPPT METHODS

### A. Power Loss

power loss	500	600	800
P&O	4	4.5	6
INC	3.1	3.5	3.5
Conv	3.6	3.6	3
Prop	3.2	3.3	3.2

### B. Tracking Time

tracking time	500	600	800
P&O	1.6	1.65	1.62
INC	1.17	0.16	0.16
Conv	0.08	0.076	0.075
Prop	0.07	0.065	0.065

### C. Voltage

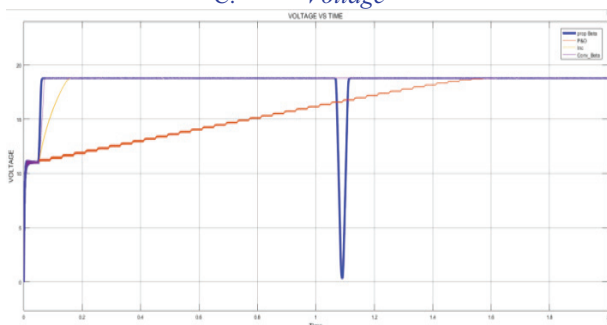


Figure 22. Simulation of MPPT Methods and their voltage (Volts)

From above all the comparison of the simulation results the proposed beta method shows higher performance by reducing the power loss and takes less tracking time.

## VII. CONCLUSIONS

The paper proposes a simple MPPT method that requires only measurements of Incremental conductance. MPPT algorithm is called Incremental conductance Method. However, by using this MPPT method we have increased the tracking efficiency. This method computes the maximum power and controls directly the extracted power from the PV. The proposed method offers different advantages which are: good tracking efficiency, response is high and well control for the extracted power.

The above MPPT method can be realized using two major stages: a) Adaptive Scaling Factor Beta (ASF-Beta) which helps in improving transient response of the system; and b) Perturb and Observe (ZOPO) which is used to eliminate steady-state errors in the system. The above methods are applied and tested under several scenarios and have been analyzed including the variation of irradiance and different load variation conditions. From the above simulation results, the higher performance of the proposed algorithm can be validated over all the other MPPT methods. From the above simulation results, it can also be demonstrated that the overall tracking speed of the proposed method is much faster when compared to other MPPT methods like P&O method, VSSINC method and conventional Beta methods. Through the transient stage, the power loss in the system can be reduced in comparison with the P&O method, VSSINC method, and conventional Beta methods due to the Zero Oscillations Perturbation and Observe method helps in reducing the steady state oscillations.

## REFERENCES

- [1] N. Femia, G. Petrone, G. Spagnuolo, and M. Vitelli, "Optimization of perturb and observe maximum power point tracking method," IEEE Trans. Power Electron., vol. 20, no. 4, pp. 963–973, Jul. 2005.
- [2] A. Safari and S. Mekhilef, "Simulation and hardware implementation of incremental conductance MPPT with direct control method using cuk converter," IEEE Trans. Ind. Electron., vol. 58, no. 4, pp. 1154–1161, Apr. 2011.
- [3] P. Lezana and G. Ortiz, "Extended operation of cascade multi-cell converters under fault condition," IEEE Trans. Ind. Electron., vol. 56, no. 7, pp. 2697–2703, Jul. 2009.
- [4] T. K. Soon and S. Mekhilef, "Modified incremental conductance MPPT algorithm to mitigate inaccurate responses under fastchanging solar irradiation level," Solar Energy, vol. 101, no. 0, pp. 333 – 342, 2014.
- [5] Q. Mei, M. Shan, L. Liu, and J. Guerrero, "A novel improved variable step-size incremental-resistance MPPT method for PV systems," IEEE Trans. Ind. Electron., vol. 58, no. 6, pp. 2427–2434, Jun. 2011
- [6] H. Yohan, S. N. Pham, Y. Taegeun, C. Kookbyung, B. KwangHyun, and K. Yong Sin, "Efficient maximum power point tracking for a distributed PV system under rapidly changing environmental conditions," IEEE Trans. Power Electron., vol. 30, no. 8, pp. 4209–4218, Aug. 2015
- [7] D. Sera, L. Mathe, T. Kerekes, S. V. Spataru, and R. Teodorescu, "On the perturb-and-observe and incremental

- conductance MPPT methods for PV Systems,” IEEE J. Photovoltaics, vol. 3, no. 3, pp. 1070–1078, Jul. 2013.
- [8] L. Xu, R. Cheng, J. Yang, “A New MPPT Technique for fast and efficient tracking under fast varying solar irradiation and load resistance,” International Journal of Photo Energy, Vol.2020, pp. 1-18.
- [9] X. Li, H. Wen, G. Chu, H. Hu, L. Jiang, "A Novel power-increment based GMPPT algorithm for PV arrays under partial shading conditions," Journal of Solar energy, vol.169, 2018, pp. 353-361.
- [10]. X. Li, H. Wen, L. Jiang, W. Xiao, Y. Du, Ch. Zhao, “An improved MPPT method for PV system with fast converging speed and zero oscillation,” IEEE Transactions on Industry, Vol 52, issue 6, 2016, pp.5050-5064.

# Design of Enhanced PLL for Single-Phase Grid Connected Transformerless Inverters

G. Janardhan<sup>1</sup>, Dr. G.N. Srinivas<sup>2</sup> and Dr. N.N.V. Surendrababu<sup>3</sup>

<sup>1</sup>Asst. Prof, CVR College of Engineering/EEE Department, Hyderabad, India  
Email: g.janardhan@cvr.ac.in

<sup>2</sup>Professor, Vice Principal, JNTUCEH/EEE Department, Hyderabad, India  
Email: gnsngns.srinivas785@gmail.com

<sup>3</sup>Professor, KIoT Wollo University/EEE Department, Ethiopia  
Email: surendrababu@ieee.org

**Abstract:** Renewable energy sources integrated with conventional sources fed grid to meet the ongoing electrical energy demands. This paper presents design of Enhanced Phase locked loop (EPLL) for single phase grid connected transformer less inverter. The knowledge of phase angle, frequency, voltage magnitude is under consideration to integrate the solar PV to single-phase grid. It is required to track exact utility voltage vector for reliable control of power to the grid. The paper also presents Simulink modeling, analysis of Enhanced PLL and compares its performance with basic phase locked loop (PLL) used.

**Index Terms:** Enhanced phase locked loop (EPLL), Transformerless inverter, single phase grid connected,

## I. INTRODUCTION

Depletion of conventional sources made an inevitable attempt to increase the percentage of renewable energy sources to be used. In this scenario the solar PV places itself on high preferred renewable energy sources, due to its simplified conversion technology [1]. As the renewable energy sources like Photo voltaic (PV) generates DC, it needs a power electronic converter to convert into AC and to feed it to grid. The converter can be DC-DC, to maintain the DC voltage at the DC link of the input of the inverter. The converter can be a DC-AC which feeds the power from PV to grid. A high frequency transformer is used in case of DC-DC converters, on DC side whereas a low frequency transformer in case of DC-AC converter on AC side. In either of the cases the transformer is used which will be integral part of the converter thus occupying space, increases the cost of the system and reduces the efficiency of the system. Thus, to reduce the cost and space occupied by the system the transformerless inverters are into practice [2]. The power electronics converters are used in the conversion of renewable energy sources from dc-dc and dc-ac. Solar PV inverters need either a high frequency transformer on dc side shown in Fig.1(a) or a low frequency transformer on ac side to provide galvanic isolation as shown in Fig.1(b). But by avoiding transformer as shown in Fig.2. efficiency of the conversion can be improved, and size of the inverter can also be reduced considerably. In view of this advantages, research on transformer less inverter has taken a quick pace. To integrate solar PV to single phase grid for low power applications, it is required to track phase angle, amplitude

and frequency of utility voltage vector and inverter output voltage. This can be done by using phase locked loop [2].

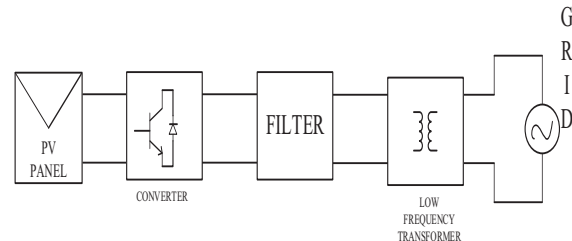


Figure 1(a). Grid connected inverter with low frequency Transformer

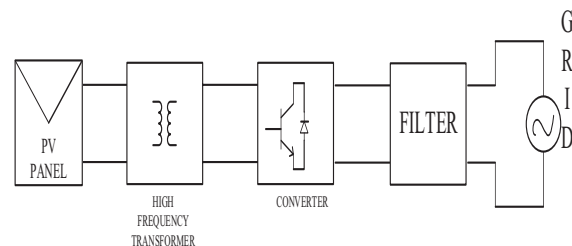


Figure 1(b). Grid connected inverter with high frequency Transformer.

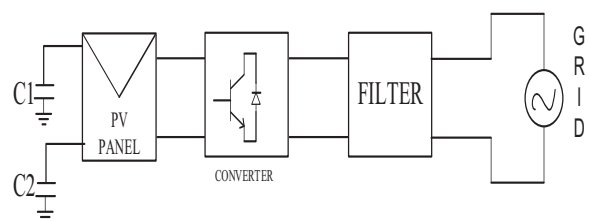


Figure 2. Transformerless Inverter.

In the grid connected inverters the output parameters like voltage amplitude, frequency and phase angle are of greater importance to inject active and reactive power to the grid. In the case if inverters are fed from solar PV it can only supply active power to the grid. To supply reactive power, it needs a distributed static compensator (DStatcom) [3]. In either of the situations to inject active and reactive power to grid decoupled controls of d-axis and q axis components of currents is employed and are controlled separately [3].

**II. PHASE LOCKED LOOP**

Phase locked loop identifies and automatically sets phase angle of a voltage or current vector generated by an inverter with that of phase angle of grid voltage or current in grid connected system. The change in frequency of inverter which is required due to change in load can be adjusted with the help of PLL [4]. Besides various other techniques of synchronization of inverter to grid phase locked loop is simple in its implementation. The Fig.3 indicates block diagram of PLL based synchronization of transformerless inverter with grid.

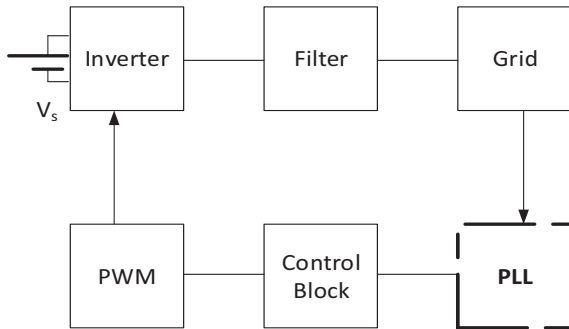


Figure 3. PLL based synchronization of transformerless inverter with grid.

The basic PLL consists of Phase detector loop filter and controller along with a voltage control oscillator as shown in Fig.4. Phase detector compares two input voltages generate an error signal that is proportional to the difference of phase angle between them. This error signal is fed to filter which will further drive voltage control Oscillator [5]. Thus, output is locked to phase at the input.

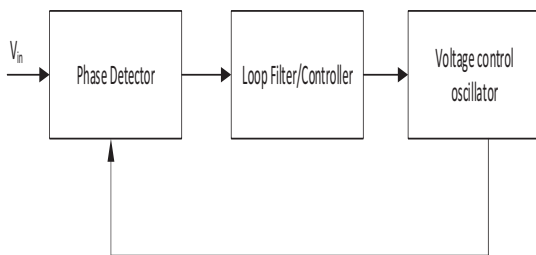


Figure 4. Block diagram of PLL.

In the literature it has been stated that three phase PLL and single phase PLL are designed with different approach. Multiple techniques of synchronization of inverter to grid are surveyed out of which inverse park based PLL is the simplest. It needs to generate a orthogonal component in single phase system unlike in three phase system, where inherently three phase system (a-b-c) can directly be converted into two phase orthogonal stationary reference frame system using Clarks transformation ( $\alpha$ - $\beta$ ). Park transformation will convert stationary reference frame to synchronously rotating reference frame which are given by the following equations [6].

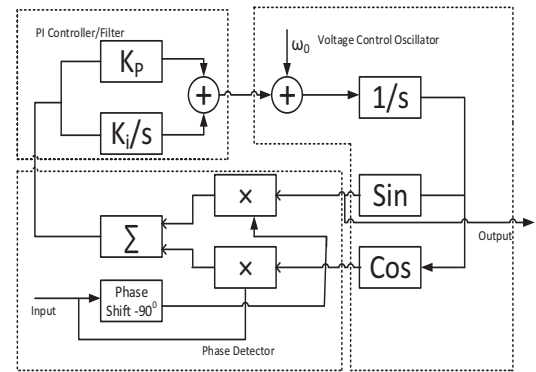


Figure 5. Mathematical modeling of PLL

Basic phase locked loop contains PI controller or filter, voltage controlled oscillator and phase detector as shown in Fig.5. The main focus of this paper is to present a comparison of basic phase locked loop structure with that of enhanced phase locked loop in terms of their performances. Enhanced phase locked loop is found to be the best option for single phase grid connected systems. Further the steady state and dynamic performance of enhanced PLL is analyzed.[8].

**III. ENHANCED PHASE LOCKED LOOP**

The EPLL overcomes the disadvantage of basic PLL i.e. double frequency error. This is done by estimating the amplitude of the input voltage or current signal with an extra loop. Besides EPLL removes double frequency error, it also gives filtered version of input quantity. In other words, EPLL not only acts as PLL but also as filter and controller which helps in direct measurement of phasor.

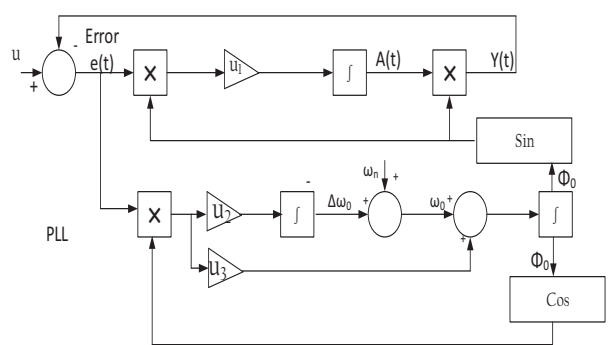


Figure 6. Block diagram of enhanced phase locked loop.

The lower portion of Fig.6 indicates basic PLL and upper loop indicates filtered input signal. Variables  $u_1$ ,  $u_2$  and  $u_3$  are positive gains to control the performance of EPLL [10].  $\Phi_0$  is estimated phase angle,  $\omega_n$  is reference frequency. In addition to constant estimate of fundamental component of input signal while the amplitude, frequency and phase are varying. It can also provide  $90^\circ$  phase shifted signal of fundamental component. Enhanced phase locked loop is best suited for single phase system whereas other techniques of

synchronization like Recursive Discrete Fourier Transform, Second order generalized integrator etc. [11].

Enhanced phase locked loop is characterized by the following equations in time domain [14].

$$A(t) = \int e(t) \cdot \sin \varphi_0(t) \cdot u_1 \cdot dt \text{----- (1)}$$

$$\Delta\omega_0(t) = \int e(t) \cdot \cos \varphi_0(t) \cdot u_2 \cdot dt \text{-----(2)}$$

$$\varphi_0(t) = \int [e(t) \cdot \cos \varphi_0(t) \cdot u_3 + \Delta\omega_0(t) + \omega_n] \cdot dt \text{-- (3)}$$

The error signal  $e(t)$  is the distortion of the input signal [12].

#### IV. SIMULINK MODELLING

This section describes the Matlab Simulink modeling of basic PLL and enhanced PLL having varied frequency and amplitude. The variation of phase angle and frequency can be observed. Fig.7. shows the Simulink model of basic PLL having a sinusoidal input with amplitude of 50 and frequency of 50Hz.

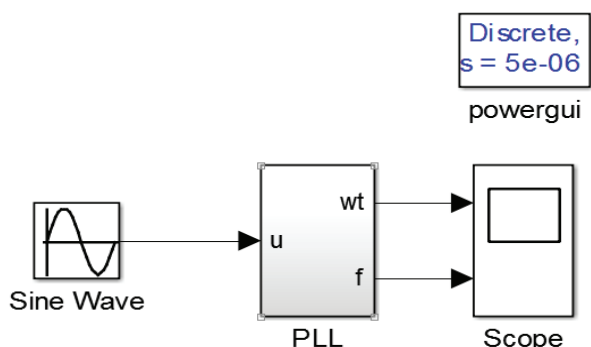


Figure 7. Simulink model of basic PLL

The parameters like input amplitude, frequency, and typical values of gains  $u_1$ ,  $u_2$  and  $u_3$  are shown in the following Table. I

TABLE I.  
DESIGN PARAMETERS OF PLL

S. No	Basic PLL (Ts=5e-6)	
	Parameter	Value
1.	Input voltage amplitude	230 Volts
2.	Frequency	50Hz
3.	Kp	400
4.	Ki	2000
Enhanced PLL(Ts=5e-6)		
1.	Input voltage amplitude	230 Volts
2.	Frequency	50Hz
3.	$u_1$	200
4.	$u_2$	20000
5.	$u_3$	400

Table. I describe the design parameters along with sampling time used basic PLL is  $T_s=5e-5$  sec. and enhanced PLL having a sampling time of  $T_s=5e-6$  sec.

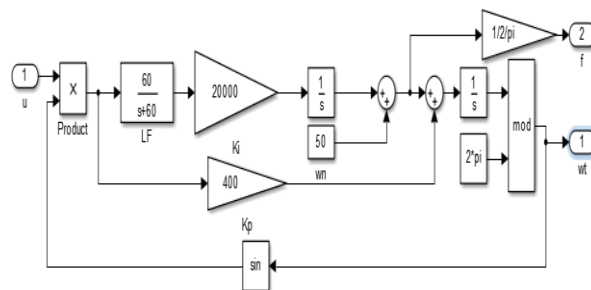


Figure 8. Simulink modeling of PLL

The input amplitude of 230 having a frequency of 50Hz is given. Fig.7. & Fig.8. are showing Simulink models of basic PLL. The Simulink model of basic PLL includes a low pass filter and PI controller as shown in Figure.8.

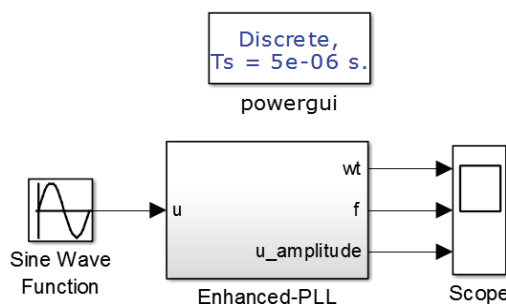


Figure 9. Simulink model of Enhanced PLL.

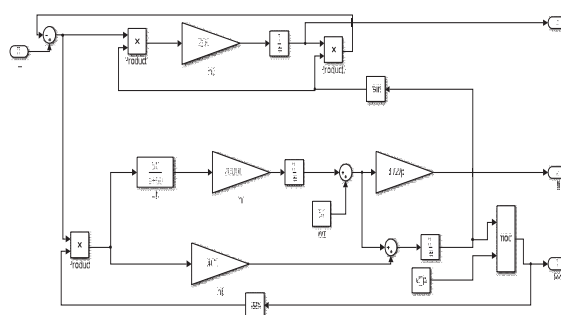


Figure 10. Simulink modeling of Enhanced PLL

Fig.9. and Fig.10. indicates Simulink modeling of enhanced PLL, which includes an extra loop for filtering the input signal so that fine control is possible [11].

#### V. RESULTS

The Simulink diagrams described above indicating the operation of basic PLL and enhanced PLL. The simulation results of both the types PLL are analyzed and compared in the section V.

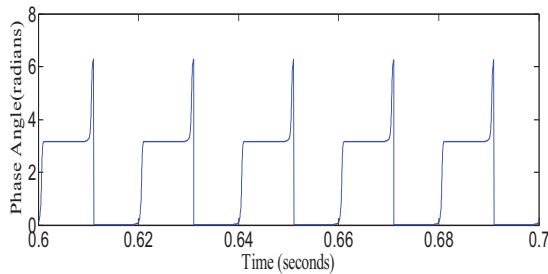


Figure 11. Variation of Phase angle using PLL

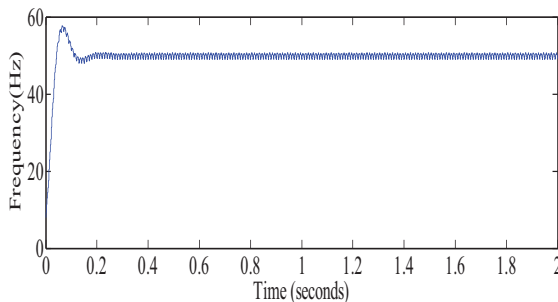


Figure 12. Frequency of basic PLL

The frequency of the given signal is determined by the PLL and is 50Hz as shown in Fig.12. Further the phase angle is determined, its value is mentioned in radians i.e. 6.28 as shown in Figure.11.

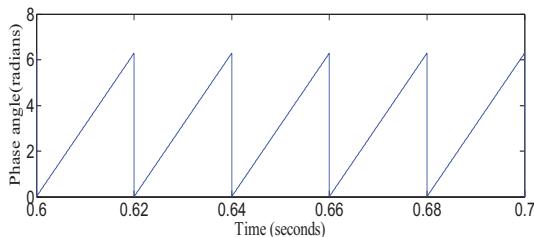


Figure 13. Phase angle of enhanced PLL

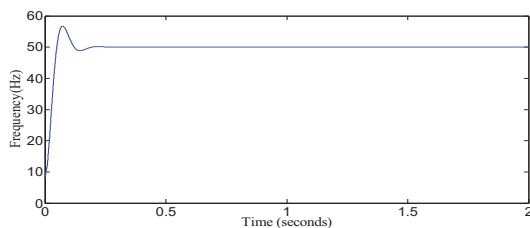


Figure 14. Frequency of enhanced PLL.

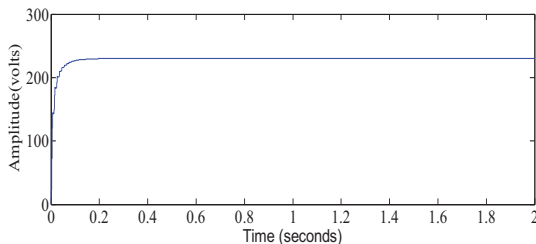


Figure 15. Voltage amplitude input signal for enhanced PLL

Fig.13. and Fig.14 are the simulation results of enhanced PLL describing phase angle and frequency. Figure.15. shows the amplitude of the input signal provided in enhanced PLL.

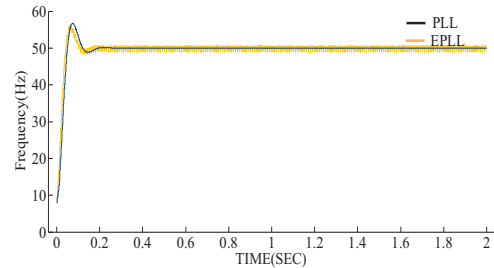


Figure 16. Comparison of frequency in PLL & EPLL.

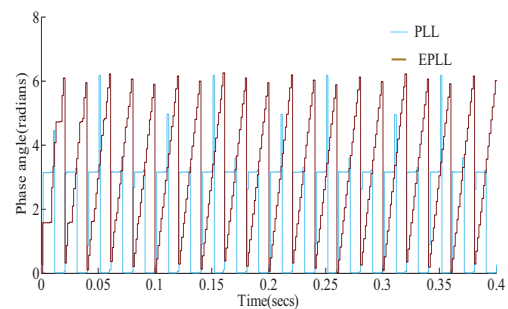


Figure 17. Phase angle Comparison in PLL & EPLL.

The control in the frequency given by basic PLL is compared with EPLL as shown in Fig.16. which describes the performance of EPLL is improved when compared to basic PLL. Fig.17. indicates phase angle variation in PLL and EPLL indicating that tracking of phase angle in EPLL is superior compared to basic PLL [16]-[18].

## VI. CONCLUSIONS

The phase angle, frequency and voltage amplitude of inverter output signal that is required to feed to grid has paramount importance in view of power control to the grid. By comparing Figure.12.and Figure.13. It can be concluded that the variation of frequency in basic PLL is found to be high i.e. +/-3-5Hz. On contrary the enhanced PLL has negligible (0.1-0.3Hz) variation in its frequency measurements. Figure.11 and Figure 13. indicates the phase angle measurement is not smooth in basic PLL compared to EPLL. Besides the accuracy in measurement and its simplicity in implementation made enhanced phase locked loop (EPLL) much popular when compared with other synchronizing methods.

## REFERENCES

- [1] E. Akpınar, A. Balıkcı, E. Durbaba, and B. T. Azizoglu, "Single-phase transformerless photovoltaic inverter with suppressing resonance in improved h6," *IEEE Trans. Power Electron.*, vol. 34, no. 9, pp. 8304–8316, 2019
- [2] N. N. V. Surendra Babu and B. G. Fernandes, "Cascaded two-level inverter-based multilevel STATCOM for high-power

- applications,” *IEEE Trans. Power Deliv.*, vol. 29, no. 3, pp. 993–1001, 2014, doi: 10.1109/TPWRD.2014.2305692.
- [3] G. Janardhan, G. N. Srinivas and N. N. V. Surendra Babu, "Realization of Constant Common Mode Voltage in Transformerless Photo Voltaic Inverter Topologies," 2018 International Conference on Circuits and Systems in Digital Enterprise Technology (ICCSDET), Kottayam, India, 2018, pp. 1-5
- [4] M. Karimi-Ghartemani and M. R. Iravani, "A method for synchronization of power electronic converters in polluted and variable-frequency environments," *IEEE Trans. Power Syst.*, vol. 19, no. 3, pp. 1263–1270
- [5] T. Köroğlu, M. Inci, K. Çağatay Bayindir, and M. Tümay, "Modeling and analysis of a nonlinear adaptive filter control for interline unified power quality conditioner," *Int. Conf. Power Eng. Energy Electr. Drives*, no. May 2013, pp. 603–608, 2013.
- [6] F. D. Freijedo, A. G. Yepes, Ó. López, P. Fernández-Comesaña, and J. Doval-Gandoy, "An optimized implementation of phase locked loops for grid applications," *IEEE Trans. Instrum. Meas.*, vol. 60, no. 9, pp. 3110–3119, 2011.
- [7] S. M. Silva, B. M. Lopes, B. J. C. Filho, R. P. Campana, and W. C. Boaventura, "Performance evaluation of PLL algorithms for single-phase grid-connected systems," *Conf. Rec. - IAS Annu. Meet. (IEEE Ind. Appl. Soc.)*, vol. 4, no. July, pp. 2259–2263, 2004.
- [8] [1] M. E. Ropp and S. Gonzalez, "Development of a MATLAB/simulink model of a single-phase grid-connected photovoltaic system," *IEEE Trans. Energy Convers.*, vol. 24, no. 1, pp. 195–202, 2009.
- [9] T. Kerekes, R. Teodorescu, P. Rodríguez, G. Vázquez, and E. Aldabas, "A New high-efficiency single-phase transformerless PV inverter topology," *IEEE Trans. Ind. Electron.*, vol. 58, no. 1, pp. 184–191, 2011.
- [10] Y. Tang, W. Yao, P. C. Loh, and F. Blaabjerg, "Highly Reliable Transformerless Photovoltaic Inverters with Leakage Current and Pulsating Power Elimination," *IEEE Trans. Ind. Electron.*, vol. 63, no. 2, pp. 1016–1026, 2016.
- [11] Gauan-chyun Hseih, James C. Hung "Phase Locked loop Techniques –A Survey."
- [12] G. Janardhan, and N. N. V. Surendra Babu, "Transformerless Photo voltaic inverter topologies for Low Power domestic applications," *CVR Journal of Science and Technology*, vol. 11, December 2016.
- [13] Q. Guan, Y. Zhang, Y. Kang and J. M. Guerrero, "Single-Phase Phase-Locked Loop Based on Derivative Elements," in *IEEE Transactions on Power Electronics*, vol. 32, no. 6, pp. 4411–4420, June 2017.
- [14] S. Golestan, J. M. Guerrero and J. C. Vasquez, "Single-Phase PLLs: A Review of Recent Advances," in *IEEE Transactions on Power Electronics*, vol. 32, no. 12, pp. 9013–9030, Dec. 2017.
- [15] K. A. Soni, N. K. Jaiswal and M. A. Lokhandwala, "Phase Locked Loop for Single Phase Grid Synchronization," 2018 2nd International Conference on Trends in Electronics and Informatics (ICOEI), Tirunelveli, 2018, pp. 1058–1063.
- [16] S. Shinnaka, "A Robust Single-Phase PLL System With Stable and Fast Tracking," in *IEEE Transactions on Industry Applications*, vol. 44, no. 2, pp. 624–633, March–April 2008.
- [17] I. P. Antchev, Mihail, "PLL for Single Phase Grid Connected Inverters," *Int. J. Electr. Eng. Technol.*, vol. 4, no. 5, pp. 56–77, 2013.
- [18] Y. Jiang, Y. Li, Y. Tian, and L. Wang, "Phase-locked loop research of grid-connected inverter based on impedance analysis," *Energies*, vol. 11, no. 11, 2018, doi: 10.3390/en11113077.

# Optimal Supplementary Controller Design for IPFC to Damp Low-Frequency Oscillations in Power Systems

Dr. Shankarappa F Kodad<sup>1</sup>, Dr. Dakka.Obulesu<sup>2</sup> and Manjunatha S C<sup>3</sup>

<sup>1</sup>Professor, Adama Science and Technology University/School of Electrical and Computing, Adama, Ethiopia.  
Email: kodadsf@rediffmail.com

<sup>2</sup>Assoc.Professor, CVR College of Engineering /EEE Department, Hyderabad, India  
Email: dakkaobulesh@gmail.com

<sup>3</sup>Asst.Professor, SJM Institute of Technology / EEE Department, Chitradurga, Karnataka, India  
Email: manjusc69@gmail.com

**Abstract:** In this paper, the use of interline power flow controller (IPFC) on damping low-frequency oscillations (LFOs) are discussed and a new genetic algorithm (GA)-based multistage fuzzy (MSF) DC-Voltage regulator is proposed for IPFC to dampen low-frequency oscillations in (Double line) power system. The suggested control strategy is estimated under various operating conditions, and then it is compared with conventional controllers to determine its effectiveness. Time-simulation studies proved the robust performance of the proposed regulator.

**Index Terms:** Flexible AC transmission systems (FACTS), IPFC, low-frequency oscillation (LFO), genetic algorithm (GA)-based multistage fuzzy (MSF) DC-voltage regulator.

## I. INTRODUCTION

Currently, in the power industry, the stability of low-frequency oscillations (LFOs) at frequencies of 0.2–2 Hz is of great interest and crucial concern [1–4].

A.prajapati, Kanchan Chaturvedi, Ch.Lokeshwar Reddy and S.Venkateshwarlu etc all discussed different FACTS devices static VAR compensator (SVC), static synchronous compensator (STATCOM), and unified power flow controller (UPFC). The article discussed how these devices could prove useful to damp oscillations, simply by adding a supplementary signal, which can in turn improve a power system's small signal stability. The FACTS controller's new concept for series compensation is interline power flow controller (IPFC). The IPFC can control power flow among multiple lines [5-18].

IPFC is the most recent happening of voltage source converter based FACTS devices, which was suggested by L.Gyugyi, Song Y.H. and k.Sen [11,12]. When the damping controller of a power system's low-power frequency oscillations is estimated for a nonlinear dynamic model, it allows damping oscillations to be accurate as well as achieve desirable operations. The highly nonlinear and stochastic nature of power systems makes fixed parameter-based conventional supplementary controllers unsuitable for IPFC, thereby necessitating the development of a flexible controller. In Fuzzy logic controllers for formation of fuzzy sets trial and error method are used, these are used for IPFC to supply better functionality, reliability, adaptability and robustness. This provoked us to develop the refined genetic algorithm based multistage fuzzy (GAMSF) DC-voltage

regulator for IPFC, which can study the practicability of damping of LFOs, besides enhancing the dynamic stability.

## II. GA-BASED FUZZY DAMPING CONTROLLER

In this section, we propose a modified GA-based MSF (GAMSF) controller that can help dampen a power system's LFOs as well as can take into consideration uncertainties arising during power system operations [6–9]. A arrangement of fuzzy PD and integral controller with switches is used by this approach. The fuzzy PD stage can eliminate fast change arising from the corresponding practical constraints, whereas the integral stage can eliminate zero steady-state error. The fuzzy rule-based control system can show good performance when the fuzzy sets are carefully designed and organized [10-15]. The work involved and cost of a fuzzy system can be further reduced utilizing a hill-climbing-based modified GA method: in addition this method optimally adjusts the membership functions in the suggested MSF controller.

The proposed arrangement, where input values are converted to truth-value vectors, of the GAMSF DC-Voltage regulator is shown in Fig.1. As is done with a single-stage fuzzy logic controller, the output truth-value vectors are not defuzzified to crisp values but are instead passed onto the next stage as a truth value vector input. During heavy loading condition of power systems ( $\delta > 70^\circ$ ), the performance of a controller can be improved with a static switch in the output controller, which can enhance the functional control signal.

Membership functions in this work are expound as triangular separation having seven segments from -1 to +1 with "0" defining the membership function centered "0" and so on. The portions are also uniformity about the zero membership functions, as shown in Fig.2.





and  $\Delta V_{dc}$  representing deviation in rotor angle, deviation in angular frequency deviation in  $P_e$  and capacitor voltage deviation  $V_{dc}$  respectively.

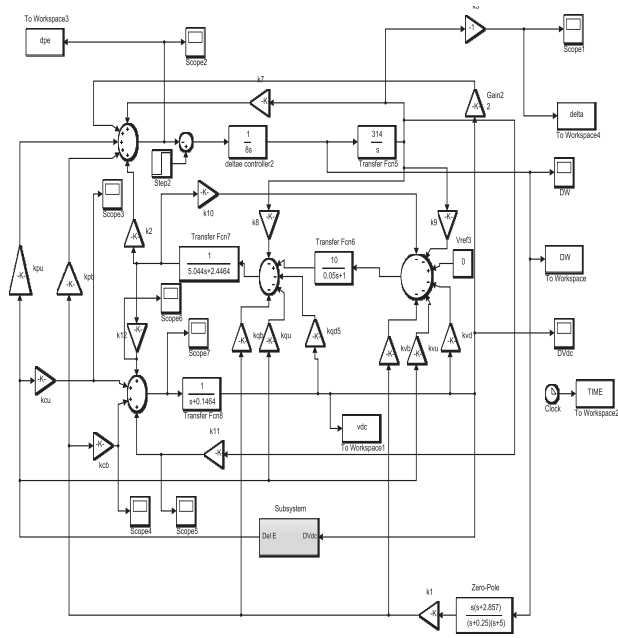


Figure 4. Simulink model of a single-machine infinite-bus system with IPFC and GAMSF Simulink model.

Fig. 3 and Fig.4. represent systems that are simulated with a step disturbance 0.1 perunit under different conditions: at point 1  $P_e$  considered as 0.8,  $Q_e$  considered as 0.15, and  $V_t$  considered as 1.032; at point 4:  $P_e$  considered as 1.1,  $Q_e$  considered as 0.28, and  $V_t$  considered as 1.032. The results obtained are shown in Figs. 5 and 6.

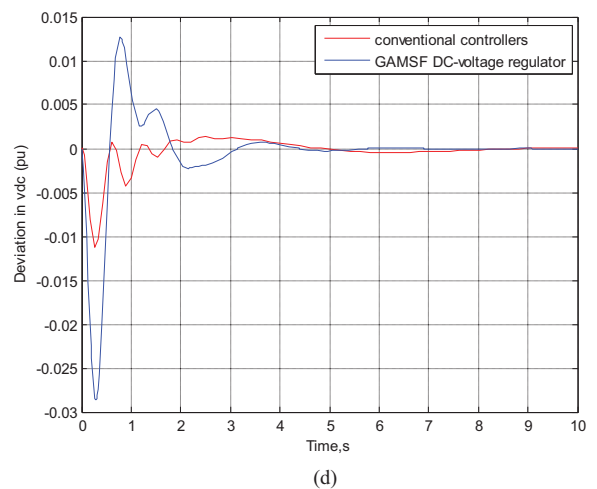
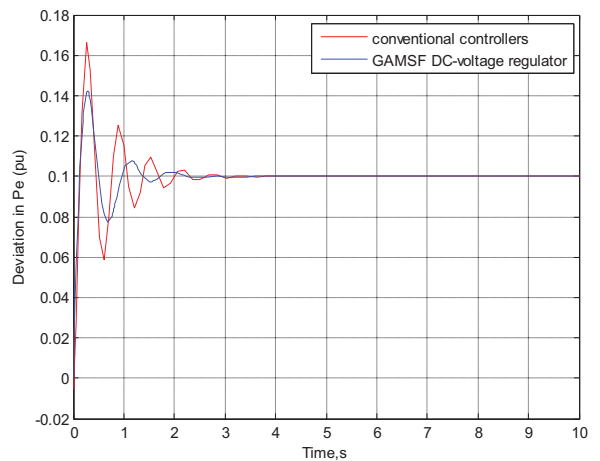
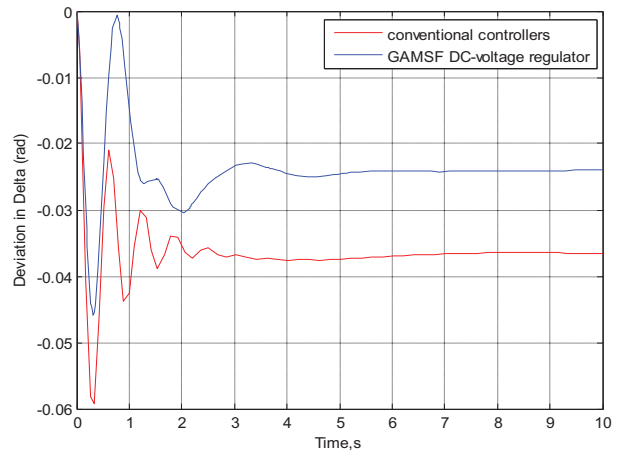
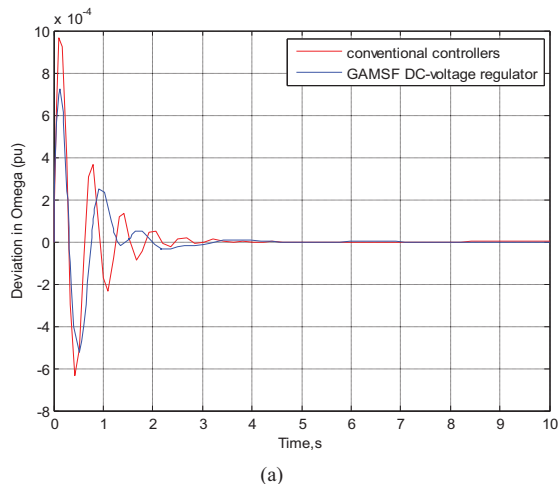
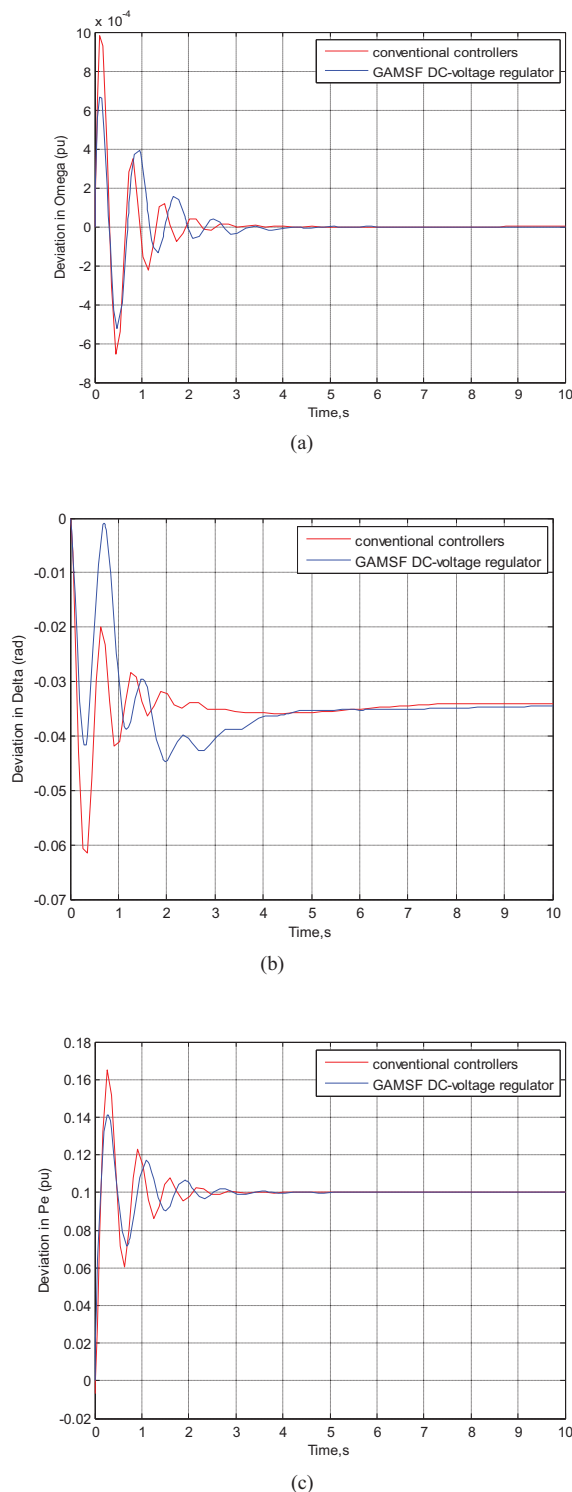


Figure 5. Time responses of (a)  $\Delta\omega$ , (b)  $\Delta\delta$ , (c)  $\Delta P_e$ , (d) of  $\Delta V_{dc}$  With conventional controller and the GAMSF DC-Voltage regulator at operating point 1.



Figs. 5 and 6 show the  $\Delta\omega$ ,  $\Delta\delta$ ,  $\Delta P_e$  and  $\Delta V_{dc}$  plots at different operating points with the GAMSF DC-Voltage regulator compared with IPFC having conventional controllers. These figures show that IPFC with a GAMSF DC-voltage regulator is more effective than conventional controllers.

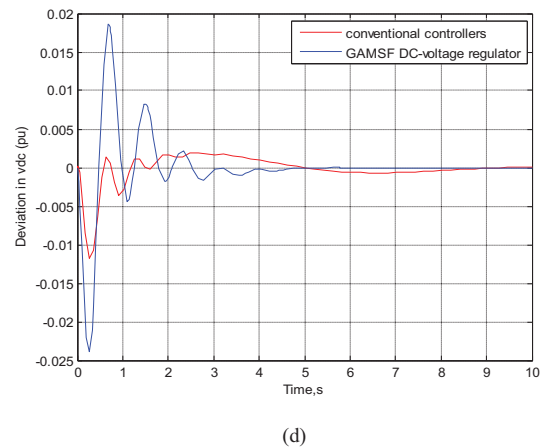


Figure 6. Time responses of (a)  $\Delta\omega$ , (b)  $\Delta\delta$ , (c)  $\Delta P_e$ , and (d) of  $\Delta V_{dc}$  With conventional controllers and the GAMSF DC-Voltage regulator at operating point 4.

#### IV. CONCLUSIONS

This paper presented robust GAMSF DC-Voltage regulator to damp low-frequency oscillations. The presented controller's effectiveness was tested on an SMIB Power system and compared with conventional IPFC controllers under various operating conditions. The results shown the effectiveness and performance of the controller proposed in this paper. The proposed controller's simple design procedure and robust performance make it potentially useful for future practical implementations.

#### REFERENCES

- [1] E.V. Larsen and D.A. Swann, "Applying Power System Stabilizers, Parts 1 - 111, *IEEE Transactions on Power Apparatus and Systems*", Vol. PAS-100, 1981, pp.3017–3046.
- [2] J. H. Chow and J. J. Sanchez-Gasca, "Pole-placement design of power System Stabilizers", *IEEE T-PWRS*, Vol.4,1989.
- [3] Alivelu,M.Parimi, IrraivanElamvazuthi et al., "Interline Power Flow Controller Application for Low Frequency Oscillations damping", *Wseas Transactions on Systems*, Issue 5, Volume 9, May 2010,PP.511–527.
- [4] Soumya deep Maity,R.Ramya, "A Comprehensive Review of Damping of Low Frequency Oscillations in Power Systems",*International Journal of Innovative Technology and Exploring Engineering(IJITEE)*ISSN: 2278–3075, Volume8, Issue6S3, April2019.
- [5] Anubha Prajapati and Kanchan Chaturvedi, "Interline Power Flow Controller Based Damping Controllers for Damping Low Frequency Oscillations", *International Journal ofElectrical,Electronics and Computer Engineering* 2(1): 83–87,2013, ISSN:2277–2626.
- [6] DakkaObulesu, S. F. Kodad, B. V. Sankar Ram, "Optimal Supplementary Controller Design for UPFC in Order to Damping Low Frequency Oscillations in Power Systems", "Journal of ATTI DELLA FONDAZIONE GIORGIO RONCHI," Italy, ISSN: 03912051.,2014
- [7] DakkaObulesu, S. F. Kodad,B. V. Sankar Ram, "GAMSF and PSOMSf based UPFC Supplementary Controllers for Damping Low Frequency Oscillations in Multi-machine

- Power Systems”, Journal of ATTI DELLA FONDAZIONE GIORGIO RONCHI,” Italy, ISSN: 03912051.,2014
- [8] DakkaObulesu, S. F. Kodad, B. V. SankarRam, “Low Frequency Oscillations Damping by UPFC with GAPOD and GADC-voltage Regulator”, accepted in Journal of Electrical and Electronics Engineering, JEEE,ISSN 2320–3331.
- [9] DakkaObulesu, Dr. S. F. Kodad, Dr. B. V. Sankar Ram, “Low Frequency Oscillations Damping by UPFC with a Multi stage Fuzzy Supplementary Controllers”, International Review of Modelling and Simulations, IREMO,ISSN: 1974–9821,2013.
- [10] Yuksel Oguz, “Fuzzy PI Control with Parallel Fuzzy PD Control for Automatic Generation Control of a Two-Area Power Systems”, Gazi University Journal of Science GU J Sci 24(4):805–816 (2011).
- [11] SONG Y.H., JOHNS AT., Flexible ac transmission systems (FACTS), (IEE Press, UK, 1999).
- [12] L. Gyugyi, K. K. Sen, and C. D. Schauder, The interline power flow controller concept: A new approach to power flow management in transmission systems, *IEEE Trans. Power Del.*, Vol. 14, No. 3, Jul. 1999, pp. 1115–1123
- [13] FARSANGI M.M., SONG Y.H., LEE K.Y., Choice of FACTS device control inputs for damping inter-area oscillations, *IEEE Trans. Power Syst.*, 19 (2),1135–43, 2004.
- [14] H. Shayeghi, H.A. Shayanfar, et al., “GA Based Multi Stage Fuzzy Controller for the UPFC”, University of PITESTI-Electronics and Computer Science, Scientific Bulletin, No. 8, Vol. 2, 2008, ISSN-1453-1119.
- [15] DakkaObulesu, S. F. Kodad, B. V. Sankar Ram, “PSOMS Based UPFC Supplementary Controller for Damping Low Frequency Oscillations in Power Systems”, Published in International Journal of Engg. Research and Industrial Applications IJERIA vol-04, no.3, August 2011, pp: 189–202. ISSN: 0974–1518.
- [16] P.Rajesh kumar,Rajib kar etc all :Analysis and simulation of STATCOM based SSR Controller on fist zone operation of Digital DistanceRelay with Remedy,CVR Journal of Science and Technology,Volume no 12,PP.36-42,Jun-2017.
- [17] Ch.Lokeshwar Reddy ,P.Rajesh kumar, “Study of star connected Cascaded H-Bridge STATCOM using Different PWM Techniques”,CVR Journal of Science and Technology,volume no 13,pp. 61-66,Dec-2017
- [18] S.Venkateshwarlu,BP.Muni,AD.Rajkumar, “Analysis of VF-DPC PWM Converter based STATCOM”, 2008 Annual IEEE Indian Conference 2,431-436.

# Cascaded H-Bridge Inverter for Wind Driven Isolated Squirrel Cage Induction Generators

G. Manohar<sup>1</sup> and K. Chiranjeevi<sup>2</sup>

<sup>1</sup>Assoc. Professor, CVR College of Engineering/EEE Department, Hyderabad, India  
E mail: manohar.gangikunta@gmail.com

<sup>2</sup>PG Scholar, CVR College of Engineering/ EEE Department, Hyderabad, India  
E mail: chiru.maheshwaram.019@gmail.com

**Abstract:** This paper describes the simulation and harmonics analysis of cascaded five-level H-bridge inverters fed induction motor load drive for islanding mode applications. The self – excited induction generator (SEIG) fed H-bridge Multi-Level Inverter (MLI) for wind energy conversion systems is chosen for several islanding mode applications. In this paper, the SEIG (for standalone systems) fed cascaded five level inverter for induction motor load applications are clearly explained with the help of MATLAB / SIMULINK models. The generated voltage of the wind driven SEIG is mainly depending on the wind velocity fluctuations and appropriate load conditions. The five level cascaded inverters have interface with the wind driven SEIG. By choosing appropriate value of Modulation Index (MI), the variable voltage and variable frequency of the generator can be finely controlled. The simulation and harmonic analysis of the proposed inverter will be discussed, and the total harmonic distortion of stator current for different modulation index at different switching frequencies are evaluated and the speed and torque of induction motor for different load torques are plotted.

**Index Terms:** Self – Excited Induction Generator (SEIG), Variable speed Wind Turbine, Multi Level Inverter (MLI), Induction Motor (IM), Modulation Index (MI).

## I. INTRODUCTION

Wind energy conversion scheme the use of a wind turbine driven SEIG, modern electricity virtual converter was modelled, analysed and completed. Generation of electrical energy from the wind the wind energy is gaining tremendous importance internationally in this decade. Modern variable frequency drives operate with the aid of changing a 3-phase voltage deliver to DC the usage of out of control rectifier. The values of capacitance required for self-excitation were analysed formerly [1]– [2]. Especially in far flung areas, Self-Excited Induction Generators are generating proper energy in comparison with specific generators. Employing static power electronic converters, the variable voltage and variable frequency of the SEIG is converted into desired voltage and standard frequency. The wind turbines employed in wind generation system have strong production, lower inertia, and run-time charge, a good deal much less preservation fee and better short universal performance.

If the capacitance is insufficient, the induction generators will not be able to construct the voltage. In order to build up the terminal voltage, a constant speed wind turbine tied

induction generator requires reactor power support which is generally provided by capacitor banks of large capacity. Wind turbines are produced in a wide scope of vertical and level pivot. Less capacity wind turbines are utilized for simple applications, such as battery charging for power traffic cautioning signs.

Turbines with moderate capacity can be exploited for making assurances to a domestic power supply while vending extra energy back to the utility provider through the electrical network. Wind turbines with a capacity of 5MW per unit are available in and used by the utilities today. Wind turbines can either can be coupled to SEIG or Doubly Fed Induction Generator (DFIG). Requirement of reactive power for building the terminal voltage is major limitation of constant speed induction generators.

## II. PROPOSED SYSTEM DESCRIPTION

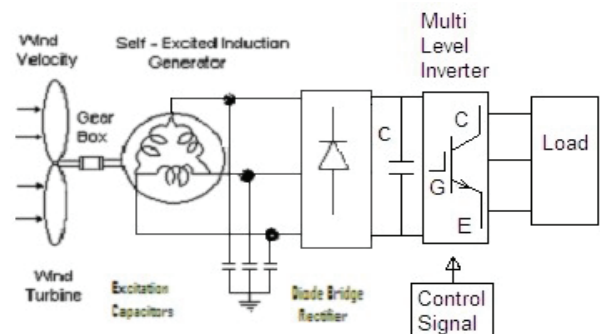


Figure 1. Proposed Impedance Source Inverter based Wind Power Generation System.

The proposed impedance source inverter-based wind energy driven SEIG encouraged burden is shown in the “Fig. 1,”. The SEIG is driven by the wind turbine and output of the induction generator is fed to five-level cascaded H bridge inverter which in turn provides the terminal voltage to induction motor. The power transformation proficiency of ZSI is improved in contrast with the conventional inverters for wind electric power application. The desired reactive power of the SEIG is provided by the three-phase capacitor banks connected at the output terminals of the SEIG. The variable yield voltage from the acceptance generator is amended and after that modified by utilizing the proposed

inverter. The ZSI can be made to operate to deliver output voltage greater than the voltage fed to it by effectively controlling the shoot through time. Overall power factor of the system can be improved by the proposed method with an additional benefit of reduced Total Harmonic Distortion (THD) in the stator current.

#### A. Wind Turbine Equations and characteristics

Due to simple construction and working principle, a horizontal axis wind turbine is preferred in wind energy systems and it will produce electric power economically. The wind turbine rotor drives the induction generator through a step-up gear box.

The mechanical power output of wind turbine is given by

$$P_w = 0.5\rho C_p A V_w^3 \quad (1)$$

where  $A$  is the area in sq. meters  
 $V_w$  is the Velocity of the wind in m/s  
 $C_p$  is power co efficient and is expressed as a function of  $\lambda$

$$\lambda = R\omega_r / V_w \quad (2)$$

$$C_p = 0.5((116/\lambda_1) - 0.4\beta - 5) e^{-16.5/\lambda_1} \quad (3)$$

where  $V_w$  is the wind speed estimated on hourly basis and it's units are kmph,  $N_m$  is the total hours in the specified period. The maximum theoretical power co efficient is equal to 0.593.

#### B. Self-Excited Induction Generator Modelling

Induction generators are broadly used, specifically polyphase induction cars that are frequently utilized in industrial drives. When the rotor of the induction machine is coupled to wind turbine and driven at a speed greater than synchronous speed, the induction machine works as induction generator generating electricity from mechanical energy. The modelling of the induction generator in d-q axis is described by the following equation [3].

$$p i_{qs} = -K_1 r_1 i_{qs} - (i_{qs}/C v_{ds} + K_2 L_m \omega_m) i_{ds} + K_2 r_2 i_{qr} - K_1 L_m \omega_m i_{dr} \quad (4)$$

$$p i_{ds} = (i_{qs}/C v_{ds} + K_2 L_m \omega_m) i_{qs} - K_1 r_1 i_{ds} + K_1 L_m \omega_m i_{qr} + K_2 r_2 i_{dr} - K_1 v_{ds} \quad (5)$$

$$p i_{qr} = -K_2 r_1 i_{qs} + L_1 K_2 \omega_m i_{ds} - (r_2 + K_2 L_m r_2) L_2 i_{qr} + (K_1 L_1 \omega_m - i_{qs}/C v_{ds} + i_{dr}) \quad (6)$$

$$p i_{dr} = -L_1 K_2 \omega_m i_{qs} + K_2 r_1 i_{ds} + (L_1 K_1 \omega_m - i_{qs}/C v_{ds}) i_{qr} + (r_2 + K_2 L_m r_2) L_2 i_{dr} + K_2 v_{ds} \quad (7)$$

where  $K_1 = L_r / (L_s L_r - L_m^2)$   
 $K_2 = L_m / (L_s L_r - L_m^2)$

#### C. Induction Motor

An induction motor is an asynchronous AC motor where power is provided to the rotating device with the useful resource of electromagnetic induction. Out of the two configurations, squirrel cage motor is extensively used in industrial and domestic applications due to its ruggedness, low maintenance cost, easy installation and superior electrical characteristics. However, in special applications where maximum starting torque is required like traction, a slip ring or wound rotor induction motor is used.

An induction motor is sometimes known as a revolving transformer due to the fact the stator (stationary element) acts as one winding of the transformer and the rotor (rotating element) is the other winding of the transformer factor.

#### D. Uncontrolled Bridge Rectifier

The output of SEIG is connected to a three-phase uncontrolled rectifier. The purpose of connecting a uncontrolled rectifier is to get a fixed DC from 3-phase AC. An ordinary low-cost diode rectifier will serve the purpose here. A series reactor connected at output terminals of the diode rectifier reduces the current ripple and a shunt capacitor reduces the ripple in the output voltage.

#### E. Multi-Level Inverters

Multilevel inverters are the ideal choice of industry to work with high voltages and is an attractive alternative in the area of high-power medium-voltage energy control. An inverter is a power electronic static device that converts constant DC voltage to alternating voltage preferably a sinusoidal voltage. The AC voltage may be at any desired voltage and frequency with the usage of appropriate transformers, switching, and manage circuits. Inverter don't have any transferring factors and are applied in a sizable sort of packages, from small switching power components in computers, to large modules that delivery bulk energy. The most common type of inverter which is used to generate AC voltage from DC Voltage is two level inverters. A two-level Inverter creates two different voltages for the load i.e. suppose we are providing  $V$  as an input to a two-level inverter then it will provide  $+V/2$  and  $-V/2$  on output [4]-[5].

The cascaded H-bridge multi-level inverter with 5 levels is chosen in the proposed simulation. H-bridge inverter is considered for simulation since it is extensively used in applications of distributed generation with renewable sources. Especially, for integrating solar energy and wind energy roof top installations H-bridge inverters in cascaded mode are employed.

Classification of Multilevel Inverter as shown in the "Fig. 2,".

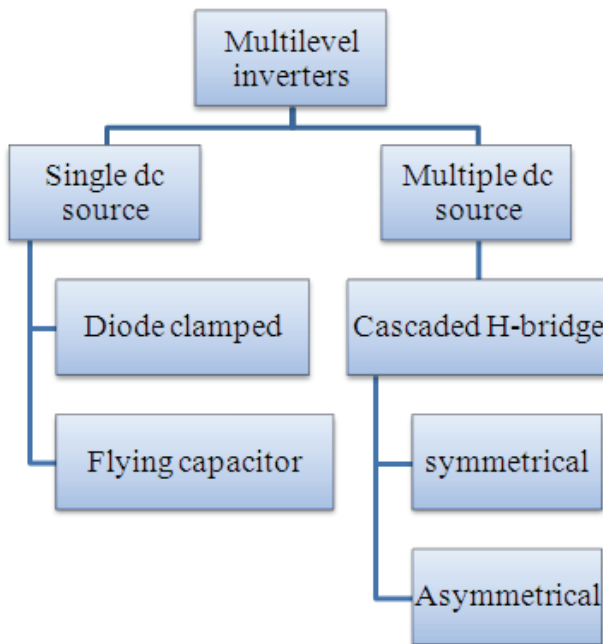


Figure 2. Classification of Multilevel Inverter

### III. SIMULATION RESULTS

In this section, the wind driven Self Excited Induction Generator (SEIG) fed with five level cascaded H-Bridge inverter for wind power conversion system using Asynchronous machine as a load is simulated using MATLAB/SIMULINK [6]-[8]. By applying different loads with respect to time on asynchronous motor rotor speed and motor torque were calculated and stator current's THD analysis has been explained with the simulation results below.

"Fig. 3," shows the MATLAB/SIMULINK of proposed system comprising of a wind turbine driving an asynchronous generator. The generator output is given back to back converters with DC link in between. Here five level H-bridge cascaded inverter is used to convert fixed DC to variable AC. This AC is used to drive an induction motor which is acting as an isolated load. "Fig. 4," shows control signal generation for single cell of H bridge inverter, "Fig. 5," shows the circuit diagram of a three-phase, five-level cascaded H-bridge inverter.

The Self Excited Induction (SEIG) generated 385 volts and 3-phase output voltage wave forms shown in the figure 6, the bridge rectifier converts that AC power to DC power and the magnitude of the rectified voltage is 312 volts as shown in the "Fig. 7."

The multilevel inverter converts the rectified DC power to the AC power and the phase voltage is 370 volts as shown in the "Fig. 8.", line voltage of multilevel inverter is 358 volts waveforms this is shown in the "Fig. 9.", line current of multilevel inverter is 3.5 amperes as shown in the "Fig. 10."

Different load torques are applied on Asynchronous machine at different intervals of time. Load torque versus time graph shown in the "Fig. 11.", Full load torque is

considered as 26.72N-m

Rotor speed in RPM and motor torque in N-m of asynchronous motor for different load torques at various values of modulation index are considered for simulation. Found speed of the rotor is inversely proportional to the motor torque as shown in the "Fig. 12,". From the "Fig. 12," rotor speed decreases by the application of load torque at different intervals. Rotor speed, asynchronous machine torque at different load torques are tabulated in the table I.

Stator currents of asynchronous machine of all three phases viz. phase A, phase B and phase C s are shown in the "Fig. 13,". The magnitude of these currents at unity slip under no load conditions is very high.

Rotor currents with respect to time on rotor of asynchronous machine of all three phases viz. phase A, phase B and phase C are shown in the "Fig. 14,". Frequency of these rotor currents is high at unity slip since rotor speed is less. As the rotor speed increases, slip of the asynchronous machine decreases and hence rotor frequency decreases.

Total Harmonic Distortion (THD) of multilevel inverter output in phase A found 8.37% as shown in the "Fig. 15,".

(i) Total Harmonic Distortion (THD) of stator current of asynchronous machine in phase A with modulation index (MI) of 1.0 at switching frequency of 1050Hz as shown in the "Fig. 16,".

(ii) Total Harmonic Distortion (THD) of stator current of asynchronous machine in phase A is shown in the "Fig. 17," The modulation index is considered as 1.0 at a switching frequency of 1550Hz.

(iii) Total Harmonic Distortion (THD) of stator current of asynchronous machine in phase A with modulation index (MI) of 1.0 at switching frequency of 2050Hz is shown in the "Fig. 18,"and

(iv) Total Harmonic Distortion (THD) of stator current of asynchronous machine in phase A with modulation index (MI) of 1.0 at switching frequency of 3050Hz is shown in the "Fig. 19,".

Total Harmonic Distortion (THD) of stator current in phase "A" for Modulation Index (MI) of 1, 0.9,0.8 and 0.7 at different switching frequencies are tabulated in tables II, III, IV and V respectively.

Phase Disposition (PD) technique with multi carrier sine waves are used to generate the gate signals for H-Bridge Inverters. Phase Opposition Disposition (POD) technique and Alternate Phase Opposition Disposition (APOD) multi carrier sine PWM techniques also can be implemented to study the behavior of asynchronous machine. Third harmonic injection pulse width modulation can also be implemented to study the behavior of the asynchronous machine for different level shifted PWM techniques discussed above.

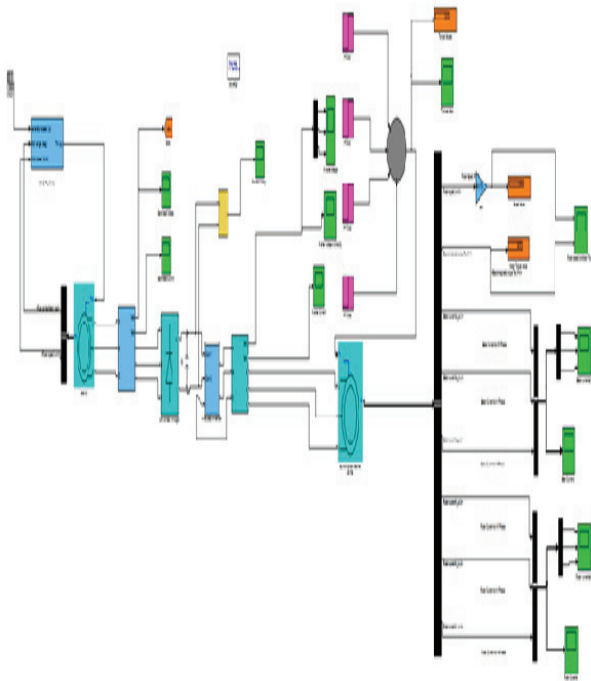


Figure 3. MATLAB/SIMULINK of proposed system.

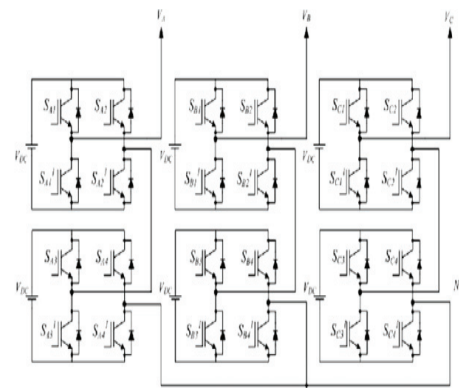


Figure 5. Three-Phase five-level cascaded H-Bridge inverter.

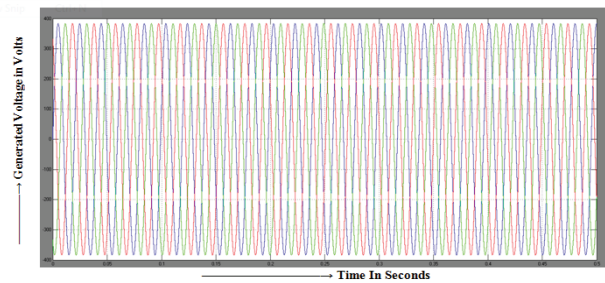


Figure 6. Self-Excited Induction (SEIG) generated voltages

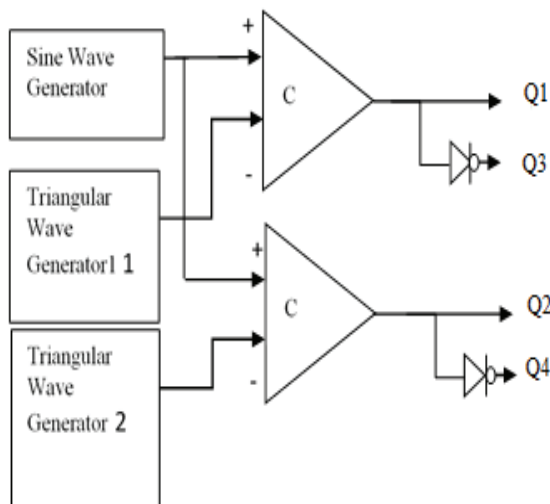


Figure 4. H-Bridge Inverter.

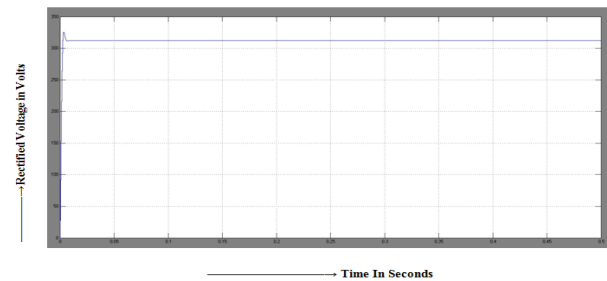


Figure 7. Rectified voltage

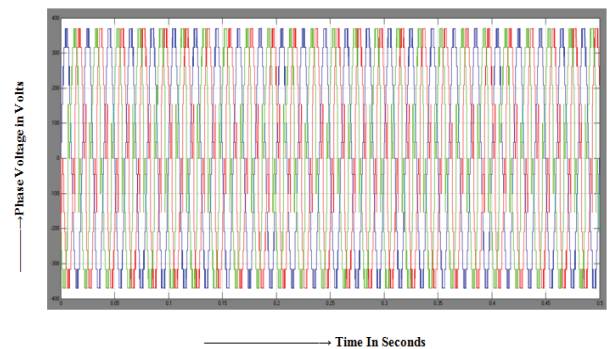


Figure 8. Multilevel Inverter output Phase voltages



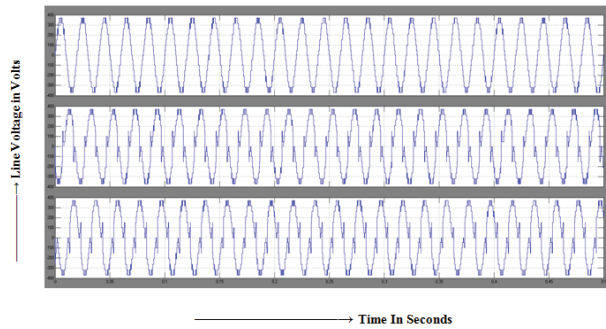


Figure 9. Multilevel Inverter output Line voltages

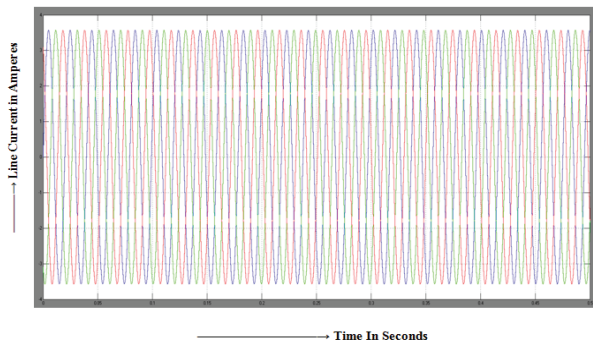


Figure 10. Multilevel Inverter output Line current

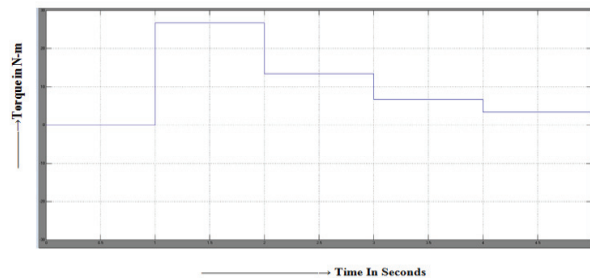


Figure 11. Applied load torque on asynchronous machine in N-m versus time in seconds.

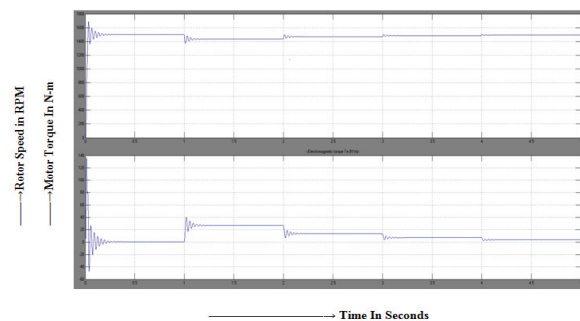


Figure 12. Rotor speed in RPM and motor torque in N-m of Asynchronous Machine

TABLE I.  
SPEED, MOTOR TORQUES AT DIFFERENT LOAD TORQUES

Load Torque setting time in seconds	Load Torque	Load Torque (TL) Value in N-m	Motor Torque (Tm) Value in N-m	Rotor Speed (N) in RPM
TL at 0 second	TL at no load	0	0	1499
TL at 1 second	TL at full load	26.72	27.16	1435
TL at 2 seconds	TL at half full load	13.36	13.8	1468
TL at 3 seconds	TL at quarter full load	6.68	7.1	1484
TL at 4 seconds	TL at octa full load	3.34	3.8	1491

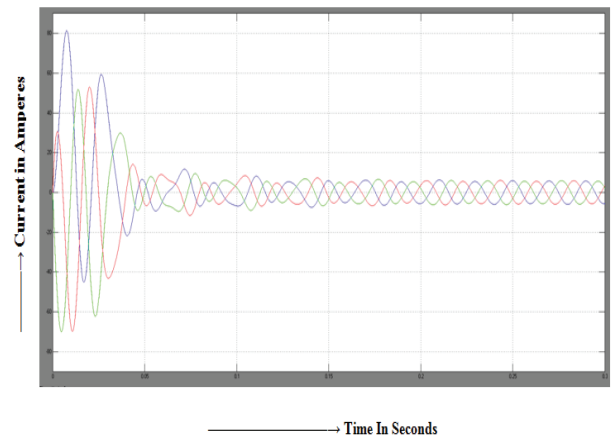


Figure 13. Stator currents of asynchronous machine w.r.t. time.

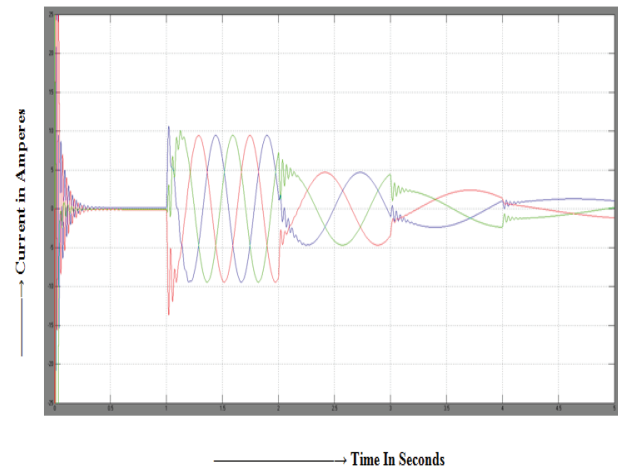


Figure 14. Rotor currents of asynchronous machine w.r.t. time.

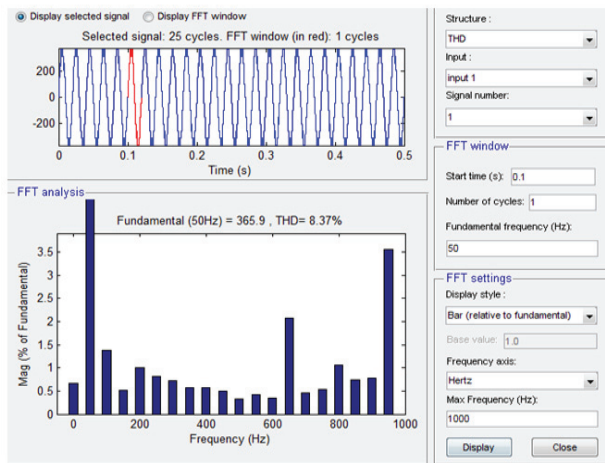


Figure 15. THD analysis of multilevel inverter output.

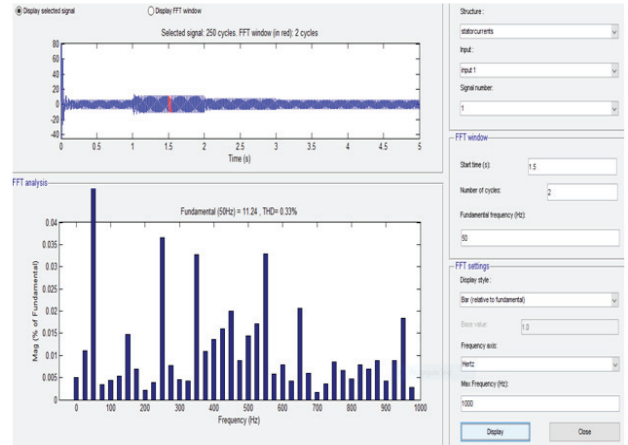


Figure 18. THD analysis of stator current of asynchronous machine in phase A at Modulation Index =0.8

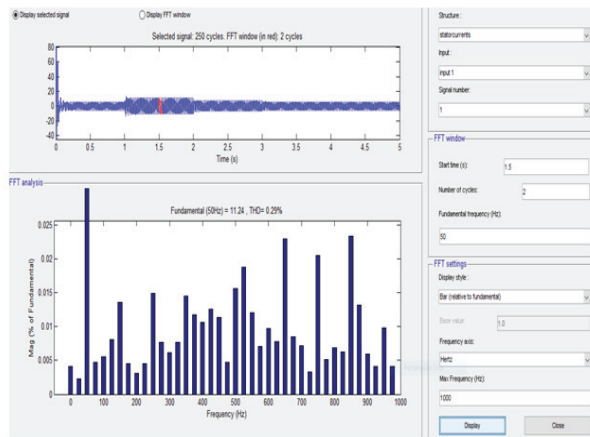


Figure 16. THD analysis of stator current of asynchronous machine in phase A at Modulation Index =1

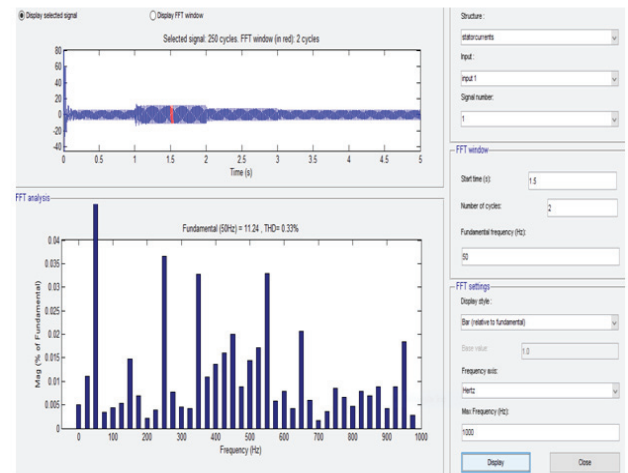


Figure 19. THD analysis of stator current of asynchronous machine in phase A at Modulation Index =0.7

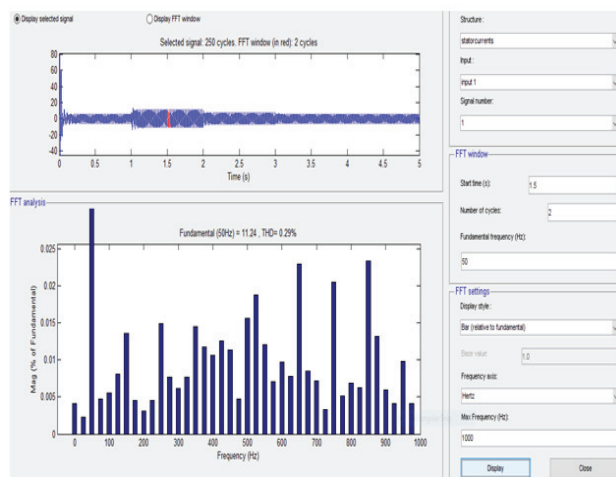


Figure 17. THD analysis of stator current of asynchronous machine in phase A at Modulation Index =0.9

TABLE II.  
THD ANALYSIS OF STATOR CURRENT IN PHASE A AT MODULATION INDEX (MI=1)

Ts	THD of Stator Current in Phase A
1050	0.29%
1550	0.29%
2050	0.33%
3050	0.33%

TABLE III.  
THD ANALYSIS OF STATOR CURRENT IN PHASE A AT MODULATION INDEX (MI=0.9)

Ts	THD of Stator Current in Phase A
1050	0.34%
1550	0.32%
2050	0.32%
3050	0.34%

TABLE IV.  
THD ANALYSIS OF STATOR CURRENT IN PHASE A AT MODULATION INDEX (MI=0.8)

Ts	THD of Stator Current in Phase A
1050	0.36%
1550	0.33%
2050	0.33%
3050	0.36%

TABLE V.  
THD ANALYSIS OF STATOR CURRENT IN PHASE A AT MODULATION INDEX (MI=0.7)

Ts	THD of Stator Current in Phase A
1050	0.37%
1550	0.32%
2050	0.33%
3050	0.37%

#### IV. CONCLUSIONS

The cascaded five level H- bridge inverter fed wind driven self-excited induction generator has been simulated and waveforms of the load (Induction motor) are observed. The multi-level inverter fed drive reduces the harmonic contents in comparison with the conventional inverter fed structures. Load torque applied on asynchronous machine with respect to time at different loads, rotor speed and motor torque observed at this respective load torques applied on this asynchronous machine. Stator currents and rotor currents are obtained with respect to load torque and time interval. Total Harmonic Distortion (THD), calculated for stator current of asynchronous machine for different modulation indexes was found to be very less and the waveforms are almost sinusoidal in nature. THD was also calculated for different switching frequencies and found that that THD decrease with increased switching frequencies.

#### REFERENCES

- [1] Ahmed, Tarek, Osamu Noro, K. Matzuo, Yuji Shindo, and Mutsuo Nakaoka. "Minimum excitation capacitance requirements for wind turbine coupled stand-alone self-excited induction generator with voltage regulation based on SVC." In The 25th International Telecommunications Energy Conference, 2003. INTELEC'03., pp. 396-403. IEEE, 2003.
- [2] Anagreh, Yaser. "Steady state performance of series DC motor powered by wind driven self-excited induction generator." Proceedings on Rev. Energ. Ren: power Engineering, pp 9-15,2001.
- [3] Slootweg, J. G., Henk Polinder, and Wil L. Kling. "Dynamic modelling of a wind turbine with doubly fed induction generator." In 2001 Power Engineering Society Summer Meeting. Conference Proceedings (Cat. No. 01CH37262), vol. 1, pp. 644-649. IEEE, 2001.
- [4] Manohar, G., and S. Venkateshwarlu. "Performance Analysis of Three Level Diode Clamped Inverter fed Induction Machine using Multicarrier PWM Techniques." *CVR Journal of Science and Technology* 16, no. 1 ,pp.59-65,2019
- [5] Daher, Sergio, Jürgen Schmid, and Fernando LM Antunes. "Multilevel inverter topologies for stand-alone PV systems." *IEEE transactions on industrial electronics* 55, no. 7 ,pp. 2703-2712, 2008.
- [6] Kasesra, Jitendra, Ankit Chaplot, and Jai Kumar Maherchandani. "Modeling and simulation of wind-PV hybrid power system using Matlab/Simulink." In 2012 IEEE Students' Conference on Electrical, Electronics and Computer Science, pp. 1-4. IEEE, 2012.
- [7] Soetedjo, Aryuanto, Abraham Lomi, and Widodo Puji Mulayanto. "Modeling of wind energy system with MPPT control." In *Proceedings of the 2011 International Conference on Electrical Engineering and Informatics*, pp. 1-6. IEEE, 2011.
- [8] Manohar, G., and S. Venkateshwarlu. " Analysis of Grid Connected Doubly Fed Induction Generator based Wind Turbine." *CVR Journal of Science and Technology*, vol. 10 ,pp.59-64, June 2016.

# Rapid Diagnosis of Malaria using Images of Stained Blood Smear

Dr. Narendra B. Mustare

Professor, CVR College of Engineering/EIE Department, Hyderabad, India

Email: drnamust@gmail.com

**Abstract:** This paper presents a technique to distinguish malaria parasite during blood checks recolored by Giemsa to improve the precision of distinguishing, on the preliminary step, the red platelet veil is extricated. It is owed toward the way that the big majority of malaria parasites live within pink platelets. At that factor, recolored components of blood, for example, pink platelets, parasites, and white platelets be extorted. On the subsequent level, pink platelet cowl is situated at the extracted recolored additives to isolate the potential parasites. By utilizing thick blood smear, quite a few blood smears can be analyzed hastily and no trouble in any respect. This work manages the programmed evaluation of parasite thickness in 'parasites according to a microliter of blood' from minuscule images of Giemsa-recolored thick blood smear. The principal factor of this examination is to look at the microscopic images of recolored dainty blood spreads using an assortment of processor apparition methods, reviewing malaria parasitemia on free factors (RBC's morphology). The projected process depends on the inductive method, shading of malaria parasites via versatile calculation of the Gaussian mixture model (GMM). Evaluation precision of RBCs is progressed, parting impediments of RBCs by separation alternate with close by maxima. Additionally, the characterization of tainted with non-contaminated RBCs has prepared for accurately evaluating parasitemia. Instruction along with assessment had completed on image dataset concerning floor facts, finding out the extent of infection with the affectability of 98 %. The exactness and skill ability of the proposed conspire about being programmed are demonstrated tentatively, outperforming other condition-of-the-art plans. Furthermore, this examination tended to the procedure with autonomous elements (RBCs' morphology).□

**Index Terms:** first term, second term, third term, fourth term, fifth term, sixth term

## I. INTRODUCTION

Malaria is considered one of the deadly international illnesses and can spark-off demise quickly on the off risk that its miles untreated. In 2015, 214 million instances of malaria were identified, which triggered around 438000 death [1]. Malaria is not unusual within tropical along with subtropical areas close to equator similar to Asia, Sub-Saharan Africa, and Latin America. It is impossible to resist malaria infection brought about through nonessential blood parasites of family Plasmodium. Malaria is Iran's main parasitic disease with a long background of episodes. Malaria fever is spread through the use of infected Anopheles female mosquitoes through their salivary glands that carry Plasmodium sporozoites. The kind Plasmodium has 4 organisms which can cause human distress: falciparum, vivax, ovale, and malaria. The famous process

of life has arranged different development within the human and mosquito structure. The sporozoites join the process as a tainted mosquito blessing from the blood of an individual and transfer to the liver where they develop abiogenetically. Since 2010, WHO has advocated malaria disease symptomatic trying out by way of both mild microscopy and rapid demonstrative, [2,27]. RDT is applied wherein microscopy microscope is not on hand; this technique gives second outcomes however number one disservice of RDT is that parasite thickness cannot be assessed. The microscopy approach is the "Best remarkable level" for recognizing malaria parasites and assessing parasite thickness [2]. Varieties of blood films are arranged for minute localization: flimsy and smooth [2]. A small bloodstain is used to distinguish parasite types since the parasite identity is preserved. To distinguish the closeness of parasite and parasite thickness a dense bloodstain is introduced. A dense blood smear is more susceptible to multiple times than a thin blood smear, as it requires a greater amount of blood to be assessed [2].□

Malaria is generally diagnosed by manual microscopic examination of blood slide, which is named as "gold standard". However, the manual method of diagnosis is tedious, requires expert technicians, and prone to human errors. Besides, it also incurs a high cost for the training of technicians [6]. Considering these problems, the automatic analysis of the microscopic images for the diagnosis of malaria disease has gained importance. This motivated us to carry out this study to develop image-contrast enhancement and segmentation methods for rapid and accurate diagnosis of malaria through microscopic blood images [14].□

## II. LITERATURE REVIEW

Sathpathi et al., have proposed Microscopy of fringe blood slender with deep movies leftovers orientation for intestinal sickness conclusion. Even though Giemsa recoloring is most regularly utilized, the Leishman recoloring strategy gives a better perception of the atomic chromatin example of cells. It is less notable whether the exactness of parasitemia evaluation is similarly precise by the last strategy.□

Naveed Abbas has proposed malaria parasitemia by the quantitative estimation of parasites within blood toward study level of disease. Light microscopy is a mainly excellent strategy used to study the blood for parasitemia assessment. Illustration evaluation of jungle fever parasitemia is relentless, tedious as well as emotional. Even though robotizing the procedure is a decent arrangement, the

accessible strategies can't assess similar cases, for example, weakness and hemoglobinopathies because of deviation from ordinary RBCs' morphology.

Katherine Torres has proposed Microscopic assessment of Giemsa-recolored blood films stays a significant type of conclusion in malaria disease and is a reference standard for learning about. Nonetheless, similarly as with other perception-based conclusions, exactness relies upon singular professional execution, making institutionalization troublesome and dependability poor. Computerized image acknowledgment dependent on AI, using convolutional neural structures, gives the potential to conquer these disadvantages. A model automatic magnifying lens system utilizing a calculation depending on AI, the Autoscope, turned into evaluated for its capacity in malaria disease microscopy. In 2016, Autoscope became an effort at two fringe health offices in the Peruvian city of Iquitos, with repeated microscopy and PCR as guide norms. The important result measurements include the effect and accuracy of diagnosis commitment from Giemsa-recolored blood films, use PCR as a guide. □

Ishan R.Dave, have created an endeavor in the preprocessing step to diminish varieties because of different components like lighting conditions and centralization of recoloring arrangement. The image is fragmented utilizing versatile thresholding, trailed by a few numerical morphological tasks. In the subsequent advance, different highlights dependent on shape, surface, shading, and recurrence space are separated. Utilizing the grouping step, the parasites are arranged into their right life stage or delegated leukocytes. The curiosity of the calculation is that it can recognize all the existence stages (ring, trophozoite, schizont, and gametocyte) of parasites and leukocytes [21]. It is not like identifying just ring life organize but is the best in class calculations. The inconsistency in the computerized parasite tally by the proposed calculation is 7.14%, which is appropriate for PC based diagnosis (CAD) of malaria disease as indicated by world wellbeing association (WHO) quality control norms.

### III. PREPROCESSING & SEGMENTATION

Right now, image is portioned into a frontal area (recolored particles for example parasites of all existence degrees, leukocytes, platelets, and numerous exclusive relics) and basis (nonstained particles as an example liaised purple platelets). Countless bogus high-quality (recolored gadgets) may come as locales of intrigue, to be wiped out in subsequent segments. The caught images are changed over in HSV color space to lessen sorts due to beauty and convergence of stain arrangement, which profoundly influences in RGB color space [4]. Stained and uncolored particles have a critical difference in their path of immersion. Owing to clamor, the picture immersion channel is divided by an ordinary channel of duration 3 along the way to reduce large variety. In Figure1, the histogram of direct immersion is considered. Since a large portion of the non-recolored molecule has poor channel appreciations for immersion, the investigation is done utilizing adaptive

histogram thresholding of segmented particles from the immersion tube. As it appears in Figure1, the recolored portion of debris covers a small quarter of the histogram's X-pivot. We can still observe that the recolored particles have a Cumulative Distribution Function (CDF) values greater than zero. Ninety-five after finding CDF. The stage of dimension is where CDF=0.95 is taken. Using this Immersion channel picture at an edge level is binarized as shown in Equation beneath.

$$\text{Pixel value} = \begin{cases} 1, & \text{if saturation value} > T \\ 0, & \text{if saturation value} < T \end{cases}$$

*where, CDF(x = T) = 0.95*

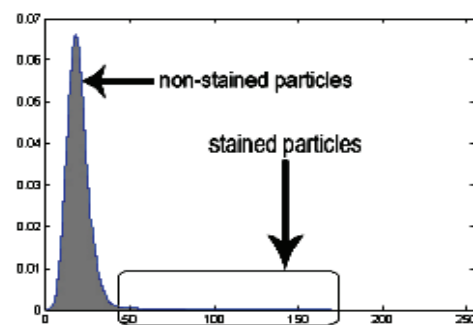


Figure 1. Histogram of saturation channel

The output of adaptive histogram thresholding is appeared in Figure 2(a). Numerical morphological tasks are utilized to remove the ideal segments from the portioned parallel image [2]. Openings are dispatched to kill little foundation regions inside the frontal area shape (Figure 2(b)). It is trailed by shutting activity to fill the little holes between segments of a similar molecule (Figure 2(c)). Shutting activity is performed utilizing a circle molded organizing component of range 3. Openings are filled again to take out foundation pixels inside closer view shapes (Figure 2(d)). □

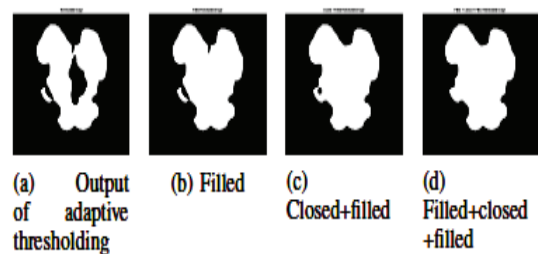


Figure 2. Mathematical morphological operations

The yield after morphological tasks appears in Figure 3.



Figure 3. The output of preprocessing & segmentation step.

#### IV. PROPOSED METHODOLOGY

##### A. Minuscule Image grabbing and preprocessing

The critical point of our framework is to observe the perimeter blood spread and distinguish any parasitemia via utilizing image investigation on the procured pix. The securing of the image is a substantial increase within the complete technique. We make use of a compound first-rate discipline magnifying lens to filter the slides in-situ. This is done through and through the body under a trained pathologist's guidance. When collecting the image of the entire frame, the pathologist selects a particular area of interest (ROI). The chosen ROI is grabbed and distributed correctly through the analysis system [4, 25]. The use of morphology [8], Shading Correction [9], and wavelet techniques, primarily based on definite techniques, has had powerful effects on the identification of malaria parasites from blood smear pix. It is clear that the pictures obtained and sent are small in quality and are boisterous. Subsequently, we use de-noise, and the picture enhances techniques to configure the suitability of the dividing file. □

We use the interscale symmetrical wavelet-based thing that is some other Stain's Objective Risk Estimator (SORE) way to cope with Unser et al-supported picture de-noise[6] for de-noise. The image histogram shows an amazing top; in the middle, we get wonderful results from using the Brightness Preserving Dynamic Histogram Equalization (BPDHE) measurement [16]. They will always remember at the department's computer and promise to go into the subtleties of the methodology of de-noise and enhancement right now.

##### B. Shading Space Conversion

Shading space transformation is the initial section in the imaging exam and carried out before running Normalized Cut (NCut) calculation for the mobile division. They are changing over the minute pics into extraordinary shading spaces (RGB to HSV, RGB to YCbCr and RGB to NTSC). Images are commonly placed away and showed inside the RGB area. Be that as it can, to guarantee the isotropy of the element area, a uniform shading area with the apparent shading contrasts anticipated with the aid of Euclidean separations have to be applied[5]. Here we are looking at the presentation of NCut calculation in 4 shading space (RGB, HSV, YCbCr, and NTSC).

##### C. Division with Normalized Cut

(Cap) the calculation above modified over shading area NCut be a solo division method that doesn't require an introduction and approaches the division issue as a chart dividing issue. NCut depends on a worldwide paradigm, and it expands both the complete divergence between the various gatherings and the absolute similitude inside the gatherings [7].

**RGB:** It is equipment situated model and is notable for its shading screen show reason. The NCuts on RGB appear empowering results yet it is likewise debased with loads of deceptive sections which make the framework not reasonable for computerized techniques.

**HSV:** Tone (H) is a shading quality that depicts an unadulterated shading, while immersion (S) characterizes the relative immaculateness or else sum of white light blended in by tone; esteem (V) alludes toward splendor of image as shown in figure (4).

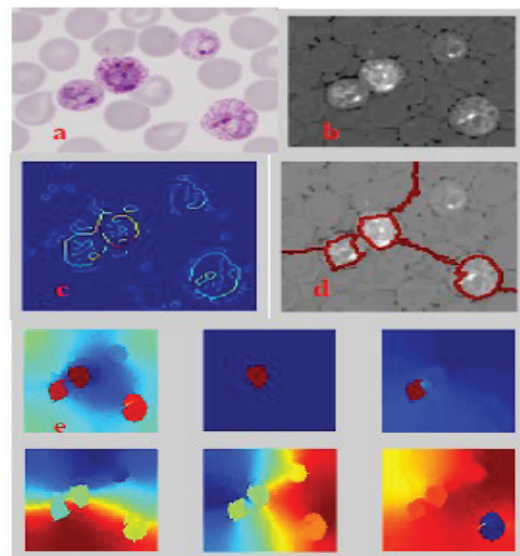


Figure 4. The images \* demonstrate segmentation in the HSV color field sing nsegment=6(a)microscope image, (b) Brightness image, (c) Edge view, (d) Segment display, (e) Eigenvectors display.

This model is seen as generally appropriate. When all is said in (and) done, HSV is generally utilized for image handling applications however the essential usage of NCut depends on RGB shading space. The outcomes here unmistakably delineate an enhanced presentation of NCut in HSV for minute images.

##### D. Extracting Red Blood Cell Mask

The vast majority of the malaria parasites exist in red platelets, along these lines if red platelets are isolated from different components of blood, the precision and speed of identifying intestinal sickness parasites are improved essentially. We rendered a paired picture to this closing by using Otsu's thresholding. It deserves to refer to the fact that

the calculation of restriction is derived from the base measure of the inner distinction of the given weight in Otsu's method, and as shown by the critical principle, it follows up on images of grayscale. This technique is a good response for getting to paired images without losing information, particularly in the blood scope tests. To have an ideal parallel picture to suit the item's early tissue, it is necessary to perfect the precision of the matched image with the aggregation of the two-aspect identification images from Canny's approach and the double image from Otsu's approach. At that point, the components which aren't stuffed, because of the absence of exactness in thresholding, can be crammed all over again. Since the discovering crimson platelets within the image are the factor of this method, undesired components that were littler than red platelets be erased through morphology activity. For doing this, a plate shape auxiliary component be utilized [8] □

**E. Cell Feature Evaluation and Selection**

When cells have identified as well as portioned from, take an entire image within the subsequent stage, we extricate every sectioned cell and portray them by their shading and surface data to recognize tainted cells from typical cells inside a learning structure. Figure 5 shows instances of separated contaminated and typical cells (first and second lines) for human-NIAID (first section) and mouse-NIAID (second and third segment) data sets.

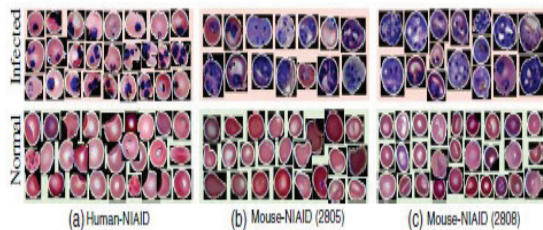


Figure 5. Separated, contaminated and Typical cells

Definitions of contaminated (first row) and regular (second row) cells collected for (a) human-NIAID, (b) mouse-NIAID dataset 2805, and (c) mouse-NIAID 2808.

We read different highlights to represent normal and anomalous cells and analyzed their appearance using SVM and ANN classifiers to pick the most unequal group of components. We analyzed the presentation on both SVM and ANN to prove that the best list of capacities beats different autonomous highlights from the classifier used [25]. In highlight assessment tests, we utilized earth fact explanations toward remove cells along with decoupling exhibition of highlights and classifiers from our programmed division outputs.

**V. RESULTS**

Plasmodium Vivax data set (37 images), includes pictures of both dense and thin blood spreads for all levels of dwelling growth (Trophozoite, Gametocytes, Ookinete, and Schizonts). Our experiments preclude gametocytes and the Ookinete classes since the human body is out of bounds. In

the trial, we break the trophozoites (ring configuration and formative levels) and the Schizonts. Figure 6 shows the. Images of diverse tiers of improvement of malaria parasite interior human blood. The formative levels are represented in discern 8 (a-h), the division outcomes of the equation are given in parent 10. The perceptions display that the consequences were given utilizing the HSV shading area gives the most precise outcomes. The facts pix containing 1-four amazing protozoa inflamed cells are notions about this deliberation.

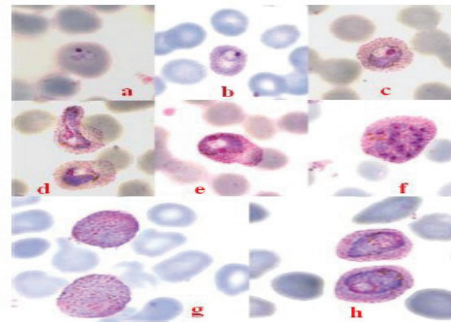


Figure 6. Images of diverse tiers of improvement of malaria parasite interior human blood grabbed using shiny challenge microscope

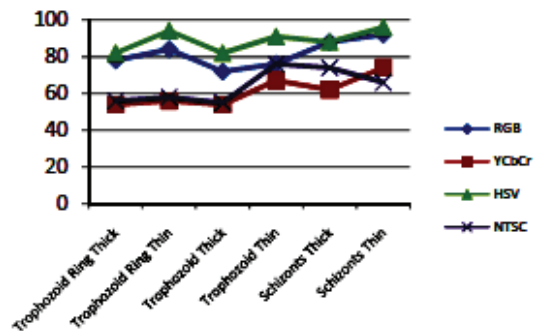


Figure 7. Presentation of segmentation

The proportional presentation of segmentation uses specific color areas on numerous ranges of parasitic proliferation the use of leveled RI's. It is shown in Figure 7. Different proportional segmentation uses different color areas on numerous ranges of parasitic proliferation. The segmentation of corresponding degrees of parasitic proliferation and degrees of improvement of the malaria parasite is shown in Figure 8.

We likewise attempted the calculation on images having diverse overlaying RBCs, comparable yields, comparable effects beneath those situations additionally. The RGB execution appears to move downward by compound multi-cell sights yet HSV is visible toward increasingly constant regardless of change of cells in the foundation and without malarial cells. Slide pix segmentation is prepared based on and without inflamed RBC's as shown in Figure 9. Recall that the special snapshots, b, e give away the polluted, flamed RBCs while c,f give away the non-inflamed RBCs.

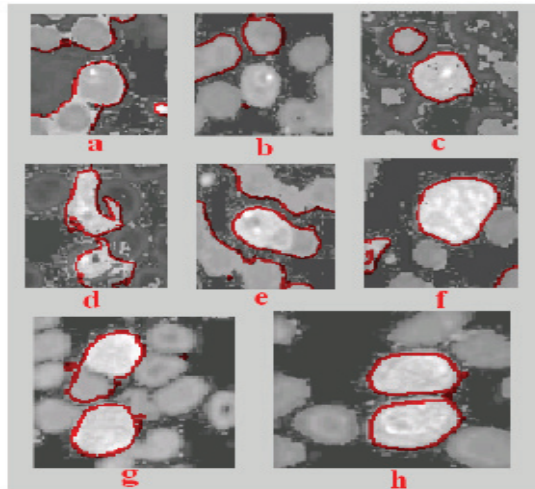


Figure 8. The segmentation of corresponding degrees of parasitic proliferation almost about numerous degrees of improvement of the malaria parasite

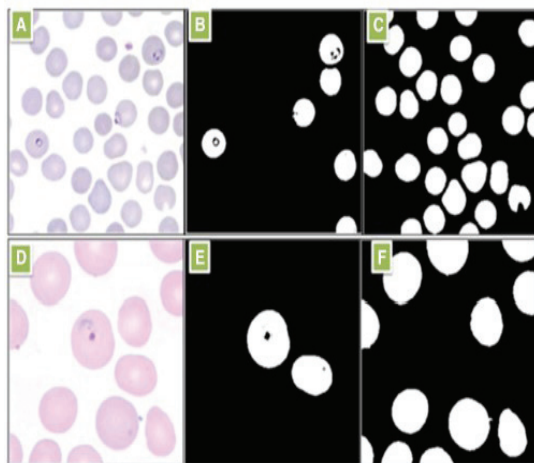


Figure 9. Slide pix segmentation system with inflamed RBCs

## VI. CONCLUSIONS

This paper presents a computationally gifted technique for branch and portrayal of malarial parasites from fringe blood smear images. Outcomes show that NCut calculation is excellent within the HSV shading region. The coloration of the parasites is the principle one in each type a property and this is the equivalent in all moderate blood smear advanced images. In any case, the methodology experiences commotion, however, we tended to it by dropping its impact is twofold totally. The method proposed is here automatic, more precise compared to other available methods, and also rapidly eliminating the human interventions in the diagnosis.

## REFERENCES

1. Sathpathi et al, 2014, “Comparing Leishman and Giemsa staining for the assessment of peripheral blood smear preparations in a malaria-endemic region in India”
2. Walliander t al, 2012 “Automated segmentation of blood cells in Giemsa stained digitized thin blood films”

3. Katherine Torres, Automated microscopy for routine malaria diagnosis: a field comparison on Giemsa- stained blood films in Peru.
4. Leila Malihi, Malaria Parasite Detection in Giemsa–Stained Blood Cell Images, 2013.
5. Ishan R. Dave, Image Analysis for Malaria Parasite Detection from Microscopic Images of Thick Blood Smear, 2018.
6. Mahdieh Poostchi, Malaria parasite detection and cell counting for human and mouse using thin blood smear microscopy, 2020.
7. Subhamoy Mandal, 2010, Segmentation of blood smear images using normalized cuts for detection of malarial parasites
8. Naveed Abbas, 2016, “Machine aided malaria parasitemia detection in Giemsa-stained thin blood smears”.
9. K. Abba, J.J. Deeks, P. Olliaro, C-M. Naing, S.M. Jackson, Y. Takwoingi, S. Donegan, and P. Garner. Rapid diagnostic tests for diagnosing uncomplicated p. falciparum malaria in endemic countries. *Cochrane Database Syst Rev*, 7, 2011.
10. L. Allen, J. Hatfield, G. DeVetten, J. Ho, and M. Manyama. Reducing malaria misdiagnosis: the importance of correctly interpreting Para check Pf. *BMC infectious diseases*, 11(1):308, 2011.
11. B.B. Andrade, A. Reis-Filho, A.M. Barros, S.M. Souza-Neto, L.L. Nogueira, K.F. Fukutani, E.P. Camargo, L.M.A. Camargo, A. Barral, A. Duarte, and M. Barral-Netto. Towards a precise test for malaria diagnosis in the Brazilian Amazon: comparison among field microscopy, a rapid diagnostic test, nested PCR, and a computational expert system based on artificial neural networks. *Malaria Journal*, 9:117, 2010.
12. J. Bailey, J. Williams, B.J. Bain, J. Parker-Williams, and P.L. Chiodini. Guideline: the laboratory diagnosis of malaria. *British Journal of Hematology*, 163(5):573–580, 2013.
13. D.N. Breslauer, R.N. Maamari, N.A. Switz, W.A.Lam, and D.A. Fletcher. Mobile phone-based clinical microscopy for global health applications. *PLoS One*, 4(7):e6320, 2009.
14. M. Everingham, L. Van Gool, C.K.I. Williams, J. Winn, and A. Zisserman. The PASCAL Visual Object Classes (VOC) Challenge. *International Journal of Computer Vision*, 88(2):303–338, 2010.
15. P. Geurts, D. Ernst, and L. Wehenkel. Extremely randomized trees. *Machine Learning*, 63(1):3–42, 2006.
16. H.J.A.M. Heijmans. *Morphological Image Operators*. Academic Press, Boston, 1994.
17. H.J.A.M. Heijmans. Connected morphological operators for binary images. *Computer Vision and Image Understanding*, 73:99–120, 1999.
18. Mobile Point-of-Care Monitors and Diagnostic Device Design
19. B. Houwen. Blood film preparation and staining procedures. *Laboratory Hematology*, 6(1):1–7, 2000.
20. D.S. Ishengoma, F. Francis, B.P. Mmbando, J.P.A. Lusingu, P. Magistrado, M. Alifrangis, T.G. Theander, I.C. Bygbjerg, and M.M. Lemnge. Accuracy of malaria rapid diagnostic tests in community studies and their impact on the treatment of malaria in an area with a declining malaria burden in north-eastern Tanzania. *Malaria Journal*, 10:176, 2011.
21. M. Kiggundu, S.L. Nsohya, M.R. Kanya, S. Filler, S. Nasr, G. Dorsey, and A. Yeka. Evaluation of a comprehensive refresher training program in malaria microscopy covering four districts of Uganda. *The American Journal of Tropical Medicine and Hygiene*, 84(5):820, 2011.
22. O.A. Koita, O.K. Doumbo, A. Ouattara, L.K. Tall, A. Konar’ e, M. Diakit’ e, M. Diallo, I. Sagara, G.L. Masinde, S.N. Doumbo, et al. False-negative rapid diagnostic tests for malaria and deletion of the histidine-rich repeat region of the hrp2 gene. *The American Journal of Tropical Medicine and Hygiene*, 86(2):194–198, 2012.



23. V.V. Makkapati and R.M. Rao. Segmentation of malaria parasites in peripheral blood smear images. IEEE International Conference on Acoustics, Speech and Signal Processing, 2009.
24. L.M. Milne, M.S. Kyi, P.L. Chiodini, and D.C. Warhurst. Accuracy of routine laboratory diagnosis of malaria in the United Kingdom. *Journal of clinical pathology*, 47(8):740–742, 1994.
25. M.G. Mubangizi, C. Ikae, A. Spiliopoulou, and J.A. Quinn. Coupling spatiotemporal disease modeling with the diagnosis. In *Proceedings of the International Conference on Artificial Intelligence (AAAI)*, 2012.
26. C.K. Murray, R.A. Gasser, A.J. Magill, and R.S. Miller. Update on rapid diagnostic testing for malaria. *Clinical Microbiology Reviews*, 21:97–110, 2008.
27. World Health Organization. Malaria light microscopy: creating a culture of quality. In *Report of WHO SEARO/WPRO workshop on quality assurance for malaria microscopy*, Geneva, 2005.
28. D. Payne. Use and limitations of light microscopy for diagnosing malaria at the primary health care level. *Bulletin of the World Health Organization*, 66(5):621, 1988.

# A Smart Machine Vision based Inspection System

Dr. Santosh Kumar Sahoo

Assoc. Professor, CVR College of Engineering/EIE Department, Hyderabad, India

Email: santosh.kr.sahoo@gmail.com

**Abstract:** This article proposes a unique optimization like Adaptive Cuckoo Search (A<sub>a</sub>CS) algorithm followed by an Intrinsic Discriminant Analysis (IDA) to design a smart intelligent object classifier for inspection of defective object like bottle in a manufacturing unit. By using this methodology, the response time is very faster than the other techniques. The projected scheme is authenticated using different benchmark test functions and in the next part of the article proposes an efficient recognition algorithm for identification of bottle by using A<sub>a</sub>CS, Principal Component Analysis (PCA) and IDA. Due to this the proposed algorithms terms as PCA+IDA for dimension reduction and A<sub>a</sub>CS-IDA for classification or identification of defective bottles. The analyzed response obtained from by an application of A<sub>a</sub>CS algorithm followed by IDA and compared to other algorithm like Least-Square-Support-Vector-Machine (LSSVM) along with Linear Kernel Radial-Basis-Function (RBF) to the proposed model, the earlier applied scheme reveals the remarkable performance.

**Index Terms:** Adaptive Cuckoo Search (A<sub>a</sub>CS) algorithm, Intrinsic Discriminant Analysis (IDA), Principal Component Analysis (PCA), intelligent object classifier, least square Support Vector Machine (LSVM), Smart inspection.

## I. INTRODUCTION

Due to rapid growth of industry to meet the society's requirement it is necessary for maintaining a quality product. In order to achieve this, most of the manufacturing unit follow the automation scheme as a result a finished quality product can be delivered to an end user within an optimum interval. So, in most of the automation, an image processing scheme is used to facilitate the model more efficient to recognize the object of interest in a smooth manner. The proposed model uses an artificial intelligent scheme for recognition of defective bottle in a manufacturing unit where the different algorithm and techniques are used to validate the suggested plan. Before object identification it is highly necessary to reduce the dimension of the captured image by an application of different linear tools such as PCA, LDA as well as some nonlinear tools like Artificial neural network scheme (ANN), isometric mapping, locally linear embedding and Laplacian Eigen maps etc. But apart from this the linear tools are the best choice because the nonlinear tools required heavy computational work for different parameter tuning and lack of handling capacity for testing data as compared to linear one. The PCA projects the high dimension data into a set of basis function to get a squeezed demo of the original data as a result dimension reduction is achieved and it mainly reflects the Eigen faces of the detected image features. Likewise, LDA reflects the features as a Fisher faces in which the data points of different classes are mapped with an optimum gap or distance. The IDA method is used to maximize the

uniqueness dissimilarities in the meantime the intrapersonal difference is minimized. Again, the selection procedure for optimal Eigen vector is inaccurate. So, to overcome this problematic condition the PCA + IDA algorithm remains used for increasing the performance level then this performance is compared with the other identification techniques like K<sup>TH</sup>NN, ANN, SVM and LSSVM method. Finally, it is concluded that the projected scheme be able to classify impaired bottle promptly as well as accurately. Therefore, the curative exploit determination be continuing on a crucial stage of manufacturing progression so that the ruin quality risk be adjusted.

Nouri et. al [1] examined a classification model for recognize a printed Arabic name using density weight and zigzag techniques. The proposed model was validated using KNN and support vector machine classifier. K Tafi et.al [2] described a breast cancer analysis scheme established on wavelet exploration and neural networks. Jayachandran et.al [3] explained about a PC aided judgment of cancer in brain MRI pictures by wavelet techniques and an Ada-Boost classifier. Nayak et.al [4] explained about a time efficient clustering algorithm for gray scale image segmentation and evaluated different clustering algorithms. Gharehchopogh et.al [5] described a novel approach for edge detection of an image by using cellular learning automata (CLA) techniques. Dixit et.al [6] demonstrated an Indian sign language recognition system using a vision approach where a multi class support vector machine algorithm was used. Dubey et.al [7] explained about different fruit disease identification by using image processing scheme like K-means clustering and multi class support vector machine classifier and their proposed model claimed an accuracy of about 93%. Win et.al [8] implemented a structural analysis-based feature extraction technique for optical character recognition system for Myanmar printed document. Anitha et.al [9] explored a cross breed hereditary procedure grounded fuzzy tactic aimed at retinal image grouping. Krol et.al.[10] implemented a real time automatic mechanism aimed at image and speech acknowledgement centered on neural network where a Neuro car-based system and Neuro scope were used to validate the proposed model. Santo.et.al [11] described different replicated forging schemes. Yaremchuk et.al [12] examined the classification of musical cords by means of artificial neural network. Xu. Et.al [13] demonstrated about an iris acknowledgement scheme by means of Intersecting Cortical Model (ICM) neural network. During investigation the captured image was processed and analyzed by ICM neural network. Xing

at.al [14] described about three-dimensional object classification based on volumetric parts in which super quadric based Geon description was implemented to representing the volumetric elements of 3D object. Tim et.al [15] examined the firmness efficiency of joint photographic three-dimensional medical images.

## II. PROPOSED ALGORITHM

This proposed optimization algorithm uses an Adaptive Cuckoo Search (AdCS) algorithm followed by an Intrinsic Discriminant Analysis (IDA) to design a smart intelligent object classifier for inspection of defective object like bottle in a manufacturing unit.

### A. BASICS ON WAVELET TRANSFORM, PCA, IDA AND CUCKOO SEARCH ALGORITHMS

#### Wavelet Transform

Object identification or inspection deals with the high dimensionality of image space under consideration. So a method termed as wavelet transform can be used to decompose the data without gaps or overlap. Considering an image of a bottle as shown in Figure 1 and corresponding segmented picture meant for faulty after preprocessing be presented in Figure 2.



Figure 1. Defective bottle's segmented image

$$\begin{bmatrix} -1 & -2 & -1 \\ 0 & 0 & 0 \\ 1 & 2 & 1 \end{bmatrix}$$

Figure 2. The mask gradient value

At this moment the wavelet constants for corresponding image are stated as [6] in equation-1 & 2:

$$w_{\psi}(I_0, L, K) = \frac{1}{\sqrt{I \times k}} \sum_{u=0}^{I-1} \sum_{v=0}^{k-1} F(u, v) \phi_{I_0, L, K}(U, V) \quad (1)$$

$$w_{\psi}^J(I, L, K) = \frac{1}{\sqrt{I \times k}} \sum_{u=0}^{I-1} \sum_{v=0}^{k-1} F(u, v) \phi_{I, L, K}^J(U, V) \quad (2)$$

Where  $\phi_{I, L, K}^1(U, V) = 2^{J/2} \varphi(P^J U - L, P^J V - K)$  and

$$\phi_{J_0, MN}^J(U, V) = 2^{J/2} \varphi(P^J U - L, P^J V - K)$$

Here  $P$  value is considered as 2. At present the Energy anticipated totally in vertical, horizontal and diagonal directions as per Figure 3 [5]. As three level of decomposition remains cast-off accordingly the Energy for each wavelet constants are [4] in equation 3.

$$e_{c,l} = \frac{1}{|x|} \sum_{I=0}^L \sum_{L=0}^L (w_{c,I,L})^2 \quad (3)$$

Where  $w_{c,I,L}$  equal to wavelet constant at  $[I, L]$  location [1-6].

Approximate Significance of pixel(3)	Horizontal meticulous significance of pixel(3)	Horizontal meticulous significance of pixel(2)	Horizontal meticulous significance of pixel(1)
Vertical meticulous significance of pixel(3)	Diagonal Meticulous significance of pixel(3)		
Vertical meticulous significance of pixel(2)		Diagonal Meticulous significance of pixel(2)	Diagonal Meticulous significance of pixel(1)
Vertical meticulous significance of pixel(1)			

Figure 3: A three level Wavelet transform structure

#### PCA

Similarly in PCA a best prediction hatchets from a composite strew of expected samples as a result the total scatter matrix is expressed as [7] in equation-4

$$M_S = \sum_{j=1}^K \sum_{i=1}^{L_i} (X_j^i - \mu)(X_j^i - \mu)^T \quad (4)$$

Where  $\mu = \frac{1}{L} \sum_{j=1}^K \sum_{i=1}^{L_i} (X_j^i)$  the mean value and the PCA

objective function is set by  $O_{PCA} = \underset{O}{\text{Arg max}} |O^T M_S O|$ .

Hence the optimum projections of PCA are

$O_1, O_2, O_3, \dots, O_n$  which basically orthogonal eigenvectors are of  $M_S$ .

**IDA:** Likewise the IDA is a linear projection based approach and based on individuality difference. It minimizes the individuality difference. The IDA based features for Object recognition are created as intrinsic objects. Let the a 'n' image sample of 'y' different classes  $(C_1, C_1, \dots, C_y)$  and each class has  $n_i$  numbers

of samples in class  $C_i$  and  $n = \sum_{i=1}^y n_i$ . Again each

image be presented as  $p \times q$  matrix and modeled as d-dimensional ( $d = p \times q$ ) vector formed through a two dimensional pixel array. As a result a set of points presented in equation-5, 6, 7, 8, 9, 10, 11, and 12

$$\begin{pmatrix} X^a, \dots, X^a & \dots & X^y, \dots, X^y \\ 1 & n_1 & 1 & n_y \end{pmatrix} \quad (5)$$

where  $X_J^I$  is the  $J^{th}$  sample in  $I^{th}$  Class are obtained. Now gathering all the points in to a single matrix  $x$  of size  $d \times n$  as [8]

$$x^J = [X_1^J, X_2^J, \dots, X_{n_j}^J] \in \mathbb{R}^{d \times n_j} \quad (6)$$

Assuming a matrix which represents the  $J^{th}$  class of images as

$$x^J = [X_1^J, X_2^J, \dots, X_{n_j}^J] \in \mathbb{R}^{d \times n_j} \quad (7)$$

, then the 'x' be able to voice as [9]

$$x = [X^1, X^2, \dots, X^y]. \quad (8)$$

If a matrix  $M_T$  is express as [10]-[11]

$$M_T = [X_1^1 - \mu, X_2^1 - \mu, \dots, X_{n_y}^y - \mu] \in \mathbb{R}^{d \times n} \quad (9)$$

Then the singular value decomposition (SVD) of  $M_T$  is expressed as [12].

$$M_T = U \Sigma V^T \quad (10)$$

Where  $U = [U_r, \overline{U_r}]$ ,  $U_r \in \mathbb{R}^{d \times n_j}$ ,  $\overline{U_r} \in \mathbb{R}^{d(d-r)}$ ,  $V = [V_r, \overline{V_r}]$ ,  $V_r \in \mathbb{R}^{n \times r}$ ,  $\overline{V_r} \in \mathbb{R}^{n(n-r)}$ ,  $\Sigma = \begin{bmatrix} \Sigma_r & 0 \\ 0 & 0 \end{bmatrix}$  is a non-singular and  $R =$

Rank .

Then after for the  $J$ th class matrix

$$M_T^J = [X_1^J - \mu, X_2^J - \mu, \dots, X_{n_j}^J - \mu] \in \mathbb{R}^{d \times n_j}, \text{ the SVD of } M_T^J \text{ as [13] } M_T^J = U^J \Sigma^J V^{JT} \quad (11)$$

Where

$$U^J = \begin{bmatrix} U_r^J & \overline{U_r^J} \\ \overline{U_r^J} & \overline{U_r^J} \end{bmatrix}$$

$$U_{r^J}^J \in \mathbb{R}^{d \times r^J}, \overline{U_{r^J}^J} \in \mathbb{R}^{d \times (d-r^J)}, r^J = \text{rank}(M_T^J)$$

An IDA can maximize the difference between the separate classes of images while minimizing the difference within the similar classes of images. Or in other hand IDA tries to make best use of the fraction of the individuality deference distributed Matrix. Now the objective function of IDA is expressed as [14]-[15]

$$O_{IDA} = \arg \max_o \frac{|O^T M_c O|}{|O^T M_i O|} \quad (12)$$

The optimal transformation vector is taken from  $q$  number of eigenvalues such that  $\lambda_1 \geq \lambda_2 \geq \dots \lambda_q$  this can be achieved by solving the eigenvalue problem  $M_c p = \lambda M_i p$ .

### Cuckoo search Algorithm:

This method considers the communal thoughtful ability of a Cuckoo bird. Generally, the Cuckoo leaves an egg in the nest of the crow's nest. The crow may

be recognizing the cuckoo's egg with a probability of then the crow through the eggs from the nest or abandons the next to form a new nest. So now every single egg in the host shell signifies a explanation and to form this one towards a mathematical model the following assumptions are taken as: Available host nests are fixed, Assuming every single Cuckoo be able to lays only single egg at a phase by the side of the randomly selected host net, the finest nets by utmost eminence eggs will transport forward for subsequent generation. Suppose is the present hunt space of Cuckoo  $J$  for ( $J=1,2,3,\dots,n$ ) at time  $t$  represented as  $x_J(t) = (X_J^1, X_J^2, \dots, X_J^d)$  in the 'd' dimension problem at that time the innovative key  $x_J(t+1)$

for the next generation of interval  $(t+1)$  be able to conveyed by way of  $x_J(t+1) = x_J(t) + \alpha \oplus \text{levy}(\lambda)$ . Where  $\alpha =$  stair dimension and usually this value should be taken as 1, the  $\oplus$  symbol signifies multiplication entry wise and  $\text{levy}(\lambda)$  reflects unsystematic walk through levy flight for distribution. Now

$$\text{levy}(\lambda) = \frac{u}{|v|^{\frac{1}{\lambda-1}}} \quad (13)$$

Considering the present generation 't' and predetermined maximum lifetime iteration  $t_{\text{Max}}$ , the Cuckoo at initial generation ( $t=1$ ) can be reflected as  $x_J^d(t=1) = \text{randx}(\text{Upper}^d - \text{Lower}^d) + \text{Lower}^d$  (14)

Where  $\text{Upper}^d$  and  $\text{Lower}^d$  are termed as upper and lower boundaries of the search space.

As the Cuckoo search algorithm uses the levy steps to discover the search space which is taken from levy distribution. Here in proposed algorithm the Cuckoo search algorithm is modeled without using levy distribution. Hence the step size or stair dimension [7] here considered remains proportionate to suitability of the singular shell in hunt galaxy for present peer group. Now this algorithm gives the step size

$$\text{as } \text{Step}_J(T+1) = \left( \frac{1}{T} \right)^{\frac{|(\text{bestf}(T) - f_J(T))|}{|(\text{bestf}(T) - \text{worstf}(T))|}}, \text{ here 'T'}$$

signifies the peer group of the Cuckoo exploration,  $f_1(T) =$  fitness cost for  $J^{th}$  nest,  $\text{best } f_1(T)$  is finest fitness cost in peer group 'T' then  $\text{worst } f_1(T) =$  worst fitness cost in the peer group 'T'.

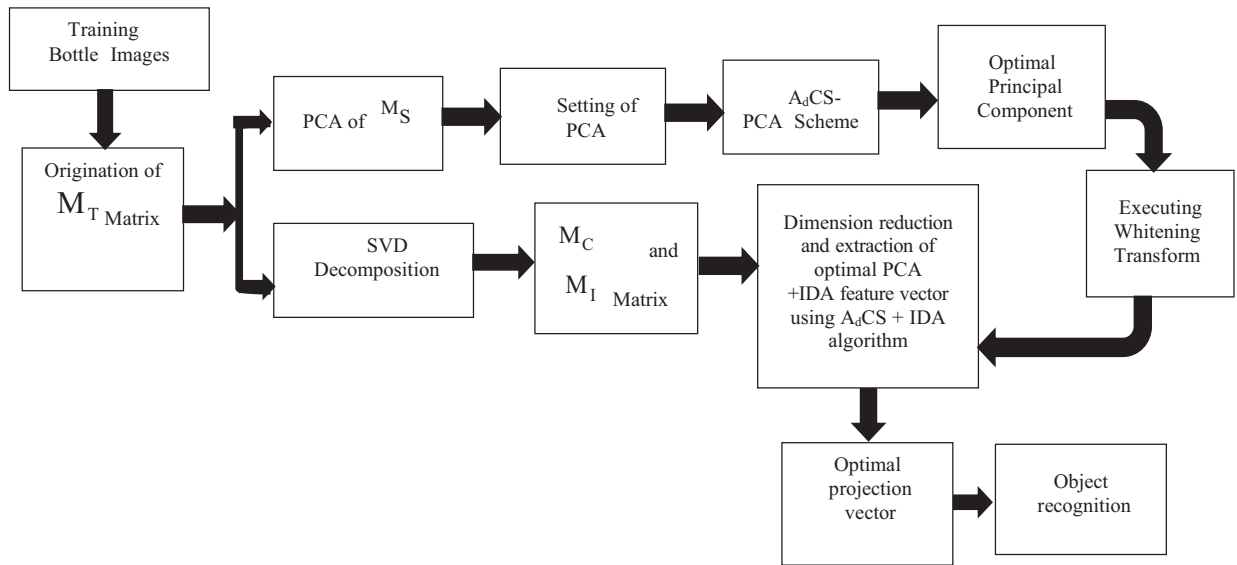


Figure 4. Bottle inspection using PCA plus IDA Scheme

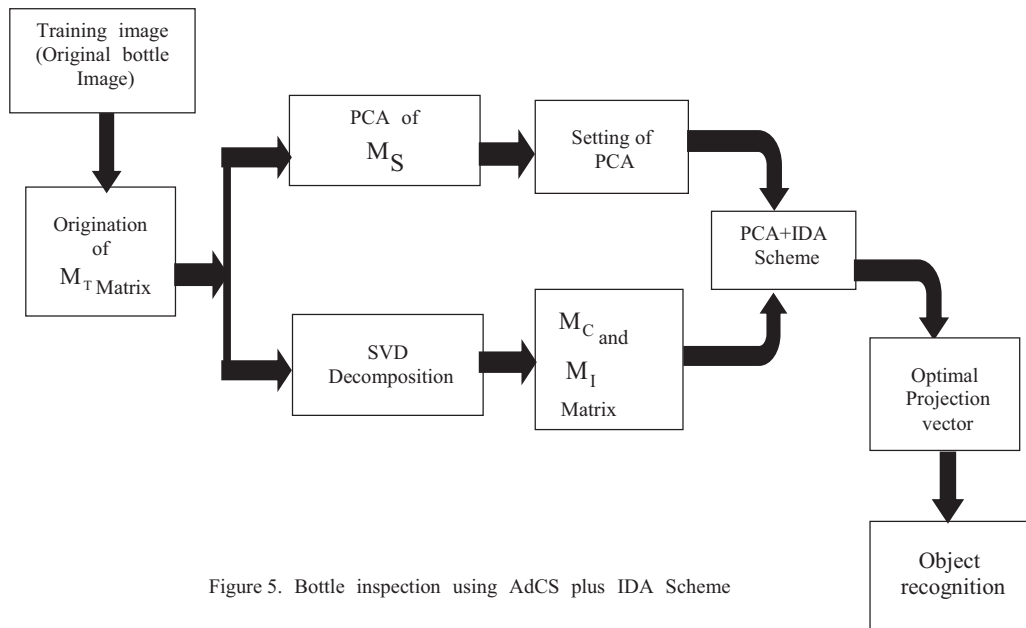


Figure 5. Bottle inspection using AdCS plus IDA Scheme

TABLE I.  
BOTTLE INSPECTION PERFORMANCE

No. of Training Image	Algorithm	Run Time (Sec)	Rank 1 in %	Rank 2 in %	Rank 3 in %	Rank 4 in %	Rank 5 in %	Rank 6 in %	Rank 7 in %	Rank 8 in %	Rank 9 in %	Rank 10 in %
3 Train	<b>A<sub>d</sub>CS-IDA</b>	<b>8.15</b>	<b>79.4</b>	<b>83.6</b>	<b>86.8</b>	<b>92.5</b>	<b>93.4</b>	<b>93.4</b>	<b>94.4</b>	<b>98.2</b>	<b>98.5</b>	<b>98.5</b>
	PCA+IDA	61.44	76	81.7	84.2	91.5	92.1	93.7	94.4	96.8	96.8	96.8
	IDA		76	76.6	79.2	89.6	89.2	89.4	92.6	92.6	94.4	94.3
4 Train	<b>A<sub>d</sub>CS-IDA</b>	<b>8.05</b>	<b>79.2</b>	<b>82.6</b>	<b>83.8</b>	<b>91.4</b>	<b>93.4</b>	<b>93.8</b>	<b>95.4</b>	<b>97.4</b>	<b>98.4</b>	<b>98.4</b>
	PCA+IDA	33.94	78.2	80.2	83.2	91.4	92.3	93.8	94.2	96.6	96.5	96.5
	IDA		76	76.6	79.2	89.6	89.2	89.4	92.6	92.6	94.4	94.4
5 Train	<b>A<sub>d</sub>CS-IDA</b>	<b>7.11</b>	<b>89.6</b>	<b>91.6</b>	<b>92.4</b>	<b>92.6</b>	<b>93.7</b>	<b>94.8</b>	<b>95.7</b>	<b>97.6</b>	<b>98.5</b>	<b>98.7</b>
	PCA+IDA	13.6	87.2	84.2	86.4	92.3	93.4	93.9	94.6	96.7	96.8	96.8
	IDA		84.2	84.8	86.7	88.4	90.4	91.8	92.8	93.2	94.8	94.8

Initially stair dimension is more, while No. of peer group rises then the step size is declines which directs overall finest solution. Now  $A_dCS$  [27] represented as  $x_j(T_m + 1) = x_j(T_m) + randn \times Step_j(T_m + 1)$ . Assuming  $T_m = T$  (15)

The above expression it is concluded that the  $A_dCS$  does not required any initial parameter and it is very faster than cuckoo search techniques. The proposed algorithm structure is shown in Figure 4 and 5. The block diagram of proposed PCA+IDA based bottle inspection scheme is shown in Figure 4 where the dimension of the feature space can be reduced to n-K. Similarly, Figure 5 represents an  $A_dCS$  based IDA bottle identification scheme in which the both dimension reduction method using PCA+IDA and dimension reduction approach using  $A_dCS$ -PCA along with a whitening procedure to develop a  $A_dCS$ -IDA algorithm for bottle inspection.

By considering a set of around 100 test images of bottle including defective and defect free the model is verified by using the proposed algorithm. In this proposed scheme we use  $A_dCS$ -PCA and PCA+IDA.

### III. RESULT ANALYSIS

For the bottle inspection where the  $A_dCS$ -PCA is used for dimension reduction and PCA+IDA used for getting optimal projection vector. By implementing PCA+IDA which gives a agitation free dimension reduction as a result higher efficiency in inspection. As PCA is agitation free so that a time essential for global optimal value evaluation for the projected procedure remains matched with the IDA as per data shown in table1, where the time required for bottle inspection corresponding to different approach or scheme is presented.

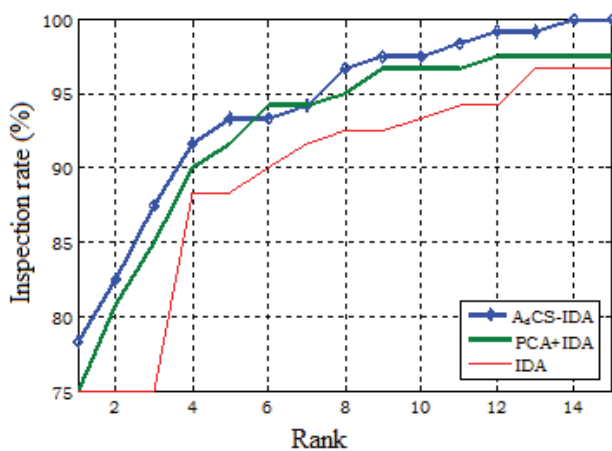


Figure 6 (a). Bottle inspection performance using proposed scheme for a 3 train Image

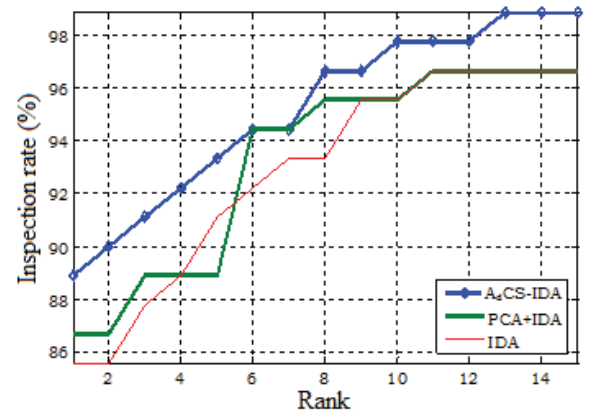


Figure 6 (b). Bottle inspection performance using proposed scheme for a 4 train Image

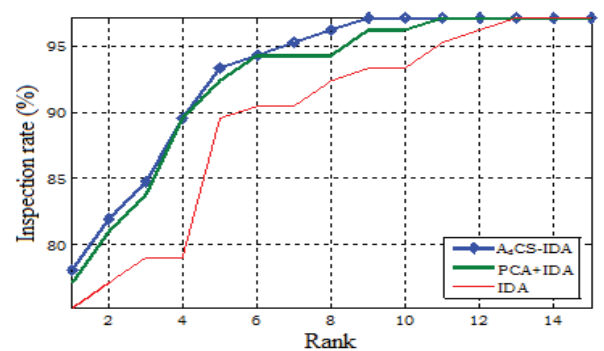


Figure 6(c). Bottle inspection performance using proposed scheme for a 5 train Image

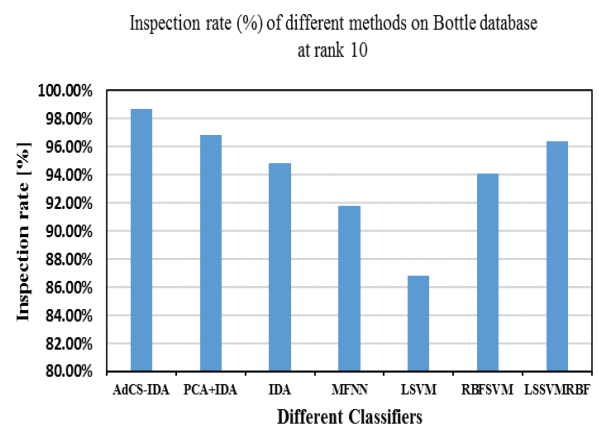


Figure 7. Inspection rate Comparison of different scheme

TABLE II.  
INSPECTION RATE (%) OF DIFFERENT METHODS ON BOTTLE  
DATABASE AT RANK10

Classifiers	Inspection rate (%)
A <sub>d</sub> CS-IDA	98.7%
PCA+IDA	96.8%
IDA	94.8%
Multi feed Neural network (MFNN)	91.78%
LSVM	86.84%
RBFSVM	94.06%
LSSVMRBF	96.35%

From the Table I it is perceived that the anticipated procedure has an improved inspection rate than the additional classical method by considering the different bottle image data base. From Table I and Figure 6(a, b, c) it is concluded that the proposed algorithm has significant improvement over IDA. By comparing two proposed algorithm the A<sub>d</sub>CS-IDA has better inspection rate than PCA+IDA. Again, the proposed A<sub>d</sub>CS-IDA consumes more time than other because of it employs the adaptive Cuckoo search techniques. Again, by using different training images for computation it is observed that the computation time is gradually reduced hence it is claimed that the proposed scheme is best suitable for bottle inspection.

#### IV. CONCLUSIONS

For Bottle inspection there are different schemes are adopted but the proposed scheme used here for the same task is a best fit and more efficient because of using an adaptive Cuckoo search technique in which the step size can be adaptably decided from the acquaintance of fitness value and current position. The proposed algorithm A<sub>d</sub>CS-IDA is used for defective bottle inspection in a manufacturing unit is known as adaptive cuckoo search intrinsic discriminant investigation. The proposed method A<sub>d</sub>CS-IDA and PCA+IDA are validated with the image data base of different bottles. The different classifiers performance when studied in Table II, concluded that the suggested scheme is a suitable one for inspection of bottle in better way.

#### REFERENCES

[1] Nouri !Said, !Fakir !Mohamed. !(2014). !Classification of !printed !Moroccan !town !and !village !names. !Journal of !Information !Technology !Research. Volume-7, !Issue-4, !Pg.111. DOI: !10. !4018 !/ !jitr.2014100101.

[2] K. Tafi, !S. Safi, !M. Fakir. !(2014). !Breast !cancer !diagnosis !system based !on !wavelet !analysis !and !neural !networks, !International !journal of !Computer !vision !and !image !processing, !4(1), !Pg.1-16, !DOI:10.4018/ !ijcvip. !2014 !010101.

[3] Jayachandran !A.,Dhanasekaran !R. !(2014). !Computer !assisted !diagnosis of !tumor !in !brain !MRI !images !using !wavelet !as !input !to !Ada-boost !classifier. !International !journal of !Energy !optimization !and !engineering, !3(3), !Pg.72-85, !DOI: !10.4018/ijeoe. !2014070105.

[4] Nayak !Nihar !Ranjan, !Mishra !Bikram !Keshari !, !Rath !Amiya !Kumar. !(2013), !A !time !efficient !clustering !algorithm !for !gray !scale !image !segmentation. !International !journal of !Computer !vision !and !image !processing, !3(1), !Pg.22-32

[5] Gharehchopogh !Farad !Soleimanian, !Ebrahimi !Samira. !(2012). !A !Novel !approach !for !edge !detection !in !image !on !cellular !learning !automata. !International !journal of !Computer !vision !and !image !processing, !2(4), !Pg.51-61.

[6] Dixit !Karishma, !Jalal !Anand !Singh. !(2012), !A !Vision !based !approach !for !Indian !sign !language !recognition. !International !journal of !Computer !vision !and !image !processing, !2(4), !Pg.25-36.

[7] Dubey !Shiv !Ram, !Jalal !Anand !Singh. !(2012), !Adapted !Approach !for !fruit !disease !identification !using !images. !International !journal of !Computer !vision !and !image !processing, !2(3), !Pg.45-58. !DOI: !10.4018 !/ijcvip. !2012070104.

[8] Win !Htwe !pa, !Khine !Phyo !Thu !Thu !, !Tun !Khin !New !Ni. !(2012). !A !structural !Analysis !based !feature !extraction !method !for !OCR !system !for !Myanmar !printed !document !images. !International !journal of !Computer !vision !and !image !processing, !2(1), !pg.16-41

[9] J. !Anitha, !C. Kezi !selva !Vijila !, !D. !Jude !Hemant !!(2010). !A !hybrid !genetic !algorithm !based !fuzzy !approach !for !abnormal !retinal !image !classification, !International !journal of !cognitive !Informatics !and !Natural !Intelligence,4(3),pg.29-43. !DOI:10.4018/jcini.2010070103.

[10] Krol !Dariusz, !Szlachetko !Boguslaw. !(2010).Automatic !Image !and !speech !recognition !based !on !neural !network. !Journal of !Information !Technology !Research, !3(2), !Pg.1-17

[11] Santo !Rafael do Espfrito, !Lopes !Roseli !de !Deus, !Rangayyan !Rangaraj !M. !(2009). !Classification of !breast !masses !in !mammograms !using !radial !basis !functions !and !simulated !annealing, !International !journal of !cognitive !Informatics !and !Natural !Intelligence, !3(3), !pg.27-38.

[12] Yaremchuk !vanessa, !Dawson !Michael !R.W. !(2008), !Artificial !Neural !Network !that !classify !musical !chords. !International !journal of !cognitive !Informatics !and !Natural !Intelligence, !Volume-2, !Issue !3, !Pg.22—30

[13] Xu !Guangzhu, !Zhang !Zaifeng, !Ma !Yide.(2008).An !efficient !iris !recognition !system !based !on !intersecting !cortical !model !neural !network. IJCINI, !Volume !2, !Issue !2, !Pg.43-57.

[14] Xing !Weiwei, !Liu !Weibin, !Yuan !Baorong. !(2008).3D !Object Classification !Based !on !volumetric !parts. !International !journal of !cognitive !Informatics !and !Natural !Intelligence, !2(1), !Pg-87-99. DOI:10.4018/jcini.2008010107

[15] Bruylants !Tim, !Munteanu !Adrian.(2015).Wavelet !based !volumetric !medical !image !compression,Elsevier,Volume-31,Pg. !112–133.

# Machine Vision based Color Recognition by Robotic Arm using LabVIEW

Y. Divya<sup>1</sup> and C. Pramod Kumar<sup>2</sup>

<sup>1</sup>Asst. Professor, CVR College of Engineering/EIE Department, Hyderabad, India  
Email: divya.reddy037@gmail.com

<sup>2</sup>Asst. Professor, CVR College of Engineering/EIE Department, Hyderabad, India  
Email: pramod.kumar@cvr.ac.in

**Abstract:** Machine vision-based color recognition by robotic arm using LabVIEW, which detects a particular color through webcam fixed in robotic arm using LabVIEW and image processing is set forth in this paper. Color recognition allows robotic arm to detect a particular color that is selected in the front panel of LabVIEW. As soon as the particular color gets identified, it collects the selected color and after some time it is placed back to its original position. The advantages of this method include the reduction of errors and the time over manual labor. And robotic arm's reliability is more.

**Index Terms:** Image processing, LabVIEW, color recognition, Arduino Uno

## I. INTRODUCTION

The aim of this paper is to control robotic arm to perform various applications like movement of robotic arm, color recognition of objects using LabVIEW[13]. The industrial robotic arm can be controlled by various means such as microcontrollers, visual basic and etc. These have certain drawbacks such as code-compilation, complex programming. To overcome these drawbacks National instruments LabVIEW [13] software is used. [7].

LabVIEW utilizes virtual instrumentation platform, which works on customized software and modular measurement hardware [13]. User defined measurement system is created, signals and graphical coding are generated by using LabVIEW [12]. This kind of robotic arm in industries can be controlled by the non-programmers too.

The main challenge is to improve the existing tracking system in the modular processing, containing 4 stations as identification, processing, selection and display with a new image processing feature. The present tracking method utilizes set of inductive, capacitive and auto sensors in identifying the object color[12].

Color identification system controlled by LabVIEW [13] through image processing [12] is presented in this paper. Objects are captured by webcam in real-time mode through Image processing [12] the color and information details are detected. Information is processed through image processing technique [12] for pick – and - place operation. The apparatus learns to identify objects based on a two - phase operative methodology which is defined as autodidactic

stage; An operative choice manner wherein items are detected, categorized the use of a decisional set of rules and decided on in real-time [11].

This work deals with an automated robotic arm controlled by LabVIEW[11]. Thereby removing the monotonous work finished through human, to achieve faster and accurate work. Objects color is captured through webcam and will send the signal to the Arduino board [12].

LabVIEW receives signals from Arduino which drives different models of the robotic arm to track the colors of the objects. Depending on the robotic detection, robot arm will be moved to the specified vicinity, releases the object and will be returned back to its original position.

## II. ROBOTIC ARM INTERFACED WITH ARDUINO

L293D motor drives robotic arm with 5 automobiles and those vehicles. L293D is a standard Motor driving force [7] or Motor Driver IC [7], which permits DC motor to run on both routes. L293D is 16 - pin IC which is able to control a set of two DC automobiles concurrently in any course. It means that it may be manipulated by DC motor with L293D IC [7]. L293D can run small and quiet huge motors as well. The cars are connected to these drivers in keeping with their automobiles, respectively.

A Magnetic Field Generating coil is placed in the filed winding for getting the motor action i.e. whenever the magnetic field is generated due to turning on and off the modem or due to switching the path of the modem within the coil. A Dc Motor has restricted magnetic field inside the stator and an armature with a sequence of extra wrapped winding in mica insulated stack slots around iron pole portions (known as stack teeth) whose ends terminating on a Mechanical Converter of DC to AC. With the assist of these motors the robotic arm action accordingly.

Now the robotic arm is interfaced with the Arduino board [14] which has a microcontroller board based on ATmega328 (datasheet)[14]. It has 14 virtual enter/output pins (out of which 6 pins can be used as PWM outputs)[14], 6 analog inputs, a 16 MHz crystal oscillator, a USB connection, an energy jack, an ICSP header, and a reset button. It includes a microcontroller, connected to a PC with USB cable or external power supply, with an AC-to-DC



adapter or battery to get started[14]. The Arduino Uno and model 1.0 may vary from each other in transferring ahead. The Uno is a series of USB Arduino forms[14]. As the signals from a laptop are shipped to the arduino board that are sent as alerts to the robot arm to go as directed.

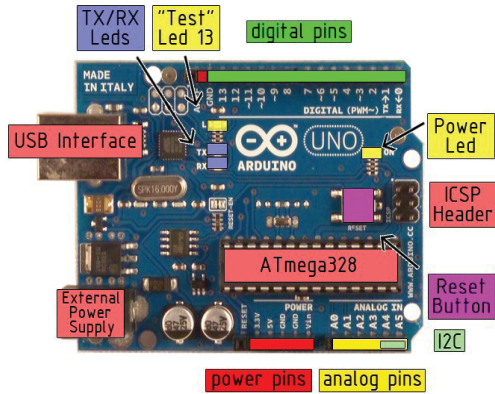


Figure 1. Technical specifications of Ardiuno board



Figure 2. Arduino board

### 2.1 Usage of Arduino

Environment is sensed by a kind of sensors and people indicators are sent to Arduino[14] which is a good way to range its environment with the aid of controlling lighting fixtures, automobiles, and other actuators. It consists 14 virtual input/output pins[14] (out of which 6pins may be used as PWM outputs), 6 analog inputs, a 16 MHz crystal oscillator, a USB connection, an power jack, an ICSP header, and a reset button[14]. It includes a microcontroller is which connected to PC with a USB cable or with an AC-to-DC adapter/battery to get started. The Uno differs from all previous forums where the FTDI USB-to-serial is not used [14]. Different instructions are to be followed according to individual OS.

### 2.2 Requirements

1. Arduino Duemilanove board
2. USB Cable
3. Nine volt battery or external power supply (for non-redundancy operation)
4. Solderless breadboard for external circuits, 22 solid wire connections.

5. Host PC running the Arduino development environment, Windows, Mac and Linux have their own versions.

### POWER SUPPLY

The board is powered through USB Connection with the computer. The external power supply is given in the range of 6 to 24V. A fashionable nine volt Battery [14] can be connected to the board by connecting the leads of a battery to Vin pin and Gnd pin. Soldering is best option to connect battery ends in a DC plug and electricity jack at the board, by taking an appropriate plug component from the wide variety available under 28760.



Figure 3. Connecting Battery to Arduino board

Polarity need to be checked while connecting the battery, as to avoid blow down of the board.

Arduino should be disconnected from the computer and Nine volt battery should be connected to the Arduino power jack using the snap battery adapter. The blinking light confirms its active state. This means the Arduino can be powered through a battery and need not be defined on having a connection to the host PC. Arduino can be connected with the computer by using USB cable [14], the green LED will glow. It will run the code if already exists in the board.[14].

Precaution to be taken: Board should not be placed on a conductive floor because pins on the backside of the board may get short circuited.

Arduino development environment can be commenced. In Arduino-speak, programs are called “Sketches”, but right here they’re just known as packages[14].

In the modifying window that comes up, input subsequent program taking note of in which semi-colons seen on the command strains.

```


Void setup()
{
Serial.begin(9600);
Serial.println(“Hello World”);
}
Void loop()

```

}  
Your window will look something like this[14]



Figure 4. Write code instruction Screenshot

Upload button need to be clicked  or to compile the program Ctrl-U and later load on the Arduino board. Select serial monitor button. If there are no errors, the serial monitor window will display message as below.

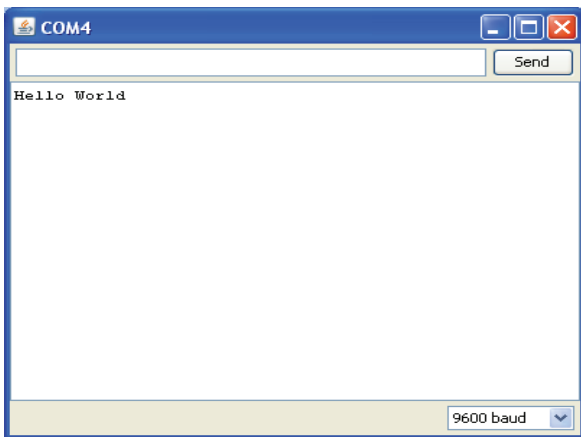


Figure 5: Displayed output

### III. DIGITAL IMAGE MATHEMATICAL INTERPRETATION

Image is handled as a matrix of  $M \times N$  factors [12]. Each element of the digitized picture (pixel) has a value that corresponds to the brightness of the factor inside the captured scene. An image whose decision in depth is of 8 bits, can take values from zero to 255. In the case of a black and white photograph it may take 0 and 1 values. In general picture is represented in a bi-dimensional matrix.

Maximum number of devices collects the pictures with an eight bit intensity. The ranges of gray for a picture [4] is from zero to two hundred and fifty five in order of the matrix elements of the image are represented by using  $x_{ij} | 0 \dots 255$ . At this point it's far handy to say that, despite the fact that the photographs are received in RGB layout, it is frequently converted into a gray scale matrix, for achieving the transformation from RGB form to Grassman stage (Wyszecki & Stiles, 1982) is employed:  $I_{gray} = I$

$R(0.299) + G(0.587) + B(0.114)$  [7]. In the example presented in Fig.4, a way to collect a virtual photograph in RGB format is suggested and grayscale layout the usage of the IMAQ toolbox [13].

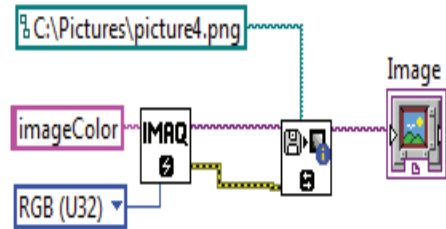


Figure 6. IMAQ Create

In this situation, there are crucial blocks: The first one is the IMAQ create block located in Vision and Motion/Vision Utilities/Image Management. This block creates [13] grayscale, HSL, and so on.), while the second block is the IMAQ Read Image which is placed in vision and movement/imaginative and prescient utilities/documents, the characteristic property of this block is to open picture file that was precisely formed in document route. All records of this opened photograph are placed in the new photograph created through IMAQ create [7]. In different form this instance is presented in Figure. 6 and the record Figure. 6 is opened as IMAQ Read Image. The facts of image are saved in a brand new photograph called image color. It is related to RGB(U32) photograph format of the gadget. In Figure.7 the picture kind is changed to Grayscale(U8) and the picture is placed in image Gray.

Another crucial feature within the picture is defined by neighborhood pixel which is classified in to 3 agencies described in Figure.6. If the neighborhood is limited to 4 adjoining pixels, it is only confirmed by diagonal pixels is the D-Neighborhood and eight surrounding pixels is eight-neighborhood, the remaining consist of Four and D-neighborhood.

### IV. HISTOGRAM IMAGE

Histogram image is a graph which contains number of pixels in an image at different intensity values. In Eight-bit gray scale showing the distribution of pixels with gray scale values as shown below [13].

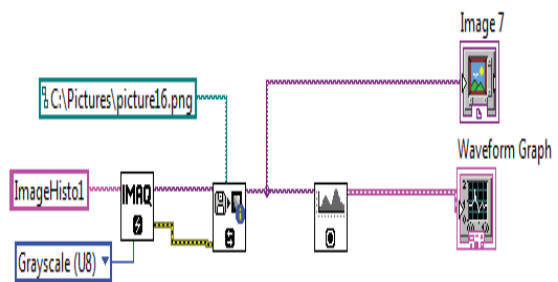


Figure 7. Read Image

When it is seen through histogram gray scale, it appears as the below given Figure 8

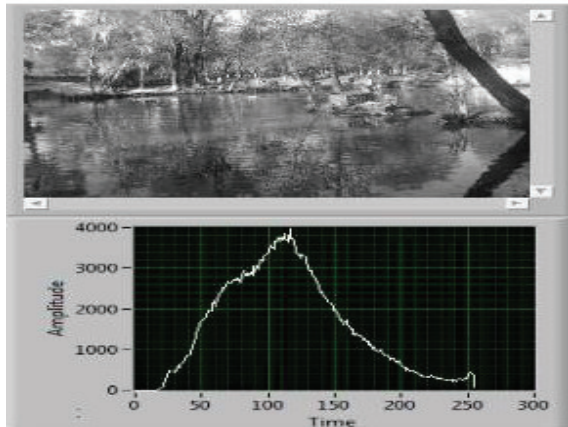


Figure 8. Histogram gray scale

The above shown are the output of grayscale histogram

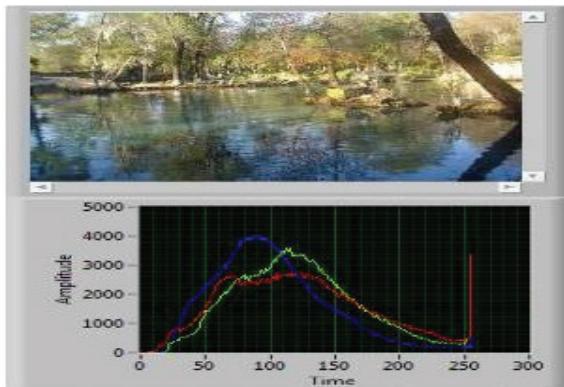


Figure 9. Histogram RGB image

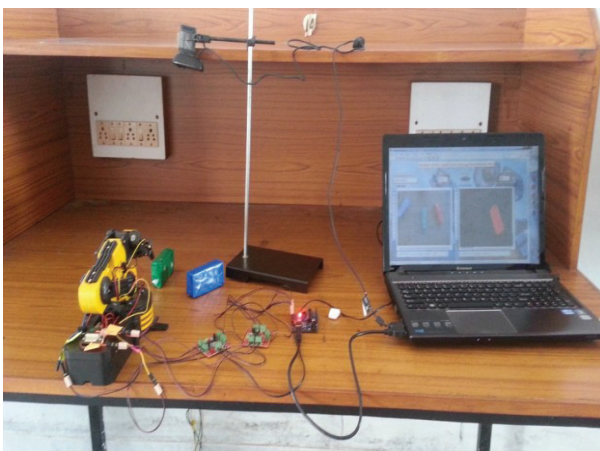


Figure 10. Robotic arm complete Setup

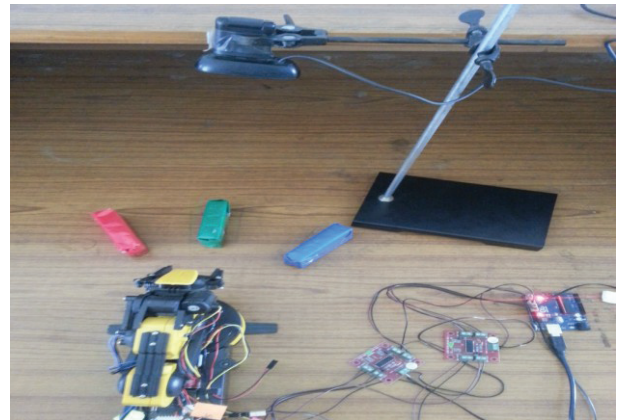


Figure 11. Image Capture through Webcam

image and RGB histogram image using [1] IMAQ histogram image Image Processing [12]. The output of the IMAQ histogram image is a waveform graph, which is connected to show obtained results.

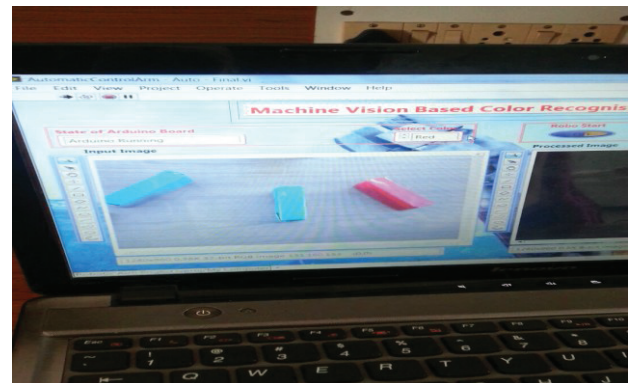


Figure 12. Input View in Front Panel

## V. RESULT



Figure 13. Operation of Robotic arm

The image of the particles is captured by the webcam connected to the retard stand. After the image is captured by the webcam in front panel the input looks in this way. As it detects the image the robotic arm automatically picks that particular object [2] and places it back to its original position.

## VI. CONCLUSIONS

Hence it is concluded from the above points is the man ability and arduous effort can be reduced using the robotic arm controlled by LabVIEW by picking and placing the objects. The robotic arm designed above is used to track the prescribed color among the different colors [10].The controlling software is also very convenient for the non-Instrumentation engineers also.

## REFERENCES

1. M. Swain, and D. Ballard, —Color indexingl, International Journal of Computer Vision, Vol No. 7, pp. 11-32, 1991.
2. B.Schiele and J. I. Crowley, —Recognition without correspondence using multidimensional receptive field histograms, International Journal of Computer Vision Vol. 36, pp. 31–50, 2000.
3. H. Schneiderman, and T. A. Kanade, —Statistical method for 3d object detection applied to faces and carsl, IEEE Computer Society Conference on Computer Vision and Pattern Recognition, Vol 1, pp. 1746, 2000.
4. S. Agarwal, A. Awan and D. Roth, — Learning to detect objects in images via a sparse, part-based representationl, IEEE Transactions on Pattern Analysis and Machine Intelligence, Vol. 26, pp. 1475 – 1490, 2004.
5. A. A. Ata, A. Rafeek and H. Yusof, —Sensory-Based color sorting automated robotic celll, Journal of Intelligent and Robotic Systems, Vol. 1, pp. 99-110, 2005.
6. Junqiu Wang and Yasushi Yagi, —Integrating Color and ShapeTexture Features for Adaptive Real-Time Object Tracking l, IEEE Transactions On Image Processing, Vol. 17, pp. 235-240, 2008.
7. P.B.Vijayalaxmi, Rohan Putta, Gayatri Shinde, Punit Lohani, —Object Detection Using Image Processing For An Industrial Robotl, International Journal of Advanced Computational Engineering and Networking, Vol.1, pp.21-26 , 2013
8. Binbin L., Yimin S., Gang D., Tao S., Yang Q., —Dimensional Synthesis of a Planar Parallel Manipulator for Pick-and-Place Operations Based on Rigid-Body Dynamics, Intelligent Robotics and Applications/Lecture Notes in Computer Science, Springer, Vol. 7506, pp. 261-270, 2012.
9. Altuzarraa O., Şandru B., Pinto Ch., and Petuya V., —A Symmetric Parallel Schönflies-Motion Manipulator for Pickand-Place Operations, Robotica, Vol. 29, Issue 06, pp. 853- 862, October 2011.
10. Wenjing Li, George Bebis and Nikolaos G. Bourbakis (2008) —3-D Object Recognition Using 2-D Views, IEEE transactions on Image Processing, Vol. 17(11), 2236-2255.
11. Adrian D. Olaru, Serban A. Olaru, Niculae F. Mihai, and Natalia M. Smidova—Animation in Robotics with LabVIEW Instrumentation, International Journal of Modeling and Optimization, Vol. 9, 2019.
12. Thomas Klinger, Image Processing with LabVIEW and IMAQ Vision, Prentice Hall Professional, 2003.
13. National Instruments, LabVIEW for color Recognition, 2019.
14. Leo Louis1, Working Principle Of Arduino And Using It As A Tool For Study And Research, International Journal of Control, Automation, Communication and Systems (IJACCS), Vol.1, No.2, April 2016.

# Loan Delinquency Prediction using Machine Learning Techniques

B. Ashwin Kumar<sup>1</sup>, Chadive Koushik Reddy<sup>2</sup>, Chilkamarri Krishna Srinivas<sup>3</sup> and Koya Lokesh Reddy<sup>4</sup>

<sup>1</sup>Asst. Professor, CVR College of Engineering/CSE Department, Hyderabad, India  
Email: ashwinvrk@gmail.com

<sup>2</sup>B. Tech Student, CVR College of Engineering/CSE Department, Hyderabad, India  
Email: koushikchadive99@gmail.com

<sup>3</sup>B. Tech Student, CVR College of Engineering/CSE Department, Hyderabad, India  
Email: krishnasrinivas3303@gmail.com

<sup>4</sup>B. Tech Student, CVR College of Engineering/CSE Department, Hyderabad, India  
Email: lokeshreddy2501@gmail.com

**Abstract:** Loan delinquency prediction is one of the most critical and crucial problems faced by financial institutions and organizations. It is a remarkable effect which could result in the demolition of the profitability rate that leads to the shattering of the organization. Delinquency is a condition that arises due to the failure of payment of loans by the borrowers, which shows tremendous effect on the evolution of financial institutions. It requires more authentications to track the periodic repayments of debts and adaptation of strategies that helps in proliferating the institutions. Based on the details like date of issuance, pay-back time, amount, account details, credit score further issuance of loan is assured this helps in disseminating the delinquency problem.

**Index Terms:** Delinquency; Prediction; Logistic Regression; Supervised Learning; Decision Tree; Random Forest; Ensemble.

## I. INTRODUCTION

According to the statistics, 40% of the economy of any organization is drowning out due to no repayments of debts by borrowers. This catastrophe can be eradicated by monitoring the stream of transactions and debts. This process of evaluation is not so easy for humans to carry out, it requires an automated system which can predict the loss percentage, delinquency rate and monitor the stream of transactions. A loan is considered "delinquent" when a borrower doesn't make a loan payment on time. Most lenders allow consumers a grace period to make up a missed payment and get their loan out of delinquency. However, once a loan is delinquent for a certain period, it gets into the risk of going into default. It's important to make timely payments to avoid defaulting, which can have negative impacts on credit score and the ability to receive credit in the future. Loans default will cause huge loss for the banks, so they pay much attention to this issue and apply various methods to detect and predict default behavior of their borrowers. Machine Learning is an efficient way to eradicate this disaster, it is an amalgamation of Classification and Clustering Algorithms with different capabilities, functionalities it can compute a simple-range - problems to a complicated decision-making.

The models use a supervised learning technique which produces a target variable, depending on the type of value

produced by the target variable (discrete or continuous) type of algorithm is considered. Here the target variable produces discrete values so we use classification algorithms.

Based on the features of the Machine Learning environment it is clear that it is the best solution for Loan Delinquency prediction which helps an organization to regain the hike in profit percentage and also helps in the portfolio of financial organization.

## II. RELATED WORK

### Literature Review

"Ref. [1]" Jian Chen, Ani Katchova, Chenxi Zhou in their paper "Agriculture loan delinquency prediction" they have used the "logistic regression model" to control delinquency their work on agriculture loan delinquency gave an insight on the efficiency of logistic regression algorithm to predict the accurate result.

"Ref. [2]" Uzair Aslam, Hafiz Ilyas, Asim Sohail in their paper "Empirical study on loan default prediction" the credit score has become an important parameter nowadays for any financial organization to approve the loan, by considering credit score as a parameter different models like "SVM, Logistic regression, Neural networks" are used to predict the default rate, it helped us to explore new techniques, their efficiencies and complexities.

"Ref. [3]" Anastasios Petropoulos, Vasilis Siakoulis, Evaggelos Stavroulakis and Aristotle Klamargias in their paper "A robust machine learning approach for credit risk analysis of loan" in their research they have shared the capabilities of a "Random Forest, Neural networks and Decision tree" and generated a solution to loan credit risk which gave an insight on efficiency of decision trees and Random forest.

"Ref. [4]" Research on "Loan default prediction using random forest classifier" by Lin Zuh, Dafeng Qui, Daji Ergu, Cai Ying consists of a crucial technique of denoising data and effectively implement the random forest classifier algorithm to predict the loan default status with various input factors. According to the paper, the establishment of a random forest model implements two steps: building a decision tree and forming a random forest.

“Ref. [5]” Research on "Loan Prediction Analysis using Decision Tree" by Nikhil Mandan, Siddharth Nanda discussed the functionalities of the decision tree and how the model will split the attributes into subsets to predict the results. This paper also enhanced the capabilities of decision trees by comparing with other classification models like SVM, Naive Bayes, Logistic Regression.

### III. PROBLEM STATEMENT

Building an efficient model using machine learning techniques to predict the status of loan delinquency of a customer. It helps banks, financial institutions to monitor the status of the borrower that helps in deciding whether to approve the loan request or to reject the loan request and also it helps in increasing the profitability of an organization.

A finance providing organization, banks or private vendors gauge some parameters of a lender like age, income of the borrower, borrower credit score, purpose of loan, type of loan, the service time of borrower, previous transactions, previous loan repayment history, loan term, unpaid principal amount, debt to income ratio, Interest to approve loan request of a lender.

To build a machine learning model, key parameters or features of a borrower like Age, Loan term, principal amount, Interest rate, Debt to Income ratio, borrower credit score, co-borrower credit score, Loan purpose are considered. These attributes help a machine learning model to predict accurate outcomes and support lenders to decide whether to approve loan requests or to reject the loan request.

### IV. PROPOSED METHOD

The main goal is to develop a solution that helps in decimating the delinquency problem. Machine learning provides decision-making classification algorithms to deal with such problems. Since the problem is a classification problem, classification decision-making algorithms are used, provided by machine learning.

Classification is a Supervised learning approach in which the program learns from the input data and then uses this learning to classify new observations.

The most widely used classification algorithms like Logistic Regression, Naive Bayes classifier, Nearest Neighbor, Support Vector Machines, Decision Trees, Random Forest and Neural Networks. Among these Logistic Regression, Random Forest and Decision Tree are considered in the model building because the response variable is categorical.

**Logistic Regression:** The idea of logistic regression is to find the relationship between features and the probability of particular outcomes.

The response variable has two values "0" or "1" that is "acceptance or rejection" which helps in decision making whether to approve the loan or disprove that controls the delinquency problem by rejecting the fault loan approvals.

**Decision Tree:** It uses tree representation to solve problems in which each leaf node represents a class label and internal nodes represent the attributes.

The decision-making process by response variable is quite different from logistic regression. In the Decision Tree, data is split multiple times based on the features provided with which subsets of data are generated; the final subsets are called "leaf nodes" or "terminal nodes".

To predict the outcome the average values of each acceptance case and rejection case are taken based on the values decision is taken. By this process efficiency increases and produces more accurate results.

**Random Forest:** Random forest is a supervised learning technique which uses ensemble learning methods for classification.

Ensemble learning is a technique in which predictions from multiple machine learning algorithms are made together to make accurate results than any individual models.

It operates by a multitude of decision trees at training time and outputs the classified response variable. Decision trees classifiers can be aggregated into a random forest ensemble which combines their inputs.

Results from different individual trees are aggregated through averaging then the decision is taken based on the averaged value. If the average value is nearer to the acceptance rate then the response or outcome of the model would be acceptance else the response would be rejection.

Based on the unique functionality and features of random forest algorithms it is more efficient and reliable which can produce results with a very high accuracy rate and capable of making precise predictions. Models developed using such an efficient algorithm for delinquency problems can generate very accurate outcomes with which the problem can be eradicated.

#### A. System Architecture

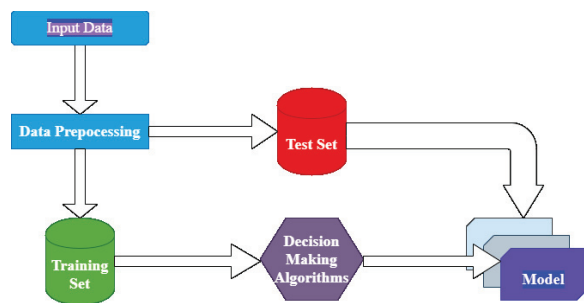


Figure 1. System Architecture.

The dataset is imported from the resource; it undergoes several phases before it is given as input to the algorithm.

Initially, data is checked for any null values or missing values then the entire data is scaled into a single format to eradicate the type errors.

In the data prep-processing stage the entire data is processed to remove anomalies or any redundancy which acts as a barrier for a model to predict accurate results. After the successful data pre-processing the entire data is divided into train and test sets, train set is used to make the model acquire knowledge regarding the features, changes, inter-

dependencies in the dataset it is also called the learning phase or knowledge phase for a machine learning algorithm.

The appropriate algorithm is used and the training data is fit into the algorithm which helps in building an efficient model.

Testing phase of a model is also known as the application phase, where some sample data is provided to verify the rate of accurate predictions by the model, if the model predictions are accurate then the model can be used for future predictions as shown in figure1.

### B. Dataset Used

The loan Delinquency dataset is considered from Analytics ML Hackathon 2019. This dataset consists of over 116059 records with 28 attributes. We have divided the dataset into train data and test data.

### C. Procedure

#### 1. IMPORTING LIBRARIES:

Library is a collection of functions and methods that allows many actions to take place without writing the code.

Libraries that are used to develop a machine learning model are:

1. Numpy
2. Pandas
3. Scikit learn
4. Seaborn
5. Matplotlib

**Numpy** is used to support large multidimensional data and also helps in high-level mathematical functions to operate on these arrays.

**Pandas** library is used to read different types of datasets and store them as a data frame and also it helps in structuring the unstructured data. It is built on Numpy.

**Scikit learn** is also known as sklearn it is a premier machine learning package which contains all machine learning algorithms

**Seaborn** is a library for making statistical graphics in Python. It is built on top of matplotlib and closely integrated with pandas data structures.

**Matplotlib** is a very powerful plotting library useful for working with Python and NumPy. The most used module of Matplotlib is Pyplot, which provides an interface like MATLAB but instead, it uses Python and it is open source.

#### 2. READING THE DATASET:

It is an important step in model building, the data may be available in any format like (.txt,.xlsx,.csv). Based on the availability of format of the dataset, an appropriate method is selected to read the data.

#### 3. SPLITTING THE DATA:

In this phase the acquired data is divided into **train** and **test sets**, the train set has 87044 records and the test set has 29015 records.

The train data helps the model to learn the patterns and test data is used to check how precisely the model has been trained.

#### 4. DATA PRE-PROCESSING:

Pre-processing refers to the transformations applied to our data before feeding it to the algorithm.

Data Preprocessing is a technique that is used to convert the raw data into a standard data set. In other words, whenever the data is gathered from different sources it is collected in raw format which is not feasible for the analysis.

#### 5. MODEL BUILDING:

Model Building is a key step in which by using the appropriate algorithms respective models are built which help in solving simple statistical problems to complex decision-making problems.

##### (I) LOGISTIC REGRESSION ALGORITHM:

Logistic regression algorithm is a module which is imported from the **linear\_module** package in **sklearn library**.

**LogisticRegression()** is a function which is used to apply the logistic regression algorithm to the data.

**fit ()** function is used to fit the train data into the logistic regression algorithm on which the model is built and trained so that future predictions can be made precisely.

##### (II) DECISION TREE ALGORITHM:

Decision tree algorithm is a decision-making algorithm which helps in dealing with complex problems.

This algorithm is inherited from the DecisionTreeClassifier module which is imported from the **tree** package present in the **sklearn** library.

**DecisionTreeClassifier()** method is used to apply decision tree algorithms to a machine learning model with decision tree functionalities.

**fit ()** is used to fit the train data into the Decision tree algorithm and the algorithm will split accordingly to generate the subsets of leaf nodes which helps in predicting the precise results.

After model building, the test data is fitted into the algorithm to verify the accuracy of the model and to check for precise results.

##### (III) RANDOM FOREST ALGORITHM:

Random forest algorithm is an ensemble learning algorithm in which inputs from different algorithms are processed to generate accurate results. This algorithm generates a

decision tree and the output of each decision tree is considered to be an input to the random forest algorithm.

The Random Forest algorithm is a module which is imported from the **ensemble** package of the **sklearn** library **RandomForestRegressor ()** is a function which is used to apply random forest algorithms to the data.

**fit ()** function is used to fit the train data to generate the model and train the data according to the changes, correlation, covariance of variables in the dataset and it is tested by using test data to verify that desired outcomes are generated or not.

### 6.DATA VISUALIZATION:

#### VISUALISATION OF LR MODEL:

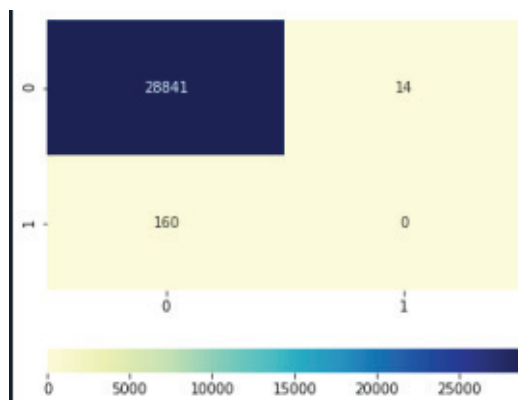


Figure 2. Heatmap diagram representing the nearness of the data predictions by the model using Logistic regression Algorithm.

The above heatmap represents the number of records falling in the acceptance range and number of records falling in the rejection range. Heatmap is generated with the help of a confusion matrix which is developed by a logistic regression algorithm.

The blue color region represents the number of accepted records (28841) other shades of the heatmap represents the number of rejected records (174) as shown in figure2.

#### VISUALISATION OF DECISION TREE:

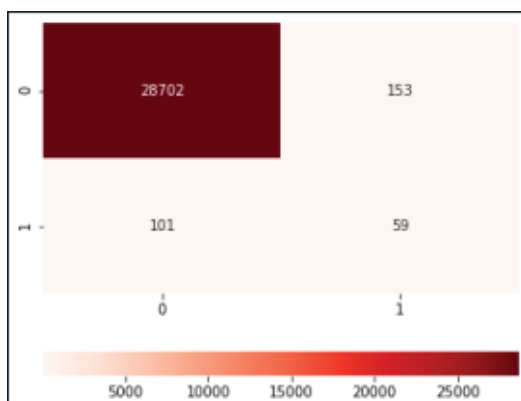


Figure 3. Heatmap diagram representing the nearness of the data predictions by the model using the Decision Tree Algorithm.

The above heatmap is generated from the decision tree algorithm. It represents the number of acceptance records based on predictions made by the algorithm. Based on the confusion matrix generated by algorithm (28702) records are accepted and remaining (313) records rejected as shown in figure3.

#### VISUALISATION FOR RANDOM FOREST:

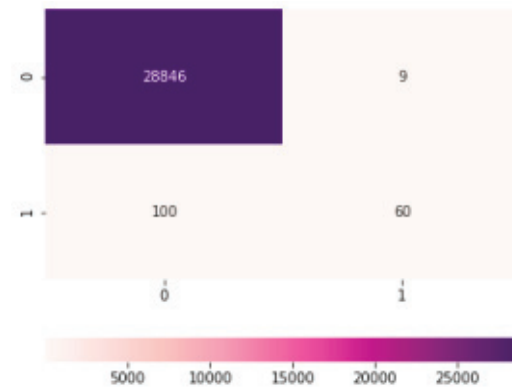


Figure. 4. Heatmap diagram representing the nearness of the data predictions by the model using the Random Forest Algorithm.

The above heatmap is generated from the random forest algorithm. It represents the number of acceptance records based on predictions made by the algorithm. Based on the confusion matrix generated by algorithm (28846) records are accepted and remaining (169) records are rejected as shown in figure4.

### V. RESULTS AND DISCUSSION

TABLE I.  
EVALUATION METRICS

S.no	Model	Accuracy	Precision	Recall
1	LOGISTIC REGRESSION	0.9741	0.9744	0.9997
2	DECISION TREE	0.9725	0.9878	0.9839
3	RANDOM-FOREST	0.9846	0.9868	0.9975

Accuracy, precision, recall of a model using a confusion matrix. Confusion matrix is a summary of the number of correct and incorrect predictions made by a classifier and broken down by each class.

Accuracy is the ratio of the number of correct predictions to the total number of input samples.



$$\text{Accuracy} = \frac{\text{TP} + \text{TN}}{\text{TP} + \text{TN} + \text{FP} + \text{FN}}$$

Precision is calculated by dividing the positive examples with the total number of positive examples.

$$\text{Precision} = \frac{\text{TP}}{\text{TP} + \text{FP}}$$

Recall is defined as the ratio of the number of correctly classified positive values to the total number of positive values.

$$\text{Recall} = \frac{\text{TP}}{\text{TP} + \text{FN}}$$

True Positive (TP): Observation is positive, and is predicted to be positive.

False Negative (FN): Observation is positive, but is predicted negative.

False Positive (FP): Observation is negative, but is predicted positive.

True Negative (TN): Observation is negative, and is predicted to be negative.

## VI. CONCLUSION AND FUTURE WORK

The proposed solution is implemented and tested successfully. This paper speaks about how to eradicate the delinquency situation by developing different machine learning models using existing algorithms and comparing them to pick the best model. The results produced by every model are accurate with respect to their algorithmic properties. In the future, the generated model can be enhanced to increase the efficacy to deal with similar problems.

## REFERENCES

[1] Aslam, Uzair & Aziz, Hafiz Ilyas Tariq & Sohail, Asim & Batcha, Nowshath. (2019). "An Empirical Study on Loan Default Prediction Models". Journal of

Computational and Theoretical Nanoscience. 16. 3483-3488. 10.1166/jctn.2019.8312.

[2] Premkumar B., Lakshmi R., Behera B. "Performance analysis and evaluation of machine learning algorithms in rainfall prediction, International Journal of Advanced Science and Technology", Volume 29, 2020

[3] Nalić, J. and Švraka, A., 2018. "Using Data Mining Approaches to Build Credit Scoring Model: Case Study—Implementation of Credit Scoring Model" in Microfinance Institution. 2018 17th International Symposium Infotech-Jahorina (INFOTECH), IEEE. pp.1–5.

[4] Baesens, B. Roesch, D. and Schedule, H., "2016.Credit Risk Analytics: Measurement Techniques, Applications, and Examples in SAS. United States, John Wiley & Sons".

[5] Sarma, K.S., "2013.Predictive Modeling with SAS Enterprise Miner."

[6] "Practical Solutions for Business Applications. SAS Institute."

[7] Abdou, H.A. and Pointon, J., "2011. Credit scoring, statistical techniques and evaluation criteria: A review of the literature. Intelligent Systems in Accounting, Finance and Management, 18(2–3), pp.59–88".

[8] Jun Hao, Qianqian Feng, Weilan Suo, Guowei Gao, Xiaolei Sun, "Ensemble forecasting for electricity consumption based on nonlinear optimization, 2019, pp."

[9] Mingyue Jiang, Guowei Gao, Yirui Deng, Chenglong Wang. "Market Risks Prevention and Control of "Going Global" for Chinese Electrical Enterprises, 2019, pp."

[10] Ben Hassen H., Elaoud A., Masmoudi K., "Modeling of agricultural soil compaction using discrete Bayesian networks."

[11] International Journal of Environmental Science and Technology, Volume 17, 2020, Zhu L., Qiu D., Ergu D., Ying C., Liu K., "A study on predicting loan default based on the random forest algorithm, Procedia Computer Science, Volume 162, 2019."

[12] Song Y., Wang Y., Ye X., Wang D., Yin Y., Wang Y. "Multi-view ensemble learning based on distance-to-model and adaptive clustering for imbalanced credit risk assessment in P2P lending, Information Sciences, Volume 525, 2020"

[13] Huang Y.-P., Yen M.-F., "A new perspective of performance comparison among machine learning algorithms for financial distress prediction Applied Soft Computing Journal, Volume 83, 2019"

[14] Chen R., Zhou H., Jin C., Zheng W. "Modeling of recovery rate for a given default by non-parametric method, Pacific Basin Finance Journal, Volume 57, 2019."

# Blockchain-based E-Voting System using Proof of Voting (PoV) Consensus Algorithm

S. Srinivas<sup>1</sup>, B. Ashwin Kumar<sup>2</sup> and R. Srishylam<sup>3</sup>

<sup>1</sup> Asst. Professor, CVR College of Engineering/CSE Department, Hyderabad, India  
Email: s.srinivas@cvr.ac.in

<sup>2</sup> Asst. Professor, CVR College of Engineering/CSE Department, Hyderabad, India  
Email: forashwink@gmail.com

<sup>3</sup> Asst. Professor, CVR College of Engineering/CSE Department, Hyderabad, India  
Email: srisailamreddypally@gmail.com

**Abstract:** Designing the Electronic Voting System is the biggest challenge, especially in India. It has to satisfy all the legal guidelines and have a robust tamper proof system. E-voting system can be made up of central and distributed network types, but the main disadvantage of central network is single point of failure. Blockchain technology is a distributed type of network many applications like Electronic medical records (EMR), IoT and E-voting. In this paper an electronic voting system using blockchain technology with powerful Proof-Of-Voting (POV) consensus algorithm is developed. This paper evaluates the legal issues that are encountered in conventional methods and how to overcome them with the help of blockchain technology. In this paper one system has made with PoV which increases security, is of low cost and low power consumption.

**Index Terms:** Blockchain Technology (BCT), Electronic Voting (E-Voting), Proof-of-voting (POV).

## I. INTRODUCTION

In early 80's and 90's some countries used traditional pen and paper method for the conduction of general elections. [1,2,3], Traditional method of conducting elections had many challenges like rigging, booth capturing and misleading the results. There was no proper mechanism to conduct free and fair elections. Many studies were conducted to overcome these issues. E-Voting System [4] is the most authentic and accurate method and good solution for conducting fair elections in the democratic countries. Now a days many countries are using E-voting systems with a micro controller, required software with the program designed for the purpose. There is every possibility to tamper or hack the system because of central accessible storage. This may affect the election results. This paper shows implementation of E-voting system with blockchain Technology taking into consideration national security, utilization of efficient man power and minimizing fraud. The mechanism can be effective if:

1. Voter information and vote casting should keep in secret.
2. Voter id verification and count of votes have to be correct.
3. No other person should not tamper the vote.

Blockchain is a digital trust with decentralized, digitized, public and shared ledger of information that is resistant to tampering. The main features of blockchain [5,6] technology is;

1. Enhanced security features, preventing fraud and data theft.
2. Improve the overall robustness and integrity.
3. Securing edge devices with authentication and data management.
4. Reduce the fishing attacks, DDoS (Distributed denial of service) attacks.

With these features of cryptography, every node in blockchain is linked with hash pointer, verified signed transactions are replicated globally on millions of nodes. For these reasons and features now 33% of organizations are using blockchain technology.

Section II gives the information about Blockchain as a service for E-voting. Section III describes proof of vote consensus mechanism. Section IV describes security analysis proposed consensus algorithm. Section V describes conclusion and future scope.

## II. BLOCKCHAIN AS A SERVICE FOR E-VOTING

In this section it is considered that E-Voting system is based on blockchain technology. Firstly, in this section will be discussed about how to create smart contracts, next about different frameworks in blockchain then how to deploy election using smart contracts and in last about the proposed system.

### A. Creating Election Smart Contracts

Smart contracts [7] include identifying the roles that are involved in election like voter, officer, nodal officer. There are different election roles can be made as smart contracts. Figure 1 shows the participants in E-Voting system and how election will be initiated. Firstly, election administrator starts the election and after particular time he closes the election, total election process monitored by election administrator. Next district officer having the information about next sub level like district-wise, next booth officer to the voter last. Booth officer will be in the polling booth and he monitors the election of

single polling booth. Smart contracts created for all of them in the network from administrator to voter. To cast vote every node has to make authentication. So that it will give perfect result and no other persons can tamper the network.

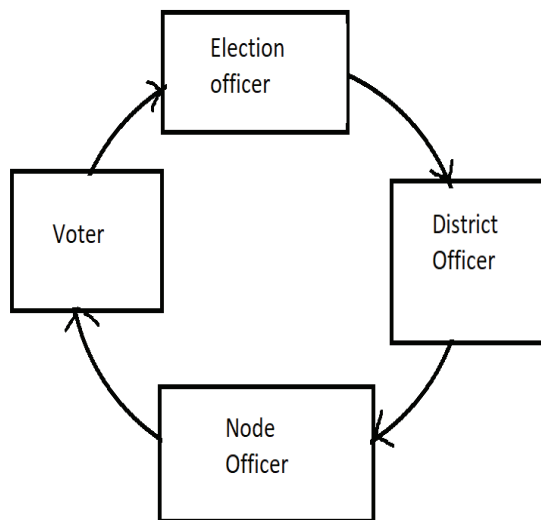


Figure 1. Election process initiation using smart contacts

**B. Election Procedure**

Election officer creates decentralized application for election procedure. Main activities of election process using blockchain technology [14,15,16] are election creation, voter registration, voter transaction, tallying results and verifying vote. Figure 2 shows how the election process done using proof of vote network [17].

A new consensus method permissioned Proof of voting [8,9] is proposing here. After initiating election process election starts with candidates list and smart contracts of every candidate. Each ballot smart contract created by node officer to particular candidate and it is verified by district and node officer. Voter registration made by using

proof of vote (POV). If the candidate’s smart contract is matching with the ballot smart contract then only voter can cast his vote, if he fails in this process then voter is not allowed to cast his vote. The same work can be done using proof of work (POW) [10,11] also, but the power consumption is very high in POW where as in POV the power consumption is low. Next session will give the information about POV consensus mechanism [18,19]. After verification done, tally of votes and voter transaction can be done by conventional methods.

**III. PROOF OF VOTING (POV) CONSENSUS FOR E-VOTING SYSTEM**

Consensus is important concept in block chain technology. Block Chain Technology (BCT) is a distributed technology so that anybody can enter in to the network if it is permission less BCT. Every node and process have to maintain same data and understanding. In permissioned BCT all nodes are known to each other where as in permission less BCT nodes [20] are unknown to each other. Some malicious nodes may not follow the consensus due to that voting data may get leaked.

In this paper the analysis made on byzantine agreement and smart contacts.

**Byzantine agreement:** it is an agreement between every node in the network that they stand up on same rules. If any of the node is not following the rules then that node is called as malicious, such nodes will be removed from network. If the malicious nodes are increasing and agreement between the nodes are break means that called byzantine failure.

**Smart contacts:** is a computer program that directly and automatically controls the transfer of digital assets between the parties under certain conditions. A smart contact works in the same way as a traditional contact while also automatically enforcing the contact.

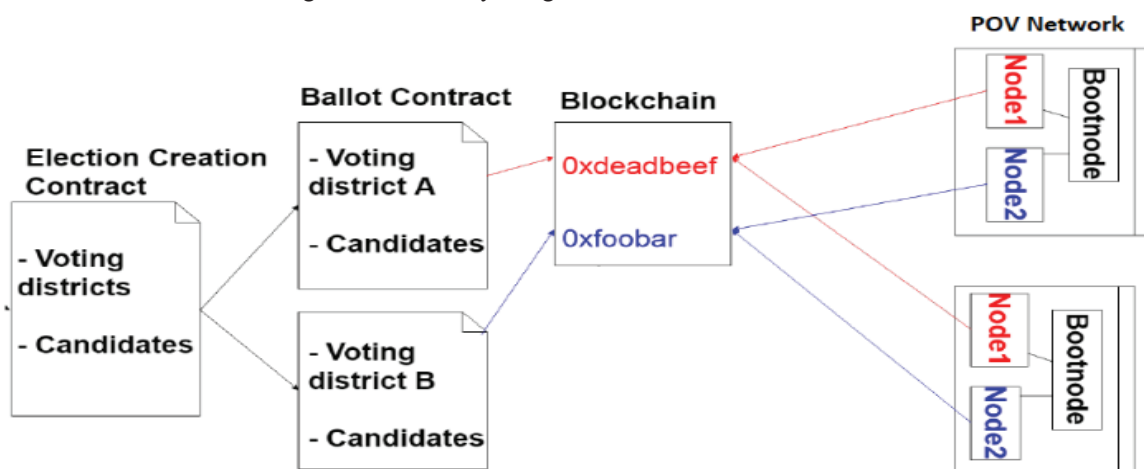


Figure 2. Election procedure using smart contacts

In this proposed consensus [12] algorithm, it will predict the malicious nodes and removes it from the Block Chain. In E-voting system it is important to remove some failures like byzantine failure [13], security failure, crash failure, software failure and temporal failure. Figure 2 shows how the consensus achieved in distributed system. In block chain if any of the node is behaving like malicious (attacker) then automatically detected by proof of vote (PoV) algorithm and those attackers will be removed from block chain.

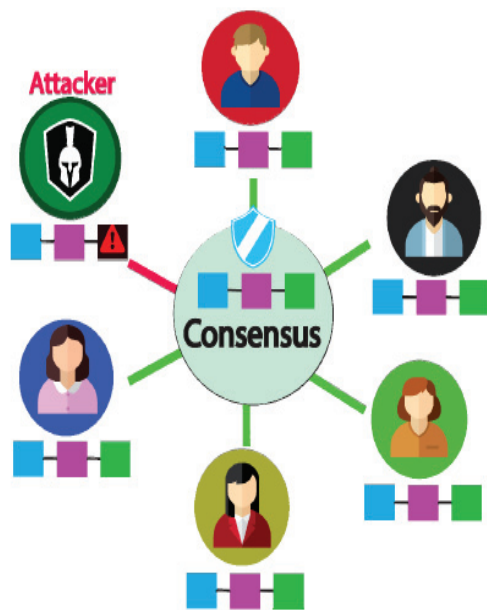


Figure 3. consensus in proof of vote (PoV)

**A. Mathematical Model For POV**

In Proof of voting consensus algorithm, blockchain systems are maintained by various enterprises around the world or country. Applications developed on this network can serve terminal users across the world. The network model for POV is shown in figure 4. There are four following roles in POV consensus process: commissioner, butler, butler candidate and ordinary user.

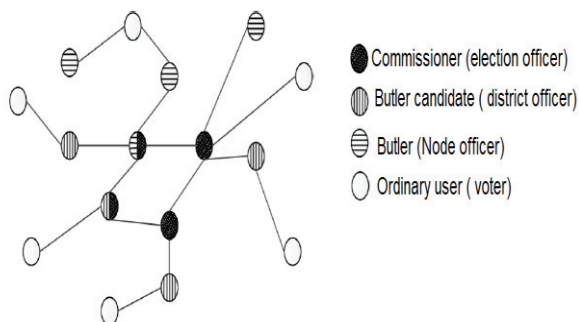


Figure 4. Proof of voting network model

**Commissioner:** several voters from different parts of the country are formed league committee, commissioner

is one of the members in league committee. In this paper commissioner is considered as election officer. Commissioner has the right to recommend, vote and evaluate the voter. A block is generated in blockchain network will be sent to all election officers for verification. When the block has received 51% votes from all commissioners then the block is considered as valid block and added to the blockchain.

**Butler:** Butler is responsible for producing blocks. The identity of the butler means the separation of a voting right and an executive right. The function of the butler is to transact the information from the network gathered by it and pack the information with the block. Node officer’s responsibility is same as butler’s responsibility.

**Butler candidate:** He is the responsible for the communication between node officer and voter. In our case butler candidate and district officer both are same. Butler candidate gathers the information of voter and if it matches with the network then checks the number of votes in the network, if the majority of networks are find then voter is marked as authenticated.

**B. Voting Process**

Two steps involved in voting procedure. Voting for the block production and voting for the candidate. The commissioners vote by returning their signature. In this analysis, it is assumed that  $N_c$ - number of commissioners,  $N_b$ - number of butler candidates,  $N_{bc}$ - number of butler and  $N_v$ - number of voters.

**Voting for block production:** Butler  $i$  generates a block and sends it to all commissioners. If a commissioner agrees to produce this block, he will encrypt the block header and returns the signature to butler  $i$ . If butler  $i$  receives at least  $N_c/2 + 1$  signatures within the predefined time, the block is valid. Otherwise, the block is invalid, and will be reproduced by the butler  $i + 1$ .

**Voting for the butler candidate:** Butler  $j$  sends requests to all commissioners for voting. After collecting and counting the ballot tickets, butler  $j$  generates a special block with election results and related records. Then butler  $j$  will send this block to all commissioners for validation.

Each block generates a random number that determines who will be the next voter, which ensures that butlers generate blocks in a random order. The random number generation algorithm is as follows:

Suppose butler receives signature from  $K$  commissioners, represented by

$$signature(i); \left( 0 \leq i \leq K, \frac{N_c}{2} \leq K \leq N_c - 1 \right) \quad (1)$$

The time it is received from the server is TimeStamp. Voter authorization made by following equations,

$$R = \left( \sum_{i=0}^{K-1} \text{signature}(i) \right) \oplus \text{Timestamp} \quad (2)$$

Voter validation can be done by following equation

$$VV = (\text{Hash}(R)) \bmod N_p \quad (3)$$

Based on VV value voter validation made if this value above 0.51 then he is a valid voter otherwise proxy voter.

#### IV. SECURITY ANALYSIS OF CONSENSUS ALGORITHM

In this the analysis of E-voting using POW and POV consensus algorithms has been made. This simulation made by using NS-3 emulator and it is assumed that the number of commissioners  $N_c=500$  and number of voters  $N_v=10$ lakhs.

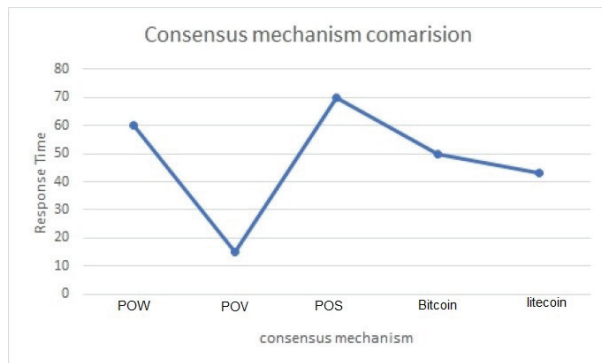


Figure 5. Comparison of different consensus protocols

Figure 5 Shows the comparison of different consensus algorithms. This analysis is made on block chain implementations and creating smart contracts using NS3. From above it is concluded that Proof of voting has fast response time for block creation as compared to other consensus mechanisms.

E-voting system using BCT is a distributed type network. Every ballot box in the network act as node and every node is connected to network. This distributed network does not allow any other malicious nodes. In this paper security analysis is made by byzantine failures. In POW the byzantine failure percentage is more comparing with POV. The statistical analysis will prove the result. Table 1 will give the total information about this.

TABLE I.  
COMPARISON STATEMENT OF POW VS POV

Consensus Mechanism	Byzantine failures	Smart contacts
Proof-Of-Work (POW)	5%	Very slow
Proof-Of-Voting (POV)	3.2%	Fast

#### V. CONCLUSIONS

In this paper, a unique blockchain-based electronic voting system that utilizes smart contracts to enable secure and cost-efficient election while guaranteeing voters privacy is introduced and also outlined the systems architecture, the design and a security analysis of the system.

#### REFERENCES

- [1] M. T. Isaai, F. Firoozi and M. R. Hemyari, "E-election in Digital Society," 2009 Third International Conference on Digital Society, Cancun, 2009, pp. 24-29.
- [2] S. S. Dash, C. Shekhar, S. Kumar and R. K. Agrawal, "Leveraging ICT for election 2014 results dissemination," 2015 2nd International Conference on Computing for Sustainable Global Development (INDIACom), New Delhi, 2015, pp. 2170-2172.
- [3] L. Sandberg, S. Jaradat and N. Dokoohaki, "The social media election agenda: Issue salience on Twitter during the European and Swedish 2014 elections," 2016 IEEE/ACM International Conference on Advances in Social Networks Analysis and Mining (ASONAM), San Francisco, CA, 2016, pp. 793-794.
- [4] S. A. Adeshina and A. Ojo, "Design imperatives for e-voting as a sociotechnical system," 2014 11th International Conference on Electronics, Computer and Computation (ICECCO), Abuja, 2014, pp. 1-4.
- [5] G. Wang, Z. Shi, M. Nixon and S. Han, "ChainSplitter: Towards Blockchain-Based Industrial IoT Architecture for Supporting Hierarchical Storage," 2019 IEEE International Conference on Blockchain (Blockchain), Atlanta, GA, USA, 2019, pp. 166-175.
- [6] S. Hodayoun, A. Dehghantanha, R. M. Parizi and K. R. Choo, "A Blockchain-based Framework for Detecting Malicious Mobile Applications in App Stores," 2019 IEEE Canadian Conference of Electrical and Computer Engineering (CCECE), Edmonton, AB, Canada, 2019, pp. 1-4.
- [7] H. L. Pham, T. H. Tran and Y. Nakashima, "A Secure Remote Healthcare System for Hospital Using Blockchain Smart Contract," 2018 IEEE Globecom Workshops (GC Wkshps), Abu Dhabi, United Arab Emirates, 2018, pp. 1-6.
- [8] S. V., A. Sarkar, A. Paul and S. Mishra, "Block Chain Based Cloud Computing Model on EVM Transactions for Secure Voting," 2019 3rd International Conference on Computing Methodologies and Communication (ICCMC), Erode, India, 2019, pp. 1075-1079.
- [9] S. Saini and J. Dhar, "An Eavesdropping Proof Secure Online Voting Model," 2008 International Conference on Computer Science and Software Engineering, Hubei, 2008, pp. 704-708.
- [10] T. Xue, Y. Yuan, Z. Ahmed, K. Moniz, G. Cao and C. Wang, "Proof of Contribution: A Modification of Proof of Work to Increase Mining Efficiency," 2018 IEEE 42nd Annual Computer Software and Applications Conference (COMPSAC), Tokyo, 2018, pp. 636-644.
- [11] N. Torii and M. Kitakami, "A Method for Stable Block Generation Time in Proof of Work," 2019 IEEE 24th Pacific Rim International Symposium on Dependable Computing (PRDC), Kyoto, Japan, 2019, pp. 53-531.
- [12] Y. Shang, "Finite-Time Weighted Average Consensus and Generalized Consensus Over a Subset," in IEEE Access, vol. 4, pp. 2615-2620, 2016.
- [13] S. Pahlajani, A. Kshirsagar and V. Pachghare, "Survey on Private Blockchain Consensus Algorithms," 2019 1st

- International Conference on Innovations in Information and Communication Technology (ICIICT), CHENNAI, India, 2019, pp. 1-6.
- [14] X. Liu and H. Ma, "Privacy Preserving Finite-time Consensus in Networks With Time-varying Topology," 2019 34rd Youth Academic Annual Conference of Chinese Association of Automation (YAC), Jinzhou, China, 2019, pp. 312-316.
- [15] D. Kim, R. Ullah and B. Kim, "RSP Consensus Algorithm for Blockchain," 2019 20th Asia-Pacific Network Operations and Management Symposium (APNOMS), Matsue, Japan, 2019, pp. 1-4.
- [16] W. Zheng, Z. Zheng, X. Chen, K. Dai, P. Li and R. Chen, "NutBaaS: A Blockchain-as-a-Service Platform," in IEEE Access, vol. 7, pp. 134422-134433, 2019.
- [17] S. Malik, V. Dedeoglu, S. S. Kanhere and R. Jurdak, "TrustChain: Trust Management in Blockchain and IoT Supported Supply Chains," 2019 IEEE International Conference on Blockchain (Blockchain), Atlanta, GA, USA, 2019, pp. 184-193.
- [18] X. Yang, Y. Chen and X. Chen, "Effective Scheme against 51% Attack on Proof-of-Work Blockchain with History Weighted Information," 2019 IEEE International Conference on Blockchain (Blockchain), Atlanta, GA, USA, 2019, pp. 261-265.
- [19] L. Wan, D. Eysers and H. Zhang, "Evaluating the Impact of Network Latency on the Safety of Blockchain Transactions," 2019 IEEE International Conference on Blockchain (Blockchain), Atlanta, GA, USA, 2019, pp. 194-201.
- [20] N. Baranwal Somy et al., "Ownership Preserving AI Market Places Using Blockchain," 2019 IEEE International Conference on Blockchain (Blockchain), Atlanta, GA, USA, 2019, pp. 156-165.

# Reducing Overfitting Problem in Machine Learning using L1/4 Activation Function

Sathya Prakash Racharla<sup>1</sup>, Mohammad Umar<sup>2</sup> and V. D. S. Krishna<sup>3</sup>

<sup>1</sup>Asst.Professor, CVR College of Engineering/CSE Department, Hyderabad, India  
Email: prakashscits@gmail.com

<sup>2</sup>Asst.Professor, CVR College of Engineering/CSE Department, Hyderabad, India  
Email: umarmohd25@gmail.com

<sup>3</sup>Asst.Professor, CVR College of Engineering/CSE Department, Hyderabad, India  
Email: varanasi.kris@gmail.com

**Abstract:** Machine learning has various applications. Machine learning model has two problems. Overfitting and Underfitting. Underfitting is a statistical model or a machine learning algorithm, it cannot capture the underlying trend of the data. A statistical model is said to be overfitted, when it is trained with a lot of data. When model has trained on fewer features, the machine will be too biased, and then the model gets underfitting problem. So, it is needed to train the model on more features and there is one more problem occurs. Overfitting problem can be reduced by using regularization functions and data augmentation. In the previous research on activation functions, Hock Hung Chieng Proposed an activation function called Flatten-T Swish: a threshold ReLU, which is a multiplication of Relu and sigmoid function.

**Index Terms:** Flatten-T swish, Machine learning, activation function

## I. INTRODUCTION

To design a machine learning model, our model has to be trained on dataset. Our model has to be trained based on some features which are given. Sometimes our model accuracy is low on new data. There may be two types of problems occur. Overfitting and Underfitting.

### A. Underfitting:

If few features are given to train the model, sometimes it can wrongly identified unknown data as shown in figure 1. To reduce this problem feature selection should be increased. In figure 1, there is an explanation about under fitting, perfect fitting and Overfitting. A statistical model [1] or a machine learning algorithm is said to have underfitting when it cannot capture the underlying trend of the data. In the figure line cannot be clustering perfectly.

### B. Overfitting:

If huge features are given to our train model also, will get problem to our statistical problem, then our model will get Overfitting problem as shown in figure 1. When model has trained on fewer features, the machine will be too biased, and then the model gets underfitting problem.

So, it is needed to train the model on more features and there is one more problem occurs. If model has trained on more and more features, more variances come into the picture, and then our model identification efficiency is very less [2]. It leads our model to become worse. This problem is known as Overfitting problem. A statistical model is said to be Overfitted, when model has trained with a lot of data. When it gets trained with so much of data, it starts learning from the noise and inaccurate data entries in our data set.

**Bias:** it calculates our model predictions. It shows the correct difference when it is compared to the actual value. **Variance:** It denotes the predictions given by our model for a given point which varies between different realizations.

How to overcome underfitting?

- Find more features
- Try high variance machine learning models (Decision tree, K-NN, SVM)

When the test error is much heavier than training error, it can be concluded that there is Overfitting problem.

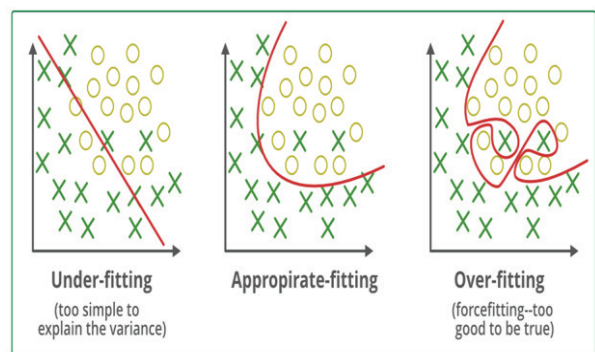


Figure 1. Underfitting and Overfitting cases in ML

## II. VARIOUS ACTIVATION FUNCTIONS IN NEURAL NETWORKS

### A. Linear Function

General equation for a straight line,  $y=mx$ , this equation is used for linear function.

- Apply this equation for input layer where activation functions to last layers.
- Linear function range is  $(-\infty, +\infty)$
- There are some issues in this linear function. If this function is differentiated, it is independent of  $x$ , i.e. input. The best example for this type of function is house rent analysis. This is regression problem, using this linear function, linear function for output layers can be added.

### B. Sigmoid Function

This activation function plotted as 'S' shape. General equation for a straight line,  $Z = 1/(1 + e^{-x})$ , this equation is used for linear function [3][10].

- Apply this equation for input layer where activation functions to last layers.
- Linear function range is  $(0, 1)$
- There are some issues in this sigmoid function, when differentiated this function depends on 'x' input.
- The best example for this type of function is house rent analysis. This is regression problem [6], using this linear function, linear function for output layers can be added.
- Result can be determined to be 1 if value is greater than 0.5 and 0 otherwise.

### C. Tanh Function

This activation function also known as **Tangent Hyperbolic function** [4]. This is far better than sigmoid and linear activation functions. This function can be derived from sigmoid activation function by using shifting principle.

$$g(x) = \tanh(x) = 2/(1 + e^{-2x}) - 1$$

or

$$\tanh(x) = 2 * \text{sigmoid}(2x) - 1$$

- Apply this equation for input layer, then activation functions to last layers.
- Linear function range is  $(-1, +1)$
- There are some issues in this linear function. If this function is differentiated, it is independent of  $x$ , i.e. input.
- Due to the range  $(-1, +1)$ , the mean becomes 0. Then the data will be centered.
- Due to this, the next layer learning becomes much easier.

### D. Rectified linear unit (RELU)

Mostly this type of activation function is used in *hidden layers* of convolutional Neural network. It is a nonlinear function [5].

General equation for a straight line,  $R(x) = \max(0, x)$ , this equation is used for linear function.

- Apply this equation for input layer, whereas activation functions to last layers.
- Activation function range is  $(0, +\infty)$
- There are some issues in this linear function. If this function is differentiated, it is independent of  $x$ , i.e. input.
- It gives an output  $x$  if  $x$  is positive and 0 otherwise.
- RELU activation function is faster than all other activation functions.

### E. Softmax Function

This activation function is also similar to sigmoid function, which is useful for all classification problems.

This activation function is a nonlinear function [7]. The activation function would squeeze the outputs for each module between 0 and 1 and also divide by the sum of these outputs.

To choose activation function, RELU can be used, which is suitable for all applications.

For binary classification applications, sigmoid activation function can be used.

### K-folds cross validation:

In K-folds cross validation, it is needed to divide our data into  $k$  different subsets or folds.  $k-1$  subsets are used to train our data and leave the last subset or last folder as test data. Average the model against each of the folds and then finalize our model, after that it has to be tested against the test set.

Final accuracy = average (round1, round2, round3 ...)

How to overcome Overfitting?

- During training only, our model has to be tested against validation data.
- If validation accuracy is lower, regularization has to be done.
- Repeat this process of regularization, until no Overfitting result.

In order to create less complex (parsimonious) model, when there are large number of features in the dataset, some of the Regularization techniques used to address Overfitting and feature selections are:

1. L1 Regularization
2. L2 Regularization

A regression model that uses L1 regularization technique is called *Lasso Regression* and model which uses L2 is called *Ridge Regression*.

The key difference between these two is the penalty term.

Ridge regression adds "squared magnitude" of coefficient as penalty term to the loss function [2]. Here the *highlighted* part represents L2 regularization element.

$$\sum_{i=1}^n (y_i - \sum_{j=1}^p x_{ij} \beta_j)^2 + \lambda \sum_{j=1}^p \beta_j^2 \quad (1)$$

Here, if *lambda* is zero then you can imagine to get back to OLS. However, if *lambda* is very large then it will add too much weight and it will lead to underfitting. Having said that



it's important how  $\lambda$  is chosen. This technique works very well to avoid Overfitting issue. Lasso Regression (Least Absolute Shrinkage and Selection Operator) adds “absolute value of magnitude” of coefficient as penalty term to the loss function.

$$\sum_{i=1}^n (y_i - \sum_{j=1}^p x_{ij} \beta_j)^2 + \lambda \sum_{j=1}^p |\beta_j| \quad (2)$$

Again, if  $\lambda$  is zero then it is good to get back to OLS whereas very large value will make coefficients zero hence it will underfit.

The key difference between these techniques is that Lasso shrinks the less important feature's coefficient to zero thus, removing some feature altogether. So, this works well for feature selection in case huge number of features are there.

Traditional methods like cross-validation, stepwise regression to handle Overfitting and perform feature selection work well with a small set of features but these techniques are a great alternative when dealing with a large set of features.

### III. PROPOSED ALGORITHM

To improve the performance in the existed algorithms, I want to develop a new algorithm which combines the convolutional neural network with proposed Activation function called S-inclined Activation function.

To reduce the Overfitting problem, regularization functions and data augmentation are used. In the previous research on activation functions, Hock Hung Chieng proposed an activation function [8] called Flatten-T Swish: a threshold ReLU, which is a multiplication of Relu and sigmoid function. In my research, I want to convolute GRelu (Gaussian) and Sigmoid functions for a better results.

$$\text{GReLU}(x) = \begin{cases} x, & x \geq 0 \\ 0, & x < 0 \end{cases}$$

$$\text{Sigmoid}(x) = \frac{1}{1+e^x}$$

Absolute value of Convolution of these functions

$$|\text{GReLU}(x) * \text{Sigmoid}(x)| = \sum_i (x_i - \hat{x}_i)^2 + \lambda \sum_i \sqrt[4]{w_i} \quad (4)$$

#### 5. Development of proposed algorithm L1/4 Regularization

As compared to L1 regularization and L1/2 regularization, our proposed regularization method L1/4- regularization will give for better performance. L1/4- regularization pushes all the weights absolute fourth order value.

#### Proposed Algorithm: L1/4 Regularization:

As compared to L1 regularization, L1/4- regularization is best opted methodology for better performance. L1/4- regularization pushes all the weights absolute fourth order value. According to XU ZongBen, ZHANG Hai [6] if the order of weight is decreased more accurate values in fitting problems can be achieved, so

$$\text{Minimize absolute } (\sum_i (y_i - \hat{y}_i)^2 + \lambda \sum_i \sqrt[4]{w_i}) \quad (3)$$

Here also, if  $\lambda$  is zero then get back to OLS. However, if  $\lambda$  is very large then it will add too much weight and it will lead to underfitting. Having said that it's important how  $\lambda$  is chosen. This technique works very well to avoid Overfitting issue.

Lasso Regression (Least Absolute Shrinkage and Selection Operator) adds “absolute value of magnitude” of coefficient as penalty term to the loss function.

#### layer 1 (Hidden layer) :-

$$X(1) = Y(1)W + z(1)$$

$$z(1) = a(1)$$

Here,

- $W(1)$  be the vectorized weights assigned to neurons of hidden layer i.e.  $w_1, w_2, w_3$  and  $w_4$
- $z(1)$  is the vectorized form of any linear function.
- $W$  be the vectorized input features i.e.  $i_1$  and  $i_2$
- $z$  is the vectorized bias assigned to neurons in hidden layer i.e.  $a_1$  and  $a_2$
- $a(1)$  is the vectorized output of layer 1

(Note: don't consider activation function here)

#### Calculation at Output layer:

#### Layer 2 (output layer) :-

// 2 is output from layer 1

$$a(2) = Z(2)a(1) + c(2)$$

$$k(2) = c(2)$$

// Replace the value of c(1) here

$$c(2) = (Z(2) * [Z(1)X + z(1)]) + a(2)$$

$$z(2) = [Z(2) * Z(1)] * X + [Z(2)*a(1) + a(2)]$$

Let,

$$[Z(2) * Z(1)] = Z$$

$$[Z(2)*a(1) + a(2)] = a$$

Final output :  $a(2) = Z*X + a$

Which is again a linear function

```

Train on 34300 samples, validate on 14700 samples
Epoch 1/10
34300/34300 [=====] - 14s - loss: 0.4231 - acc: 0.8652 - val_loss: 0.1756 - val_acc: 0.9461
Epoch 2/10
34300/34300 [=====] - 12s - loss: 0.1771 - acc: 0.9487 - val_loss: 0.1526 - val_acc: 0.9573
Epoch 3/10
34300/34300 [=====] - 13s - loss: 0.1296 - acc: 0.9625 - val_loss: 0.1111 - val_acc: 0.9683
Epoch 4/10
34300/34300 [=====] - 13s - loss: 0.1055 - acc: 0.9691 - val_loss: 0.1137 - val_acc: 0.9688
Epoch 5/10
34300/34300 [=====] - 12s - loss: 0.0924 - acc: 0.9739 - val_loss: 0.1184 - val_acc: 0.9677
Epoch 6/10
34300/34300 [=====] - 12s - loss: 0.0821 - acc: 0.9755 - val_loss: 0.1059 - val_acc: 0.9712
Epoch 7/10
34300/34300 [=====] - 13s - loss: 0.0714 - acc: 0.9794 - val_loss: 0.1103 - val_acc: 0.9699
Epoch 8/10
34300/34300 [=====] - 13s - loss: 0.0635 - acc: 0.9812 - val_loss: 0.0965 - val_acc: 0.9766
Epoch 9/10
34300/34300 [=====] - 13s - loss: 0.0588 - acc: 0.9825 - val_loss: 0.1133 - val_acc: 0.9718
Epoch 10/10
34300/34300 [=====] - 15s - loss: 0.0572 - acc: 0.9826 - val_loss: 0.1085 - val_acc: 0.9729
    
```

Figure 2. Results of L1/4 activation function for 34,000 samples

**IV. CONCLUSIONS**

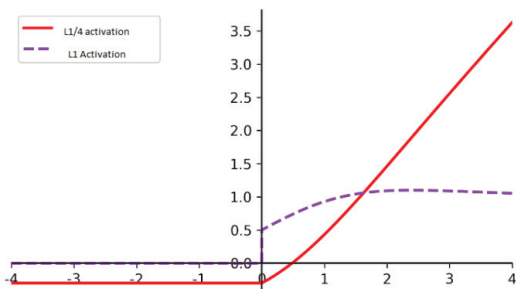


Figure 3. Efficiency of ML model

TABLE I.

COMPARISON OF ACTIVATION FUNCTIONS

Activation function	accuracy	Learning rate
sigmoid	90.58	1.35
ReLU	89.9	0.56
L1	91.58	0.78
L2	96.5	2.72
L1/4	96.9	3.5

L1 regularization has the tendency to produce sparse coefficients. Which means Lasso shrinks the less important feature’s coefficient to zero thus removing some feature altogether. L2 regularization on the other hand does not remove most of the features.

L1 regularization formula does not have an analytical solution but L2 regularization does. So, it is computationally more efficient to do L2 regularization.

**REFERENCES**

[1] I. Bilbao and J. Bilbao, "Overfitting problem and the over-training in the era of data: Particularly for Artificial Neural Networks," 2017 Eighth International Conference on Intelligent Computing and Information Systems (ICICIS), Cairo, 2017, pp. 173-177.

[2] M. Molinier and J. Kilpi, "Avoiding Overfitting When Applying Spectral-Spatial Deep Learning Methods on

Hyperspectral Images with Limited Labels," IGARSS 2019 - 2019 IEEE International Geoscience and Remote Sensing Symposium, Yokohama, Japan, 2019, pp. 5049-5052.

[3] A Flexible Sigmoid Function of Determinate Growth xinyou yin, jangoudriaan, egbert a. lantinga, janvos, huub j. spiertz Annals of Botany, Volume 91, Issue 3, February 2003, Pages 361–371, <https://doi.org/10.1093/aob/mcg029> Published: 01 February 2003.

[4] On Overfitting in Model Selection and Subsequent Selection Bias in Performance Evaluation Gavin C. Cawley, Nicola L. C. Talbot; 11(70):2079–2107, 2010.

[5] D. Stursa and P. Dolezel, "Comparison of ReLU and linear saturated activation functions in neural network for universal approximation," 2019 22nd International Conference on Process Control (PC19), StrbskePleso, Slovakia, 2019, pp. 146-151.

[6] R. Murugadoss and M. Ramakrishnan, "Universal approximation using probabilistic neural networks with sigmoid activation functions," 2014 International Conference on Advances in Engineering & Technology Research (ICAETR - 2014), Unnao, 2014, pp. 1-4.

[7] Journal of Data Science 12(2014),563-574 Softmax Model as Generalization upon Logistic Discrimination Suffers from Overfitting F. Mohammadi Basatinil and Rahim Chinipardaz2\* 1 Department of Statistics, Shoushtar Branch, Islamic Azad University. 2 Department of Statistics, ShahidChamranUniversity

[8] Flatten-T Swish: a thresholdedReLU-Swish-like activation function for deep learning Hock Hung Chieng, Noorhaniza Wahid, Pauline Ong, Sai Raj Kishore Perla Neural and Evolutionary Computing (cs.NE); Machine Learning (cs.LG); Machine Learning (stat.ML) journal reference:International Journal of Advances in Intelligent Informatics, 4(2), 76-86 DOI:10.26555/ijain.v4i2.249

[9] B. Ding, H. Qian and J. Zhou, "Activation functions and their characteristics in deep neural networks," 2018 Chinese Control And Decision Conference (CCDC), Shenyang, 2018, pp. 1836-1841.

[10] K. Hara and K. Nakayamma, "Comparison of activation functions in multilayer neural network for pattern classification," Proceedings of 1994 IEEE International Conference on Neural Networks (ICNN'94), Orlando, FL, USA, 1994, pp. 2997-3002 vol.5.

[11] Khoshgoftaar, T.M., Allen, E.B. Controlling Overfitting in Classification-Tree Models of Software Quality. *Empirical Software Engineering* 6, 59–79 (2001). <https://doi.org/10.1023/A:1009803004576>.

# Yttrium Chloride as Corrosion Inhibitor for 6061Al- SiC Composites in 1:1 mixture of HNO<sub>3</sub> + HCl

P.LavaKumar

Assoc. Professor, CVR College of Engineering/Mechanical Engg. Department, Hyderabad, India  
Email: kumar.lava7023@gmail.com

**Abstract:**The corrosion studies were conducted on Al 6061-15% SiC composites in a 1:1 mixture of HNO<sub>3</sub> and HCl solution of different concentrations viz. 1M, 0.5M and 0.1M at 30, 40 and 50°C using Tafel Extrapolation Technique. Corrosion Inhibition studies were carried out using Yttrium Chloride in different concentrations viz. 50, 100 and 200 ppm. From the data gathered, various thermodynamic and kinetic parameters were calculated. Al – SiC composite was found to be severe to corrosion in 1M HCl+HNO<sub>3</sub>.The corrosion rate of composite increases with increase in temperature. Yttrium Chloride is found to be effective in decreasing the corrosion rates about 91% inhibition was observed at 200 ppm concentration of the inhibitor in HCl+HNO<sub>3</sub>.The efficiency of inhibition increases with concentration of inhibitor.

**Index Terms:** Al 6061-SiC composites, 1:1 mixture of HNO<sub>3</sub> and HCl, Corrosion inhibition, Yttrium Chloride inhibitor, physisorption, Frumkin adsorption isotherm.

## I. INTRODUCTION

Aluminum alloys 6061 reinforced with SiC have a wide range of applications like space engineering and defense [1-5]. There is a decrease in Corrosion resistance of Aluminium Silicon carbide composites compared to its base alloy. A protective oxide layer increases corrosion resistance of Aluminium alloys. But inclusion of SiC particles causes discontinuities in the surface film and increases the number of sites where corrosion can be initiated and makes the composite more vulnerable [1,2,3,6-9]. The intensity of pitting corrosion observed on 6061 Aluminium Silicon carbide composite was greater compared to corresponding unreinforced alloys. It is also showing that corrosion of composites greater than the base alloy. [10]

## II. LITERATURE SURVEY

[1] P. D Reena Kumari, Jagannath Nayak and A. Nityananda Shetty studied the inhibition action of 3-Ethyl-4-amino-5-mercapto-1,2,4-triazole on 6061 Aluminium Silicon carbide composites in sodium hydroxide solution by using potentiodynamic polarization and electrochemical impedance spectroscopy. They found that adsorption of inhibitors on composite through physisorption.

[2] Geetha Mable Pinto , Jagannath Nayak & A. Nityananda Shetty studied inhibition action of 4-(N,N-Dimethylamino) Benzaldehyde Thiosemicarbazone on 6061 Aluminium Silicon carbide composites in Sulfuric acid medium of different concentrations at various temperatures using Tafel Extrapolation and AC impedance

spectroscopy. They observed 70% inhibition efficiency in 0.5 M sulfuric acid. The adsorption of inhibitors on composite was found to be through physisorption. [3] Geetha Mable Pinto , Jagannath Nayak & A. Nityananda Shetty studied the corrosion behavior of 6061 Aluminium Silicon carbide composites in different concentrations of 1:1 hydrochloric acid and sulphuric acid medium at different temperatures. The results showed that an increase in the corrosion rate of composite with temperature and concentration of medium.

## III. EXPERIMENTAL PROCEDURE

### A. Material

The 6061 Aluminium Silicon carbide composites, having SiC particles of size 25 microns and 99.8% purity, were casted in the form of cylinders. The composites were extruded at 450°C- 500°C. The tests were conducted on composite in extruded rod form of 11.5 mm diameter. The composition of the composite under use is presented in Table.I and the microstructure is shown in Fig.1

TABLE I.  
COMPOSITION OF BASE (6061 Al) ALLOY

Element	Cu	Mg	Si	Cr	Al
Weight %	0.25	1.0	0.6	0.25	Balance

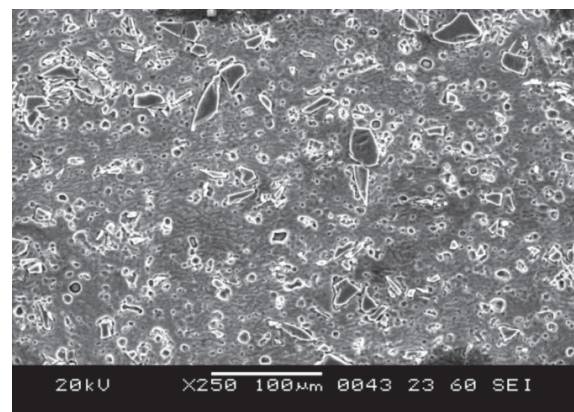


Figure 1. Microstructure of the 6061 Al-SiC sample Etchant: Keller's reagent

**B. Medium**

The corrosion studies were conducted in a 1:1 mixture of HNO<sub>3</sub> and HCl solution of different concentrations viz. 0.1M, 0.5M and 1M at three temperatures; 30, 40 and 50°C. Inhibition studies were carried out using Yttrium Chloride which was used at different concentrations viz. 50, 100 and 200 ppm.

**C. Method**

Tafel extrapolation studies were performed on cross sectional surface of cylindrical 6061 Aluminium Silicon carbide composites by exposing the surface to acid medium with and without inhibitor at above testing conditions by using CH instrument electrochemical analyzer. For each test, corrosion potential and corrosion current density were determined from a graph between Potential(E) and log i. Then, Corrosion rate and inhibition efficiencies were calculated by using following formula

$$CR = \frac{0.129 \times EW \times i_{corr}}{D}$$

Where CR is the corrosion rate in mpy; i<sub>corr</sub> is the corrosion current density in μA/ cm<sup>2</sup>, EW is the equivalent weight and D is the density.

The surface coverage (θ) is calculated as

$$\theta = \frac{(i_{corr(uninh)} - i_{corr(inh)})}{i_{corr(uninh)}}$$

Where, i<sub>corr(uninh)</sub> is the corrosion current density in the absence of inhibitor and i<sub>corr(inh)</sub> is the corrosion current density in the presence of inhibitor.

The percentage inhibition efficiency (% IE) = θ × 100.

**IV. RESULTS AND DISCUSSIONS**

**A. Corrosion behavior in 1:1 mixture of HNO<sub>3</sub> and HCL medium**

The corrosion rates were determined using Tafel extrapolation technique as mentioned earlier and typical plots are shown in following figures

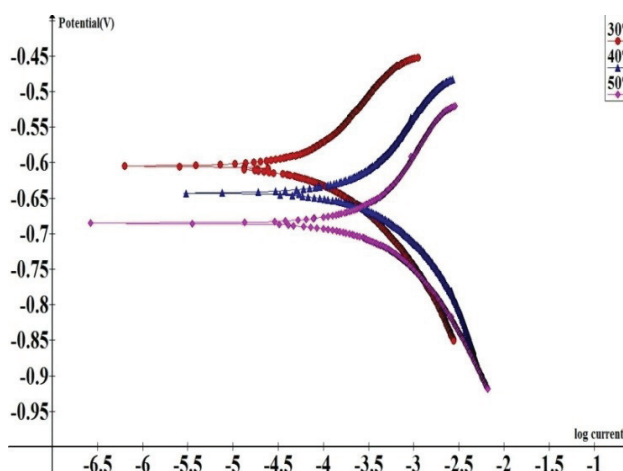


Figure 2. Tafel plot for 0.1M (HNO<sub>3</sub>+HCl) solution at different temperatures.

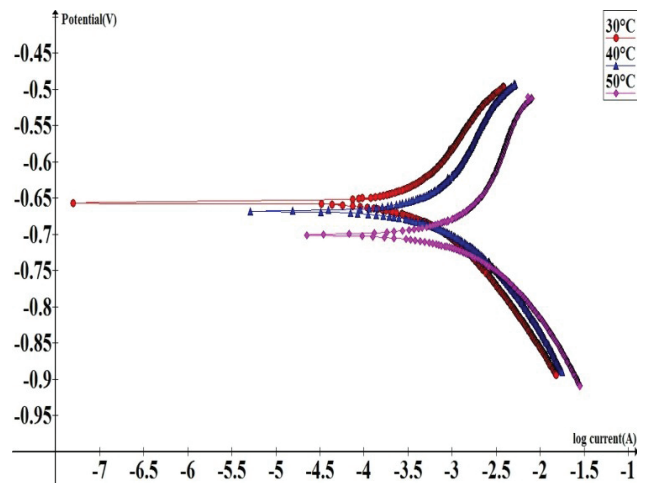


Figure 3. Tafel plot for 0.5M (HNO<sub>3</sub> +HCl) at different temperatures

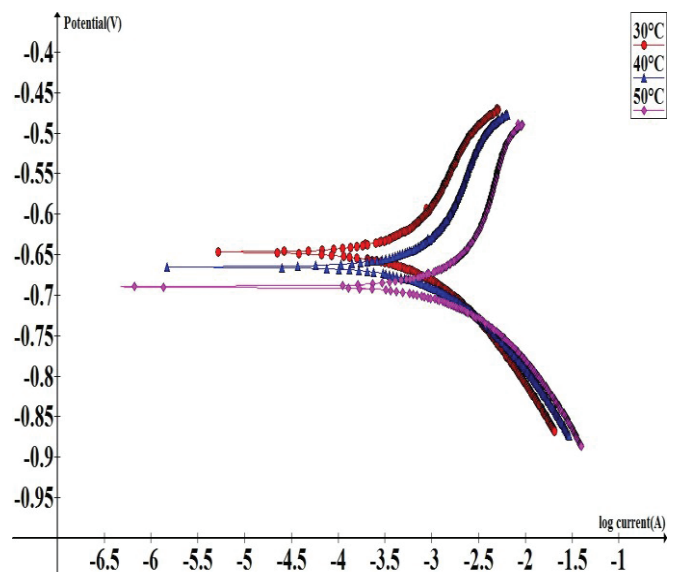


Figure 4. Tafel plot for 1 M (HNO<sub>3</sub> +HCl) at different temperatures

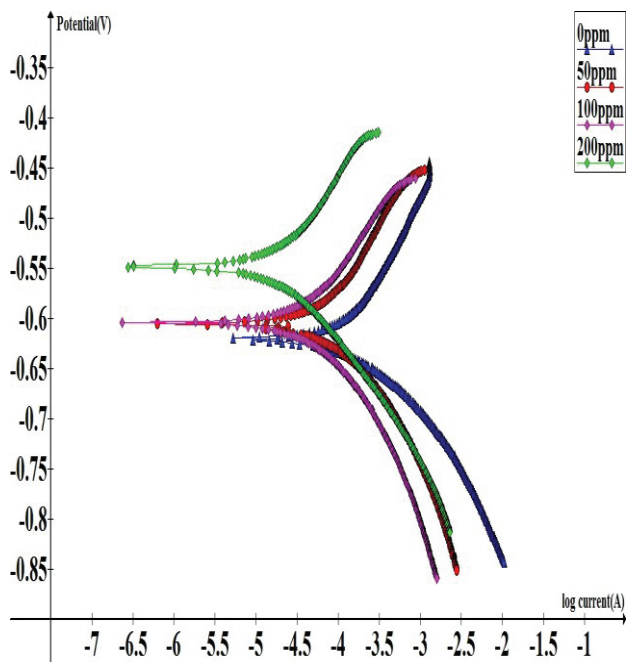


Figure 5. Tafel plot for 0.1 M (HNO<sub>3</sub> +HCl) at 30°C with different concentrations of Yttrium chloride

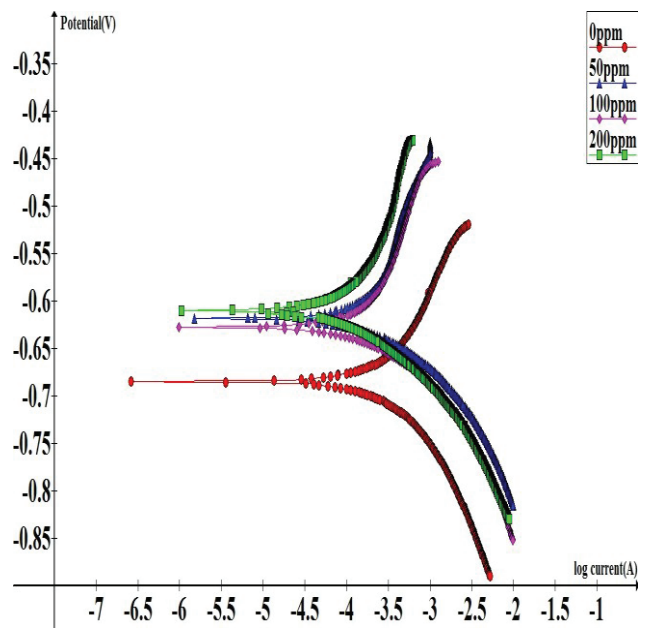


Figure 7. Tafel plot for 0.1 M (HNO<sub>3</sub> +HCl) at 50°C with different concentrations of Yttrium chloride.

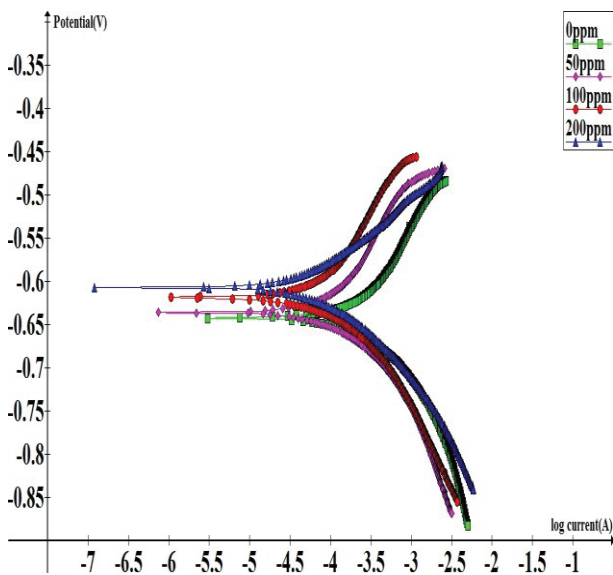


Figure 6. Tafel plot for 0.1 M (HNO<sub>3</sub> +HCl) at 40°C with different concentrations of Yttrium chloride

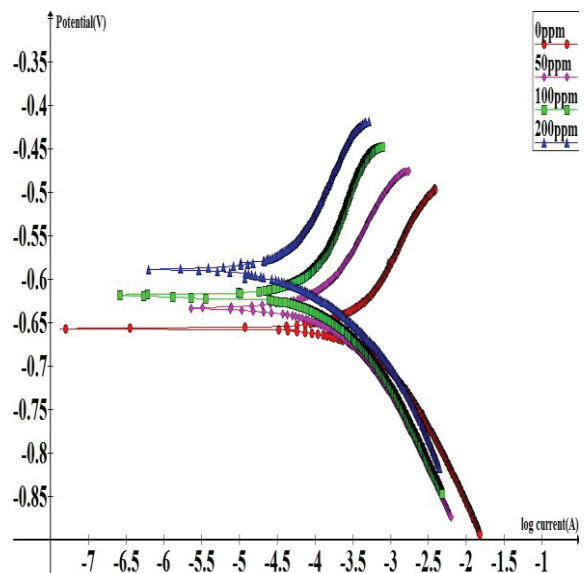


Figure 8. Tafel plot for 0.5 M (HNO<sub>3</sub> +HCl) at 30°C with different concentrations of Yttrium chloride

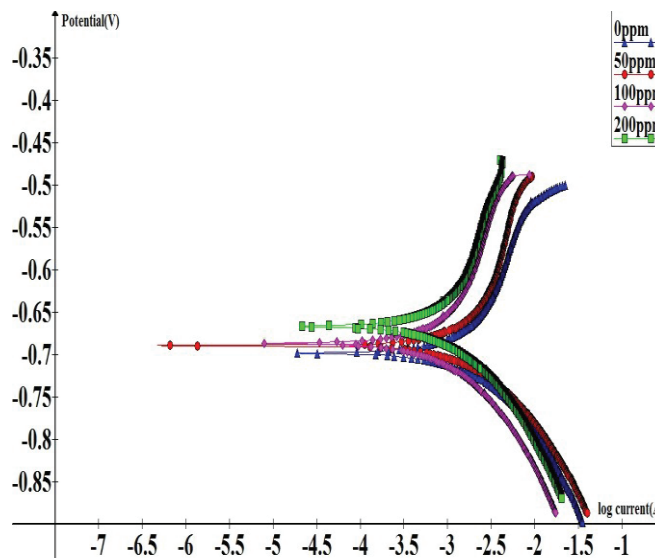


Figure 9. Tafel plot for 1 M (HNO<sub>3</sub> +HCl) at 50°C with different concentrations of Yttrium chloride.

Average values of corrosion rates in 1:1 mixture of HNO<sub>3</sub> + HCl solution obtained for different temperatures are presented in the Table. II

TABLE II.  
CORROSION RATES OF 6061Al-SiC COMPOSITE IN DIFFERENT CONCENTRATIONS OF (HNO<sub>3</sub>+HCL) AT DIFFERENT TEMPERATURES

Medium	Temperature (°C)	Corrosion Rate (mpy)
1M HCl+HNO <sub>3</sub>	30	450.46
	40	1030.17
	50	1579.57
0.5M HCl+HNO <sub>3</sub>	30	235.21
	40	730.63
	50	1183.84
0.1M HCl+HNO <sub>3</sub>	30	118.93
	40	334.81
	50	370.55

The above table shows that corrosion rate increases as temperature increases at each concentration of medium. And, corrosion rate increases as the concentration of medium increases.

Average values of corrosion rates after adding inhibitor in various concentrations to different concentrations of HNO<sub>3</sub>+HCL at different temperatures is presented in Table III.

TABLE III.  
CORROSION RATES OF 6061Al-SiC COMPOSITE IN DIFFERENT CONCENTRATIONS OF (HNO<sub>3</sub>+HCL) AT DIFFERENT TEMPERATURES WITH YTTRIUM CHLORIDE

Medium	Temperature (°C)	Corrosion Rate (mpy)			
		Inhibitor concentration			
		0ppm	50ppm	100ppm	200ppm
1M HCl+HNO <sub>3</sub>	30	450.46	135.05	88.94	83.77
	40	1030.17	798	742.63	657.59
	50	1579.57	1263.2	847.04	765.37
0.5M HCl+HNO <sub>3</sub>	30	235.21	93.12	77.46	62.47
	40	519.4	519.4	458.46	330.86
	50	1183.84	848.72	775.05	594.44
0.1M HCl+HNO <sub>3</sub>	30	118.93	79.69	24.73	10.63
	40	334.81	160.52	98.93	56.41
	50	370.55	215.29	135.05	68.03

The above table is showing that addition of inhibitors decreased the corrosion rate at each temperature and concentration of the medium.

TABLE IV.  
INHIBITION EFFICIENCY OF YTTRIUM CHLORIDE IN 1:1 (HNO<sub>3</sub> +HCL)

Medium	Temperature (°C)	Inhibition efficiency (%)		
		Inhibitor concentration		
		50ppm	50ppm	50ppm
1M HCl+HNO <sub>3</sub>	30	70.54	80.6	81.7
	40	22.9	27.9	51.53
	50	20.2	46.3	36.16
0.5M HCl+HNO <sub>3</sub>	30	62	67.06	73.43
	40	30.2	38.2	55.4
	50	28.3	34.5	49.78
0.1M HCl+HNO <sub>3</sub>	30	32.9	79.2	91.05
	40	52.05	70.45	82.77
	50	36.4	60.1	79.92

From the above table, we can see that a maximum inhibition efficiency of about 91% was achieved with 200 ppm of inhibitor addition in 0.1M (HCl+HNO<sub>3</sub>) at 30°C.

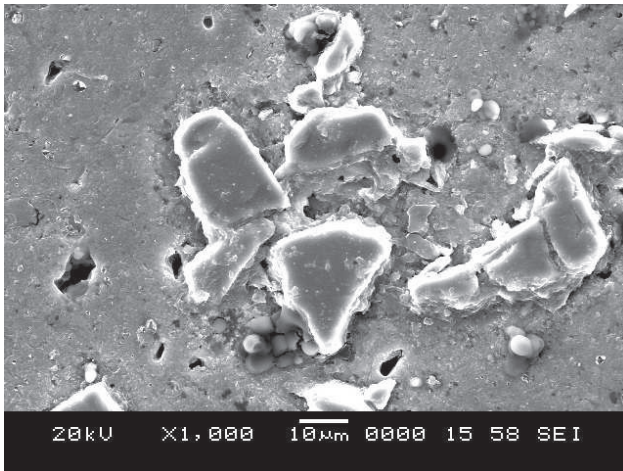


Figure 10. Corroded sample of 6061 Al-SiC in 1M HCl+HNO<sub>3</sub> at 30°C.

The SEM image of the corroded sample as shown in the Fig. 10 indicates that there is uniform corrosion along with corrosion around SiC particles. This is because of the galvanic effect between particle and the matrix in which matrix acts as anode.

#### V. CONCLUSIONS

- ✚ 6061 Aluminium Silicon carbide composite is subjected to corrosion in 1:1 (HCl+HNO<sub>3</sub>) solution.
- ✚ Corrosion rate of composite increases with increase in temperature and with increase in concentration.
- ✚ An addition of 200 ppm Yttrium Chloride achieved 91% inhibition efficiency and is found to be effective inhibitor

#### REFERENCES

- [1] P.D. Reena Kumari, Jagannath Nayak and A. Nityananda Shetty, *Portugaliae Electrochimica Acta*, 29 (2011), 445-462.
- [2] Geetha Mable Pinto, Jagannath Nayak and A. Nityananda Shetty, *Synthesis and Reactivity in Inorganic, Metal Organic and Nano-Metal Chemistry*, 41 (2011) 127-140.
- [3] Geetha Mable Pinto, Jagannath Nayak and A. Nityananda Shetty, *Int. J. Electrochem. SCI*, 4 (2009), 1452-1468.
- [4] C. Monticelli, F. Zucchi, G. Brunoro, G. Trabonelli, *J. Appl. Electrochemistry*, 27(1997)325
- [5] A. Pardo, M.C. Merino, S. Merino, F. Viejo, M. Carboneras, R. Arrabal, *Corrosion Science*, 47(2005) 1750.
- [6] A. Pardo, M.C. Merino, S. Merino, M. D. Lopez, F. Viejo, M. Carboneras, *Mater. Corros.*, 54(2003) 311.
- [7] C. E. Da Costa, F. Velasco, J. M. Toralba, *Rev. Metal. Madrid.*, 36(2000)179.
- [8] P. K. Rohatgi, *Journal of Metals*, 43(4) (1991)10.
- [9] A. J. Trowsdale, B. Noble, S. J. Harris, I. S. R. Gibbins, G. E. Thomson, G. C. Wood, *Corrosion Science*, 38(1996) 177.
- [10] R. C. Paciej, V. s. Agarwala, *Corrosion* 42(1986)718.

# Hazard Rate Diagnosis of Heavy Earth Moving Machinery using 2-parameter Weibull Analysis

A. Suresh

Asst. Professor, CVR College of Engineering/Mechanical Engg. Department, Hyderabad, India  
Email: suri0341@gmail.com

**Abstract:** Hazard rate is a parameter of importance for understanding the machine completely. If a machine could perform to its full potential it has to go through a series of well-defined maintenance policies along with supervision and care. However, the performance of a machine alters based on the time as defined by the bath tub curve. It is a property by law. Hence a fixed way of familiarization may not hold good to access and ascertain the performance of the machine. Thus, for the machines in particular of heavy earth moving machinery are to be emphasized for the hazard rate by a meticulous and cumbersome method that can protect and prevent the machine by analyzing its condition periodically. Weibull analysis is one of the ways of such method that holds good to this purpose. Apart from the many other methods, a 2-parameter weibull analysis is an effective method to find the hazard rate of heavy earth moving machinery (HEMM). The data of HEMM is taken from the operating conditions of the machines in the field. Usually the HEMM are subjected to many number of failures, sometimes same failure may happen multiple of times. The hazard rate lies in how vulnerable is the failure, as well as what is the root cause for the failures. In practice it is also found from the investigation the major components or parts that are contributing the maximum portion for the failure of the machinery. These findings are very essential for the formulation of the suitable maintenance policy along with the vital areas of the machinery for preventive actions. And also the maintenance policies are different for the different periods of machine operation. Hence the position of the machine in bath tub curve is also found from the investigation. In order to archive that the collected data is refined as per the requirements for the assessment of the performance of HEMM, Weibull analysis is an effective method for the assessment of the reliability; availability and also the hazard rate. Machines follow different failure distributions hence it is very important to know the failure distribution of the HEMM. During the investigation of the hazard rate the failure distribution of the HEMM is calculated. In the present work the 2-parameter weibull analysis, the scale and shape parameters are found and based on the findings, the hazard rate of the HEMM is found, also the position of the machine is obtained.

**Index Terms:** Hazard rate diagnosis, heavy earth moving machinery, reliability, availability

## I. INTRODUCTION

The heavy moving machineries play an important role in the performance of plant and production. They are the key machines among all machines present in the industry. In addition to it the problems associated with these machines are more compared to any other conventional machines because of its operations in hazardous environment. HEMM are generally subjected to more number of failures hence the probability of failures for HEMM is more and there by the hazard rate. Before going to the actual assessment of the

hazard rate, the term hazard rate is to be understood in a more elaborative and elucidative way to understand its role in an industry [1,2,3].

The trend of the machine is an important indicator for the machine's growth or decline. As per the bathtub curve any machine has three stages in its lifetime. They are the starting or early age, middle age and the end death declining or death stage. Based on the position of the machine the suitable maintenance policies are suggested to the operations and maintenance personnel. It is often observed in the industry about the vital few trivial many concepts; the same Perato's principle is also applied to the HEMM components. Those failures which are giving the maximum effect over the performance of the machines are assessed from that the preventive and protective measures are suggested.

Hazard rate is the statistic that defines the amount of risk present in the machine if it continues its operation on the present state. It indicates the problems associated with the machine and shows how the machine behaves against the time of operation. It is a usual experience to see that a machine often experiences less performance as the time lapses. But because of that fact the industry should not suffer any more. This is possible if and only if the machine is settled down as per its performance. Hence the performance and capability of the machine is prime concern in all the places. There is no short cut for the assessment of the performance of the machine. As described in the bath tub curve, a machine has usually three stages of life. They are the infant age, the young age and the old age. By observing the bath tub curve, the failures pattern gradually decreases and reaches a constant, after that there is an increase in the failure rate. Hence it is very difficult to identify and assess the nature of the failure distribution of HEMM. In addition to that the failures trend of the HEMM is difficult to find. This problem is solved by adopting the 2-parameter weibull analysis. Here in this analysis the 2 parameters namely shape parameter and scale parameter are used. These two parameters lay an arena to identify the failure and repair distribution based upon the reliability, availability and maintainability are found. Here in this research the impact of machine's failure rate that is hazard rate is identified and then the distribution of failures is found. By that the hazard rate is found there by the know-how analysis is made towards the action to be taken for the machine to work. The detailed methodology is given in the flow chart shown below in figure 1.

Heavy earth moving machinery performance is more important particularly in mining industry. Here in this research the dumpers used in coal mines of singareni collieries are considered for investigation of performance. It



is a usual practice to use the dumpers in the mining industry to transport the raw materials from the mining area to the place of shipping yard. As a part of dumpers operation, the machines are often subjected to multiple numbers of failures. However the impact of failures over the performance of the industry alters from situation to situation. As a part of those failures the intensity of them are accessed by hazard rate in other terms the effect of machine failures over the system performance.

Even though there are many number of ways to find the hazard rate the weibull analysis is by default an effective and efficient method to ascertain the status of the machine in terms of its performance. This method uses two parameters viz shape parameter and scale parameter. These two parameters show the pattern of the machine failures and their distribution with time. In graphical representation the x axis denotes the time and y axis denotes the impact of failures of the machine, here in this case the dumpers. Based on the values of the shape parameter and scale parameter the intensity and nature of hazard is understood. On the other hand in addition to the hazard rate the reliability and availability of the machine (dumpers) is accessed. Here the noteworthy thing to understand is the ability of the machine to perform the intended tasks with minimum number of failures is the reliability of the machine. But the failure of the machine, which affects abruptly the entire process of the industry, is known as hazard rate. If the machine whether it is operating or not but available for work is the availability of the machine. These parameters give the complete details of the condition of the machine. By considering the wide spread applications of the heavy earth moving machinery in the field of engineering and production, the weibull analysis helps a lot.

The finding of the hazard rate, reliability, availability and maintainability alone will not constitute the solution to the problem. The application of these parameters into the wide spread performance of the machine is very important. Hence the emphasis made on the applicability of the above mentioned parameters to find the most effective and efficient solution is made. As a part of that the cause and effect diagram is made for the finding of the most critical cause that accounts to huge loss.

## II. LITERATURE SURVEY

The hazard rate diagnosis is the matter of interest particularly in the HEMM, because a rapid failure of such machine may result in unrecoverable loss. This is the reason many of the researches often emphasize the diagnosis mechanisms or methodologies, which certainly yields a better solution. But it is a factious thought that all the routes do not yield a same and required solution. However if the diagnosis of HEMM made through the weibull analysis makes the factious thoughts into reality. Because it is the best result oriented method that yields better results among its competitive methods. In addition to that the weibull analysis gives multiple results and they are useful for further investigation. It also evolves and describes the spread of the distribution of the failures or the outcomes of the machine [4,5,6]. This gives the foundation for the assessment of the reliability, availability and maintainability. But most of the

researches have suggested about the investigation of the reliability by homogeneous or non-homogeneous processes. Out of all the methods the weibull analysis gives the best results. In spite of many other ways to access the performance of the machine hazard rate is emphasized because of its impact on the productivity. If a machine is failed because of some reason it may lead to some loss but if a machine is failed abruptly, it will create a catastrophic situation that will make the entire industry failure.

The trend of the failures of the machine is an alarming parameter that can constitute the framing of the suitable and sound measures for the betterment of the productivity. There are many methods available for the assessment of the HEMM failures trend. Out of them the following methods are used for the finding of the trend they are Eye ball test and cumulative plot test. Each test is performed for Time Between Failures (TBF) and Time To Repair (TTR). The majority of the outcomes of the above tests are considered for the decision making.

## NOMENCLATURE

$\alpha$ :	Scale Parameter
$\beta$ :	Shape Parameter
$\gamma$ :	Location Parameter
$\sigma$ :	Log Mean Standard Deviation
$\xi$ :	Log Mean Value
$\phi$ :	Standard Normal Cumulative Distribution Function
(t):	Time
CDF:	Cumulative Distribution Function
CTBF:	Cumulative Time Between Failures
F(t):	Cumulative Probability
f(t):	Instantaneous Density Function
H:	Hazard Rate and Hazard Function
HPP:	Homogeneous Poisson Process
i.i.d:	Independently Identically Distributed
MCCF:	Mean Cumulative Cost Function
MCRF:	Mean Cumulative Repair Function
MTBF:	Mean Time Between Failures
MTTR:	Mean Time To Repair
N or n:	Number of Failures;
n(t):	Function of Cumulative Number of Failures on time 't' (general)
N(t):	Cumulative Number of Failures at time 't' (instantaneous)
NHPP:	Non Homogeneous Poisson Process
OTBF(or OT):	Ordered Time Between Failures
PDF:	Probability Density Function
R(t):	Reliability Function
R:	Reliability function
ROCOF:	Rate of Occurrence of Failures
RP:	Renewable Process
$S_i$ :	Sum or Total Time on Test up to $i^{th}$ failure
TBF:	Time Between Failures

$t_j$  : Failure time at  $j^{\text{th}}$  failure  
TTR: Time To Repair  
TTT: Total Time to Test

**III. METHODOLOGY**

The detailed methodology is shown in the below figure no 1. The complete procedure of hazard rate diagnosis is given in the flow chart. Even though there are many number of earth moving machines available in the company the emphasis is made on the dumpers because of their

importance. At first the trend analysis is carried out then the trend of the HEMM found. After finding the trend of the machines using the 2 parameters weibull analysis is performed for the finding of the hazard rate, reliability, availability. There are some assumptions for the analysis of the HEMM, they are the effects of the weather changes during the machines working is neglected. The human working hours are not considered for the assessment of the machines. Emotions and attitudes of the persons operating the HEMM are also neglected. A maximum of 20 hours per day is considered for the HEMM operations.

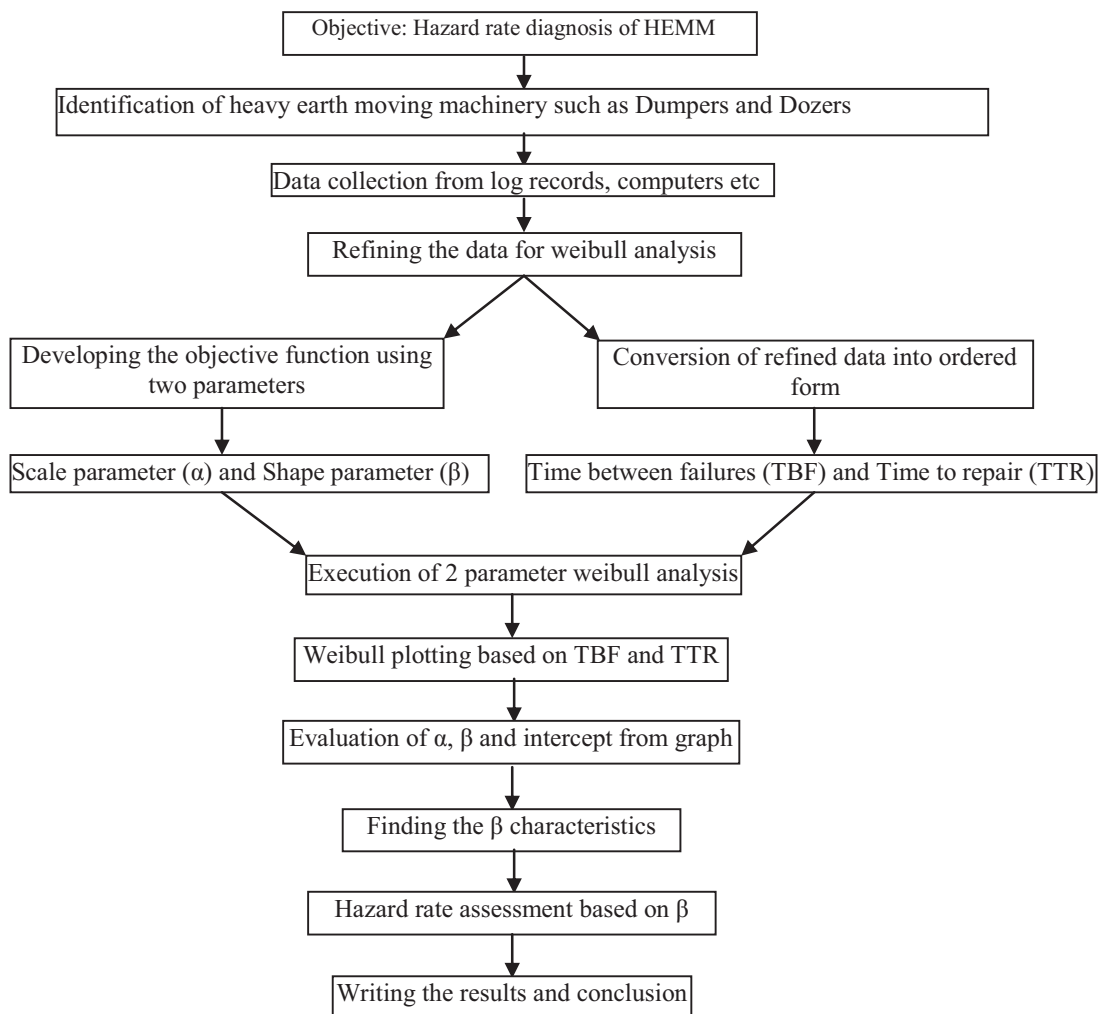


Figure 1. Methodology of 2-parameter weibull analysis for hazard rate diagnosis

As briefed above in the figure 1 it is made in such a way that the hazard rate is analyzed by the weibull analysis with two parameters scale ( $\alpha$ ) and shape parameters ( $\beta$ ). Out of all, the collection of data is a cumbersome task because of

the heavy and difficult climatic conditions of the working environment. There is a maintenance period of 5 days for every 100 days of dumper operation for the maintenance apart from the intermittent failures.

**IV. ANALYSIS**

The results of the trend tests are given below the table no. I. Based on the outcomes of the two tests the below results are obtained. In some cases two tests have resulted two different outcomes. Yet the most appropriate outcome is

selected for the decision. There are three possible outcomes for the trend analysis namely positive trend, negative trend and no trend. There were two ways in which the machine’s performance with respect to trend analysis is calculated one

is TBF and the other is TTR. Positive trend indicates the machine is increasing in its performance. Negative trend indicates the machine is decreasing in performance and no trend indicates that the machine has constant performance.

TABLE I.  
TREND TESTS RESULTS

S. No	HEMM No	Cumulative Trend Test	Eye Ball Trend Test	Trend
1	C-3611	+Ve Trend	+Ve Trend	+Ve Trend
2	C-3690	No Trend	Weak -Ve Trend	No Trend
3	C-3752	+Ve Trend	Strong +Ve Trend	+Ve Trend

The analysis is made based on the performance of the heavy earth moving machinery used in Singreni collieries company limited Godavarikhani during the year 2019. The heavy

earth moving machinery here in this research used is the dumper. A dumper is heavy earth moving machinery used in the company for the transportation of the coal from the mines to the dump yard and or to the supply station. The analysis started with the collection of the failure data from the site [7,8,9]. Basically the failure data is recorded in three modes. They are number of failures, frequency of failures and the third one the cost of failures. Here in this analysis, the number and frequency of failures are considered. After reeving the data, the classification of the data into required form such as TBF and TTR is made. From that data the weibull analysis is done as shown in table 1 below for the assessment of the dumpers stage in bath tub curve and also the ability and capability of the machine. Here in this analysis two parameters scale parameter ( $\alpha$ ) and shape parameter ( $\beta$ ) are used. Hence the method named as two parameter weibull analysis [10,11,12].

**GRAPHS OF EYE BALL TEST**  
(Time Between Failures Vs Cumulative Failure No)

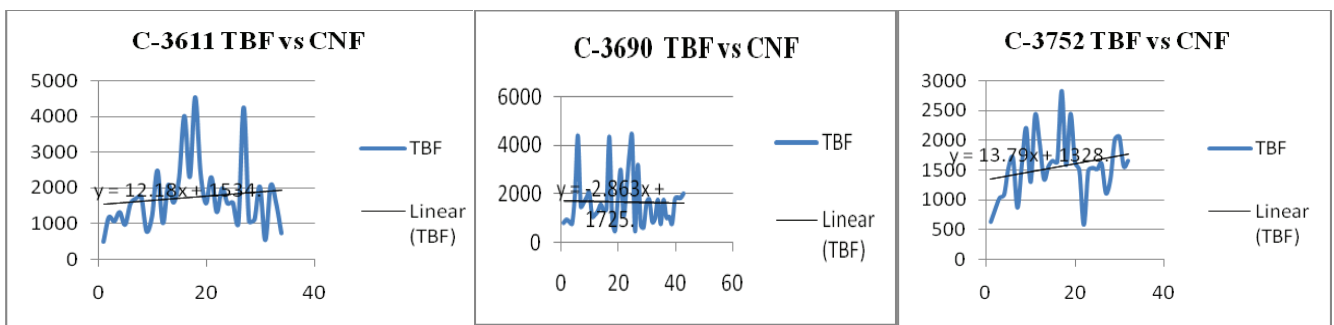


Figure 2. Graphs showing the cumulative plot test

**GRAPHS OF CUMULATIVE PLOT TEST**  
(Cumulative Time Between Failures Vs Cumulative Failure No)

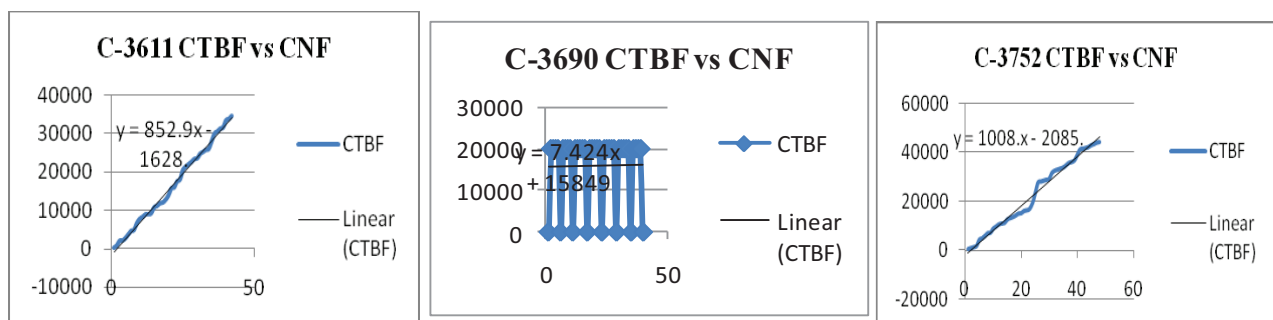


Figure 3. Graphs of eye ball test

In the above figure no 3 the graph shows the results of eye ball test. In the each graph the x axis is taken as cumulative failure numbers and on y axis the cumulative time between failures. For the HEMM no C-3611, the graph indicates the positive trend. For the HEMM no C-3690 the graph indicates no trend. For the HEMM no C-3752 the graph indicates the positive trend. In the above figure no 2

the graphs indicate the results of eye ball test. In the each graph the x axis is taken as cumulative failure numbers and on y axis the time between failures. For the HEMM no C-3611 the graph indicates the positive trend. For the HEMM no C-3690 the graph indicates weak negative trend. For the HEMM no C-3752 the graph indicates the strong positive trend.

TABLE II.  
WEIBULL ANALYSIS

S No	TBF	f(t)	1 / (1-f(t))	(x) = ln(t)	(y) = ln ln (1 / (1-f(t)))
1	2	0.017677	1.017995	4.276666	-4.0266
2	6	0.042929	1.044855	4.564348	-3.12634
3	92	0.068182	1.073171	5.257495	-2.65048
4	92	0.093434	1.103064	5.257495	-2.32185
5	40	0.118687	1.13467	5.480639	-2.06876
6	40	0.143939	1.168142	5.480639	-1.86166
7	64	0.169192	1.203647	5.575949	-1.68547
8	88	0.194444	1.241379	5.66296	-1.53144
9	12	0.219697	1.281553	5.743003	-1.39403
10	84	0.244949	1.324415	5.950643	-1.26951
11	84	0.270202	1.370242	5.950643	-1.15522
12	80	0.295455	1.419355	6.173786	-1.04924
13	80	0.320707	1.472119	6.173786	-0.9501
14	04	0.34596	1.528958	6.222576	-0.85664
15	28	0.371212	1.590361	6.269096	-0.76795
16	576	0.396465	1.656904	6.356108	-0.68329
17	576	0.421717	1.729258	6.356108	-0.60204
18	600	0.44697	1.808219	6.39693	-0.52367
19	600	0.472222	1.894737	6.39693	-0.44773
20	672	0.497475	1.98995	6.510258	-0.37381
21	672	0.522727	2.095238	6.510258	-0.30155
22	696	0.54798	2.212291	6.54535	-0.23064
23	720	0.573232	2.343195	6.579251	-0.16074
24	744	0.598485	2.490566	6.612041	-0.09156
25	768	0.623737	2.657718	6.64379	-0.02279
26	888	0.64899	2.848921	6.788972	0.045872
27	912	0.674242	3.069767	6.81564	0.114758
28	984	0.699495	3.327731	6.891626	0.184229
29	1104	0.724747	3.633028	7.006695	0.254694
30	1152	0.75	4	7.049255	0.326634
31	1152	0.775253	4.449438	7.049255	0.400639
32	1224	0.800505	5.012658	7.109879	0.477455
33	1512	0.825758	5.73913	7.321189	0.558076
34	1560	0.85101	6.711864	7.352441	0.643892
35	1776	0.876263	8.081633	7.482119	0.73697
36	1848	0.901515	10.15385	7.521859	0.840641
37	1848	0.926768	13.65517	7.521859	0.960927
38	1944	0.95202	20.84211	7.572503	1.110862
39	2064	0.977273	44	7.632401	1.330832

The failure data of the HEMM is collected based on TBF and TTR and then that data is transformed into the Ordered Time Between Failure (OTBF). Based on the two parameter weibull analysis is done and from the above derived table as per the methodology of the weibull analysis the ordinate values are obtained and they are further formulated into the distribution graph along with the trend as shown in figure no. 8. Based upon the trend of the distribution the equation of weibull analysis obtained as  $y = 1.98x - 7.583$ . From that equation beta value (shape parameter) is found as 1.98 and the scale parameter ( $\alpha$ ) = 46.05.

In the same way the weibull analysis is done with the failure data of the time to repair (TTR), the result of the

analysis is given below in the figure no 7. Based upon the trend of the distribution the equation of weibull analysis obtained as  $y = 1.345x - 5.960$ . From that equation beta value (shape parameter) is found as 1.745 and the scale parameter ( $\alpha$ ) = 30.43. Similarly, for the HEMM 2 and 3 the  $\alpha$  and  $\beta$  values based on the TBF and TTR are listed below in table no 2.

TABLE III.  
A AND B VALUES FOR DUMPER 2 AND 3

Parameter	TBF		TTR	
	$\alpha$	B	A	$\beta$
Dumper 2	32	1.584	44.60	1.745
Dumper 3	90	1.555	39.34	1.476

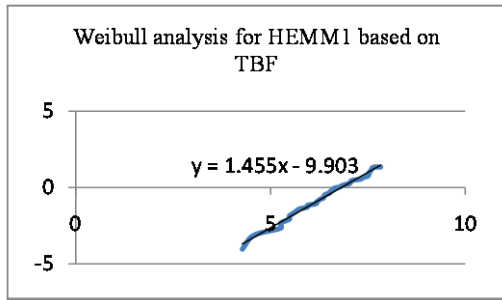


Figure 4. Weibull plot for dumper 1 based on TTR

Above figure no 4 shows the weibull analysis of dumper3 based on the time between failure (TBF) with the trend of  $y = 1.455x - 9.903$ . From the above figure it is understood that the dumper is showing a positive trend with time.

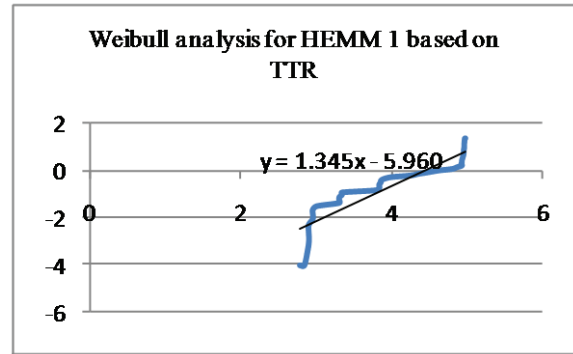


Figure 7. Weibull analysis for HEMM1- TTR

Above figure no 7 shows the weibull analysis of dumper3 based on the time to repair (TTR) with the trend of  $y = 1.345x - 5.960$ . From the above figure it is understood that the dumper is showing a positive trend with time.

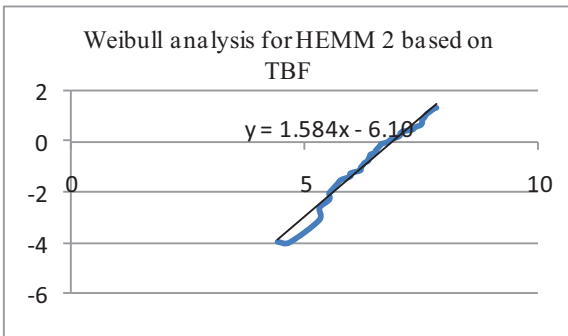


Figure 5. Weibull analysis for HEMM2- TBF

Above figure no 5 shows the weibull analysis of dumper based on the time between failure (TBF) with the trend of  $y = 1.548x - 6.10$ . From the above figure it is understood that the dumper is showing a positive trend with time.

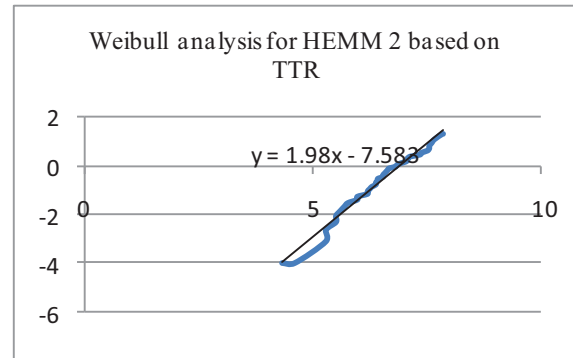


Figure 8. Weibull analysis for HEMM2- TTR

Above figure no 8 shows the weibull analysis of dumper3 based on the time to repair (TTR) with the trend of  $y = 1.98x - 7.583$ . From the above figure it is understood that the dumper is showing a positive trend with time.

Below figure no 6 shows the weibull analysis of dumper3 based on the time between failure (TBF) with the trend of  $y = 1.555x - 7.70$ . From the above figure it is understood that the dumper is showing a positive trend with time.

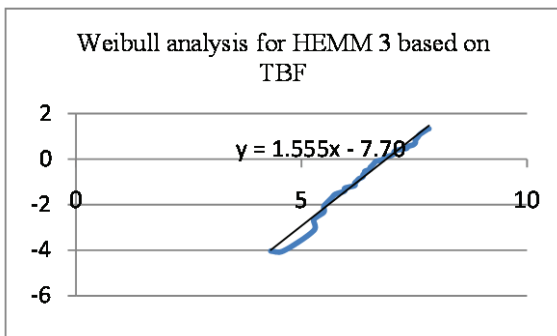


Figure 6. Weibull analysis for HEMM3- TBF

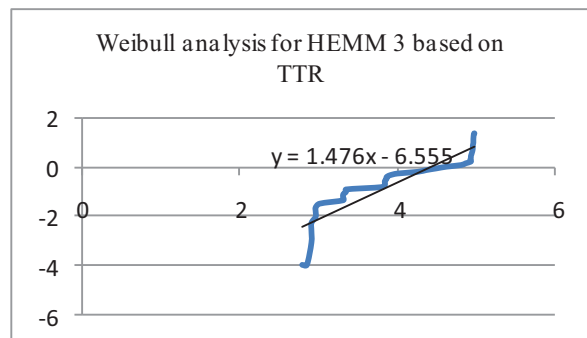


Figure 9. Weibull analysis for HEMM3- TTR

Above figure no 9 shows the weibull analysis of dumper3 based on the time to repair (TTR) with the trend of  $y = 1.476x - 6.555$ . From the above figure it is understood that the dumper is showing a positive trend with time.

**A. Reliability**

Reliability: It is the ability of a machine to work with minimum or zero number of failures and it is indicated as a probability value. Its value is directly proportional to the life of a machine with minimum or zero number of failures. It can be calculated using the equation

$$R(t) = e^{-\lambda t} \tag{1}$$

For dumper 1

$$R(t) = e^{-(1/781.2)*1032} = 26.6 \%$$

For dumper 2

$$R(t) = e^{-(1/678.3)*1046} = 21.39 \%$$

For dumper 3

$$R(t) = e^{-(1/803.2)*1055} = 26.88 \%$$

**B. Availability**

Availability: It is the ability of a machine to work with minimum or zero number of failures and it is indicated as a probability value. Its value is directly proportional to the life of a machine with minimum or zero number of failures. It can be calculated using the equation

$$A(t) = e^{-\lambda t} \tag{2}$$

For dumper 1

$$A(t) = e^{-(1/942.2)*1060} = 32.46 \%$$

For dumper 2

$$A(t) = e^{-(1/932.4)*1039} = 32.81 \%$$

For dumper 3

$$A(t) = e^{-(1/951.2)*1090} = 31.79 \%$$

**C. Hazard rate**

Hazard rate: It is the failure rate at an instance is expressed on conditional basis that a machine performs its functions needs to function as well in the next instance too without failure.

$$\lambda(t) = \frac{f(t)}{1-F(t)} \tag{3}$$

For dumper 1

$$\lambda(t) = \frac{f(t)}{R(t)} = \frac{0.674}{0.266} = 2.53$$

For dumper 2

$$\lambda(t) = \frac{f(t)}{R(t)} = 0.7861/0.2139 = 3.67$$

For dumper 3

$$\lambda(t) = \frac{f(t)}{R(t)} = 0.7312/.2688 = 3.16$$

The hazard rate is in between 2-3 for dumper 1 it indicates that the risk of failure is more and hence the machine is to be monitored frequently as well as replacement is to be scheduled as soon as possible. And for dumper 2 and dumper 3 the value is furthermore and is in between 3 and 4. That indicates that these two dumpers are in old age too and are for replacement.

**V. RESULTS**

The 2-parameter weibull analysis of the HEMM (dumpers) has given the following results. As the  $\beta$  value for the TBF (reliability) and TTR (availability) analysis have came in between 1 and 2.

TABLE IV.  
LIST OF RESULTS

Parameter		Dumper 1	Dumper 2	Dumper 3
TBF	A	46.05	32	90
	B	1.98	1.584	1.555
TTR	A	30.43	44.60	39.34
	B	1.745	1.745	1.476
Reliability		26.6	21.39	26.88
Availability		32.46	32.81	31.79
Hazard rate		2.53	3.67	3.16
Dumper position in life cycle		Old stage	Old stage	Old stage

Hence it is the clear indication that the machine has increasing failure rate. And the distribution follows the concave shape. And this indicates that the machine is in the old age as per the bath tub curve. Hence the machine is towards the replacement and or changing condition. And the scale parameter shows that the availability of the HEMM is more than that of reliability as detailed in table no III.

It is because of the fact that the machine has more amount of time to repair. It happens because there are certainly many number of associated and or dependent problems existed in the dumper. And also it is to be understood that the machine often experiences the repairs in the old age.

Therefore, it is resulted that the dumpers are in the old or death stage and it is further understood that the replacement to be done accordingly.

## VI. CONCLUSIONS

The hazard rate diagnosis is performed based on the 2 parameter weibull analysis; the two parameters are scale parameter ( $\alpha$ ) and shape parameter ( $\beta$ ). The HEMM (dumpers) are identified that, they are in the death stage and hence the dumpers does not require any further maintenance except the replacement. This analysis is very useful for the assessment of the machine (dumper) performance.

As there are many other ways to assess the position of the machine in the bath tub curve. The weibull analysis is an efficient and effective tool for the understanding of the exactness of the machine performance. And it is not an easy task to understand the HEMM (dumper) condition but with this method the exactness of the machine is found. In the mining industry this analysis is very useful.

## REFERENCES

- [1] Y. Ren, L. Liu, Z. Wang, X. Chen and S. Liu, "A Fault Analysis and Prediction of Aircraft Based on Association Rules and Weibull Distribution," 2019 10th International Conference on Information Technology in Medicine and Education (ITME), Qingdao, China, 2019, pp. 570-578.
- [2] D N Prabhakar Murthy, Khairy A H Kobbacy, Haixia Wang, Jay Lee, "New technologies for maintenance",2016, DOI: 10.1007/978-1-84800-011-7\_3
- [3] Prakash kumar, "Condition based maintenance and machine diagnosis system for heavy duty earth moving machinery", International Journal of Science Engineering and Technology, Vol 8, Issue 2, 2018 ISSN: 2348-4098
- [4] Safi Ur Rahman, Sikander Bilal Khattak, Sabir Islam, Anwar Ullah, "Maintenance system for heavy earth moving equipment", Int. Journal of Engineering and Applied sciences, Vol 32, Issue 2, Dec-2016.pg 47-53.
- [5] Vineet R Kamat, Ehsan Rezazadeh Azar, "Earth moving equipment automation: A review of technical advances and future outlook", International Journal of Information Technology in construction", Volume 22, Oct 2017.
- [6] Lulu Zhang , Guang Jin, and Yang You, Reliability Assessment for Very Few Failure Data and Weibull Distribution, Hindawi Mathematical Problems in Engineering Volume 2019, Article ID 8947905, 9 pages, <https://doi.org/10.1155/2019/8947905>
- [7] Ali, S., Ali, S., Shah, I. et al. Reliability Analysis for Electronic Devices Using Beta Generalized Weibull Distribution. Iran J Sci Technol Trans Sci 43, 2501–2514 (2019). <https://doi.org/10.1007/s40995-019-00730-4>
- [8] Abd EL-Baset A. Ahmad and M.G.M. Ghazal, Exponentiated additive Weibull distribution, Reliability Engineering & System Safety, doi: 10.1016/j.res.2019.106663, (106663), (2019).
- [9] Abdulkareem M. Basheer (2019) Alpha power inverse Weibull distribution with reliability application, Journal of Taibah University for Science, 13:1, 423-432,DOI:10.1080/16583655.2019.1588488
- [10] N. S. Temraz, Availability and Reliability Analysis for System with Bivariate Weibull Lifetime Distribution, International Journal of Scientific & Engineering Research, Volume 8, Issue 2, February-2017, ISSN 2229-5518
- [11] Dr. Mandela Govinda Raj, Ch S N Murthy, Balaraju Jakkula, "Reliability analysis and failure rate evaluation of load haul dump machines using weibull distribution analysis",2017, DOI: 10.18280/mmep.050209
- [12] Somya Tiwari, Neha Gupta, Weibull Parameter Estimation For Wind Energy At Different Elevations Using Graphical Method ,International Journal Of Scientific & Technology Research Volume 8, Issue 10, October 2019 Issn 2277-8616.

# CFD Analysis of DI Diesel Engine using Exhaust Gas Recirculation

Sk. Mohammad Shareef<sup>1</sup>, A.L.N. Arun Kumar<sup>2</sup> and T. Venkatesh<sup>3</sup>

<sup>1</sup>Asst. Professor, CVR College of Engineering/Mechanical Engg. Department, Hyderabad, India  
Email: shareefshaik4@gmail.com

<sup>2</sup>Asst. Professor, CVR College of Engineering/Mechanical Engg. Department, Hyderabad, India  
Email: aln.arunkumar@gmail.com

<sup>3</sup>Asst. Professor, CVR College of Engineering/Mechanical Engg. Department, Hyderabad, India  
Email: venkatesh2711991@gmail.com

**Abstract:** NO<sub>x</sub> is produced by a diesel engine due to high temperatures available in the combustion chamber. Nitrogen is in diatomic nature in the air, but at high temperatures available in the combustion chamber, it will divide into monatomic form and this monatomic nitrogen reacts with Oxygen to form NO<sub>x</sub>. To reduce this NO<sub>x</sub> formation in the diesel engine oxygen content is to be reduced in the intake air. It will be achieved by re-circulating some amount of exhaust gas into the combustion chamber through intake air.

This present work discusses the piston bowl design and control of nitric oxides by using exhaust gas recirculation in direct injection diesel engine. Hemispherical piston bowl of the direct injection diesel engine is created with the help of PRO-E software. This piston is used in CFD for analysis of emissions reduction by the method of Exhaust gas recirculation at different percentages. It is proposed to analyze this in CFD by using STAR-CD as a tool.

The results, which are obtained from the CFD are compared with Experimental results which are available in the literature.

**Index Terms:** Hemispherical piston bowl, PRO-E, Direct injection diesel engine, piston bowl, Exhaust gas recirculation, CFD, NO<sub>x</sub> emissions, CO Emissions.

## I. INTRODUCTION

Enhancing combustion engine efficiency is a prime concern today. Plenty of research has gone in to improving the thermal efficiency of the Internal Combustion Engines, to urge more work from the identical amount of fuel burned and also the energy present within the combustion chamber just part, which gets changed over into useful output power. Because combustion happens inside the combustion chamber, the performance of the internal combustion engine relies greatly on the cylinder bowl shape. The complete combustion depends on the amount of air entered the combustion chamber and movement of air. This movement of the air is controlled by cylinder bowl shapes. Thus, there are different varieties of bowl shapes like shallow, hemispherical, cylindrical and toroidal.

The present study focuses on the combustion chamber area of a single-cylinder diesel engine with a specification of 5HP, 1500 rpm. The use of piston crowns in a top portion of piston is the most advantageous for proper combustion timing and increasing the volumetric efficiency of the engine. CFD analysis of the diesel engine has been carried out with hemispherical bowl geometry validated with experimental data. From the available results, it is concluded

that there is a reasonable agreement between CFD and experimental results.

Jaffer Hussain et.al. [1] has conducted an experiment on the direct injection diesel engine to reduce NO<sub>x</sub> emissions by using method exhaust gas recirculation at 0%EGR,5%EGR,10%EGR and 15% EGR. The performance characteristics like Thermal efficiency, Basic fuel consumption, and volumetric efficiency calculated, and emission characteristics like NO<sub>x</sub> and CO values are observed in results.

NV Raghavendra reddy and Dr. Jayashankara [2] have conducted CFD simulation on a direct injection diesel engine with a flat head and W shape toroidal piston. The cylinder temperature, cylinder pressure, Apparent heat release, NO<sub>x</sub>, CO emissions, and soot are calculated and discussed in results.

A.M. Indoria et.al.[3] has investigated the geometry of different combustion chamber of direct injection diesel engine by CFD modelling of in-cylinder flow and concluded which geometry gives more swirl motion of air and calculates the NO<sub>x</sub> emissions and compared these results with experimental data.

B. Jayashankara and V.Ganesan[4] have studied the effect of fuel injection timing and intake pressure on the performance of direct injection diesel engine and performance characteristics of the engine are investigated at different transient conditions using CFD. The results which are obtained by CFD are validated with experimental results. Emissions like NO<sub>x</sub> and soot are presented and discussed in results.

Dr.G.Prasanthi and E Anitha [5] have conducted an experiment on the direct injection diesel engine to investigate the effect of exhaust gas recirculation and calculated the performance and emission characteristics by using Moringa Oliefera oil as biodiesel. This paper concluded that how the emissions and performance characteristics are changed by changing the bio-diesel percentage and EGR rate.

Kota Sridhar et.al.[6] has conducted a computerized simulation of the spark-ignition internal combustion engines. The discrete phase model is used for simulating fuel injection, evaporation, and droplet boiling. The simulation model developed for the single-cylinder spark-ignition engine operating with hexane as fuel and results were noted with different crank angles at a different flow rate.



S Gavudhama Karunanidhi et.al [7] has conducted simulation on direct injection diesel engine by split injection. The performance characteristics and emissions characteristics like Engine efficiency, NOx, and soot are presented and discussed in results.

Shengli Wei et.al.[8] has conducted numerical analysis on direct injection diesel engine by changing the swirl ratios on the swirl chamber and results are observed.

V Kolhe et.al.[9] has conducted simulation on direct injection diesel engine with Pongamia pinnta oil as biodiesel in Computational Fluid Dynamics using FLUENT as a tool and compared these results with experimental results.

V. Kongre and Vivek K.Sunnapwar [10] have conducted simulation work on a direct injection diesel engine fueled with diesel in CFD using FLUENT as a tool and compared Cylinder pressure, Cylinder temperature with experiment data in results.

In this project, the exhaust gas recirculation method is used for reducing emissions of direct injection diesel engine by changing the different rates of EGR using CFD analysis by concluding which rate is best for diesel engine

**II. COMPUTATIONAL PROCEDURE**

The computational mesh is created using either the “Trimming” or the “Mapping” method.

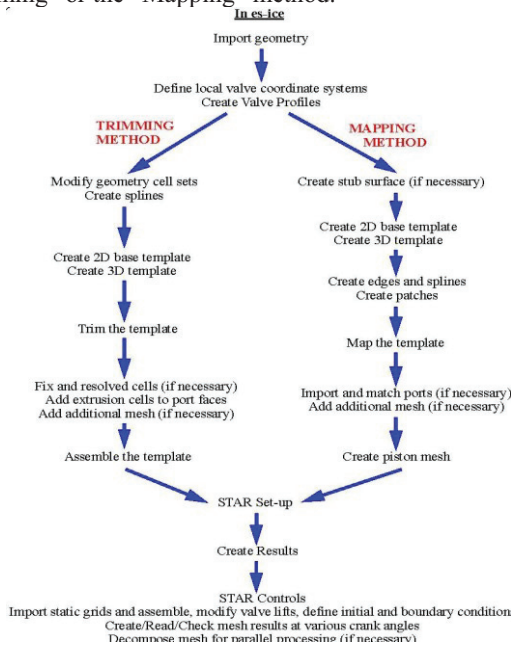


Figure1. Basic steps creating computational mesh

Fig.1 shows the basic steps to create computational piston mesh which is used in CFD for analysis purpose.

Pro-STAR is the general pre-/post-processor of the STAR-CD suite, both the model and CFD analysis parameters need to be defined in pro-STAR, after one has finished working in es-ice. Analyses can be run using serial or parallel processing shown in Fig.2

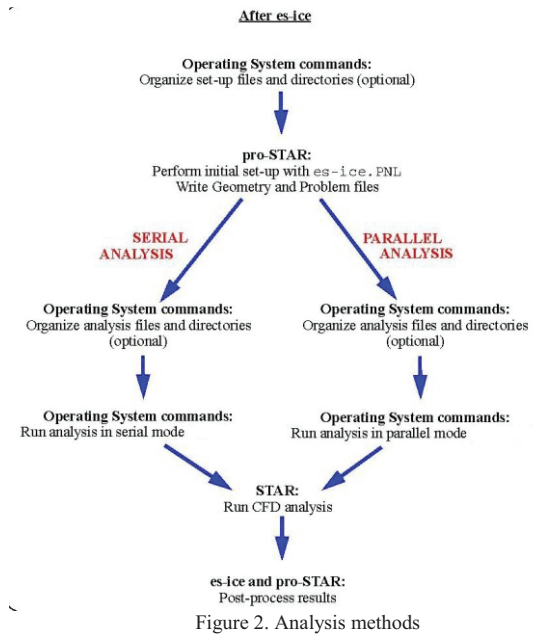


Figure 2. Analysis methods

**A. Generating piston bowl geometry**

CFD simulation begins with the geometry of the piston bowl. The piston bowl shape is prepared from the standard computer-aided-design-package. The co-ordinates are got from the piston crown. After getting co-ordinates of the piston by using commands which is available in the es-ICE (Expert system – Internal combustion engine) the vertexes are created.

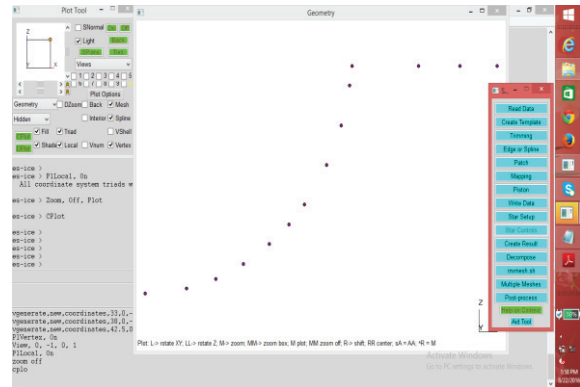


Figure 3. Vertices on geometry window

Fig.3 shows the vertices created on the geometry window. After creating vertices using the spline command, the spline is created in the geometry window.

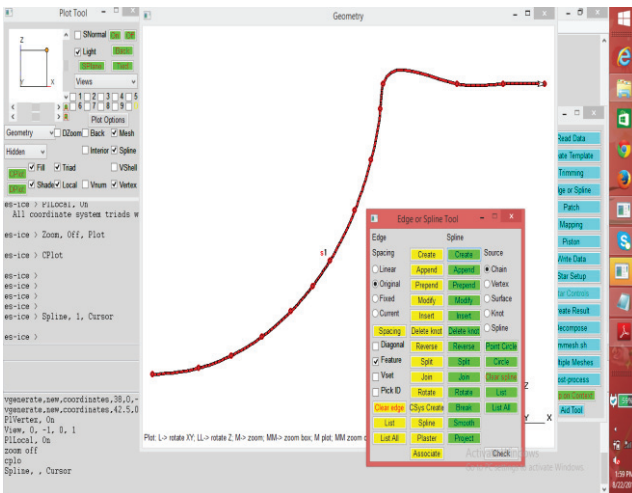


Figure 4. Displaying the spline on geometry window

Fig.4 Shows the spline representing the bowl shape after joining the vertices.

The final stage in the sector meshing process is to trim the bowl splines and generate the 3D sector mesh representing the cylinder sector. A 45-degree sector mesh is made taking advantage of the symmetric form of cylinder domain.

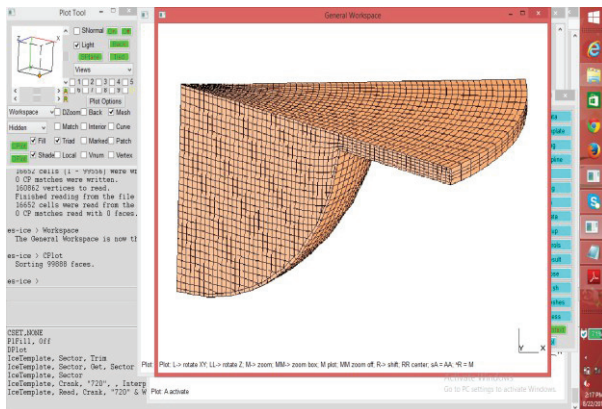


Figure 5. A 45 degree Sector mesh at BDC



Figure 6. A 45 degree Sector mesh at TDC

Fig.5 and Fig.6 show the sector mesh at Bottom dead center and Top dead center of the piston.

This 45-degree sector mesh is used for analysis in CFD software.

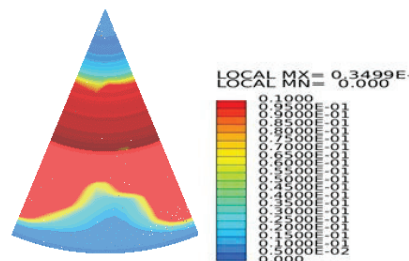
**B. Boundary Conditions.**

TABLE I.  
INPUT PARAMETERS OF CFD DOMAIN

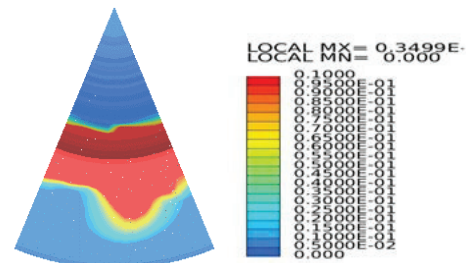
Parameter	magnitude
Crank shaft speed	1500 rpm
Crank radius	47 mm
Bore	85 mm
Stroke	110 mm
Fuel	HSD

Table 1 shows the boundary conditions used for simulation purpose in CFD.

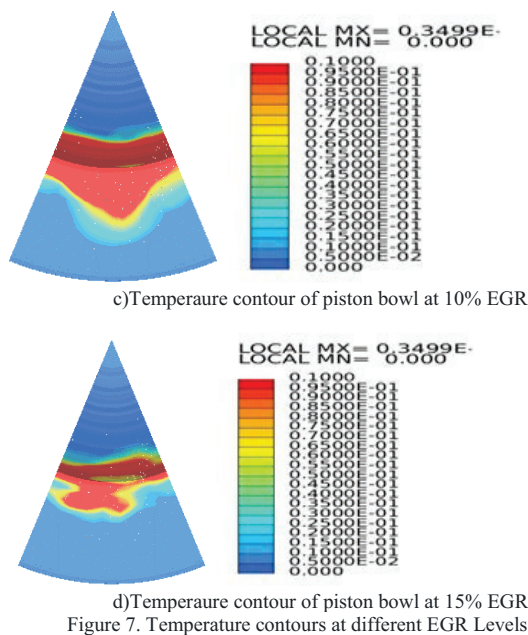
The temperature and pressure available within the combustion chamber of an immediate injection internal-combustion engine are high because of high compression ratios within the combustion chamber of an immediate injection a direct to regulate this high temperature and pressure available within the combustion chamber, a tiny low amount of exhaust gas is mixed with fresh air then introduced into the combustion chamber. This modifies the fuel/air ratio and EGR, which lowers the high temperature in order that the chemical action rate between nitrogen and any unused oxygen is strongly reduced. The engine parameters are applied to 45° Sector mesh for simulation. The CFD Simulation starts at 680 °CA to 800 °CA because this is often the crucial period of investigation towards the evaluation performance and pollutant formation.



a) Temperature contour of piston bowl at 0% EGR



b) Temperature contour of piston bowl at 5% EGR



From Fig.7 it is observed that the temperature contours, high for the piston when the exhaust gas recirculation is more i.e 0%. Because of the high reactions present between oxygen and nitrogen atoms. The temperature contours are decreasing with increasing the EGR levels from 0% to 15%. At 15%EGR the temperature contours are less because of the less reaction present between nitrogen and oxygen.

### III. RESULTS AND DISCUSSIONS

To verify the results from the simulation, the pressure data computed is compared against experimental data from Dr.G.Prasanthi and E.Anith [5]. Table 2 shows the specifications of engine dimensions and combustion parameters. Validation of the current simulation work is carried out with experimental data of Dr.G.Prasanthi and E.Anitha [5]. The computed in-cylinder pressure data from numerical simulation are in good agreement with the experimental data.

TABLE II.  
ENGINE SPECIFICATIONS

S.No	Particulates	Specifications
1	Engine	KIRLOSKAR ENGINE
2	Type	Water cooled
3	Ignition system	Compression ignition
4	Cylinder arrangement	Vertical
5	Maximum speed	1500 rpm
6	Number of Cylinder	1
7	Bore	85mm
8	Stroke	110mm
9	Compression Ratio	16.5:1
10	Maximum HP	5HP
11	Fuel	HSD

#### A. Cylinder Pressure

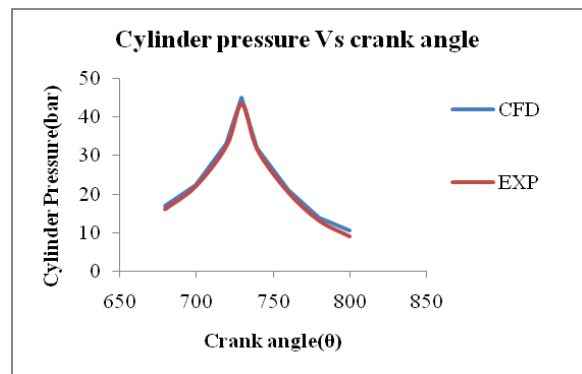


Figure 8. Comparison of Computed and Experimental pressure data with a crank angle

Fig.8 shows the variation cylinder pressure with respect to the crank angle for CFD and Experimental. It is observed that cylinder pressure from CFD is 45 bars and from experimental is 43.2 bars.

#### B. Cylinder Temperature

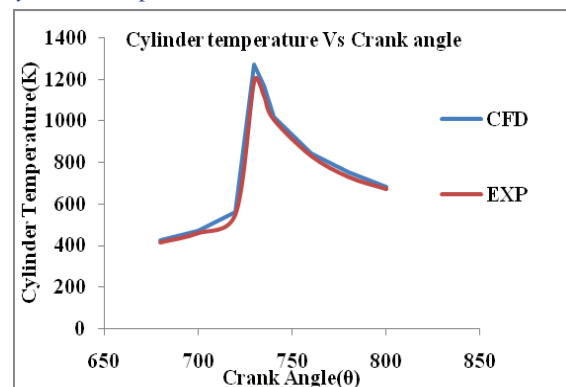


Figure 9. Comparison of Computed cylinder temperature and Experimental cylinder temperatures with a crank angle

Fig.9 shows the variation cylinder temperature with respect to the crank angle for CFD and Experimental. It is observed that cylinder temperature from CFD is 1250<sup>0</sup>K and from experimental is 1197<sup>0</sup>K.

#### C. Cylinder Pressure at different EGR

Cylinder parameters such as pressure, temperature, NO<sub>x</sub>, and soot emissions are predicted numerically for the same piston geometry which is used by Dr.G.Prasanthi and E.Anith[5].EGR is varied from 0% to 15%. This is normally achieved in a heavy-duty direct injection diesel engine. The cylinder pressures increase till 736 deg Crank angle due to diffusion combustion and thereafter decreases as expected. It is found that the peak pressure during the simulation reaches nearly 45 bars at nearly 740<sup>0</sup> Crank angle for 0% of EGR, at 15% EGR, the cylinder pressure drops to 39 bars is shown in Fig10.

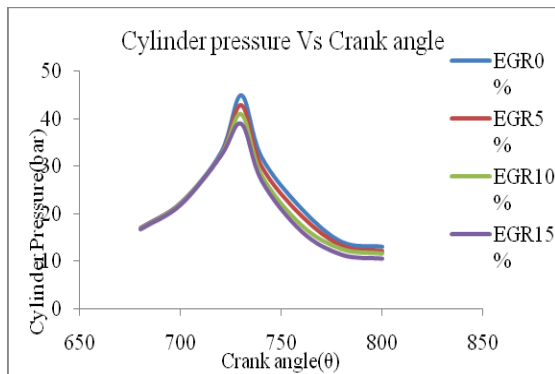


Figure 10. The variation of cylinder pressure with a crank angle at different EGR

**D. Cylinder Temperature at different EGR**

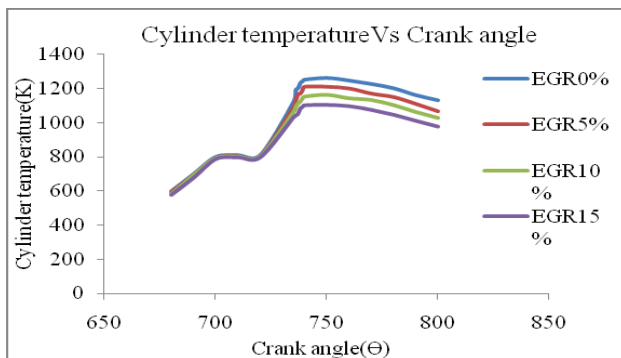


Figure 11. The variation of cylinder temperature with a crank angle at different EGR

Fig.11 shows the cylinder temperature with a crank angle at different EGR levels. It is observed that peak cylinder drops from 1250<sup>0</sup>K to 1102<sup>0</sup>K as EGR has increased from 0% to 15%. It can be observed that the cylinder temperature is lowered as EGR increased from 0% to 15%.

**E. Apparent Heat Release at different EGR**

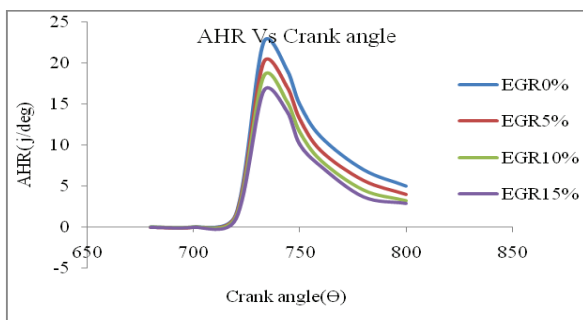


Figure 12. The variation of apparent heat release with a crank angle at different EGR

Fig.12 shows the Apparent hear release with the crank angle at different EGR levels. It is observed that apparent heat release drops from 22.5 joules/deg to 16.5 joules/deg EGR increased from 0% to 15%. It is observed that the

apparent heat release is lowered as EGR increased from 0% to 15%.

**E. NO<sub>x</sub> at different EGR**

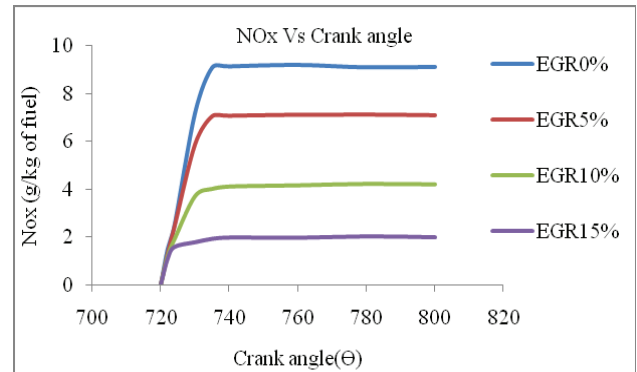


Figure 13. The variation of NOx with a crank angle at different EGR

Fig.13 shows that NOx formation with a crank angle at different EGR levels. It is observed that the reduction of nitrogen oxide levels from 9.1 g/kg of fuel to 2.01 g/kg of fuel. NOx increases due to the peak temperature rises.

**F. Soot at different EGR**

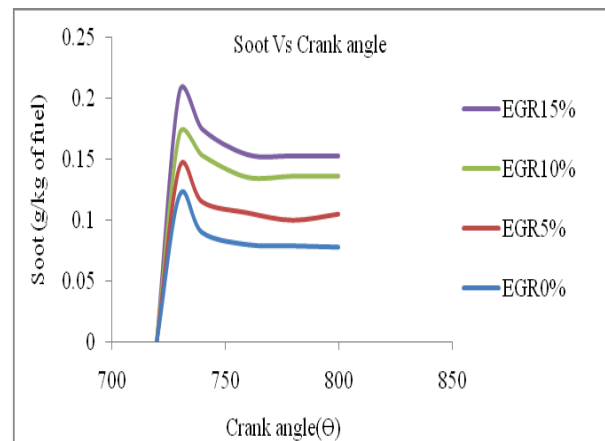


Figure 14. The variation of Soot with a crank angle at different EGR

Fig.14 shows the soot formation at different EGR levels with respect to the crank angle. The soot levels rise from 0.08 g/kg of fuel to 0.182 g/kg of fuel. This is due to improper combustions the reaction is regressed when EGR is increased. Soot is formed from unburned fuel that nucleates from the vapor phase to a solid phase in fuel-rich regions at elevated temperatures.

TABLE III.  
COMPARISON BETWEEN CFD AND EXPERIMENTAL WORK

	CFD	Experimental Work
Pressure (bars)	45	43.2
Temperature (°K)	1250	1197

Table.3 shows that the values of pressure and temperature from experimental work are nearer to the values obtained by CFD.

TABLE IV.  
COMPARISON OF PRESSURE, TEMPERATURE, NO<sub>x</sub>, APPARENT HEAT RELEASE AND SOOT AT DIFFERENT EGR LEVELS

	Pressure (Bar)	Temperature (°K)	Apparent Heat Release (joules/deg)	No <sub>x</sub> (g/kg of fuel)	Soot (g/kg of fuel)
0%EGR	45	1250	22.5	9.1	0.08
5%EGR	42	1192	19.3	7.5	0.14
10%EGR	40	1153	17	3.9	0.165
15%EGR	39	1102	16.5	2.01	0.182

Table.4 shows the values of pressure, temperature, apparent heat release, NO<sub>x</sub>, and soot of a direct injection diesel engine at 0%EGR, 5%EGR, 10%EGR and 15%EGR. It is observed that pressure is decreased from 45 bars to 39 bars, the temperature is decreased from 1250 K to 1102 K, apparent heat release is decreased from 22.5 j/deg to 16.5 j/deg, NO<sub>x</sub> is decreased from 9.1 g/kg of fuel to 2.01 g/kg of fuel and soot is increased from 0.08 g/kg of fuel to 0.182 g/kg of fuel. Soot is increased due to improper combustion.

#### IV. CONCLUSIONS

This paper concludes that by varying the rates of exhaust gas recirculation there is a reduction in NO<sub>x</sub> emissions due to the decrease of the cylinder pressure and temperature.

It is observed that at 15% of the EGR rates the engine produced fewer emissions than that of 0% EGR.

#### REFERENCES

- [1] Jaffar Hussain, K. palaniradja, and N. Alagumurthi, R. Manimaran, "Effect of Exhaust Gas Recirculation (EGR) on Performance and Emission characteristics of a Three-cylinder Direct injection Compression Ignition Engine" *Alexandria Engineering Journal* (2012)51, 241-247.
- [2] Raghavendra Reddy NV and Dr. Jayashankara B "CFD Simulation of Direct Injection CI Engine with Flat Piston Bowl and W Shape Toroidal Piston Bowl Combustion Process", *Journal of Engineering Research and Application* www.ijera.com ISSN: 2248-9622, Vol. 8, Issue5 (Part -IV) May 2018, pp 56-61.
- [3] A.M. Indrodia, N.J. Chotai, and B.M.Ramani "Investigation Of Different Combustion Chamber Geometry Of Diesel Engine Using Cfd Modelling of In cylinder Flow for Improving the Performance of Engine.", *5th International & 26th All India Manufacturing Technology, Design and Research Conference (AIMTDR 2014)* December 12th–14th, 2014, IIT Guwahati, Assam, India
- [4] B. Jayashankara and V. Ganesan "Effect of fuel injection timing and intake pressure on the performance of a DI diesel engine – A parametric study using CFD", *Energy Conversion and Management* 51 (2010) 1835–1848.
- [5] Dr.G.Prasanthi and E .Anitha "Experimental investigation on the effect of exhaust gas recirculation on performance and emission characteristics of diesel engine fueled with moringa oleifera oil", *International Journal Of Trend in Research and Development (IJTRD)*, e-ISSN:2394-9333, Volume.2, Issue5, September–October 2015.
- [6] Kota Sridhar, R.B.V.Murali, Sk.Mohammad Younus and K.Mohan Lakshmi "Computerised Simulation of Spark Ignition Internal Combustion Engine", *IOSR Journal of Mechanical and Civil Engineering (IOSR-JMCE)* e-ISSN: 2278-1684 Volume 5, Issue 3 (Jan. - Feb. 2013), PP 05-14.
- [7] S Gavudhama karunanidhi, Manu Narayanan P M. G Subba Rao and S G Karunanidhi et al "CFD Studies of Split Injection on the Combustion and Emission Characteristics in DI Diesel Engine" *Int. Journal of Engineering Research and Applications*. ISSN: 2248-9622, Vol. 4, Issue 7(Version 1), July 2014, pp.55-58.
- [8] Shengli Wei, Feihu Wang, Xianyin Leng, Xin Liu and Kunpeng "Numerical analysis on the effect of swirl ratios on swirl chamber Combustion system of DI diesel engines" *Energy Conversion and Management* 75 (2013) 184–190.
- [9] V. Kolhe, Rajesh E. Shelke and S. S. Khandare Jordan "Combustion Modeling with CFD in Direct Injection CI Engine Fuelled with Biodiesel", *Journal of Mechanical and Industrial Engineering*, Volume 9 Number 1, February.2015 ISSN 1995-6665 Pages 61- 66.
- [10] V. Kongre and Vivek K. Sunnapwar "CFD Modeling and Experimental Validation of Combustion in Direct Ignition Engine Fueled with Diesel", *International Journal Of Applied engineering Research, Dindigul* Volume 1, No 3, 2010, Issn 0976-4259 Pages 509-517.

# Optimization of Machining Process by Desirability Function Analysis (DFA): A Review

Pathalavathi Bhaskar<sup>1</sup> and Sarat Kumar Sahoo<sup>2</sup>

<sup>1</sup>Asst. Professor, CVR College of Engineering/Mechanical Engg. Department, Hyderabad, India  
Email: bhaskarnaik459@gmail.com

<sup>2</sup>Asst. Professor, CVR College of Engineering Mechanical Engg. Department, Hyderabad, India  
Email: saratkumar222@gmail.com

**Abstract:** The most essential goal of the optimization process is to minimize the cost and maximize the profit. In the case of industrial decision-making, optimization plays a major role. In the optimization process, the main target is to maximize 1 or some process parameters by keeping other parameters within constraints. Desirability function analysis (DFA), is a technique for the optimization of multiple response variables extensively used in the industry. DFA is based on the concept of the "quality" of the product or process having several quality characteristics. This method operates on the conditions which give the "most desirable" response values. In this review paper, the main concentration is on the optimization of a number of manufacturing processes which has been optimized by using DFA method. The previous review work by earlier researchers on the manufacturing process was not performed on such a large scale at a time on the DFA method by considering different processes. In the future, this review work can be worthwhile for the information at a single place for the succeeding researchers, in order to conclude their research work on the DFA technique.

**Index Terms:** Analysis, Optimization, Desirability function, DFA, Machining process

## I. INTRODUCTION

Recently, manufacturing industries have attempted to introduce different optimization techniques to get the required specification of components with minimal input requirements. In order to achieve this, the operator of the machine has to choose suitable machining parameters. Optimization is a technique to maximize or minimize some function relative to some other set, representing a variety of choices accessible in a certain situation. The function allows in comparison of the various choices and to find out which might be the "best". In the manufacturing process, the outputs are maximized with the minimization of input parameters for higher productivity. Like, maximization of a number of products produced, increasing the quality of product and minimization of input material, minimization of time of production, minimization of cost production, etc. In manufacturing industries, usually multi-objective optimization is used for the overall growth of the industries for high production rates with a low cost of the product. By using a multi-objective optimization process all the outputs are optimized simultaneously and better quality products with a low cost are produced. Desirability function analysis (DFA) is one of the multi-objective optimization processes used for the optimization of different machining processes. It can be used for the optimization of more than one output parameter simultaneously [1,2].

Desirability function analysis (DFA), is a technique for the optimization of multiple response variables extensively used in the industry. DFA is based on the concept of the "quality" of the product or process having several quality characteristics, with some of them out of "desired" limits that are completely unacceptable. This technique finds operating conditions  $x$ , which provide the "most desirable" response values [1-4].

The following steps are used in DFA for optimization of the process parameters.

1st Step: Individual desirability index, 'di' for the corresponding responses can find out by using the formula given below. As per the response values, there are 3 types of desirability functions. i. Nominal - the best

$$d_i = \begin{cases} \left(\frac{y_j - y_{min}}{T - y_{min}}\right)^s, & y_{min} \leq y_j \leq T, s \geq 0 \\ \left(\frac{y_j - y_{min}}{T - y_{min}}\right)^s, & T \leq y_j \leq y_{max}, s \geq 0 \\ 0 & \end{cases} \quad (1)$$

' $y_j$ ' is necessary to get desired target  $T$ . Desirability value becomes 1, when ' $y$ ' equals to  $T$ . Desirability value becomes 0, when ' $y$ ' exceeds a particular range from the target and that situation indicates the worst case. Here, ' $s$ ' is the weightage value whose value normally taken as 1.

ii. Larger-the better

Larger the value of ' $y_j$ ', is expected to be better than the overall characteristics. When ' $y$ ' exceeds a specific value, the desirability value becomes 1. When ' $y$ ' value falls below a specific value, the desirability value becomes 0, which is unacceptable.

$$d_i = \begin{cases} 0, & y_j \leq y_{min} \\ \left(\frac{y_j - y_{min}}{y_{max} - y_{min}}\right)^r, & y_{min} \leq y_j \leq y_{max}, r \geq 0 \\ 1, & y_j \geq y_{max} \end{cases} \quad (2)$$

iii. Smaller-the better

$$d_i = \begin{cases} 1, & y_j \leq y_{min} \\ \left(\frac{y_j - y_{max}}{y_{min} - y_{max}}\right)^r, & y_{min} \leq y_j \leq y_{max}, r \geq 0 \\ 0, & y_j \geq y_{max} \end{cases} \quad (3)$$

Smaller the value of ' $y_j$ ', is expected to be better than the overall characteristics. When ' $y$ ' value falls below a specific

value, the desirability value becomes 1. When ‘y’ exceeds a specific value, the desirability value becomes 0, which is unacceptable. “Smaller the better” and “larger the better” characteristics are applied to calculate the individual desirability values to minimize or maximize the response. Here, ‘r’ is the weightage value whose value is normally taken as 1.

2<sup>nd</sup> Step: Overall desirability, ‘d<sub>0</sub>’ can be calculated by using the ‘d<sub>i</sub>’ values of all responses. This is done by using the formula given below. Here, w<sub>1</sub>, w<sub>2</sub>, w<sub>3</sub> etc. are the weight factor whose summation is equal to 1.

$$d_0 = \sqrt[w]{(d_1^{w_1} \times d_2^{w_2} \dots \dots d_i^{w_i})} \quad (4)$$

3<sup>rd</sup> Step: In this step, we need to find out the optimal parameter and its level sequence. Higher ‘d<sub>0</sub>’ value suggests a better quality product. Hence, the optimum level of each parameter can find out by using the ‘d<sub>0</sub>’ value.

In the manufacturing process, the raw material is converted into the final product by various processes, namely joining of materials, removal of unwanted materials (i.e. Machining), by deforming the materials, melting of materials, etc. Presently, traditional machining processes are used along with non-traditional machining processes to make the product from the bulk material to the final product. In this review work, the following machining processes are considered.

Turning is a material removal process, where the undesired material is removed with the help of a single-point cutting tool (point contact with the workpiece). Here, cutting forces are applied through the cutting edge to the workpiece for the removal of material. Turning is the most commonly used machining process used in industries.

Drilling is a process where a multi-point cutting tool is used for the removal of unwanted materials in order to produce the desired hole. This process is mainly used to create cylindrical holes in a workpiece. Similarly, Laser drilling is the process of drilling holes with the help of a

laser source. The laser is also used for a curve cutting of parts to make it to the final product. In milling process, a multi-point cutting tool in form of a rotary cutter is used to remove materials from. The important cutting parameter in milling operation includes the cutting velocity, feed per tooth and depths of cut (radial and axial).

EDM (i.e. Electric discharge machining) is a spark machining process to produce the desired shape of components by using electrical discharges (sparks). Similarly, wire-EDM is used to cut the components by using wire as a tool with the use of electrical discharges (sparks).

For all the machining process, a number of factors are associated, which can be optimized for better results.

## II. OPTIMIZATION OF MACHINING PROCESSES BY DESIRABILITY FUNCTION ANALYSIS (DFA)

Aggarwal et al. [1] have studied the turning process of AISI P-20 steel metal by using the cryogenic cutting environment of with coolant of liquid nitrogen and by changing four controllable factors namely; feed, cutting speed, depth of cut, and nose radius. RSM technique used for modelling of the response variables and face centred central composite design was used for the experiment. They have optimized multiple output parameters namely; surface roughness, cutting force, power consumption and tool life by using the desirability of function technique.

Bara et al. [2] have studied Nd:YAG laser micro drilling of the workpiece (304 stainless steel) by varying input parameters namely; nitrogen gas pressure, nozzle standoff distance, and average power consumption. They have optimized output parameters of laser micro-drilling like entry circularity, taper angle and exit circularity by desirability function approach. They found that, for laser drilling maximum contribution percentage shared by ‘N<sub>2</sub>’ gas pressure and nozzle stand-off distance i.e. 54.62% and 27.69% respectively towards the overall output parameters (overall desirability). But, average power contribution is the lowest i.e. 2.98% towards overall output parameters. Figure 1 shows the percentage contribution of input parameters on the overall desirability index.

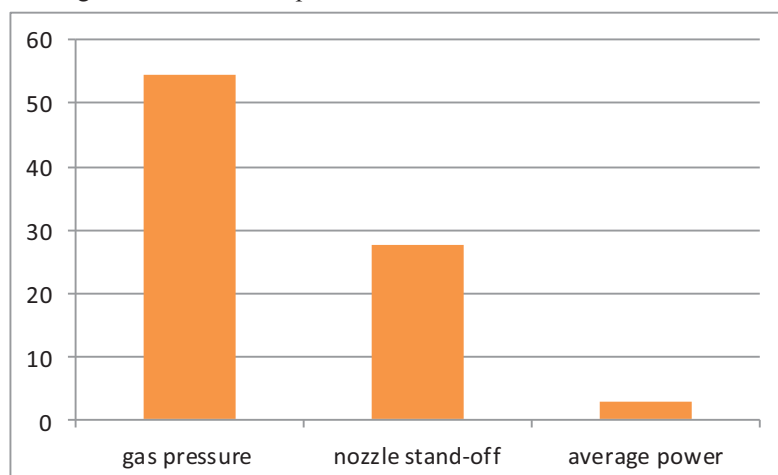


Figure 1. Percentage contribution of input parameters on overall desirability index in laser drilling [2]

Sahu et al. [3] have studied electro-discharge machining (EDM) of nitinol by taking different tools and varying the EDM input parameters and optimized the output surface parameters namely; max. Profile height, avg. roughness and avg. profile height by using DFA technique. Percentage contribution of tool type, duty cycle, current and voltage on overall performance are; 61.98, 10.94, 3.79 and 2.79 respectively, which is shown in Fig. 2.

Kamguem et al. [4] have studied the surface roughness and emission of metallic particles during the milling process of aluminum alloys (2024-T351, 6061-T6, 7075-T6) with two coated carbide tools (TiCN, TiCN+Al<sub>2</sub>O<sub>3</sub>+TiN). The varying input parameters are speed, feed, depth of cut, coated inserts and type of workpiece material. RSM technique is used to perform the experiments and DFA technique is used to optimize the output.

dalarasan and Santhanakumar [5] have studied wire-EDM of Al6351/20%Al<sub>2</sub>O<sub>3</sub> composite workpiece by using copper wire by varying input parameters voltage, capacitance, feed and tension of the wire. RSM technique is used to perform the experiments and DFA technique is used to optimize the output.

Assarzadeh and Ghoreishi [6] have studied electric discharge machining of aluminum oxide (Al<sub>2</sub>O<sub>3</sub>) powder mixed in kerosene dielectric in machining of CK45 die steel by the use of the copper tool. RSM technique with FCC composite design model is used to perform the experiments. Current, voltage & pulse on time are input parameters that vary during the process. DFA technique is used to optimize the output parameters like MRR (material removal rate) and surface finish.

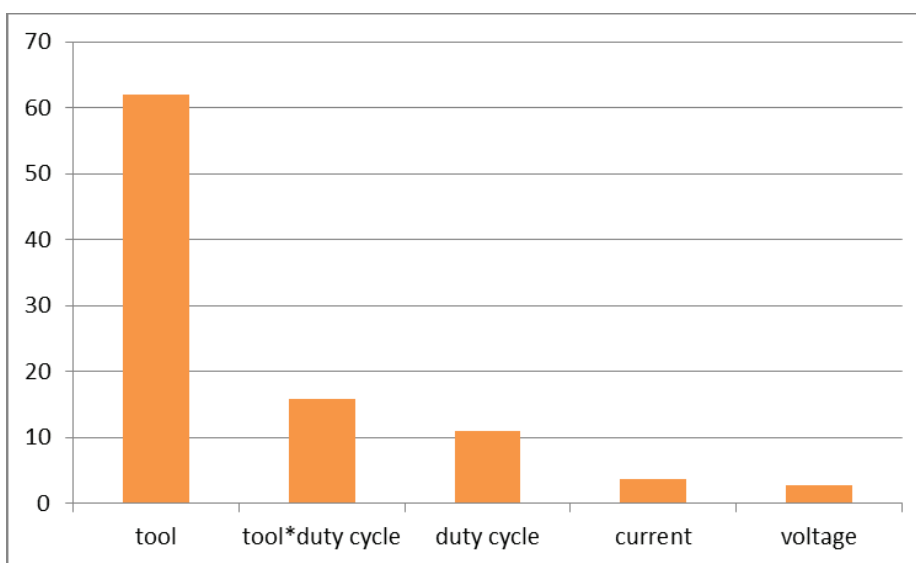


Figure 2. Contribution % of individual input parameters on overall desirability index in EDM [3]

Garg et al. [7] have studied the machining of Aluminium with ZrO<sub>2</sub> metal matrix composite by wire-EDM process by varying input parameters pulse on time, pulse gap, servo voltage, wire feed rate and wire tension by the use of RSM with central composite design. Desirability function technique is applied to optimize the wire-EDM process parameters namely; cutting velocity & surface finish.

Gopalakannan and Thiagarajan [8] have studied the EDM of Al 7075 alloy by using copper tool based on a central composite design by changing input parameters namely; pulse on time, pulse off time, voltage & current. They have studied the performance of the process by taking the output as electrode wear rate, material removal rate & surface roughness. Desirability function technique is applied to optimize the output of the EDM process parameters simultaneously. The ramp function graph of the desirability index for the EDM process Al+10wt% SiC MMC is shown in Fig. 3.

Kumar et al. [9] have performed wire-EDM of Monel-400 by varying input parameters namely; pulse on time, pulse off time, current and servo voltage. The experimental design based on RSM with face centered central composite design.

The output responses namely; machining rate and surface finish have been studied. The desirability function technique is applied to optimize the response parameters.

Kumar et al. [10] have performed wire cut EDM operation of titanium workpiece material by considering the varying input parameters as pulse-on time, pulse-off time, current, voltage, wire tension & wire feed rate. The experimental design is based on the RSM Box-Behnken technique. The output responses taken into consideration are MRR and overcut. The desirability function technique is applied to optimize the response parameters. The multi-response optimization to maximize MRR and minimize overcut during wire cut EDM of titanium by using DFA is shown in Fig. 4.

Mythuraman and Ramakrishnan [11] have studied wire-EDM of WC-Co composites by using zinc-coated copper wire. They have studied effect of input parameters namely; percentage of Co, current, wire tension, pulse on time, delay time, wire feed, and dielectric fluid pressure on the output parameters like material removal rate and surface roughness. The o/p responses are optimized by the desirability function approach.



Pandey and Panda [12] have studied bone drilling by using high speed steel (HSS) drill bit by varying inputs feed rate and spindle speed. They have considered the outputs

temperature and thrust force and optimized for the minimization the outputs by using desirability function approach.

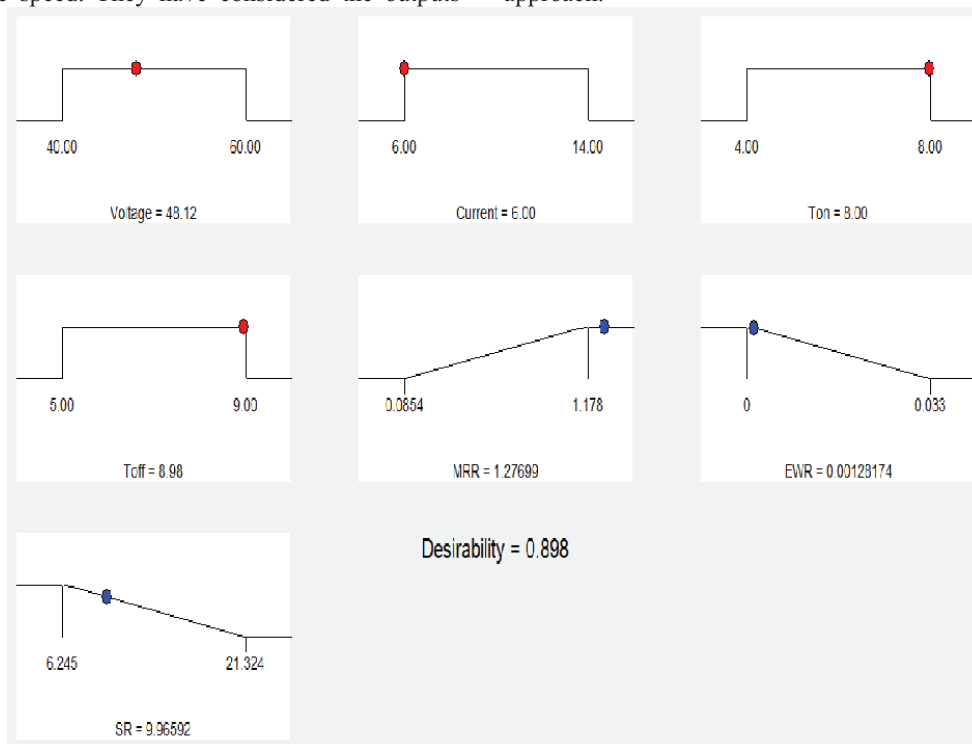


Figure 3. Ramp function graph of desirability index for EDM process [8]

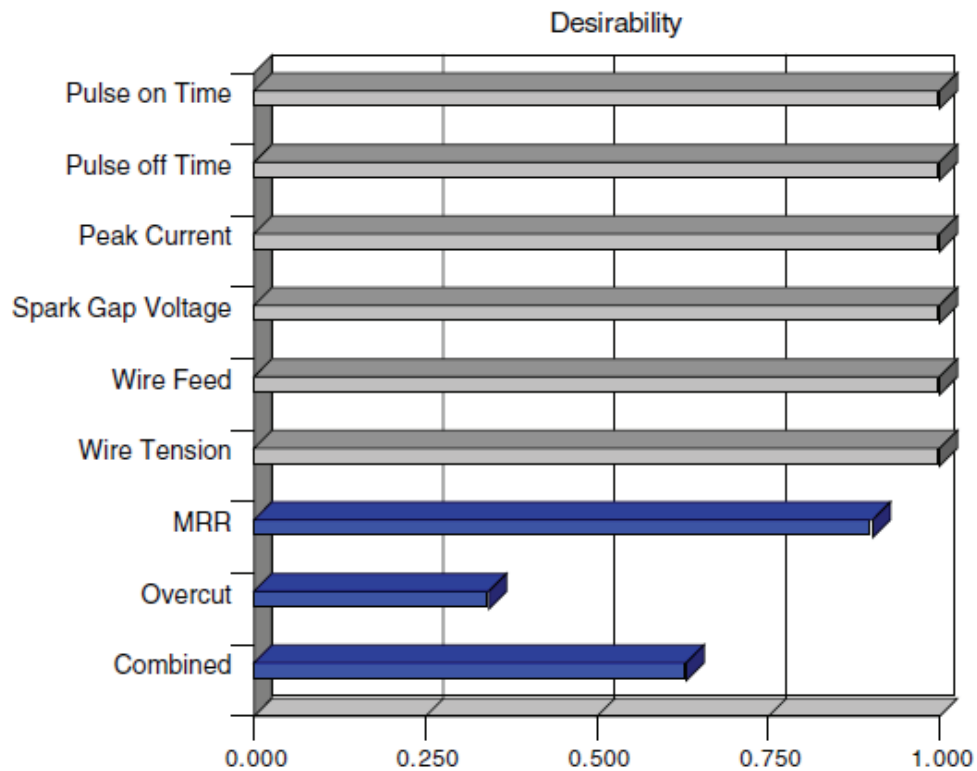


Figure 4. Multi response optimization result for maximum MRR and minimum overcut using DFA [10]

Pandey and Panda [13] have studied bone drilling by using high speed steel drill by varying inputs feed rate and spindle speed. They have considered the outputs parameters as; maximum force, maximum temperature and average surface roughness. The responses are optimized for the minimization of the outputs by the help of fuzzy based desirability function technique.

Prakash et al. [14] have studied the drilling of medium density fiberboards and optimized delamination factor by desirability function approach.

Ramanujam et al. [15] have studied end milling of Inconel alloy by changing input parameters like feed, speed and depth of cut. They have optimized the end milling process by considering output parameters as surface roughness and MRR by using desirability function approach.

Sahu and Mahapatra [16] have optimized electric discharge machining of titanium alloy by using desirability function approach. They have considered the output parameters as maximum profile height, average roughness and avg. profile height.

Sait et al. [17] have studied the machining of glass fiber reinforced plastic (GFRP) pipes by the use of coated carbide tool K20 inserts. They have considered input parameters as cutting velocity, feed rate and depth of cut with consideration of output parameters as flank wear, crater wear, force and surface roughness. Taguchi method is used for the design of the experiment and desirability function analysis using optimization of the machining process.

Selaimia et al. [18] have studied in dry face milling of austenitic stainless steel by varying parameters as, cutting speed, feed and depth of cut. The output parameters considered are surface finish, cutting force, and MRR. RSM technique is used for the design and statistical analysis of data. Desirability function method used to optimize the process parameters.

Sengottuvel et al. [19] have studied the EDM of Inconel 718 by the help of copper electrode of different tool shapes like circular, square, rectangular and triangular shape. They have optimized the EDM process by using desirability function technique and fuzzy modeling by considering MRR, TWR and surface smoothness as output parameters.

Sharma and Kumar [20] have studied laser curve cutting of composites Aluminium metal by taking inputs parameters as speed of cutting, power of laser, gas pressure, stand-off distance, nozzle diameter, SiC reinforcement and arc radius. They have optimized the process by desirability function approach considering surface finish and kerf deviation as o/p parameters.

Sharma et al. [21] have examined turning of GFRP composite materials and applied Fuzzy logic modeling and multi-objective optimization of desirability function analysis. The response process parameters are MRR, TWR & surface roughness.

PSingaravel and Selvaraj [22] have studied turning of EN25 steel metal by CVD and PVD coated carbide tool inserts. The input machining parameters are coated tools, feed, cutting speed and depth of cut. The response variables are MRR, cutting force and surface irregularity. They have

optimized the machining process by desirability function analysis.

Vasudevan et al. [23] have studied drilling characteristics of epoxy composite materials by varying input parameters speed of spindle, feed rate, the thickness of the material and drill size. They have optimized the drilling by desirability coupled with Taguchi method for multi-objective optimization by taking output parameters as delamination factor and surface roughness.

### III. SUMMARY

In this review work, desirability function analysis (DFA) one of the prominent optimization techniques has been summarized especially in relation to the manufacturing processes. This method is simple and involves less number of computational steps as compared to other multi-objective optimization techniques. In this study, the application of the desirability function technique for the optimization of multi-criteria optimization problems is analyzed by taking the literature of previous researchers. The DFA has the potential for the optimization of the multi-objective optimization process for different manufacturing processes such as electro-discharge machining, wire-electro-discharge machining, turning, milling, drilling, and laser drilling of different materials. The DFA can be well suitable in manufacturing industries for optimization of the machining process to get higher output with minimization of input parameters for their growth of manufacturing industries in today's competitive market.

### REFERENCES

- [1] G Aman Aggarwal, Hari Singh, Pradeep Kumar and Manmohan Singhd, "Optimization of multiple quality characteristics for CNC turning under cryogenic cutting environment using desirability function" journal of materials processing technology, vol. 205, pp. 42–50, 2008.
- [2] Alok Bara, Sarat Kumar Sahoo, Sunita Sigh Naik, Anshuman Kumar Sahu and Siba Sankar Mahapatra, "Multi Response Optimization of Nd:YAG Laser Micro Drilling Characteristics of 304 Stainless Steel using Desirability Function Approach", Materials Today: Proceedings, Vol. 5, pp. 18975–18982, 2018.
- [3] Anshuman Kumar Sahu, Suman Chatterjee, Praveen Kumar Nayak and Siba Sankar Mahapatra, "Study on effect of tool electrodes on surface finish during discharge machining of Nitinol", IOP Conf. Series: Materials Science and Engineering, Vol. 338, 2018.
- [4] R. Kamguem, A. Djebara and V. Songmene, "Investigation on surface finish and metallic particle emission during machining of aluminum alloys using response surface methodology and desirability functions", Int J Adv Manuf Technol, Vol. 69, pp. 1283–1298, 2013.
- [5] R. Adalarasan and M. Santhanakumar, "Response Surface Methodology and Desirability Analysis for Optimizing  $\mu$ WEDM Parameters for Al6351/20% Al2O3 composite", International Journal of ChemTech Research, CODEN (USA): IJCRGG ISSN: 0974-4290, Vol.7, No.6, pp. 2625-2631, 2014-2015.

- Al2O3 powder-mixed electrical discharge machining (PMEDM) parameters, *Int J Adv Manuf Technol*, Vol. 64, pp.1459–1477, 2013.
- [7] Sanjeev K. Garg, Alakesh Manna and Ajai Jain, “An Investigation on Machinability of Al/10% ZrO<sub>2</sub>(P)-Metal Matrix Composite by WEDM and Parametric Optimization Using Desirability Function Approach”, *Arab J Sci Eng*, Vol. 39, pp.3251–3270, 2014.
- [8] Subramanian Gopalakannan and Thiagarajan Senthilvelan, “Optimization of machining parameters for EDM operations based on central composite design and desirability approach”, *Journal of Mechanical Science and Technology*, Vol. 28, pp. 1045-1053, 2014.
- [9] Vinod Kumar, Vikas Kumar and Kamal Kumar Jangra, “An experimental analysis and optimization of machining rate and surface characteristics in WEDM of Monel-400 using RSM and desirability approach”, *J Ind Eng Int*, Vol. 11, pp.297–307, 2015.
- [10] Anish Kumar, Vinod Kumar and Jatinder Kumar, “Semi-empirical model on MRR and overcut in WEDM process of pure titanium using multi-objective desirability approach”, *J Braz. Soc. Mech. Sci. Eng.*, Vol. 37, pp. 689–721, 2015.
- [11] V. Muthuraman and R. Ramkrishnan, “Multi Parametric Optimization of WC-Co Composites using Desirability Approach”, *Procedia engineering*, Vol. 38, pp. 3381-3390, 2012.
- [12] Rupesh Kumar, Pandey and S. S. Panda, “Optimization of Bone Drilling Process with Multiple Performance Characteristics Using Desirability Analysis”, *APCBEE Procedia*, Vol. 9, pp. 48 – 53, 2014.
- [13] Rupesh Kumar Pandey and S. S. Panda, “Optimization of bone drilling using Taguchi methodology coupled with fuzzy based desirability function approach”, *J Intell Manuf*, Vol. 26, pp.1121–1129, 2015.
- [14] S. Prakash, K. Palanikumar and N. Manoharan, “Optimization of delamination factor in drilling medium-density fiberboards (MDF) using desirability-based approach”, *Int J Adv Manuf Technol*, Vol. 45, pp.370–381, 2009.
- [15] R. Ramanujam, Lohithaksha M. Maiyar, K. Venkatesan and Mithun Vasani, “multi-response optimization using anova and desirability function analysis: a case study in end milling of inconel alloy”, *ARNP Journal of Engineering and Applied Sciences*, Vol. 9, NO. 4, 2014.
- [16] Anshuman Kumar Sahu and Siba Sankar Mahapatra, “Optimization of Surface Roughness Parameters by Different Multi-Response Optimization Techniques During Electro-Discharge Machining of Titanium Alloy, DOI: 10.4018/978-1-5225-6161-3.ch004, 2019.
- [17] A. Naveen Sait, S. Aravindan and A. Noorul Haq, “Optimisation of machining parameters of glass-fibre-reinforced plastic (GFRP) pipes by desirability function analysis using Taguchi technique”, *Int J Adv Manuf Technol*, Vol. 43, pp.581–589, 2009.
- [18] Abdel-Ali Selaimia, Mohamed Athmane Yallese, Hamza Bensouilah, IKhlas Meddour, Riad Khattabi and Tarek Mabrouki, “Modeling and optimization in dry face milling of X2CrNi18-9 austenitic stainless steel using RMS and desirability approach”, *Measurement*, Vol. 107, pp. 53–67, 2017.
- [19] Sengottuvel.P, Satishkumar.S and Dinakaran.D, “Optimization Of Multiple Characteristics Of EDM Parameters Based On Desirability Approach And Fuzzy Modeling”, *Procedia Engineering*, Vol. 64, pp. 1069 – 1078, 2013.
- [20] Vikas Sharma and Vinod Kumar, “Multi- objective optimization of laser curve cutting of aluminium metal matrix composites using desirability function approach”, *J Braz. Soc. Mech. Sci. Eng.*, Vol. 38, pp.1221–1238, 2016.
- [21] Shiv Sharma, Santosh Tamanga, D.Devarasiddappab and M.Chandrasekran, “Fuzzy logic modeling and multiple performance optimization in turning GFRP composites using desirability function analysis”, *Procedia Materials Science*, Vol. 6, pp. 1805 – 1814, 2014.
- [22] B. Singaravel and T. Selvaraj, “Application of Desirability Function Analysis and Utility Concept for Selection of Optimum Cutting Parameters in Turning Operation”, *Journal of Advanced Manufacturing Systems*, Vol. 15, No. 1, pp. 1–11, 2016.
- [23] Hari Vasudevana, Ramesh R. Rajgurub, Naresh and Deshpande, “Multiobjective Optimization of Drilling Characteristics for NEMA G-11 GFRP/Epoxy Composite using Desirability coupled with Taguchi Method”, *Procedia Engineering*, Vol. 97, pp. 522 – 530, 2014.

# Microwave Assisted One Pot Synthesis of Functionalized Pyrrole Derivatives Catalyzed by Uranyl Nitrate Hexa Hydrate

Dr. K. Venkatesan<sup>1</sup>, Dr. Pagadala Ramakanth<sup>2</sup> and Dr. Ch. Anjaneyulu<sup>3</sup>

<sup>1</sup>Asst. Professor, CVR College of Engineering/H&S Department (Chemistry), Hyderabad, India  
Email: venkipk@gmail.com

<sup>2</sup>Asst. Professor, CVR College of Engineering/H&S Department (Chemistry), Hyderabad, India  
Email: pagadalaramakanth@gmail.com

<sup>3</sup>Professor, CVR College of Engineering/H&S Department (Chemistry), Hyderabad, India  
Email: anjaneyulu\_22@yahoo.co.in

**Abstract:** An effective and simple method for the functionalized pyrrole synthesis has been developed using a  $\text{UO}_2(\text{NO}_3)_2 \cdot 6\text{H}_2\text{O}$  catalyst under conventional method. Pyrrole synthesis with uranyl nitrate hexa hydrate catalyst has various advantages, such as fast activity, good yields and reduces reaction times in ethanol media. The synthesized target compounds were characterized by FT-IR, elemental analysis,  $^1\text{H}$  and  $^{13}\text{C}$  NMR.

**Index Terms:** Microwave, Uranyl nitrate, Pyrrole.

## I. INTRODUCTION

The heterocyclic compounds contain nitrogen atom in their structures which provide a wide array of biological activities; the valence electron of nitrogen atom contribute to promoting the building of several supramolecular structures. Pyrrole moieties are among the most important compound in heterocyclic chemistry [1]. Pyrrole derivatives have been higher attention in recent times because they could be used in many therapeutic areas such as anti-HIV [2] and antimicrobial agents [3-7].

There have been significant advances in the methodology of multi-component reactions (MCRs) over the past decade and substantial efforts continue to develop new MCRs. The pyrrole ring has found a massive number of therapeutic applications and seems to be found in several natural products [8] Pyrroles tend to build the main framework of porphyrin rings in chlorophyll, heme and vitamin B12, with an increasing medically important drug molecules, like atorvastatin and tolmetin (Fig.1). Several synthetic methods for the construction of pyrroles have been developed till date [9, 10].

Among the most common pathways to construction of pyrroles is the Paal–Knorr reaction in which 1,4-dicarbonyl compounds in the presence of primary amines are converted to pyrroles. Some catalysts such as montmorillonite KSF [11], iodine [12], montmorillonite [13],  $\text{Zr}(\text{KPO}_4)_2$  [14],  $\text{Sc}(\text{OTf})_3$  [15], alumina [16], microwave irradiation [17,18], ionic liquid [19],  $\text{InCl}_3$  [20] and  $\text{Ga}(\text{OTf})_3$  [21]  $\text{ZrCl}_4$ /ultrasonic irradiation [22], have been used for this conversion.

Aryl glyoxal containing functional groups such as aldehyde and ketone undergo condensation reaction, play a vital role in organic synthesis, particularly in heterocyclic molecule synthesis. The cost effective and easy method for the synthesis of pyrrole derivatives under mild conditions from a one-pot reaction of aryl glyoxal derivatives and equimolar mixture of 1,3-dicarbonyl compounds in the presence  $\text{UO}_2(\text{NO}_3)_2 \cdot 6\text{H}_2\text{O}$  catalyst.

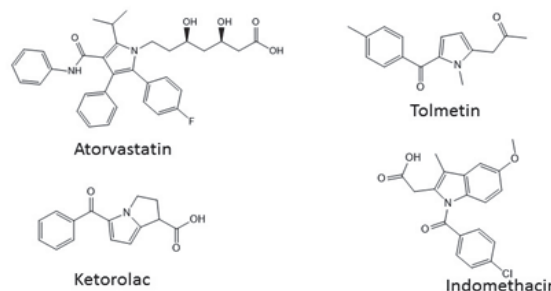


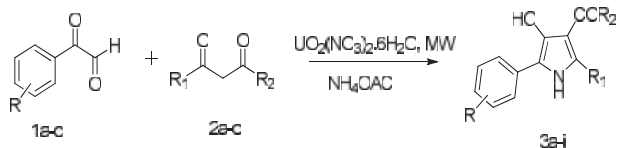
Figure.1 Pharmaceutically active molecules containing pyrrole ring

## II. RESULTS AND DISCUSSION

As a basic model system, the reaction between aryl glyoxal (1 mmol) with an equimolar amount of 1,3-dicarbonyl compound and catalytic amount of uranyl nitrate was investigated to assess the efficiency of the method and enhance the reaction conditions. Choosing a suitable reaction medium is well known to be of crucial importance for efficient synthesis. The mixture of the reactions was tested under various conditions. Solvent and temperature outcomes for this reaction have been measured, and the findings are summarized in Table 1.  $\text{UO}_2(\text{NO}_3)_2 \cdot 6\text{H}_2\text{O}$  is a more economical catalyst compared to the other Lewis acid catalysts mentioned in the literature for the synthesis of functionalized pyrrole compounds.

The reaction conditions were efficiently established using condensation of aryl glyoxal and 1,3-dicarbonyl compound

with catalytic quantities of uranyl nitrate in classical and microwave irradiations using diverse solvent systems such as dichloromethane, chloroform, ethanol, acetonitrile, methanol and various percentage of catalytic mole ratio also examined, and the results were also summarized.



SCHEME 1 Facile one pot synthesis of functionalized pyrrole derivatives.

Table 1 showing that polar solvents such as methanol, ethanol, and acetonitrile yielded better than nonpolar solvents like chloroform, dichloromethane and the results suggesting that ethanol was the best solvent for this type of conversion. The results show that the reaction under microwave irradiation continues more effectively compared with traditional heating. Additionally, the catalyst loading effect was observed. The maximum percentage of the mole catalyst was 10 mole%. There was no change in the yield percentage when we increased the catalyst mole percentage.

TABLE I.  
EFFECT OF SOLVENT

S. No	Solvents	Catalyst (mol %)	Time (min.)	Yield (%)
1	CHCl <sub>3</sub>	10	20	16
2	DCM	10	20	23
3	Ethanol	10	15	85
4	Methanol	10	18	73
5	Acetonitrile	10	19	65

After examination of the optimized reaction conditions, this approach was used for the preparation of pyrrole using different aryl glyoxal and 1,3-dicarbonyl compounds under microwave and traditional heating conditions for the development of new pyrrole compounds in presence of uranyl nitrate catalyst. (Table 3). The highly water-soluble catalyst could be isolated by washing with more amount of ice-cold water by filtration. All the constructed derivatives distinguished by IR, elemental analysis, <sup>1</sup>H and <sup>13</sup>C NMR.

TABLE II.  
EFFECT OF CATALYSTS LOADING

S. No	Catalyst	Catalyst (mol %)	Time (min.)	Yield (%)
1	UO <sub>2</sub> (NO <sub>3</sub> ) <sub>2</sub> ·6H <sub>2</sub> O	5	15	75
2	UO <sub>2</sub> (NO <sub>3</sub> ) <sub>2</sub> ·6H <sub>2</sub> O	10	15	85
3	UO <sub>2</sub> (NO <sub>3</sub> ) <sub>2</sub> ·6H <sub>2</sub> O	15	15	85
4	UO <sub>2</sub> (NO <sub>3</sub> ) <sub>2</sub> ·6H <sub>2</sub> O	20	15	85
5	Conc. H <sub>2</sub> SO <sub>4</sub>	1 mL	12 h	55

### III. EXPERIMENTAL PROCEDURE

#### General protocol for the preparation of pyrrole derivatives (3a-i):

##### General Method

A mixture of aryl glyoxal (1 mmol), 1,3-dicarbonyl compound (1 mmol), ammonium acetate (2 mmol), 10 mL of ethanol and uranyl nitrate (10 mol percent) was refluxed as shown in Table 3. After TLC indicated completion of the reaction, the reaction blend was transferred into ice-cold water. Stir the mixture for about 15-20 minutes and left 10 hours. The obtained solids were collected by the filtration through a funnel, washed with cold water and then purified from hot ethanol to provide 3a-i pure derivatives.

TABLE III.  
EXPERIMENTAL RESULTS AND PHYSICAL DATA OF PYRROLE DERIVATIVES

Comp ound	R	R <sub>1</sub>	R <sub>2</sub>	Reaction Time (min)	Yield (%)	m.p. (°C)
3a	H	Me	Me	15	91	dec. 234
3b	H	Me	OMe	16	90	dec. 231
3c	H	Me	OEt	17	86	dec. 233
3d	4-F	Me	Me	18	83	dec. 229
3e	4-F	Me	OMe	18	85	dec. 247
3f	4-F	Me	OEt	19	83	dec. 236
3g	4-NO <sub>2</sub>	Me	Me	19	83	dec. 246
3h	4-NO <sub>2</sub>	Me	OMe	18	86	dec. 224
3i	4-NO <sub>2</sub>	Me	OEt	18	82	dec. 243

##### Microwave irradiation

In a small beaker, a mixture of aryl glyoxal (1 mmol), 1,3-dicarbonyl compound (1 mmol), ammonium acetate (2 mmol), uranyl nitrate (10 mol percent) and ethanol 5 mL was taken and then microwave irradiation was applied to the reaction mixture at an interval of 2 min at 180 W for 11-18 minutes summarized in table 3. The reaction was monitored by TLC. After the reaction was finished, the reaction blend poured into cold water and the separated adduct was filtered, dried, and then purified from hot methanol to provide pure 3a-i compounds, and their physical data are provided in Table 3.

**Compound (3a):** mp: Decomp at 234 °C; FT-IR (KBr): ν 3370, 3123, 3023, 1676, 1532, 1454, 1387, 1216, 1083 cm<sup>-1</sup>; <sup>1</sup>H NMR (400 MHz, DMSO, ppm), δ<sub>H</sub> = 10.65 (s, 1H, NH), 9.23 (s, 1H, OH), 7.09 (d, *J* = 7.3 Hz, 2H, Ar-H), 6.45 (t, *J* = 7.0 Hz, 2H, Ar-H), 6.51 (t, *J* = 7.23 Hz, 1H, Ar-H), 2.12 (s, 3H, CH<sub>3</sub>), 1.79 (s, 3H, CH<sub>3</sub>). <sup>13</sup>C NMR (100.128 MHz, DMSO, ppm), δ<sub>C</sub> = 196.9, 142.3, 134.4, 130.5, 127.5, 123.3,

121.3, 109.4, 109.1, 22.9, 14.4; Elemental analysis, calculated for  $C_{13}H_{13}NO_2$ : C, 72.54; H, 6.09; N, 6.51. Experimental: C, 72.51; H, 6.10; N, 6.53%.

**Compound (3b):** mp: Decomp at 231 °C; FT-IR (KBr):  $\nu$  3430, 3079, 2976, 2872, 1698, 1643, 1523, 1423, 1313, 1191, 1012  $cm^{-1}$ ;  $^1H$  NMR (400 MHz, DMSO, ppm),  $\delta_H$  = 10.43 (s, 1H, NH), 8.98 (s, 1H, OH), 7.34 (m, 2H, Ar-H), 7.28 (m, 3H, Ar-H), 2.12 (s, 3H,  $CH_3$ ), 1.79 (s, 3H,  $CH_3$ );  $^{13}C$  NMR (100.128 MHz, DMSO, ppm),  $\delta_C$  = 169.4, 142.1, 132.4, 131.4, 126.5, 125.9, 121.8, 113.7, 109.9, 61.2, 16.2; Elemental analysis, calculated for  $C_{13}H_{13}NO_3$ : C, 67.52; H, 5.67; N, 6.06. Experimental: C, 67.87; H, 5.65; N, 6.22%.

**Compound (3c):** mp: Decomp at 233 °C; FT-IR (KBr):  $\nu$  3338, 3067, 2978, 1688, 1667, 1523, 1421, 1312, 1178, 1087, 1023  $cm^{-1}$ ;  $^1H$  NMR (400 MHz, DMSO, ppm),  $\delta_H$  = 10.23 (s, 1H, NH), 8.98 (s, 1H, OH), 7.56 (d,  $J$  = 6.9 Hz, 2H, Ar-H), 7.12 (t,  $J$  = 7.23 Hz, 2H, Ar-H), 7.06 (t,  $J$  = 7.12 Hz, 1H, Ar-H), 3.87 (q,  $J$  = 6.98 Hz, 2H,  $CH_2$ ), 2.45 (s, 3H,  $CH_3$ ), 1.42 (t,  $J$  = 6.95 Hz, 3H,  $CH_3$ ).  $^{13}C$  NMR (100.128 MHz, DMSO, ppm),  $\delta_C$  = 169.4, 146.7, 132.9, 131.2, 127.6, 123.9, 121.7, 110.1, 109.7, 60.1, 18.1, 15.2; Elemental analysis, calculated for  $C_{14}H_{15}NO_3$ : C, 68.56; H, 6.16; N, 5.71. Experimental: C, 68.56; H, 6.09; N, 5.76%.

**Compound (3d):** mp: Decomp at 229 °C; FT-IR (KBr):  $\nu$  3448, 3205, 3030, 1684, 1632, 1509, 1409, 1303, 1225, 1168, 1094, 1076  $cm^{-1}$ ;  $^1H$  NMR (400 MHz, DMSO, ppm),  $\delta_H$  = 10.81 (s, 1H, NH), 8.69 (s, 1H, OH), 7.67 (dd,  $J$  = 8.94 Hz, &  $J$  = 5.25 Hz, 2H, Ar-H), 7.05 (m, 2H, Ar-H), 2.23 (s, 3H,  $CH_3$ ), 2.05 (s, 3H,  $CH_3$ );  $^{13}C$  NMR (100.128 MHz, DMSO, ppm),  $\delta_C$  = 194.3, 165.4, 131.4, 129.3, 127.8, 116.4, 115.9, 112.8, 111.9, 25.8, 16.9; Elemental analysis, calculated for  $C_{13}H_{12}FNO_2$ : C, 66.94; H, 5.19; N, 6.01. Experimental: C, 66.88; H, 5.14; N, 6.06%.

**Compound (3e):** mp: Decomp at 247 °C; FT-IR (KBr):  $\nu$  3325, 3067, 2976, 1703, 1659, 1514, 1505, 1489, 1314, 1218, 1158, 1098, 1080  $cm^{-1}$ ;  $^1H$  NMR (400 MHz, DMSO, ppm),  $\delta_H$  = 10.43 (s, 1H, NH), 8.65 (s, 1H, OH), 7.64 (m, 2H, Ar-H), 7.09 (t,  $J$  = 7.9 Hz, 2H, Ar-H), 3.28 (s, 3H,  $CH_3$ ), 2.24 (s, 3H,  $CH_3$ );  $^{13}C$  NMR (100.128 MHz, DMSO, ppm),  $\delta_C$  = 168.5, 161.9, 134.9, 131.2, 126.8, 120.0, 115.9, 112.8, 111.9, 52.4, 18.1; Elemental analysis, calculated for  $C_{13}H_{12}FNO_3$ : C, 62.65; H, 4.85; N, 5.62. Experimental: C, 62.76; H, 4.89; N, 5.39%.

**Compound (3f):** mp: Decomp at 236 °C; FT-IR (KBr):  $\nu$  3345, 3086, 3010, 1738, 1548, 1545, 1528, 1329, 1252, 1173, 1102, 1084, 1028  $cm^{-1}$ ;  $^1H$  NMR (400 MHz, DMSO, ppm),  $\delta_H$  = 10.32 (s, 1H, NH), 8.37 (s, 1H, OH), 7.67 (dd,  $J$  = 5.4 Hz,  $J$  = 7.6 Hz, 2H, Ar-H), 7.08 (m, 2H, Ar-H), 3.92 (q,  $J$  = 6.78 Hz, 2H,  $CH_2$ ), 2.29 (s, 3H,  $CH_3$ ), 1.06 (t,  $J$  = 6.9 Hz, 3H,  $CH_3$ );  $^{13}C$  NMR (100.128 MHz, DMSO, ppm),  $\delta_C$  = 167.9, 161.9, 131.4, 131.0, 129.2, 117.4, 115.9, 112.8, 111.7, 52.3, 18.3, 13.9. Elemental analysis, calculated for  $C_{14}H_{14}FNO_3$ : C, 63.87; H, 5.36; N, 5.32. Experimental: C, 63.83; H, 5.45; N, 5.32%.

**Compound (3g):** mp: Decomp at 246 °C; FT-IR (KBr):  $\nu$  3482, 3345, 1647, 1583, 1511, 1318, 1213, 1176, 1098, 1043, 1011  $cm^{-1}$ ;  $^1H$  NMR (400 MHz, DMSO, ppm),  $\delta_H$  = 11.12 (s, 1H, NH), 10.43 (s, 1H, OH), 8.17 (d,  $J$  = 8.8 Hz, 2H, Ar-H), 7.67 (d,  $J$  = 8.2 Hz, 2H, Ar-H), 2.42 (s, 3H,  $CH_3$ ), 2.12 (s, 3H,  $CH_3$ );  $^{13}C$  NMR (100.128 MHz, DMSO, ppm),  $\delta_C$  = 197.3, 148.6, 142.6, 138.9, 134.2, 123.6, 121.5, 109.8, 196.7, 28.7, 14.9; Elemental analysis, calculated for  $C_{13}H_{12}N_2O_4$ : C, 60.00; H, 4.65; N, 10.76%. Experimental: C, 60.23; H, 4.35; N, 10.54%.

**Compound (3h):** mp: Decomp at 224 °C; FT-IR (KBr):  $\nu$  3523, 3432, 1676, 1621, 1512, 1312, 1232, 1163, 1198, 1056, 1031  $cm^{-1}$ ;  $^1H$  NMR (400 MHz, DMSO, ppm),  $\delta_H$  = 11.43 (s, 1H, NH), 8.98 (s, 1H, OH), 8.18 (d,  $J$  = 8.6 Hz, 2H, Ar-H), 7.87 (d,  $J$  = 8.9 Hz, 2H, Ar-H), 3.76 (s, 3H,  $CH_3$ ), 2.34 (s, 3H,  $CH_3$ );  $^{13}C$  NMR (100.128 MHz, DMSO, ppm),  $\delta_C$  = 168.7, 148.9, 142.3, 139.6, 135.7, 123.7, 121.9, 109.6, 100.7, 50.7, 13.9; Elemental analysis, calculated for  $C_{13}H_{12}N_2O_5$ : C, 56.52; H, 4.38; N, 10.14%. Experimental: C, 56.34; H, 4.45; N, 10.48%.

**Compound (3i):** mp: Decomp at 243 °C; FT-IR (KBr):  $\nu$  3498, 3434, 1683, 1589, 1532, 1323, 1212, 1178, 1102, 1054, 1023  $cm^{-1}$ ;  $^1H$  NMR (400 MHz, DMSO, ppm),  $\delta_H$  = 11.65 (s, 1H, NH), 9.05 (s, 1H, OH), 8.19 (d,  $J$  = 8.3 Hz, 2H, Ar-H), 7.79 (d,  $J$  = 8.7 Hz, 2H, Ar-H), 4.29 (q,  $J$  = 6.9 Hz, 2H,  $CH_2$ ), 2.23 (s, 3H,  $CH_3$ ), 1.23 (t,  $J$  = 6.7 Hz, 3H,  $CH_3$ );  $^{13}C$  NMR (100.128 MHz, DMSO, ppm),  $\delta_C$  = 168.5, 148.6, 144.3, 139.7, 135.7, 123.8, 121.9, 111.5, 100.3, 61.2, 14.9, 14.0; Elemental analysis, calculated for  $C_{14}H_{14}N_2O_5$ : C, 57.93; H, 4.86; N, 9.65%. Experimental: C, 57.99; H, 4.79; N, 9.89%.

#### IV. CONCLUSIONS

A simple and effective method for the synthesis of acetyl-4-hydroxy-2-methyl-5-phenyl-1H-pyrrole derivatives was proposed using  $UO_2(NO_3)_2 \cdot 6H_2O$  as a catalyst for the condensation of various substituted aryl glyoxal, 1,3-dicarbonyl compounds and ammonium acetate under traditional heating and microwave irradiation conditions. The profits of this technique are operational simplicity, short reaction time, easy work-up, easily available catalyst and high conversion of yields.

#### REFERENCES

- [1] E. Y. Schmidt, A. I. Mikhaleva, A. M. Vasiltsov, A. B. Zaitsev and N. V. Zorina, *Arkivoc.*, 2005, 7, 11.
- [2] S. Jiang, H. Lu, S. Liu, Q. Zhao, Y. He and A. K. Debnath, *Antimicrob. Agents Chemother.*, 2004, 48, 4349.
- [3] W. Burli, D. McMinn, J. A. Kaizerman, W. Hu, Y. Ge, Q. Pack, V. Jiang, M. Gross, M. Garcia, R. Tanaka and H. E. Moser, *Bioorg. Med. Chem. Lett.*, 2004, 14, 1253.
- [4] M. S. Mohamed, R. Kamel and S. S. Fatahala, *Eur. J. Med. Chem.*, 2010, 45, 2994.
- [5] R. R. Khanwelkar, G. S. Chen, C. N. Chang, H. C. Hsu, H. C. Lin, Y. C. Shih, S. H. Chou, H. W. Tseng, C. P. Liu, C. M. Tu, T. L. Hu, Y. J. Tsai and J. W. Chern, *Bioorg. Med. Chem. Lett.*, 2010, 18, 4674.

- [6] J. Lehuède, B. Fauconneau, L. Barrier, M. Ourakow, A. Piriou and J. M. Vierfond, *Eur. J. Med. Chem.*, 1999, 34, 991.
- [7] A. Tafi, R. Costi, M. Botta, R. D. Santo, F. Corelli, S. Massa, A. Ciacci, F. Manetti and M. Artico, *J. Med. Chem.*, 2002, 45, 2720.
- [8] A. Trost, A. Gutierrez and R. Livingston, *Org. Lett.*, 2009, 11, 2539.
- [9] L. Wen, Y. Shi and G. Liu, *Org. Chem.*, 2012, 77, 4252.
- [10] D. Hong, Y. Zhu, Y. Li, X. Lin, P. Lu and Y. Wang, *Org. Lett.*, 2011, 13, 4668.
- [11] R. Ballini, L. Barboni, G. Bosica and M. Petrini, *Synlett.*, 2000, 3, 391.
- [12] S. Samadjar, F. F. Becker and B. K. Banik, *Heterocycles.*, 2001, 55, 1019.
- [13] B.K. Banik, S. Samajdar, I. Banik, *J. Org. Chem.*, 2004, 69, 213.
- [14] G. Song, B. Wang, G. Wang, Y. Kang, T. Yang and L. Yang, *Synth. Commun.*, 2005, 35, 1051.
- [15] M. Curini, F. Montanari, O. Rosati, E. Lioy and R. Margarita, *Tetrahedron Lett.*, 2003, 44, 3923.
- [16] B. Wang, Y. Gu, C. Luo, T. Yang, L. Yang and J. Suo, *Tetrahedron Lett.*, 2004, 45, 3417.
- [17] J. Chen, H. Wu, Z. Zheng, C. Jin, X. Zhang and W. Su, *Tetrahedron Lett.*, 2006, 47, 5383.
- [18] T. N. Danks, *Tetrahedron Lett.*, 1999, 40, 3957.
- [19] K. Venkatesan, *CVR Journal of Science and Technology.*, 2018, 14, 112.
- [20] Z. H. Zhang, J. J. Li and T. S. Li, *Ultrason. Sonochem.*, 2008, 15, 673.
- [21] J. X. Chen, M. C. Liu, X. L. Yang, J. C. Ding and H. Y. Wu, *J. Braz. Chem. Soc.*, 2008, 19, 877.
- [22] J. Chen, X. Yang, M. Liu, H. Wu, J. Ding and W. Su, *Synth. Commun.*, 2009, 39, 4180.

# Template for the Preparation of Papers for Publication in CVR Journal of Science and Technology

First Dr.A. Author<sup>1</sup> and Second B. Author<sup>2</sup>

<sup>1</sup>Designation, Name of Institution/Department, City, Country

Email: first.author@hostname1.org

<sup>2</sup>Designation, Name of Institution/Department, City, Country

Email: second.author@hostname2.org

**Abstract:** These instructions give you basic guidelines for preparing camera-ready papers for CVR College journal Publications. Your cooperation in this matter will help in producing a high-quality journal.

**Index Terms:** first term, second term, third term, fourth term, fifth term, sixth term

## I. INTRODUCTION

Your goal is to simulate the usual appearance of papers in a Journal Publication of the CVR College. We are requesting that you follow these guidelines as closely as possible. It should be original work. Format must be done as per the template specified. Diagrams with good clarity with relevant reference within the text are to be given. References are to be cited within the body of the paper. Number of pages must not be less than five with minimum number of 4000 words and not exceeding eight pages. The journal is published in colour. Colours used for headings, subheadings and other captions must be strictly as per the template given in colour.

### A. Full-Sized Camera-Ready (CR) Copy

Prepare your CR paper in full-size format, on A4 paper (210 x 297 mm or 8.27 x 11.69 in). No header or footer, no page number.

**Type sizes and typefaces:** Follow the type sizes specified in Table I. As an aid in gauging type size, 1 point is about 0.35 mm. The size of the lowercase letter “j” will give the point size. Times New Roman has to be the font for main text. Paper should be single spaced.

**Margins:** Top and Bottom = 24.9mm (0.98 in), Left and Right = 16 mm (0.63 in). The column width is 86mm (3.39 in). The space between the two columns is 6mm (0.24 in). Paragraph indentation is 3.7 mm (0.15 in).

Left- and right-justify your columns. Use tables and figures to adjust column length. On the last page of your paper, adjust the lengths of the columns so that they are equal. Use automatic hyphenation and check spelling. Digitize or paste down figures.

For the Title use 24-point Times New Roman font, an initial capital letter for each word. Its paragraph description should be set so that the line spacing is single with 6-point spacing before and 6-point spacing after. Use two additional line spacings of 10 points before the beginning of the double column section, as shown above.

TABLE I.  
TYPE SIZES FOR CAMERA-READY PAPERS

Type size (pts.)	Appearance		
	Regular	Bold	Italic
6	Table caption, table superscripts		
8	Tables, table names, first letters in table captions, figure captions, footnotes, text subscripts, and superscripts		
9	References, authors' biographies	Abstract	
10	Section titles, Authors' affiliations, main text, equations, first letters in section titles		Subheading
11	Authors' names		
24	Paper title		

Each major section begins with a Heading in 10 point Times New Roman font centered within the column and numbered using Roman numerals (except for REFERENCES), followed by a period, two spaces, and the title using an initial capital letter for each word. The remaining letters are in SMALL CAPITALS (8 point). The paragraph description of the section heading line should be set for 12 points before and 6 points after.

Subheadings should be 10 point, italic, left justified, and numbered with letters (A, B, ...), followed by a period, two spaces, and the title using an initial capital letter for each word. The paragraph description of the subheading line should be set for 6 points before and 3 points after.

For main text, paragraph spacing should be single spaced, no space between paragraphs. Paragraph indentation should be 3.7mm/0.21in, but no indentation for abstract & index terms.

## II. HELPFUL HINTS

### A. FIGURES AND TABLES

Position figures and tables at the tops and bottoms of columns. Avoid placing them in the middle of columns. Large figures and tables may span across both columns. Leave sufficient room between the figures/tables and the main text. Figure captions should be centered below the figures; table captions should be centered above. Avoid placing figures and tables before their first mention in the



text. Use the abbreviation “Fig. 1,” even at the beginning of a sentence.

To figure axis labels, use words rather than symbols. Do not label axes only with units. Do not label axes with a ratio

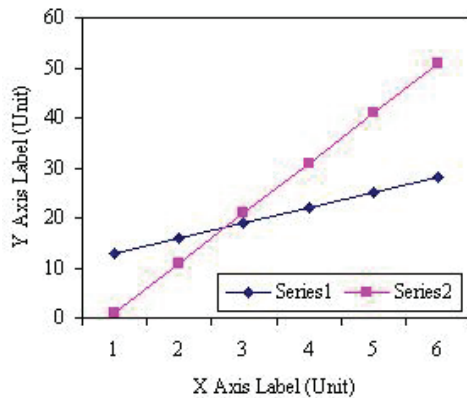


Figure 2. Note how the caption is centered in the column.

of quantities and units. Figure labels should be legible, about 8-point type.

All figures, tables and references must be cited in the text.

Please indicate the broad area/specializations into which the research paper falls, in the covering letter/mail to the Editor, so that reviewers with those specializations may be identified.

### B. References

Number citations consecutively in square brackets [1]. Punctuation follows the bracket [2]. Use “Ref. [3]” or “Reference [3]” at the beginning of a sentence:

Give all authors’ names; use “et al.” if there are six authors or more. Papers that have not been published, even if they have been submitted for publication, should be cited as “unpublished” [4]. Papers that have been accepted for publication should be cited as “in press” [5]. In a paper title, capitalize the first word and all other words except for conjunctions, prepositions less than seven letters, and prepositional phrases. Good number of references must be given.

**Latest references in the area must be included and every reference must be cited in the text of the research article.**

### C. Footnotes

Number footnotes separately in superscripts <sup>1, 2, ...</sup>. Place the actual footnote at the bottom of the column in which it was cited, as in this column. See first page footnote as an example.

### D. Abbreviations and Acronyms

Define abbreviations and acronyms the first time they are used in the text, even after they have been defined in the

abstract. Do not use abbreviations in the title unless they are unavoidable.

### E. Equations

Equations should be left justified in the column. The paragraph description of the line containing the equation should be set for 6 points before and 6 points after. Number equations consecutively with equation numbers in parentheses flush with the right margin, as in (1). Italicize Roman symbols for quantities and variables, but not Greek symbols. Punctuate equations with commas or periods when they are part of a sentence, as in

$$a + b = c . \tag{1}$$

Symbols in your equation should be defined before the equation appears or immediately following. Use “(1),” not “Eq. (1)” or “equation (1),” except at the beginning of a sentence: “Equation (1) is ...”

### F. Other Recommendations

Use either SI (MKS) or CGS as primary units. (SI units are encouraged.) If your native language is not English, try to get a native English-speaking colleague to proofread your paper. Do not add page numbers.

## III. CONCLUSIONS

The authors can conclude on the topic discussed and proposed, future enhancement of research work can also be briefed here.

## REFERENCES

- [1] G. Eason, B. Noble, and I. N. Sneddon, “On certain integrals of Lipschitz-Hankel type involving products of Bessel functions,” *Phil. Trans. Roy. Soc. London*, vol. A247, pp. 529–551, April 1955.
- [2] J. Clerk Maxwell, *A Treatise on Electricity and Magnetism*, 3<sup>rd</sup> ed., vol. 2. Oxford: Clarendon, 1892, pp.68–73.
- [3] I. S. Jacobs and C. P. Bean, “Fine particles, thin films and exchange anisotropy,” in *Magnetism*, vol. III, G. T. Rado and H. Suhl, Eds. New York: Academic, 1963, pp. 271–350.
- [4] K. Elissa, “Title of paper if known,” unpublished.
- [5] R. Nicole, “Title of paper with only first word capitalized”, *J. Name Stand. Abbrev.*, in press.
- [6] Y. Yorozu, M. Hirano, K. Oka, and Y. Tagawa, “Electron spectroscopy studies on magneto-optical media and plastic substrate interface,” *IEEE Transl. J. Magn. Japan*, vol. 2, pp. 740–741, August 1987 [Digests 9<sup>th</sup> Annual Conf. Magnetism Japan, p. 301, 1982].
- [7] M. Young, *The Technical Writer's Handbook*. Mill Valley, CA: University Science, 1989.
- [8] T. Ali, B.K. Subhash and R.C. Biradar, “A Miniaturized Decagonal Sierpinski UWB Fractal Antenna”, *PIERS C*, vol. 84, pp. 161-174, 2018.

## *In the next issue (Vol 19, December 2020)*

- 1. Performance and Emission Characteristics of Diesel Engine by Semi Ellipsoidal Arc grooves on Piston Crown Using Apricot oil*  
*Sk. Mohammad Shareef, A.L.N.Arun Kumar, T.Venkatesh, M.RaviKumar*
- 2. Parametric optimization of submerged arc welding using Taguchi method on P91 steel*  
*Vidyanand Kumar, Dr. Manjeet Kharub, Neeraj Kumar Jha*
- 3. Structural Analysis of Centrifugal Compressor Impeller using ANSYS*  
*T. Venkatesh, A.L.N. Arun Kumar, Sk. Mohammad Shareef, P. Lava Kumar*
- 4. Study of Condensation on PDMS Substrates for Enhanced Solar Still*  
*M. Udaya Kiran, Sk. Mohammad Shareef, A. L. N. Arun Kumar*
- 5. Analysis of Powder-Mixed EDM Process Characteristics of Tungsten Carbide alloy by using GRA technique*  
*Jagdeep Singh, Dr. Manjeet Kharub, Sarat Kumar Sahoo*

## ABOUT THE COLLEGE

CVR College of Engineering (A UGC Autonomous Institution) was established in the year 2001, and its fifteenth batch of students graduated from the College. This college has been ranked **141** by **NIRF** among the Engineering institutions of the country for the fourth time in a row in the 101-150 range. The college also stands 3<sup>rd</sup> in Telangana for the 4<sup>th</sup> time consecutively.

The College was the **first** college in Telangana that was promoted by NRI technology professionals resident in the US. The NRI promoters are associated with cutting-edge technologies of the computer and electronics industry. They also have strong associations with other leading NRI professionals working for world-renowned companies like IBM, Intel, Cisco, Facebook, AT&T, Google and Apple who have agreed to associate with the College with a vision and passion to make the College a state-of-the-art engineering institution.

The college has many accomplishments and to name a few, it obtained **NBA Tier 1 accreditation for its UG Programs**, **NAAC 'A' grade**, **UGC autonomous status**, **National Employability Award** for seventh year in a row and received a very high rating by several ranking agencies including the most recent Education World ranking of third best college in Telangana and Outlook magazine, rating CVR CE, one among the **top 100 colleges in the country**, and **AAAA grade** from Careers 360.

The college has been sanctioned Rs.2.87 Crores from NEWGEN IEDC from the Department of Science and Technology. NEWGEN centre has been established to enable the staff and students to work on NEWGEN projects. 15 projects were completed in 2019-20 and 19 projects are lined up for the academic year 2020-21.

Faculty members are working on Rupees One crore worth projects with funding from AICTE, UGC and ISRO.

The students have brought home laurels by winning prizes in competitions outside the college. A batch of six students under the mentorship of Dr. Gaurav Sharma of the department of ECE won the **FIRST** prize of **Rs.1 Lakh** in the hardware version of the Smart India Hackathon in June 2019. A Group of three students of EIE and one student of IT have won the bronze cup along with a cash prize of **Rs. 50,000** in the Design contest by Mitsubishi Electric.

The college has been creating records year after year. With more than 100 companies visiting CVR and more than 750 placements for the 2018-19 academic year, it is the highest among the peer group of colleges. The highest offer of Rs. 30.25 Lakh PA was bagged by 7 students and close to 25 students got offers higher than Rs. 10 Lakh PA. About 65 offers are higher than Rs. 7 Lakh PA and another 60 offers are higher than Rs. 5 Lakh PA. With this, CVR became the leading college in entire Telangana in terms of the offers with higher salaries. CVR has made huge progress in a short span of time and was preferred by the students and parents during the EAMCET counseling this year and is among the top 3 colleges in the state.

In keeping with the current global emphasis on green and eco-friendly energy generation, 360kW Solar PV plant has been installed on the campus to meet the power requirements of the college to a significant extent.

### **CALL FOR PAPERS:**

**Papers in Engineering, Science and Management disciplines are invited for Publication in our Journal. Authors are requested to mail their contributions to Editor, CVR Journal of Science and Technology (Email Id: [journal@cvr.ac.in](mailto:journal@cvr.ac.in)). Authors can also submit their papers through our online open journal system(OJS) [www.ojs.cvr.ac.in](http://www.ojs.cvr.ac.in) or [www.cvr.ac.in/ojs](http://www.cvr.ac.in/ojs). Papers are to be written using a Standard Template, which may be obtained on request from the Editor. It is also available on the college website [www.cvr.ac.in](http://www.cvr.ac.in) under In-House Journal.**



# CVR JOURNAL OF SCIENCE AND TECHNOLOGY



## CVR COLLEGE OF ENGINEERING

(UGC Autonomous- Affiliated to JNTU Hyderabad)

Mangalpalli (V), Ibrahimpatnam (M),

R.R. District, Telangana - 501510

<http://cvr.ac.in>